Rotating Thin Films: the Vortex Fluidic Device

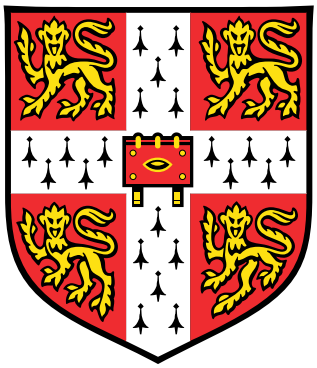

Evgenia Leivadarou
Queens' College

Supervisor: Prof. Stuart Dalziel
Department of Applied Mathematics and Theoretical Physics
University of Cambridge

A dissertation submitted for the degree of
Doctor of Philosophy

March 2019

Personal Declaration

I hereby declare that the contents of this thesis are original and have not been submitted in whole or in part for consideration for any other degree or qualification in this, or any other university. This thesis is my own work and contains nothing which is the outcome of work done in collaboration with others, except as specified in the text and Acknowledgements.

Evgenia Leivadarou
GK Batchelor Laboratory, DAMTP
University of Cambridge
March 2019

Abstract

Rotating Thin Films: the Vortex Fluidic Device

Evgenia Leivadarou

The motivation of this thesis, is the understanding of the role of fluid mechanics in the performance of the Vortex Fluidic Device (VFD), developed by the Raston laboratory at Flinders University, Australia. The VFD is a novel technology in the synthesis of organic chemicals and in material processing, and is considered a green technology device, achieving enhanced chemical reactivity without temperature variations or the use of additional catalysts. This is the first research project focused in the fluid mechanics of the VFD, thus relevant literature is limited to the performance of the device with respect to chemical reactivity.

The methodology employed to pursue this understanding is based on the two processing methods, i.e. confined mode (CM) and continuous flow (CF). In CM, a fixed volume of liquid is placed at the base of the VFD before rotation is initiated, with the characteristics of the film at steady state describing the fluid mechanics environment for most of the processing time. In CF, droplets fall periodically in a rotating tube which sustains a liquid thin film developed along the walls.

To explore the dynamics of droplet landing and spreading, experiments were conducted using flat and hemispherical disks. In every spinning disk experiment the radial evolution of single droplets and the onset of instabilities, at the contact line and along the free surface of the film, were explored for a range of parameters. The parameters under investigation were the rotation rate, the height of release, the droplet volume, the smoothness and the geometry of the disk. During the spreading, the droplet was divided in two different areas, the film and the ring, with the ring volume being an important component for the onset of instabilities. The fluid motion related to ring volume variations (initially growing and later decreasing in volume, leaving liquid behind), described in this thesis, has not been found in existing literature. Perturbations at the contact line lead to fingering instability, with the fingers unfolding retrograde to the rotating disk. In parallel, spiral waves appear at the free surface of the film, unfolding prograde to the rotating disk.

In the VFD, experiments were conducted under CM, exploring the film development over time, the film thickness and the reaction rate at a steady state of rotation. In CF, the entrainment of droplets in an already rotating film was explored. The film thickness tends to be the most critical parameter for the performance of the device as it defines whether the reaction occurs under turbulent or laminar conditions. Neutron imaging experiments, conducted at the Australian Nuclear Science and Technology Organisation (ANSTO), gave an insight to the film thickness at steady state in CM. The technique is more appropriate for stationary objects, thus a new methodology was developed in this thesis for rotating objects. Knowing the film thickness, pressure gradients along the film were determined. Keeping all the non-fluid related parameters the same, increased rotation rate leads to decreased thickness, which works in favour of homogeneous distribution of the reactants and increased pressure differences, directly related to variations in diffusion and advection.

Overall, mathematical approximations were developed to describe the experimental observations both in the rotating disks and in the VFD. A new spreading pattern, was observed in the rotating disks, while mechanisms for enhanced diffusion and advection were observed in the VFD.

Acknowledgement

First of all, I would like to thank my supervisor, Prof. Stuart Dalziel, for giving me this opportunity to pursue my PhD studies at the Department of Applied Mathematics and Theoretical Physics (DAMTP) and enabling my transition from civil engineering - to a fluid dynamicist. I am also grateful for his continuous support and encouragement, and for his patience with my countless questions. His commitment to make the GK Batchelor Laboratory an inclusive environment, despite my physical limitations, made this PhD possible.

A special thank you goes to Dr Jamie Partridge who helped me overcome my physical limitations and conduct my experiments and to the technicians of the GK Batchelor Laboratory (Mr David Page-Croft, Mr Andy Denson, Mr Mark Hallworth, Mr Colin Hitch, Mr John Milton and Mr Paul Mitton) who constructed the set–up of my experiments and more importantly helped me deal with the technical problems of my wheelchair.

I would also like to thank Prof. Colin Raston, who trusted me to conduct research on the fluid mechanics of his invention, the Vortex Fluidic Device (VFD). A special thank you goes to Dr Daniel Mangos, a post doctoral researcher at the Raston group, who helped me organise my trip to Australia, to Mr David Harvey, one of the PhD students of Prof. Raston, who suggested chemical reactions, used in this thesis, and to Dr Timothy Solheim who provided motivation on VFD research during his visit at DAMTP and helped me organise my visit to the Australian Nuclear Science and Technology Organisation (ANSTO).

I gratefully acknowledge the financial support of the John S. Latsis Foundation, Tima Foundations, Minas Kulukundis Trust, Muscular Dystrophy Association Hellas, DAMTP, Queens' college, the Disability Resource Centre and the Engineering and Physical Sciences Research Council (EPSRC). I should also thank Ms Valia Fragkou, Ms Hara Papakanderaki and the late Mr Dionisis Bouloukos, who provided their support in the process of funding my research.

Finally, I would like to thank my family, who taught me to be persistent and stay motivated. I would also like to thank Dr Perla Sousi for being a true inspiration to me and a very good friend throughout my PhD. I should also thank my first mentor, Prof. Mark Bonazountas, for his advice to pursue an academic career abroad. A special thank you goes to Mr Theodoris Georgiadis, who assisted me to my two–month trip to Australia. I would also like to thank Dr Grigorios Fournodavlos, Mr Benjamin Jackson, Mr David Parker and Mx Jonny Michael Foonlan Tsang for their useful insights to the theoretical background of my research. Thank you also goes to Mr Balazs Jakab, my physiotherapy instructor, who kept me healthy during the years of my research in Cambridge and to an 'army' of friends who stood by my side, dealing with physical limitations and providing support, especially during the more stressful times of this research.

"$\tau\grave{\alpha}\ \pi\acute{\alpha}\nu\tau\alpha\ \rho\epsilon\tilde{\imath}\ \kappa\alpha\grave{\imath}\ \mu\eta\delta\acute{\epsilon}\pi\sigma\tau\epsilon\ \kappa\alpha\tau\acute{\alpha}\ \tau'\ \alpha\upsilon\tau\acute{o}\ \mu\acute{\epsilon}\nu\epsilon\iota\nu$"

$\boldsymbol{H\rho\acute{\alpha}\kappa\lambda\epsilon\iota\tau\sigma\varsigma,\ 544-484\ B.C.}$

Contents

Symbols

Acronyms

ANSTO	Australian Nuclear Science and Technology Organisation
CF	Continuous flow
CM	Confined mode
FB	Flat brass disk
FG	Flat glass disk
fps	Frames per second
GT	Glass tube
HD	Hemispherical disk
NBR	Nitrile Butadiene Rubber
OPAL	Open pool Australian lightwater reactor
PIV	Particle image velocimetry
QT	Quartz tube
RMS	Root–mean square
rpm	Rotations per minute
SDR	Spinning disk reactor
VFD	Vortex fluidic device

Greek Symbols

α	Contact angle
β	Inclination angle
β_m	Momentum correlation factor
γ	Surface tension between liquid and air
γ_{sa}	Surface tension between solid surface and air
γ_{sl}	Surface tension between solid surface and liquid
δ	Boundary layer thickness
$E_\nu^{'}$	Viscous dissipation at the transient stage
ζ	Vorticity
θ	Polar angle from negative z axis - spherical coordinate
θ_r	Polar angle from negative z axis at the leading edge of the ring
κ	Boltzmann constant
λ	Wavelength
μ	Dynamic viscosity
ν	Kinematic viscosity
ρ	Density
ρ_b	Density of bromothymol blue
Σ	Summation
Σ_a	Absorbed neutrons
Σ_s	Scattered neutrons
$\underline{\underline{\sigma}}$	Stress tensor
σ	Standard deviation
τ	Viscous drag
τ_0	Viscous drag at $z = 0$
Φ	Dissipation per unit mass
ϕ	Azimuthal angle at cylindrical and spherical polar coordinates
ω	Angular velocity

Roman Symbols

A	Initial cross–sectional area in a gravity current
$[A]$	Concentration of reactant A
a	Function coefficient
B	Functional variable
$[B]$	Concentration of reactant B
Bo	Bond number
b	Function coefficient
C	Functional variable
$[C]$	Concentration of mixing product C
C_0	Model coefficient
C_ω	Model coefficient
Ca	Capillary number
C_b	Concentration of bromothymol blue
c	Function coefficient
c_p	Phase velocity
D	Diffusion coefficient
D_f	Optical thickness
D_m	Reaction coefficient
E	Ekman number
E_α	Activation energy of the reaction
E_c	Centrifugal potential energy
E_f	Free energy by Gibbs
E_g	Gravity potential energy
E_H	Enthalpy
E_i	Internal energy
E_k	Kinetic energy release time
E_k'	Kinetic energy contact time
E_k''	Kinetic energy transient time
E_s	Surface energy release time
E_s'	Surface energy contact time
E_s''	Surface energy transient time
F_c	Centrifugal force
F_g	Gravitational force
F_ν	Viscous force
Fr	Froude number
g	Gravity
g'	Rotational acceleration in the VFD
H	Height from the solid substrate to the centre of the droplet mass
h	Thickness
h_0	Height of the droplet immediately after the impact
h_f	Thickness of the film
h_r	Thickness of the ring
I	Light intensity
I_0	Neutron imaging incident beam
I_{max}	Maximum intensity
k	Wave number
L	Length of the film in the hemispherical disk and in the VFD.
L_c	Critical arc length
L_{max}	Maximum film length in the VFD
l	Characteristic length scale of the ring
l_D	Length of reaction due to diffusion only
l_R	Length of reaction

Roman Symbols

m	Mass
N_f	Number of fingers
P	Pressure
Pe	Péclet number
p	Functional parameter
Q	Volume flux
q_r	Radial flow per unit length
R	Internal radius of the hemispherical disk or of the VFD tube
R_a	Ideal gas constant
Re	Reynolds number
Ro	Rossby number
r	Radial coordinate in cylindrical polar coordinates
$\mathbf{r}$	Position vector in cylindrical pollar coordinates
r_0	Initial radius of the droplet at release and contact time
r_b	Radius from the z axis to the free surface at the base of the tube
r_c	Critical radius
r_f	Radius of the film at the intersection with the ring
r_m	Radius of a single molecule
r_r	Radius of the wet area at the contact line
r_t	Maximum transient radius
S	Entropy
s_ϕ	Spiral angle
T_e	Temperature
t	Time variable
t_i	Induction time
t_c	Critical time
t_t	Time to reach the transient radius
t_m	Mixing time
U	Surface velocity
$\mathbf{u}$	Vector velocity of the fluid element
u_r	Radial velocity in the flat disk
u_θ	Velocity of arc length L in the hemispherical disk
u_ϕ	Velocity in the ϕ direction - hemispherical disk or the VFD
u_z	Velocity in the z direction.
$\bar{u}$	Depth-averaged velocity
$\hat{u}$	Velocity profile
V	Droplet volume
We	Weber number
$x_{I_{max}}$	Location of maximum pixel intensity
Z	Collision rate
Z_s	Film shape

Chapter 1

Introduction

Flow chemistry is the process of performing chemical reactions continuously. Reactive components are pumped together as continuous streams that flow through the device. Flow chemistry devices have the advantage of reduced reaction times, flow uniformity, green processing and environmentally friendly products. Chemical reactions are strongly coupled with hydrodynamic transport processes, such as advection and diffusion. The formation of thin films is believed to be one of the main factors that makes these devices outperform compared to traditional methods of processing, such as batch reactors (Pask et al., 2012).

Many devices, that work with the formation of films, consist of rotating substrates. The thin film thickness in spinning devices usually ranges from some nanometres to several micrometres. The spinning surface is used either to provide uniform coating or to accelerate chemical reactions. For uniform films in spinning disks, the rotation rate is relatively low, approximately up to 3,000 rpm, suppressing fluid mechanics instabilities (Bhatelia et al., 2009). For the acceleration of chemical reactions in continuous flow devices, the rotation rate is increased, reaching 16,000 rpm (Ahmed & Youssef, 2012). This thesis attempts to connect fluid mechanics in rotating films with the performance of chemical reactions in spinning devices.

Within thin films, diffusion and shearing create a dynamic environment, i.e. the tendency to minimize variations, e.g. in concentration or heat, throughout the film. The correlation between chemical reactions and fluid mechanics is an open question of a research area called fluctuating hydrodynamics, combining the scientific input from mathematics, physics, chemistry and biology (Bhattacharjee et al., 2015).

1.1 Spinning Devices

Spinning devices are extensively used for several industrial applications, such as in coatings for optics, material processing for electronics and chemical reactions for the production of pharmaceuticals. The most popular use of spinning devices is called spin coating. In spin coating, a rotating disk causes viscous drag to the fluid, which leads to centrifugal forces that guide the fluid outwards, forming a thin film. The air boundary is also set in rotation at the interface with the liquid and leads to fast drying times. There are several patents available, that suggest a flat spinning disk with varying additional features, that mainly alter the fluid spreading in the device. Most of the spin coating devices consist of spinning disks and work placed horizontally,

tilted or covered by a shield. The presence of a shield for example, could have a detrimental effect to the dynamics of the air at the interface with the liquid film. The detailed description of these devices is outside the spectrum of this project. However the configuration of a flat and a hemispherical disk and the tilting of the devices are investigated in this thesis, with the analysis covering the fundamental characteristics of many of the thin film devices.

Although spin coating reduces the processing time, industries have raised concerns regarding the wasted materials. The residence time is limited, lowering the performance of production for nano-materials, which require more time for phase separation and aggregation of self-assemblage. Most of the material is eventually expelled from the device and only the material coated can be used. Therefore, flow chemistry devices with extended processing time become more attractive for industrial applications.

This thesis is focused on the fluid mechanics of flat and hemispherical disks and on a new flow chemistry device, the Vortex Fluidic Device (VFD), with great potential in terms of scalability, energy efficiency, control of processing time and waste reduction.

1.2 The Vortex Fluidic Device

The VFD is a novel technology in the synthesis of organic chemicals and in material processing, developed by the Raston laboratory at Flinders University, Australia. There is significant interest in the VFD as it provides a new 'greener' alternative for many industrial applications, with advantages ranging from reduced energy requirements and waste streams, to high flow rates and the avoidance of clogging. It is a platform with applications in exfoliating graphene (Wahid et al., 2013*a*), in wrapping algal cells to control cellular replication (Wahid et al., 2013*b*), in processing aromatic aldehydes and ketones (Yasin et al., 2012) and in enhancing protein folding and pharmaceutical production (Eroglu et al., 2013), amongst a myriad of other applications.

The VFD is a device that consists of a rapidly rotating tube, as illustrated in Figure 1.1, that develops a liquid thin film along the walls. The reactants interact in the film during the processing time. The feeding of the reactants and the collection of the product of the reaction vary according to the mode of processing. The VFD can operate in two different processing modes. Assuming that the reactants are in liquid phase, in the case of 'confined mode' (CM), the liquid volume is placed in the tube before the initiation of motion. The VFD, in CM, operates as a batch processing device. The tube is set into rotation, and the solution reaches a steady state of rotation, with a predetermined processing time. The product of the reaction is extracted when the tube returns to rest. In 'continuous flow' (CF), pipettes feed liquid continuously into the tube, in the form of droplets, while the tube is already at a steady state of rotation. The liquid propagates along the walls, in the form of a thin film. The product of the reaction is extracted from the top of the tube. Detailed analysis of the parts of the device follows in section 3.2.1.

The length and the thickness of the thin film in CM and the residence time in CF are related to the rotation rate, flow rate, the position of the pipette and the tilt angle β of the tube (Britton et al., 2015). In contrast with the spinning disks, the residence time and the tube geometry, i.e. length and radius, are decided by the user. In CF, ignoring complications such as fluid instabilities and mechanical vibrations, high shear stress exists in the boundary layer during the

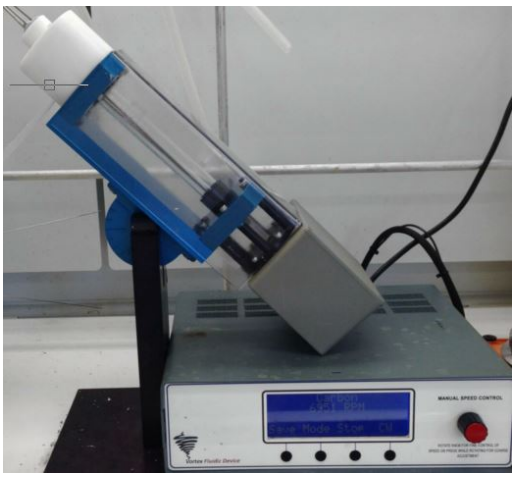

(a)

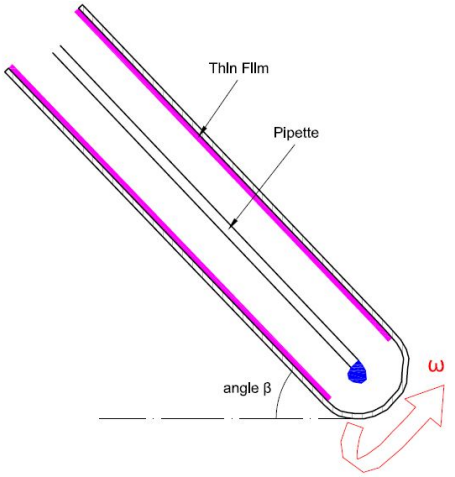

(b)

Figure 1.1: The Vortex Fluidic Device: (a) the VFD, developed by the Raston laboratory, (b) a sketch of the device showing the feeding of the reactants, via the pipette, in the form of droplets and the development of a thin film along the walls. (the picture in this Figure has been provided by the Raston laboratory, Flinders University, Australia).

acceleration after the droplet landing. The droplet once detached from the pipette, falls under the force of gravity onto the rotating film. The VFD is designed to work inclined from 0° to 85°. Due to the inclination of the tube, the droplet lands always at the walls of the tube and not at the hemispherical base. The fluid elements, entering the rotating film, experience high shear stress, and while this is intense, a given fluid element is only exposed to it briefly before it is absorbed by the thin film, where shearing is still present but significantly reduced.

A recent publication by Britton et al. (2016), reports the synthesis of di-carboxylate esters, using the VFD tilted at 45°, at room temperature, with a flow rate of 0.45 ml/min. A maximum product yield of 90% was achieved at approximately 7,500 rpm, with a residence time of 3.25 minutes or less. To demonstrate the improved efficiency of the VFD, the same solution, left for one hour in a round bottom flask, resulted in a 69% product yield.

Another suitable application for the VFD is the slicing of carbon nanotubes. During processing, a single cylindrical carbon nanotube of 200 nm length bends with a radius of curvature of $\mathcal{O}(10)$ nm. The strained bonds are eventually ruptured by a laser irradiation. Both in CM and in CF maximum performance was achieved with a tube of 20 mm diameter, tilted at 45°, from 7,000 rpm to 8,000 rpm (Vimalanathan et al., 2016).

The most relevant publication to this thesis was very recently available as a collaboration between the Raston laboratory, the GK Batchelor Laboratory in the Department of Applied Mathematics and Theoretical Physics (DAMTP) and the Australian Nuclear Science and Technology Organisation (ANSTO) (Solheim et al., 2019). Solheim et al. determine the film shape of a liquid film rotating at steady state in the VFD, balancing gravitational and centrifugal force. The shape model was also developed in parallel for this thesis (with Solheim and the present author not directly collaborating), as the two laboratories are in collaboration and we were unaware of the time the publication of Solheim et al. would be publicly available. The shape model follows in chapter 6 (section 6.3.1).

Solheim et al. also attempted to verify the shape model by conducting a first round of neutron imaging experiments at ANSTO. The film thickness was determined by the user, measuring manually the number of pixels of maximum intensity at two different cross–sections along the tube. With the configuration of the first round of experiments, Solheim et al. were unable to obtain measurements for rotation rates greater than 5,000 rpm. Therefore, a second round of more detailed neutron imaging experiments followed, while the present author was visiting ANSTO, and are presented in this thesis along with a new methodology for the interpretation of the results. The more detailed experiments were obtained by using maximum resolution and maximum neutron flux at ANSTO. The description of the experiments follows in chapter 3 (section 3.2.3.1).

1.3 Research aim and hypothesis

The Raston laboratory has found that the performance of the VFD appears to be optimised, for a range of reactions and processes, at approximately 7,000 rpm to 8,000 rpm, with the device tilted at 45°, both in CF and in CM. Beyond or below that range, the product yield is reduced. However, the reasons for this optimum configuration have not been determined. One of the main research questions is whether at this range of rotation rates there is an alteration in the fluid mechanics properties that could effect chemical reactivity.

Chemical reactivity can be achieved due to diffusion and advection. The main hypothesis, in the VFD and in this thesis, is that the fluid mechanics of the spinning devices can influence the reaction rate by increasing the conditions of diffusion and shearing. This project attempts to determine the nature of fluid mechanics that increase chemical reactivity in the VFD. The results describe the investigated mechanisms and indicate the optimum conditions for the maximum performance of the spinning disks and especially of the VFD. Temperature variations are ignored as one of the aims of 'green' chemistry is the avoidance of heating.

With the exception of CM in the VFD, the residence time in the reactor greatly depends on the rotation rate of the device, so that higher shear comes at the cost of shorter residence times, for a given tube length, flow rate and inclination angle. Chemical reactions in the VFD have been tested, by the Raston laboratory, at rotation rates ranging from 1,000 rpm to 9,000 rpm. This thesis uses the same range of rotation rates, focusing on the shear stress and the instabilities during the droplet spreading, the film development and the film at steady state. The optimisation also focuses on other fluid mechanics parameters such as the flow rate, wettability and contact line dynamics, gravity, the orientation and the geometry of the tube.

The problem is initially simplified into a single liquid droplet, spreading on a rotating surface, resulting in complex fluid motion. While the spreading dynamics in spin coating of constant flux are relatively well understood, the pattern for the axisymmetric spreading of single droplets and the wave regime described in this thesis have not previously been reported in detail. Furthermore, the fluid mechanics in the VFD have previously been poorly described and mostly qualitatively.

This thesis is the first work of quantitative results from a fluid mechanics perspective in the VFD. In addition to traditional experimental diagnostic techniques, a new method is developed for assessing the results from neutron imaging experiments in rotating objects. Mathematical

approximations are also developed, describing the film formation and investigating possible contact line instabilities.

In order to investigate the complex mechanics in the VFD, we explore separately the base of the tube as the initial stage of spreading and the film formation at the walls. A combination of experiments on flat and hemispherical disks helped in the description of the motion at the hemispherical base of the tube. In addition, experiments in the VFD determined important characteristics, such as the rate of film development along the walls, the film thickness and reaction rates. The experimental process, is the timeline of this thesis and was developed according to the devices in use, is illustrated in Figure 1.2.

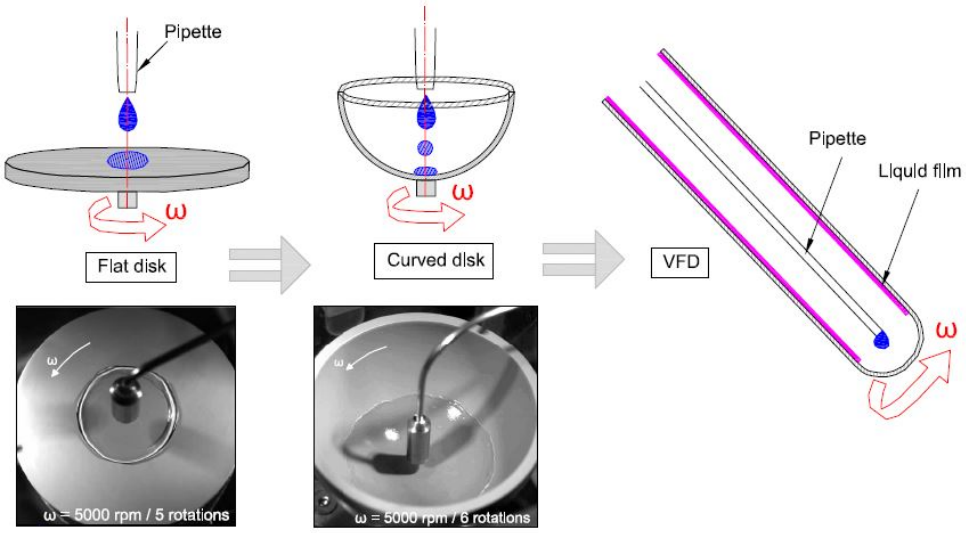

Figure 1.2: Methodology - geometrical approach: Investigation of the spreading pattern on a flat disk and comparison with the spreading pattern on a hemispherical disk will give useful insight to the fluid motion at the base of the VFD.

Two main simplifications have been made in order to relate the problem of spreading droplets in rotating surfaces with the VFD. Firstly, as the VFD can be operated with a single pipette feeding pre-mixed liquid to the base, the project focuses on the use of one pipette and the spreading pattern of a single droplet. Secondly, as the film is thin, the base of the tube can be considered locally flat. Therefore, the spreading of single droplets on rotating disks is useful for the understanding of the early stages of droplet spreading in the VFD.

1.4 Stages of film development

The research problem, i.e. understanding the fluid mechanics in the VFD, is approached according to the stages of film development. The spinning disks and CF of the VFD have an important similarity, regarding the liquid feeding. Despite the continuous flow of the syringe pump, the surface tension of the fluid promotes, at the lower edge of the pipette, the formation of discrete droplets, which detach from the pipette and fall under the force of gravity onto the substrate which rotates with angular velocity ω.

When the droplet lands on the axis of rotation, the bottom of the liquid droplet adheres on the surface and is simultaneously dragged by the moving substrate. The top of the droplet,

reshapes and expands above the rotating volume due to the inertia of the impact. The top of the droplet and the base of the droplet move with different velocities, with the motion at the bottom of the droplet initiated by the rotating disk. The information of the rotating substrate is dissipated upwards. The thickness of the rotating film, at early times ($\omega t \ll 1$), increases as a 'Rayleigh layer', scaling as $\delta \sim (\nu t)^{1/2}$, where ν is the kinematic viscosity of the fluid.

The transition to the second stage, ignoring surface tension, occurs when the thin boundary layer that is brought into rotation reaches the height of a 'von Kármán layer', $\delta \sim (\frac{\nu}{\omega})^{1/2}$, after approximately 1 rotation period. The fluid within the von Kármán layer is ejected centrifugally outwards, driving a radial and an azimuthal motion (Moulin & Flór, 2004). The fluid above the boundary layer descends, and replaces the liquid expelled outwards. At the third stage, the fluid ejected by the von Kármán layer, spreads axisymmetrically with viscous forces balancing the centrifugal force as a 'Nusselt film'. This term comes from Wilhelm Nusselt's theoretical analysis (1916) of falling liquid films, assuming laminar flow with a flat, smooth and shear-free gas–liquid interface (Moran et al., 2002). The velocity profile can be determined either by applying the Navier–Stokes equation or directly from a force balance for a fluid element in the film. On the flat disk, the film is eventually drained out. On the hemispherical disk, the liquid climbs the curved base and depending on ω, the liquid may be ejected from the device or reach a steady state of rotation. In CF in the VFD the liquid climbs the hemispherical base, forms a thin film that reaches a steady state of rotation. A representation of the stages of film development in CF is shown in Figure 1.3.

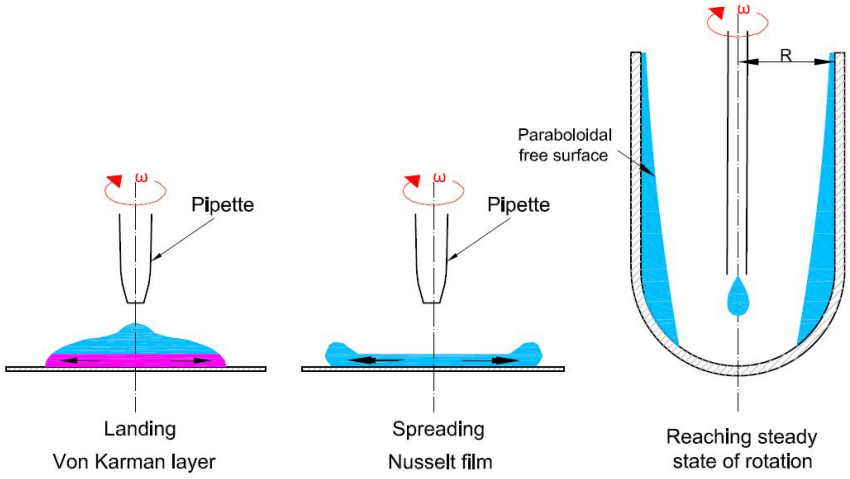

Figure 1.3: Stages of spreading in CF, assuming a vertically positioned tube, with the hemispherical base locally flat, where initially the fluid is expelled from the von Kármán layer, spreads axisymmetrically as a Nusselt film and climbs the walls, reaching eventually a steady state of rotation.

In CM, assuming a vertically positioned VFD with a flat base tube, the boundary layer at the base of the tube and the rotating walls bring the fluid into rotation. The circulation of the constant thickness boundary layer, allows viscous stresses to increase the volume of the fluid that is rotating. At the base of the tube, the von Kármán layer expels fluid radially outwards. The fluid at the region above the von Kármán layer is irrotational. This almost stationary volume of fluid moves downwards, towards the base of the tube, replacing the fluid that has been expelled and feeding the von Kármán layer. The propagation along the walls depends

mainly on ω, which creates a pressure gradient in the radial direction. The pressure gradient guides the liquid upwards, with the fluid eventually reaching a steady state of rotation. The free surface of the film forms a parabola with the length of the elevation of the upper liquid edge scaling as $L \sim \frac{\omega^2 R^2}{g}$ (Wilkes & Bike, 1999), where R is the internal radius of the tube and g is gravity. As the fluid propagates upwards the lower edge of the free surface meets the base of the tube and eventually forms a thin film. In this thesis, L is defined as the length between the lower and the upper edge of the film. A representation of the stages of film development in CM is shown in Figure 1.4.

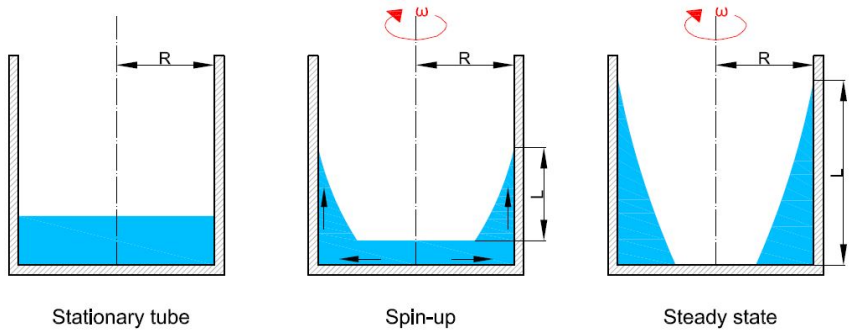

Figure 1.4: Stages of spreading in CM, assuming a vertically positioned tube with a flat base. Initially the fluid is at rest in the stationary tube. Once the tube is set into rotation the fluid is expelled from the von Kármán layer, spreads axisymmetrically and moves within the Stewartson layers along the walls. Eventually the fluid reaches a steady state of rotation.

We will see later that the film thickness is an important factor for the determination of the fluid mechanics in the VFD. At this point we set the boundary layer thickness that will be compared to the film thickness measured in the VFD. During the early stages of spin–up in CM, the von Kármán layer at the base drives the formation of two Stewartson layers. The Stewartson layer with upwards motion scales as $\sim R\left(\frac{L}{R}\right)^{1/3}(E)^{1/3}$, while the Stewartson layer, which in the classical spin–up problem drives the liquid towards the interior, scales as $\sim R\left(\frac{L}{R}\right)^{1/4}(E)^{1/4}$, where $E = \frac{\nu}{\omega R^2}$ is the Ekman number (Van de Vooren, 1992). Eventually the film reaches its maximum length and rotates at steady state. We shall see later that once the fluid reaches a steady state of rotation the film becomes very thin with marginal azimuthal displacement. The stages of spin–up are related only to the early stages of processing in CM and consist a very small portion of the total processing time. Thus, most of the research is focused on the film at a steady state of rotation.

A parameter that makes the spin–up in the VFD differ from the classical spin-up problem, is the inclination of the tube. The VFD works best, with respect to chemical reactivity, tilted and with angular velocity high enough, to drain the base of the tube. Due to the inclination of the tube, there is a radial component of gravity, with a fluctuating direction in the rotating frame of reference, which causes a small azimuthal acceleration and deceleration of the flow in each rotation. Thus, at steady state we assume that the boundary layer at the walls scales as a Stokes layer of thickness $\delta \sim (\frac{\nu}{\omega})^{1/2}$. The fluid mechanics with respect to chemical reactivity are both important during the time-dependent spin-up and the film shape at steady state and are both investigated in this thesis.

1.5 Structure of thesis

The thesis is structured according the stages of spreading. The extensive literature on the formation of thin films, using spinning disks, has proven a useful tool in approaching the VFD mechanics. Chapter 2 is a literature review, describing experiments and mathematical approximations of the radial evolution and the instabilities of liquid films in spinning surfaces. The methodology of the experiments is developed in chapter 3 and divides the problem in two distinctive areas of investigation, according to the devices in use.

The first area is the base of the tube and is studied by conducting experiments on spinning disks. Mathematical approximations and experimental results on flat spinning disks are presented in chapter 4, giving an insight to the early times of spreading right after the droplet reaches the rotating surface. Mathematical approximations and experiments of droplets spreading in a hemispherical disk are presented in chapter 5, as an indication of the early times of the film development when the geometry is similar to the base of the VFD tube.

The second area is the film development at the walls of the tube and chapter 6 describes mathematical approximations and experimental results in the VFD. The main conclusions are summarised in chapter 7 along with connections to the literature review and ideas for future research.

Chapter 2

Literature Review

This chapter gives an overview of the literature related to thin film efficiency in chemical processing and on the fluid mechanics of thin film development. First, a review of the new area of fluctuating hydrodynamics is presented. This new area of research consists of theoretical and experimental studies, providing a framework to describe molecular fluctuations, in a manner consistent with statistical mechanics and fluid dynamics. Then, the literature review explores work that has been undertaken, relating on the individual stages of droplet spreading and film development and the relevant fluid mechanics instabilities that occur on spinning disks and inclined planes.

Most of the publications on spinning droplets focus on fingering instabilities. The Bond number, for spinning droplets, is used to describe the flow conditions and is defined as

$$Bo = \frac{\rho \omega^2 V}{\gamma},$$

where ρ is density, γ is surface tension between liquid and air and V is the droplet volume. To our knowledge, most of the experimental work has been conducted with single droplets for $Bo < 100$. Previous publications on axisymmetric spreading, focus mostly on constant flux and at rotation rates up to 3,000 rpm (Bhatelia et al., 2009). Publications at rotation rates beyond 5,000 rpm, focus mostly on experimental observations for constant flux, fed at the centre of the disk, and investigate the mean droplet size produced around the rim of spinning disk atomizers, without detailed analysis on the characteristics of the film development (Ahmed & Youssef, 2012). In this project, single droplets spread on surfaces that rotate from 1,000 to 9,000 rpm, with the most interesting area being above 4,000 rpm ($Bo \geq 100$), where axisymmetric spreading starts.

The literature review on spinning droplets, although at lower rotation rates, is directly related to the spinning disk experiments of this thesis. Literature on constant flux is more related to the motion in the VFD. Several publications mention the benefits of intense shearing in the VFD and focus mostly in the potential applications of the device (Tong et al., 2013; Chen et al., 2012; Goh et al., 2013). However, there is minimal literature describing the fluid mechanics in the VFD. The analysis of the fluid mechanics in the VFD uses literature and experimental observations in spreading films on spinning disks and inclined planes.

Publications on rotating tubes focus mostly on rimming flows, have little relevance so are not reviewed in this thesis. The main direction of the flow in rimming flows is the azimuthal

direction. For example, Ashmore et al. (2003) determined the governing equations for the thickness of a film, in a horizontally placed rotating cylinder, as a function of the azimuthal angle with the solutions for the film thickness profile determined for large, moderate and small ratios of gravity to viscous forces. Two publication were found relevant to the stability of thin films in vertically positioned cylinders, with a co–flowing and a counter–flowing layer of air. The problem was investigated for a stationary tube (Esmail et al., 1975) and for a rotating tube (Sarma et al., 1971). In both cases the focus is on a two-phase flow problem, solved by employing the lubrication approximation in the long wave regime. Both publications conclude that theses two–phase flow problems are unstable to small long–wavelength perturbations over a wide range of gas fluxes, film thickness and rotation rates (for the rotating case), relating the instability with a limit of pressure gradients at the interface of the two fluids. However, the theoretical model developed in chapter 6, focuses on the film evolution in the VFD without taking into consideration air flow, i.e. assuming the gas is co–rotating and considering no shear at the gas–liquid interface. Therefore the film evolution in the VFD is more related to a two–dimensional film development in inclined planes or rotating disks with constant flux.

2.1 Fluctuating hydrodynamics

A new area of research connecting chemistry and fluid mechanics, is called fluctuating hydrodynamics and attempts to connect mass transfer in micro-scales of μm, and macro-scale fluid mechanics. The micro-scale is characterised by the molecular structures while the macro-scale is defined by the dimensions of the fluid domain. Assuming a stagnant flask that contains two stratified liquids, mass transfer proceeds via steady-state molecular diffusion at the interface (Whitman, 1923). Assuming a well mixed bulk of two liquids, the mass is transferred from the phase with higher chemical potential (higher concentration or pressure) to the phase with lower potential until a new equilibrium is reached (Kashid et al., 2011).

To date, research into fluctuating hydrodynamics mostly consists of computational methods and a few applications on experimental level. Models consist of deterministic computational techniques, simulating transport phenomena including effects such as cross-diffusion (i.e. a gradient in the concentration of one species induces a flux of another chemical species), barodiffusion (i.e. flux of the heavier molecules to areas with higher pressure and the lighter molecules to areas with lower pressure), thermodiffusion (i.e. flux caused by a temperature gradient) (Bhattacharjee et al., 2015).

Diffusion and advection enhance chemical reactivity, with both mechanisms benefiting from thin film formation. In this section we explore the principles of diffusion and advection and the benefits of thin films, which will be correlated with the analysis of our experimental observations in the VFD.

2.1.1 Diffusion principles

Diffusion is the net movement of molecules, atoms or ions from a region of high chemical potential to a region of lower chemical potential. Diffusion has been described in thermodynamic laws of ideal gases with respect to pressure P, temperature T_e, volume V and concentrations. Ideal

gases follow Newtonian dynamics (i.e. kinetic theory) and describe a gas as a large number of particles, all of which are in constant and random motion.

Diffusion occurs so that the free energy of the molecules is minimized and is therefore driven by the gradient of free energy. Free energy is defined by Gibbs (1873) as $E_f = E_H - T_e S$, where $E_H = E_i + PV$ is the enthalpy of the system and S is the entropy of the system. The internal energy E_i can be defined by excluding the kinetic energy of motion and the potential energy of the system due to external forces and account only for changes of internal state. Entropy is the characteristic that describes the consistency of the microstates of the system with the macrostate.

The excess of free energy dE_f, required to reach the activation energy E_α and achieve a chemical reaction, assuming constant T_e, is defined as

$$dE_f = dE_H - T_e \; dS,$$

where under the assumption that there is no change of state so that $S,\ E_i$ and V are constant,

$$dE_f \propto V dP.$$

The activation energy E_α, is specific for each reaction and defined by the Arrhenius equation (1889). For a model first order reaction $A + B \rightarrow C$, the reaction proceeds as

$$\frac{\partial [C]}{\partial t} = Z[A][B] \exp^{-E_\alpha / R_a T_e}, \tag{2.1}$$

where Z is a collision rate coefficient of the reactants with respective concentration $[A]$ and $[B]$, producing $[C]$ and R_a is the ideal gas constant.

An important component in diffusivity according to Fick's law is the diffusion coefficient D. The diffusion coefficient in a liquid medium, can be obtained from kinetic theory and the Stokes-Einstein equation (Edward, 1970), as

$$D = \frac{\kappa T_e}{6 \pi \mu r_m},$$

where $\kappa \sim 10^{-23}$ J/K is the Boltzmann constant, μ is dynamic viscosity and r_m is the radius of a single molecule, assumed a spherical shape and varying according to their bonding structure. A bacterium has a typical radius of $\mathcal{O}(10^{-6})$ m, a virus has a typical radius of $\mathcal{O}(10^{-8})$ m, while ammonia and methane consist of smaller molecules with a bond length of $\mathcal{O}(10^{-10})$ m. Water has a bond length of $\mathcal{O}(10^{-10})$ m (Serdyuk et al., 2007).

The diffusion coefficient varies with temperature and is also a function of the medium in which diffusion occurs. Some representative values are presented and will be compared to the experimental results in the VFD. The diffusion coefficient, in liquid water of 25°, ranges from 10^{-9} m^2/s for H^+ (ionized hydrogen), Na^+, K^+ and Urea to 10^{-12} m^2/s for Hemoglobin and DNA (PhysiologyWeb, 2016). Pressure is also correlated with deviations of D. For example, D of H^+, in liquid water of 25°, reaches maximum $D \sim 10^{-8}$ m^2/s at approximately $1,000$ atm $\sim 10^8$ N/m^2 (Walker et al., 2016).

2.1.2 Collision rates and advection

The reaction between two molecules is a combination of two types of collisions. The perikinetic collisions are initiated by molecular diffusion whereas the orthokinetic collisions are caused due

to shear (Orihara et al., 2011). No pure orthokinetic collision can actually exist, because diffusion is always present, regardless of the flow field. It is therefore likely that the collision rate in the VFD is a result of a coupling between diffusive motion (perikinetic collisions) and convective motion due to shear in the flow direction (orthokinetic collisions). This approach has been previously used in several publications both for laminar (Iwashita & Yamamoto, 2009) and for turbulent flows (Konermann, 1999).

Collision models of solid spheres have been extensively used for simulations of liquid molecules, such as the Smoluchowski model which assumed spherical molecules in laminar flow, with only two molecules participating in the collision (Chadler, 1974). Another approach compares the time scales of diffusion and advection by focusing on the kinetics of the molecules. According to the advection–diffusion equation accounting for shear flow, the mean-square displacement is (Katayama & Terauti, 1996),

$$r^2(t) = 2Dt + \frac{2}{3}D\left(\frac{\partial \bar{u}}{\partial z}\right)^2 t^3, \quad z^2(t) = 2Dt, \tag{2.2}$$

where $\bar{u}$ is the depth–averaged velocity. The time dependence t^3 along the flow in equation 2.2 indicates that the presence of shearing produces a radical change in the motion of the particles. The time determined for a molecular displacement, only due to diffusion, equal to the radius of the molecule $r_m \sim \mathcal{O}(10^{-10})$ m, in the z direction, is $\frac{r_m^2}{2D}$. Comparing the diffusion component with the shear component, assuming the same time scale and the same displacement in the direction of the flow, and taking into account only the shear flow factor,

$$\frac{\partial \bar{u}}{\partial z} \ll D r_m^{-2}. \tag{2.3}$$

Both the Smoluchowski model of collision frequency and equation 2.3 extracted from the convective–diffusion equation of mean-square displacement indicate that diffusion is always the dominant factor of reactions while advection enhances the process. The condition implies that the main effect of shearing is to change the time dependence of the variance of the position along the flow from t to t^3 behaviour, thus to enhance diffusion. Both models assume 50% concentration of the reactant $[A]$ and 50% concentration of the reactant $[B]$. The condition imposed by equation 2.3 essentially relates to Taylor dispersion, where shear flow increases diffusivity at high Péclet numbers, with $Pe = \frac{uh}{D}$. The definition and the determination of the magnitude of the Péclet number follows for a droplet spreading in a rotating flat disk in section 4.3.

2.1.3 Thin film benefits

The idea of thin films being beneficial came from the theory that all action (fluid flow and mass transfer) occurs in a thin layer at the interface between two fluids. The idea was first introduced for a liquid flowing down a vertical wall with constant flux and interacting with the adjacent gas (Nernst & Lerch, 1904). Overall the performance of a thin film reaction system is characterised by the level of mass transfer at a molecular level (diffusion) and mass transfer at a hydrodynamic level (advection).

Thin liquid films have excellent heat/mass transfer properties. The short diffusion and conduction path length, normal to the length of the thin films, is the basis for the very high

transport rates within the film. Moreover, very high heat and mass transfer rates are associated with the thin films on rotating disks. Rotating disks have the ability to produce thin films continuously under the action of large centrifugal forces with the film being thrown off the disk at very large velocities. Additionally, wave-induced mixing and the increased surface area per unit volume, associated to rippling effects, also contribute to improving the transport processes.

Mixing is used to reduce the degree of nonuniformity or gradient of a property such as temperature, viscosity, or concentration in a system, in order to achieve a desired degree of homogeneity at various length scales. Mixing is also important in promoting both heat and mass transfer when a system is undergoing a chemical reaction. The quality of mixing of materials greatly determines the success and efficiency of many industrial processes, with effective mixing resulting in considerable economic and environmental benefits. Whether a chemical reaction is influenced by the mixing process depends on the relative time scales of mixing and reaction. Thus, if mixing is relatively slow compared to the reaction rate, the product yields can be considerably affected. Mixing is correlated to the fluid mechanics environment of the chemical process. Therefore, the processing device, which determines the environment of the reaction, preferably should control the fluid mechanics of fast micro– and marco– mixing.

Micro–mixing is the mixing of elements at molecular level. Efficient micro-mixing conditions are achieved when the mixing time, t_m, is shorter than the induction time t_i, which is the overall time required for the reaction ($t_m \ll t_i$), and then the induction time should be shorter that the residence time (Cafiero et al., 2002). The correlation of these time scales has been used in literature testing the efficiency of spinning disk reactors for several chemical reactions (Moore, 1986, Ghiasy et al., 2013).

The effect of acceleration of molecular diffusion by the presence of viscous–convective processes is considered to be an important feature in micromixing (Baldyga & Pohorecki, 1995). Especially in spinning disks, the level of micro–mixing, is investigated experimentally, in comparison to other reactor systems, such as a stirred-tank reactor. A technique used to investigate the level of mixing uses iodide–iodate reaction systems, also known as the Dushman reaction:

$$\mathrm{I_2 + I^- \longrightarrow I_3^-}$$
$$\mathrm{IO_3^- + 5\,I^- + 6\,H^+ \longrightarrow 3\,I_2 + 3\,H_2O},$$

with decreased concentration of I_3^- in the final product implying efficient micro-mixing.

A testing example for mixing efficiency in rotating films was conducted by Boodhoo & Al-Hengari (2012), where the iodide–iodate solution and the sulfuric acid streams were fed under constant flux onto a rotating disk. The disk was allowed to run for 5 min before three samples were collected at 2-min time intervals and subjected to tri-iodide ($\mathrm{I_3^-}$) absorbance analysis, via a single–beam UV/Vis spectrophotometer. The comparison with other devices was conducted with the use of a segregation index, i.e. the ratio between the undesired product in the spinning disk and the undesired product in the compared device. Low ratio of segregation indicates efficient mixing. The mixing efficiency was investigated for variations in the rotation rate (300 - 2,400 rpm), viscosity ($10^{-6} - 10^{-5}$ m^2/s), and flow rate (1 - 5 ml/s). In all variations and comparisons the segregation index was determined close to zero, indicating that the rotating disk achieved increased micro-mixing, compared to the other device. The segregation index was decreased with increased rotation rate, decreased viscosity and increased flow rate. These

results are in good agreement with several other publications investigating mixing and reaction efficiencies in similar experimental set-ups (Pask et al., 2012, Hasaidl et al., 2016, D'Alonzo et al., 2017).

2.2 Fluid mechanics in thin films

Having explored the benefits of thin films, from a chemical perspective, it is clear that fluid mechanics affect the mixing efficiency and the reaction rate. In this section we describe the fluid mechanics of droplet spreading and film formation that are relevant to our experiments and potentially contribute to efficient mixing. The section is arranged according to the stages of film formation, starting from the droplet landing. Next, the fluid mechanics research in film formation and instabilities is explained for rotating disks. The instabilities mostly refer to fingering instabilities at the contact line and wave formation at the surface of the film. Finally, the literature review explores the film formation under the force of gravity, attempting to connect existing literature to the spin-up in the VFD.

2.2.1 Droplet Impact

This section sets the principles of the determination of transient radius for a stationary substrate. The review is useful for the analysis of the energy conservation equation components, for a droplet landing on a rotating frame, following in section 4.1.1. Assuming a rotating substrate, at high rotation rates, a droplet lands on the substrate, reaches its maximum transient radius, which from now on will be referred to as 'transient radius', and before the droplet retracts to its sessile shape, centrifugal force acts on the fluid and continues the spreading radially and azimuthally. Hence, the transient radius is important for the evolution of the spreading film. Upon impact, the droplet shape is observed to be a function of both the droplet speed and the surface speed. The literature review

Assuming a static horizontal surface, the transient radius reached by an initially spherical droplet of radius r_0 and volume V, is increased with increased height of release, decreased viscosity, surface tension (Lee et al., 2016) and substrate roughness (Mundo et al., 1995). Using the equations of energy conservation

$$\underbrace{E_k + E_g + E_s}_{\text{contact time}} = \underbrace{E'_k + E'_g + E'_s + E'_\nu}_{\text{transient time}}, \tag{2.4}$$

where $E_k = \frac{1}{2}\rho V u_z^2$, is the kinetic energy and u_z is the velocity of the droplet before the impact, while E'_k is the kinetic energy at the transient radius and is negligible, $E_s \sim \pi r_0^2 \gamma$ is the surface energy of the droplet before the impact, E_g and E'_g are the gravity potential energy before the impact and at the transient radius respectively and are both considered negligible and E'_ν is the dissipated energy at the final stage, when the droplet has reached the transient radius. The surface energy at the transient time can be expressed as $E'_s = E_k + E_s - E'_\nu$.

Assuming a hemispherical droplet cap and using the Young – Laplace equation, i.e. $\gamma_{sa} - \gamma_{sl} = \gamma \cos\alpha$, where γ_{sa} is the surface energy between solid and air, γ_{sl} is the surface energy between solid and liquid and α is the contact angle, the final surface energy is (Ghai et al., 2013)

$$E'_s = (\text{area of the cap}) \times \gamma + (\text{area of the base}) \times (\gamma_{sa} - \gamma_{sl}),$$

$$E'_s = \pi r^2 \gamma + \pi r^2 \gamma \cos\alpha = \pi r^2 \gamma (1 + \cos\alpha). \tag{2.5}$$

The dissipated energy is

$$E'_\nu = \int_0^{t_t} \int_V \Phi dV dt, \tag{2.6}$$

where $t_t \sim \frac{r_0}{u_z}$ is the time taken by the droplet to spread to its transient radius. The dissipation per unit mass of the fluid scales as

$$\Phi \sim \mu \left(\frac{u_z}{h}\right)^2, \tag{2.7}$$

where h is the thickness once the droplet reaches the transient radius, i.e. at the maximum extent before the droplet retracts to its sessile shape (Chandra et al., 1991) or more accurately h can be approximated with the boundary layer thickness (Pasandideh-Fard et al., 1996).

The landing of a droplet is strongly affected by the air boundary layer above the solid substrate, which can cause air entrapment or detachment of liquid fragments. For a stationary surface, the pressure in the air gap, between the liquid and the solid surface, increases as the droplet approaches, flattening the droplet and potentially leading to bubble entrapment. Numerical simulations by Mehdi-Nejad et al. (2003) for a droplet of initial radius of 1 mm and an impact velocity of 1 m/s, showed that 0.3 mm away from the substrate the air pressure is approximately 4 Pa, at 0.06 mm the pressure is increased to 100 Pa and right before the impact at 0.02 mm the pressure reaches 3,000 Pa. The air film trapped between the falling droplet and the solid substrate, retracts into a spherical bubble, minimising its surface energy. During the retraction, capillary waves are transferred along the air-liquid free surface (Lee at al., 2012). The capillary waves are likely to consist of an additional mechanism that affects the transient radius and possibly the pattern of spreading.

In rotating disks, for an off-axis landing, when the ratio between the velocity of the droplet before the impact and the azimuthal velocity of the substrate is $\frac{u_z}{\omega r} < 0.15$, corresponding to small droplet velocity before the impact u_z, the droplet passes through the boundary layer and enters into contact with the surface. Beyond that limit, the behaviour of the landing droplet varies with the size of the droplet and the rotation of the disk. Assuming the same azimuthal disk velocity, for increased values of u_z, as the droplet approaches the disk, the lower part of the droplet contacts the disk surface and is carried along with it, but the upper part is hardly displaced in the direction of rotation. As a result of the velocity gradient in the boundary layer, a wedge of air forms under the droplet. The wedge of air creates a lifting force which eventually separates some fragments of the droplet from the disk surface and projects them beyond the limits of the boundary layer (Povarov et al., 1976).

Setting the foundations to determine the radial evolution at the initial stage after the impact and the transient radius on a stationary surface is useful for the determination of the same characteristics in a rotating frame. The maximum transient radius is important to define the limit after which the centrifugal force becomes the dominant factor of spreading. This limit is expected to be identified by a change in the time dependence of spreading.

2.2.2 Nusselt film approximation

A technique with a broad range of industrial application that uses the Nusselt approximation is spin coating. Spin coating consists of two processing methods. The first method places the

volume of liquid onto an initially stationary disk, which is then accelerated. The second method requires an already rotating disk and feeds the liquid at a constant flux. Continuous flow leads to the formation of an axisymmetric film, with axisymmetric waves travelling to the disk periphery and finally helical waves being superimposed to the axisymmetric waves (Matar et al., 2004).

Regarding the spreading of droplets on rotating disks, there is extensive literature analysing the radial evolution and the film thickness. The droplet, landing at the axis of rotation, spreads initially with gravity being balanced by capillary forces. The droplet has a circular shape and the radius depends on the droplet volume and the contact angle. Under the action of the centrifugal force, the droplet radius increases from this initial value. The initial spherical cap rapidly evolves into a profile, which is nearly flat, except near the contact line, where a ridge of liquid develops. The flattened area is referred to as the 'film' and the capillary ridge around its perimeter is referred to as the 'ring', as shown in Figure 2.1. In the ring, near the contact line, surface tension and capillary pressure gradients determine the interface shape. The contact line remains circular for times less than the onset time of instabilities. An azimuthal modulation in the height of the capillary ridge is visible, with the thickest parts eventually turning into fingers.

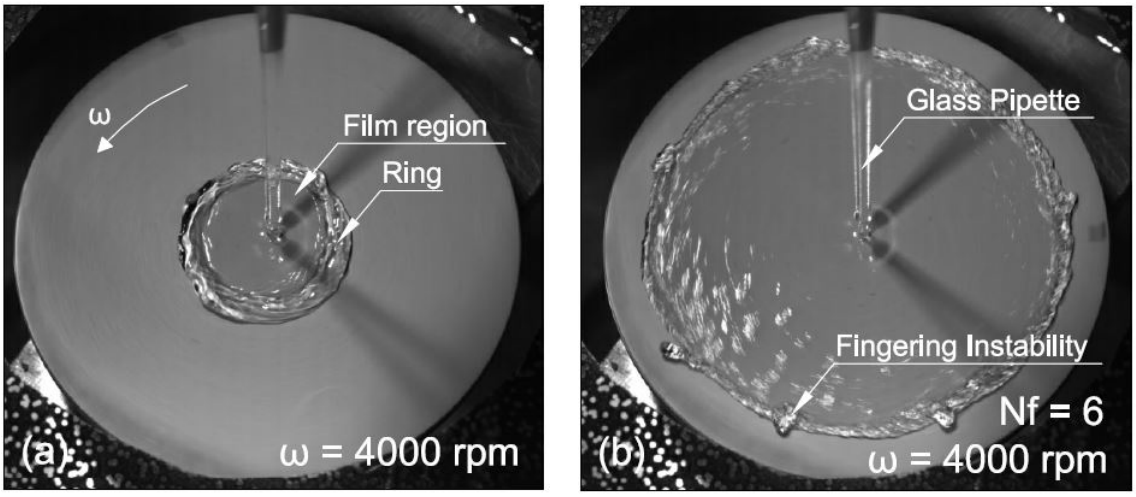

(a) (b)

Figure 2.1: Typical experiment of continuous flow on a spinning disk at 4,000 rpm where (a) initially the film and the ring areas are formed, leading later to (b) a fingering instability.

The Navier–Stokes equation, describing the spreading pattern, of a volume of liquid onto a spinning disk, in the rotating frame, can be expressed as

$$\rho\frac{D\mathbf{u}}{Dt} = -\nabla P + \mu\nabla^2\mathbf{u} - 2\rho\,\boldsymbol{\omega}\times\mathbf{u} - \rho\,\boldsymbol{\omega}\times(\boldsymbol{\omega}\times\mathbf{r}) + \rho\mathbf{g}, \tag{2.8}$$

where $\mathbf{u}$ is the velocity of the fluid element, P is pressure, ω is the angular velocity of the disk rotating about the z axis, $\mathbf{r}$ is the position vector in cylindrical polar coordinates (r, ϕ, z) and μ is the dynamic viscosity of the liquid.

Using the thin film regime ($h \ll r$), in the rotating frame of reference, inertia can be ignored. Incorporating simplifications such as that surface tension, Coriolis force $\left(\omega^2 r \gg 2u_\phi\omega\right)$ and gravity $\left(\omega^2 r \gg g\right)$ can be ignored, the spreading can be approached using the Nusselt film approximation. Balancing the centrifugal force with the viscous resisting force, assuming film

uniformity and with boundary conditions $u = 0$ at $z = 0$ and $\frac{\partial u_r}{\partial z} = 0$ at $z = h$, the radial velocity is

$$\mu \frac{\partial^2 u_r}{\partial z^2} \sim \rho \omega^2 r \ \rightarrow \ u_r = \frac{\omega^2 r}{\nu} \left(hz - \frac{1}{2} z^2 \right). \tag{2.9}$$

The radial flow per unit length is

$$q_r = \int_0^h u_r dz = \frac{\omega^2 r h^3}{3\nu}. \tag{2.10}$$

To obtain a differential equation for h we take into consideration that $u_r \gg u_z$ and $u_\phi \sim u_z$ so that the equation of continuity can be expressed as

$$\frac{\partial h}{\partial t} = -\frac{1}{r} \frac{\partial (r q_r)}{\partial r}. \tag{2.11}$$

Setting the boundary condition that $h = h_0$ at $t = 0$ s and integrating equation 2.11 we get

$$h = \frac{h_0}{\left(1 + \frac{4\omega^2 h_0^2}{3\nu} t \right)^{\frac{1}{2}}}. \tag{2.12}$$

Setting the principles of the Nusselt film approximations we proceed to define the radius evolution both for constant flux and for constant volume.

2.2.2.1 Constant flux

Early research on spinning disks focused on experiments with constant flux. For the film region, Emslie et al. (1958) analysed the flow, assuming film uniformity, without waves altering the film thickness. Considering that r is a function of time then

$$\frac{\partial h}{\partial t} = \frac{\partial h}{\partial t} + \frac{\partial h}{\partial r} \frac{\partial r}{\partial t}. \tag{2.13}$$

Tanking into consideration the boundary condition that $r = r_0$ at $t = 0$ s and integrating equation 2.13 we get

$$r = r_0 \left(1 + \frac{4\omega^2 h_0^2}{3\nu} t \right)^{\frac{3}{4}}. \tag{2.14}$$

Thus the film radius under constant flux increases as $t^{3/4}$, whereas the thickness decreases as $t^{-1/2}$.

Later, Esping and Hoyle (1965), in their experiments using water of constant flux, observed three different flow regimes over the spinning disk. Near the inlet region, the flow is waveless laminar, followed by a flow characterized by axisymmetric wave formation, and finally by a turbulent region, containing three–dimensional surface waves that are a combination of axisymmetric and helical waves. Esping and Hoyle show that when the thickness measurements include the crests of the waves, the maximum thickness of the film, is about 40% larger than the value given by the Nusselt approximation, assuming uniform film thickness defined as

$$h = \left(\frac{3}{2\pi} \frac{Q\nu}{\omega^2 r^2} \right)^{\frac{1}{3}}. \tag{2.15}$$

Other empirical studies also suggest a much closer fit to the Nusselt model, though still below the Nusselt prediction (Leneweit et al., 1999). Recent experimental studies of constant flux,

compared experimental observations and showed that for large Reynolds numbers, the film thickness was estimated only 10% lower than the Nusselt film estimation (Burns et al, 2003).

Regarding theoretical predictions beyond the Nusselt film approximation, most of the mathematical modelling investigates analytically and numerically the profiles of spreading on spinning disks, under constant flux, focusing on mass transfer and surface waves. These studies use the thin film approximation and have determined self-similar solutions and asymptotic solutions in the limit of large Reynolds number as well as numerical solutions for finite Reynolds numbers (Sisoev et al., 2003). Many studies consider other effects such as those of Coriolis force (Matsumoto et al., 1989, Matar et al., 2004), solvent evaporation (Holloway et al., 2007), the presence of surfactants (Pareira et al., 2007), surface topography and flow rate modulations (Matar et al.,2008), gas absorption at the interface with the air boundary layer (Sisoev at al., 2005) and van der Waals effects (Froehlich, 2009).

2.2.2.2 Single droplet

Spinning disk experiments have also been investigated for single droplets of volume V. Considering volume conservation and uniform film thickness we get

$$V = \pi r^2 h. \tag{2.16}$$

Replacing equation 2.12 to equation 2.16 the radial evolution can be expressed as

$$r \sim r_0 \left(1 + \frac{4\omega^2 h_0^2}{3\nu} t\right)^{\frac{1}{4}}. \tag{2.17}$$

Thus in the asymptotic regime, using lubrication approximation ($h \ll r$) and ignoring Coriolis force, the droplet radius increases as $t^{1/4}$, whereas the thickness decreases as $t^{-1/2}$.

Melo et al. (1989) conducted experiments up to 5,000 rpm, using silicon oil droplets of 50μl, to measure the time evolution of the droplet profile, the critical radius r_c for the onset of contact line instabilities, and the fastest growing instability wavelength. The droplet was initially placed in a slowly rotating disk, which was then accelerated to a pre–decided angular velocity. According to Melo et al., r_c is defined as the radius where the ring develops waves that modulate the contact line and the ring profile in a direction perpendicular to the main flow. Melo et al. found that, for $Bo < 50$, the most unstable angular wavelength is independent on both droplet volume and rotational speed, while the onset of instability, at r_c, and the number of fingers increase when $Bo > 50$. Melo et al. also observed a deviation from the expected radial evolution $\sim t^{1/4}$ and measured a faster radial evolution $\sim t^{1/3}$.

The experimental work by Fraysse & Homsy (1994), is the most relevant to the spinning disk experiments conducted in this thesis. Fraysse & Homsy focused on the spreading of single droplets onto spinning disks, investigating the fingering instability for droplet volume up to 100 μl, at rotation rates up to 600 rpm, using silicon oil with viscosity ranging from 10^{-4} m^2/s to 10^{-3} m^2/s. The droplets were initially placed in a motionless disk, and after a few minutes of resting time the disk was set in rotation. Before the onset of the instability the droplet radius yields the radial evolution. The definition of r_c, was dependent on the shape of the contact line, with the circumference of the droplet transforming from circular to polygonal. The theoretical approach was based on the Navier–Stokes equations, making use of the lubrication

approximation. The height evolution was determined using continuity equation, accounting for centrifugal force, viscosity and surface tension only, and obeys

$$\frac{\partial h}{\partial t} + \nabla \cdot \left[\frac{h^3}{3\mu} (\rho \omega^2 \mathbf{r} + \gamma \nabla \nabla^2 h) \right] = 0, \tag{2.18}$$

where $\mathbf{r}$ is the position vector (r, ϕ, z) in cylindrical polar coordinates. The local curvature is approximated by $\nabla^2 h$ (in the limit where $\frac{\partial h}{\partial r} \ll 1$).

The ring was considered of rectangular shape, with a characteristic radial length, l, given by a balance between surface tension and centrifugal force in (2.18) as

$$\mu U \sim \gamma \frac{h^3}{l^3}, \tag{2.19}$$

where U is the surface velocity

$$U \sim \frac{\omega^2 r h^2}{\nu},$$

giving

$$l \sim \left(\frac{\gamma V}{\rho \omega^2 r^3} \right)^{\frac{1}{3}}. \tag{2.20}$$

All the experiments performed with a given liquid exhibited fingering instability and developed approximately the same number of fingers, independent of droplet volume and rotational speed. Due to the repeatability observed through all the experiments, possible wetting defects of the glass substrate do not govern either the instability or the number of fingers that are observed, but slight inhomogeneities in wetting properties may play a role in the determination of the exact arrangement of the fingers at the droplet periphery.

Fraysse & Homsy also observed the deviation of the radial evolution similar to Melo et al., questioning the decision to consider the droplet asymptotically entirely flat and suggesting that the volume in the ring might be a crucial component for the onset of fingering instability. Based on this argument they also observed that the ring radial length l evolves in time and imposed a correction factor to $l \sim 0.1r$, where r was the total radius. This observation of the deviation from the Nusselt spreading and the importance of the volume of the ring is in accordance with our experimental observations in section 4.5.1, where we suggest a new mechanism for the ring volume evolution.

Regarding liquid flux, an experiment of spin coating was conducted at 3,000 rpm, varying the discharge rate of 1 ml of silicon oil (Wang et al., 2014). Wang et al, showed that both r_c and t_c are increased with increased discharge rate. The effects of discharge rate on r_c and t_c are almost negligible as long as the whole volume of liquid has been discharged before the onset of fingering instability. Thus as long as the discharge continues r_c is increased.

Regarding Coriolis force, the Coriolis term in the radial velocity equation is of the same order as the inertia terms and is therefore negligible (Myers et al., 2001). The Navier–Stokes equation has been solved both analytically and numerically (Momoniat & Mason, 1998) illustrating that, as long as the thickness of the film is within the von Kármán layer, Coriolis force has no significant effect in the spreading pattern. However experimental studies with silicon oil, showed that, although the Coriolis force has negligible effect on the height of the spreading film, the Coriolis force affects the onset of fingering instability, the angle of fingers' flowing direction and the shape of the fingers. When $Bo < 100$, the Coriolis force affects the deflective angle of the fingers only.

When $Bo > 100$, the Coriolis force deviates the fingers' movement and increases the wet area azimuthally (Cho et al., 2005). The angle of the fingers' deflection is expressed proportionally to h^2, where away from the axis, the film is thinner and the streamline is approximately radial. As Coriolis force is systemically ignored in spinning disks, detailed analysis follows, customised to the VFD in subsection 6.4.

Regarding surface tension, a numerical comparison was conducted for the spreading of a rotating droplet with and without including surface tension (Wilson et al., 2000). Ignoring surface tension and using linear stability analysis with a precursor layer, and with slip coefficients it is impossible to choose parametric values so that any of these solutions can reproduce experimental data of previous studies (Melo et al., 1989, Fraysse & Homsy 1994 and Spaid & Homsy, 1996). For finite γ, using a slip coefficient with a fixed contact angle, the solution approximately predicts the experimental data. As expected, numerical simulations show that the initially parabolic profile flattens at the centre and quickly develops the distinctive capillary-ridge profile near the contact line. The effect of surface tension in spinning disks has been analysed in many publications. This thesis takes into consideration surface tension during the time-dependent evolution of the film in the VFD in subsection 6.4.

2.2.3 Fingering instability

The mechanism of fingering instabilities, for a droplet spreading in a rotating frame, was first described by Melo et al. (1989), who studied fingering for a range of viscosities, rotation speeds, and fluid volumes using silicon oil. The mechanism is similar to fingering instability developed for a flow in an inclined plane.

The instability starts as an azimuthal perturbation in the ring, which alters the curvature near the contact line. The perturbations cause azimuthal variations in pressure, triggering a secondary azimuthal flow. The azimuthal flow guides the fluid towards areas of lower pressure, increasing the amplitude of the perturbations, forming thicker regions that advance more rapidly. The increasing azimuthal variations in height lead to a fingering instability. Analysis of this instability has been treated theoretically in the context of lubrication theory and depends on the contact line model. Linear stability analysis has been performed, for Newtonian base state profiles, generated to avoid contact line singularities, with both slip (Boettcher & Ehrhard, 2014) and precursor film contact line models (Bonn et al., 2009).

Linear stability analysis with a precursor film, shows that the position of the maximum growth rate is nearly independent of the precursor thickness over a wide range of values, with the most unstable wavelength predicted to be $\lambda \sim 14l$, where l can be retrieved from equation 2.20. A correlation between the number of fingers N_f, for $50 < Bo < 100$ and the critical radius r_c has been defined as (Fraysse & Homsy, 1994)

$$N_f = \frac{\pi}{7} \frac{r_c}{V^{1/2}} Bo^{\frac{1}{3}}. \tag{2.21}$$

When Bo > 100, e.g. at higher rotation rates, the number of fingers increases rapidly with Bo (Wang and Chou, 2001). When $Bo < 50$, the Capillary number, ($Ca = \frac{\mu U}{\gamma}$), approaches an asymptotic value of $Ca \sim \mathcal{O}(10)$ and the ring region can be ignored. The liquid droplet is still reshaping after landing, as there is still some inertial momentum, which may become the disturbance promoting the onset of a single rivulet (Lai et al., 2008).

Experiments conducted with single drops on rotating substrates up to 1,000 rpm observed the formation of a single finger, formed at the location of an initial outward deviation from axisymmetry. This fingering is qualitatively different from the contact line instability, and appears to be a localized phenomenon that occurs when the stress at some point on the perimeter of the droplet exceeds the yield stress (Holloway et al., 2009). In a few cases, more than one finger appeared but not simultaneously, nor are they equally spaced around the perimeter, and there are no systematic trends relating the appearance of multiple fingers to the experimental conditions.

2.2.4 Waves instabilities

The flow of a thin film over a spinning disk is accompanied by the formation of large amplitude waves and the formation of fingers at the contact line (Craster et al., 2009). Regarding the formation of waves, under both laminar and turbulent conditions, shear flow can be unstable such that, an initially small perturbation of the liquid surface amplifies with time and with distance downstream, until a well–defined wave pattern is observed. When the flow is unstable, a minor perturbation of the liquid surface could induce the formation of waves.

Finite–amplitude waves have been observed in the axisymmetric flow over a rotating disk, with the majority of experimental investigations focusing on measurements of the local wavelength. Espig & Hoyle (1965) measured the wave thickness by using a steel needle that touched the tip of the wave crests. Charwat at al. (1972) were the first to observe that spiral waves unwind in the direction of rotation and are stationary in the rotating frame of reference. Woods (1995) conducted experiments with water of constant flux on a rotating flat disk and distinguished the length of the three regions, first described by Esping and Hoyle (1965), for a range of rotation rates (100-600 rpm). Woods found that the spiral waves, beyond the laminar area, increase in wavelength with increased ω, while the area of irregular waves, close to the rim of the disk increases in length with increased ω.

Another study explored the effect of wave regimes to reaction rates. Two waves regimes were observed, of spiral and irregular form. The reaction rate was investigated by using a photocatalytic reaction and UV light, altering the rotation rate (50–400 rpm) and the flux (5-35 ml/s). The film thickness was determined by the Nusselt approximation and depending on the rotation rate and the flux, varied between 1.6×10^{-4} and 4.5×10^{-4} m. Ink injection experiments at 5, 20 and 35 ml/s and at rotation rates of 50, 150 and 300 rpm revealed that the liquid film, for all observed flow regimes, appeared to be laminar, with the waves not contributing to mixing (Boiarkina et al., 2011).

It should be noted that most of the studies focus on flows imposed by a rotating substrate with the liquid film considerably thicker than the boundary layer thickness (Matar et al., 2006). Two different instabilities have been observed experimentally by Moisy et al. (2003) and they are easily identified by the direction of the corresponding spirals, as shown in Figure 2.2. The experiment used two concentric disks separated by a distance, which could vary from a few mm to several cm. The two disks formed a cylindrical tank filled with a solution of water and glycerine. Each disk could rotate with its own angular velocity. When only the top disk rotated clockwise, boundary layer instabilities were observed, unfolding in the direction opposite to the rotation of the disks, as shown in Figure 2.2a. The formation of these spirals will be referred

to as 'retrograde spirals'. In this case viscous effects dominate the flow and the boundary layer breaks. In the counter-rotating regime, as shown in Figure 2.2b, shear flow instabilities were observed, unfolding in the direction of rotation of the top disk and will be referred to as 'prograde spirals'.

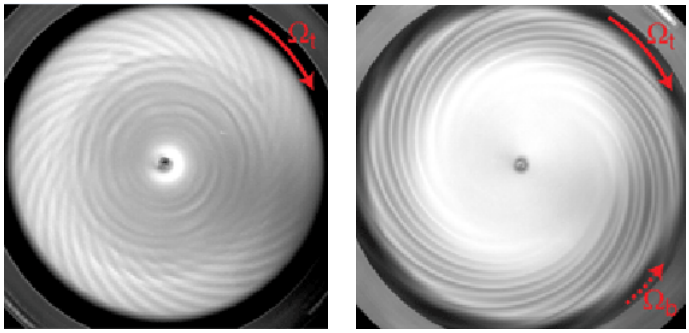

(a) (b)

Figure 2.2: (a) Circles and retrograde spirals in the rotor-stator regime, as a result of a boundary layer instabilities, with only the top disk rotating clockwise. (b) Prograde spirals in the counter-rotation regime, resulting from a shear layer instability, where the top disk rotates clockwise and the bottom disk anticlockwise (Moisy et al., 2003).

A correlation between the wave formation and the von Kármán boundary layer was reviewed by Lingwood & Alfredsson (2015). It is a boundary layer that exhibits a cross–flow instability, giving rise to cross–flow vortices that are stationary, with respect to the rotating surface. The rotating disk acts as a centrifugal fan, such that the liquid near the surface is pulled into azimuthal circulation by viscous stresses and without a radial pressure gradient to balance the centrifugal forces, is thrown radially outwards and is replaced by an axial downward flow. The growth of stationary vortices saturates at $Re \sim 550$. The experiments, mentioned in the Lingwood & Alfredsson review, refer to a rotating liquid at steady state. The disk has side walls so that the liquid is confined within the rotating frame. The resulting velocity distribution in the boundary layer is three–dimensional and has an inflection point in the radial direction. The cross-flow instability is essentially a transition of a laminar boundary layer to turbulence. In this project, a pattern of almost stationary wave instability is observed in the spinning disks that will be compared with the instabilities of the von Kármán boundary layer.

2.2.5 Gravity driven films

In rotating disks gravity acts normal to the main direction of the flow and is considered negligible. We shall see later in chapter 6 that in order to solve analytically the spin-up in the VFD, we simplify the problem from a three–dimensional to a two–dimensional approximation, assuming negligible azimuthal motion. The common characteristic with gravity currents is that the centrifugal force in the VFD works normal to the direction of the flow as the equivalent gravity component down an inclined plane. The main difference is that in gravity currents the liquid moves downwards, to reduce E_g, with the tangential gravity component working in favour of the flow, while in the VFD the motion is upwards, reducing the total potential energy and relaxing towards a static stable equilibrium shape. Hence, publications in films formed by gravity currents were taken into consideration in order to approach the spin–up problem in the VFD.

Laboratory experiments have shown that a thin film of a Newtonian fluid flowing down an inclined plane can form a capillary ridge at the front, become unstable and split into a series of fingers. Huppert (1982) derived an expression for the flow prior to the instability, ignoring contact line effects, and predicted that the front of the film should advance as $t^{1/3}$. The fingering instability observed, could not be explained by viscous effects only, as the cross–slope variations in film thickness tend to be diminished by the pressure gradient the thickness variation induces. Taking surface tension into account and using lubrication approximation, it was estimated that the wavelength of the fingers is a function of surface tension and scales as

$$\lambda \sim \frac{A^{1/2}\gamma}{\rho g \sin\beta},$$

where A is the initial cross–sectional area of the fluid (and is therefore proportional to the fluid volume) and β is the inclination angle.

Schwartz (1989) performed numerical simulations of the flow of a thin layer of a viscous fluid down a plane, using equations derived by the lubrication approximation. When a no-slip boundary condition was imposed at the edges of the plane (corresponding to the experimental constraint of a wall at the edges) an instability of the contact line was observed, driven by the boundary conditions, which propagated inward from the edges, leading to the formation of periodic fingers.

Troian et al. (1989) studied the lubrication equations, including contact line effects. The flow profile prior to the onset of instability was derived and matched to a thin precursor wetting film. A linear stability analysis indicated that the straight front was unstable to periodic perturbations over a range of wave numbers, with the maximum growth rate corresponding to a wavelength of

$$\lambda \ = 14l,$$

where $l = h/(3Ca)^{-1/3}$, where Ca is the Capillary number, balancing gravitational and surface tension effects, similarly to the spinning disk, where Ca balances centrifugal force and surface tension.

Takagi and Huppert (2010) extended previous studies, of gravity driven thin films, by investigating moving contact lines on curved surfaces. Experiments were conducted, with instantaneous release of a constant volume of viscous fluid from a point source, at the top of a stationary cylinder and a sphere respectively. Especially for the sphere, which is related to the spinning disks, a time dependence for the film evolution was scaled as $t^{1/4}$ while the film thickness was found to decrease as $t^{-1/2}$.

Many publications use two–dimensional models based on lubrication theory and predict the film development in the asymptotic regime for gravity currents (Silvi and Dussan, 1985, Goodwin and Homsy, 1991). However, there are very limited publications on liquids propagating upwards, 'climbing' an inclined plane, which would be more relevant to the spin–up problem in the VFD. Fluid climbing an inclined plane was investigated for surfactant-laden films, using a two–dimensional, nonlinear evolution equation for the interface coupled to convective-diffusion equation for the surfactant, derived using lubrication theory (Mayromoustaki et al., 2012). Another publication referred to droplets climbing an oscillating inclined plane (Benilov & Billingham 2011). A shallow-water model, incorporating surface tension and inertia, was used, which resulted only in qualitative representations of the main features of relevant experimental observations (Brunet et al., 2007). Linear stability analysis showed that these films are unstable

with respect to long-wave instability when the Reynolds number, Re, is larger than the critical value, $Re > 5 \cot \frac{\beta}{6}$ (Lin & Kondic, 2010). Below a critical inclination angle the base state is linearly stable and the capillary ridge in the profile vanishes (Bertozzi & Brenner 1997). These publications were not studied in detail but are mentioned to show that we were unable to find publications similar to a climbing film.

We also consider the presence of roll waves that is observed at the free surface of gravity currents. We shall see later in chapter 4 that the spiral waves observed in the flat disk exhibiting a radial and an azimuthal motion in the rotating frame of reference. The roll waves are explored here in an attempt to correlate the roll wave characteristics with the spirals in the flat disk. The amplitude of the roll waves increases gradually as they move downstream until a crest is formed and the wave breaks (Julien and Hartley, 1986). The ratio of the phase velocity, c_p, to the depth–averaged velocity is proportional to the Froude number defined as $Fr = \frac{u}{\sqrt{gh}}$. Thus for unstable flows, Fr$>$ 0.5, the ration becomes

$$\frac{c_p}{\bar{u}} \sim \beta_m + \sqrt{\frac{1}{Fr^2} + \beta_m(\beta_m - 1)},$$

where $\beta_m \sim 1.2$ is a momentum correlation factor. For $Fr \sim 1$ the ration becomes $\frac{c_p}{\bar{u}} \sim 2.3$. The above relations were tested for several slopes, flow rates and channel widths (Aghebatie and Hosseini, 2016).

2.3 Summary

There is growing literature on the performance of the VFD with respect to chemical reactions and material processing, but the fluid mechanics of the device are poorly understood. It is believed that a key element for the optimum performance of the VFD is the formation of a rotating thin film. A substantial body of research correlates thin films with efficient chemical reactivity due to excellent heat/mass transfer properties. There are several mechanisms of thin film production but the focus is in rotating systems, attempting to understand the mechanics in the VFD.

Various experimental configurations can be employed to study the evolution of films in rotating frames. Much experimental work has been done on spin coating with constant flux, where the difficulty is the achievement of uniform film thickness. Spinning droplets have been investigated at low rotation rates ($< 3,000$ rpm or $Bo < 100$), focusing mostly on fingering instabilities at the contact line. The mathematical approximations use the Nusselt film approach or lubrication theory taking into consideration surface tension, while Coriolis force can be ignored. The wet area is divided in the film and the ring. Linear stability analysis, either with a precursor film or with a slip condition, to avoid contact line singularities, is used to describe the perturbations at the ring which turn into fingers. Apart from the fingering instability at the contact line, another wavy instability can form at the free surface. The waves can be concentric or in spiral configuration. The formation of a capillary ridge near the contact line and the mathematical approximations are similar to research studies in inclined planes, with the difference than in inclined planes the wavy instabilities, at the free surface, have the form of roll waves.

In this project the focus is on spinning droplets, at high rotation rates, ($\omega \geq 4,000$ rpm or $Bo \geq 100$), investigating spreading patterns and instabilities that could enhance chemical reac-

tions. The Nusselt film approximation and lubrication theory are employed for the mathematical description of the experimental results in rotating disks. Furthermore the VFD is treated as an inclined plane with an upstream film development. The film development and the observed instabilities are described both in CM (with a volume of liquid placed in the device before the spin-up) and in CF (film produced by a sequence of droplets).

Chapter 3

Methodology

As mentioned in chapter 1, the VFD is a device under development and experimentation. One of the motivations of this thesis, is the understanding of the role of fluid mechanics in the performance of the device. The methodology employed to pursue this understanding is based on the two processing methods, i.e. confined mode (CM) and continuous flow (CF).

In CM, a fixed volume of liquid is placed at the base of the VFD before rotation is initiated. The development of the film is essentially the spin-up problem in the VFD. The characteristics of the film at steady state describe the fluid mechanics environment for most of the time of processing. In CF, droplets fall periodically on a dry rotating tube or on a rotating tube which sustains a liquid thin film developed along the walls. The dynamics of CF, are investigated by conducting experiments of single droplets landing on rotating disks and inside the VFD. All experiments are conducted at room temperature.

To explore the early times of spin-up and the dynamics of droplet landing and spreading, experiments were conducted using flat and hemispherical disks. In every spinning disk experiment two main flow characteristics were explored: the spreading evolution of the droplet at the ring edge, and the onset of instabilities. The experimental results, both for the flat and the hemispherical disk, showed a droplet evolution dependence in time, different from the Nusselt evolution $\sim t^{1/4}$ (see section 2.2.2). A mathematical approximation describing the fluid droplet evolution on the spinning disks was necessary, thus a scaling was developed describing the spreading pattern. The time dependence, determined by the scaling, was tested experimentally altering one control parameter at a time, i.e. rotation rate ω, height of release H, surface roughness and droplet volume V. The instabilities observed in the experiments were analysed in detail and the analysis focused mostly on the phenomena that are likely to be present in the VFD.

Moreover there is no literature on the fluid mechanics for the film development in the VFD. Therefore, a mathematical model was developed, describing the film shape at steady state and was compared to the experimental results. The control parameters in the VFD were ω, V or fluid flux Q, gravity relative to the inclination angle β and tube internal radius R. In addition, an analytical solution using the Navier–Stokes equations was attempted, describing the spin-up of the film, using lubrication approximation, where centrifugal and gravitational forces were balanced by viscosity, while Coriolis force was ignored. Surface tension was also taken into consideration as an important factor near the contact line.

The film development for the horizontal disk and the VFD was expressed using cylindrical polar coordinates (r, ϕ, z), while for the hemispherical disk using spherical polar coordinates (r, θ, ϕ). In all cases, the rotating frame of reference was chosen for convenience, as inertia is negligible in this frame, and so the left hand-side of the Navier–Stokes equation can be ignored. Thin film approximations were used for the formulation of equations and so $h \ll R$. For each device simplifications were made mainly neglecting azimuthal motion, turning the problem from three dimensions to two dimensions. An illustration of the coordinate systems in the VFD and the applied body forces is shown in Figure 3.1.

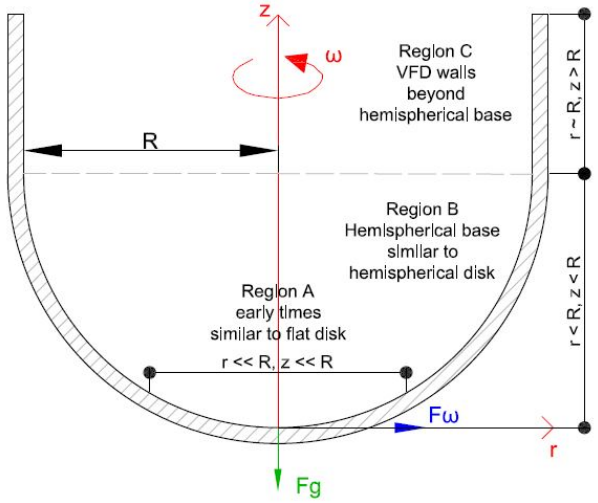

Figure 3.1: Divisions of the VFD in regions, relating to the spinning disk devices. Region A, where $r \ll R$, represents the early times of spreading in the flat and the hemispherical disk. Region B, where $z < R$, represents the spreading in the hemispherical base of the VFD, similar to the spreading in the hemispherical disk. Region C, where $z > R$, represents the film development along the walls of the VFD.

The main differences between the disks and the VFD are the directions of centrifugal force and gravity, with respect to the main direction of the flow. On the flat spinning disk, at the base of the hemispherical disk and at the base of the VFD, where $r \ll R$, centrifugal force is in the direction of the flow. Once the fluid climbs the walls of the VFD, centrifugal force is normal to the direction of the flow. Gravity at the base, acts normal to the direction of the main flow and can be neglected, as explained for the flat disk case in section 2.2.2.1. Gravity in the VFD is correlated to the inclination angle of the device. When the VFD has an inclination angle, $\beta > 0°$, the component of gravity in the z direction works against the direction of the main flow.

In this chapter the set-up of each experiment is explained in detail, including fluid dyes and additional visualisation techniques such as neutron imaging. A table of experiments is presented for each device, describing the control parameters and the technical features of the tools in use. Due to the large number of experiments, every table attributes a unique code to each experiment.

The processing of the experiments was conducted at the University of Cambridge using image processing techniques. DigiFlow (Sveen and Dalziel, 2005) and Matlab were the main software used for image processing, dye attenuation and time series handling. Mathematical modelling was developed, to explain experimental observations, for the disks and the VFD.

3.1 Experiments with spinning disks

The apparatus of the spinning disks was designed and constructed by the technicians at the GK Batchelor Laboratory, University of Cambridge. The aim in the spinning disk experiments was to understand and describe mathematically the spreading pattern of single droplets. The pattern was characterised by the spreading evolution, the onset of instabilities at the contact line and the instabilities that developed at the free surface.

3.1.1 Basic experimental set–up

Two main classes of experiments were formed according to the geometry of the disk. The first class, refers to single droplets spreading on flat disks of 50 mm diameter. In this category, one flat disk was made of brass and painted with automotive primer (FB) and the other flat disk had a surface made of black glass (FG). The second class refers to experiments on a hemispherical brass disk (HD) also painted with automotive primer, with internal diameter of 55 mm. Photographs of the disks are shown in Figure 3.2.

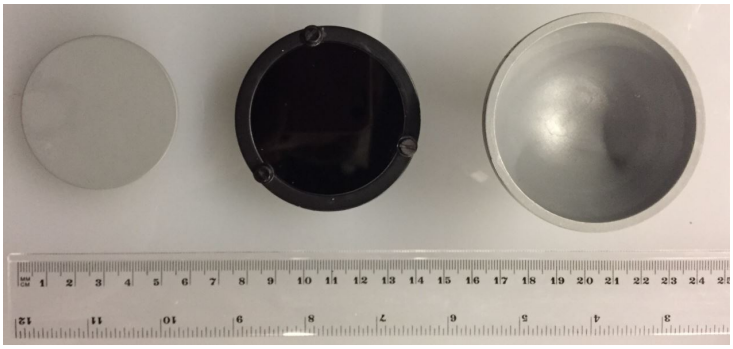

Figure 3.2: Disks used for spin-up experiments from the left to the right, the first disk is the flat brass disk of 50 mm diameter, in the middle is the black glass disk of the same diameter and on the right is the hemispherical disk of 55 mm diameter.

Each of the disks was specially adapted to mount onto a Maxon EC-i 40 DC brushless motor, with the controlled speed ranging from 50 to 13,000 rpm. The motor was secured at the centre of an acrylic tank, as shown in Figure 3.3. The disks were designed to easily be secured onto the motor shaft, thus the bulk of the experiments were conducted in the cylindrical acrylic tank. The tank was secured on a metallic base, that kept the set-up static. The metallic base had the ability to tilt the apparatus.

Droplets were released by an adjustable pipette. The pipette could move horizontally and vertically, changing the point and the height of the droplet release. The displacement of the pipette was achieved by two screw–operated linear stages, one vertical and one horizontal. The motor and the disk were surrounded by vertical walls connected to each other, forming an open rectangular box. The internal dimensions of the box were 10 cm $\times$ 10 cm $\times$ 10 cm. The walls were made of Perspex (acrylic) to allow flow visualisation. A third screw–operated linear stage could move the walls vertically. The walls worked as shields, protecting the user and the camera from the expelled liquid.

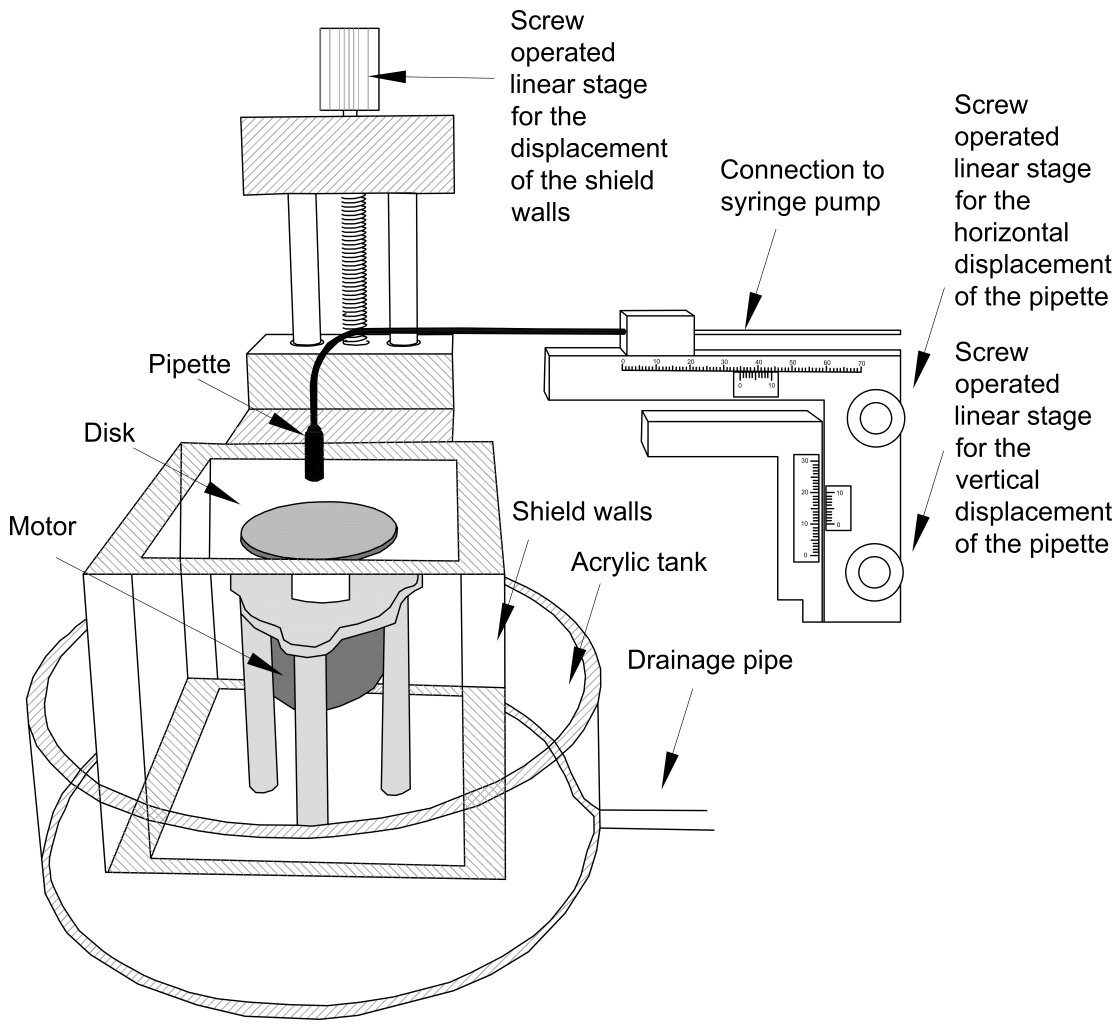

Figure 3.3: Experimental set-up for spinning disks.

Each class of experiments refers to one device and starts with a base case scenario that is representative of the fluid dynamics in the device. Each class of experiments is divided in groups of experiments exploring the effect of one parameter at a time. The control parameters investigated in each group are: the rotation rate, the height of the release, the droplet volume, the smoothness of the solid surface, the wetting of the solid surface and the geometry of the tube. Each set of experiments, within every group, refers to the range of rotation rates under investigation. Every case within a set, had 5 to 10 realisations. The multiple realisations are essential for the calculation of the ensemble averages of the radial evolution and the critical length.

For every realisation, simple flow visualisation was sufficient to obtain qualitative and quantitative information about the droplet spreading. This was particularly advantageous as multiple runs could be executed in short time intervals. After every realisation, the disk was cleaned with tap water and dried with lens tissues. More aggressive chemical cleaners would have been problematic with respect to the painted finishing of the disks. Besides, the results are very close if not identical for repeated realisations and so we concluded that there is no need for further decontamination.

For the spinning disk experiments, the fluid under consideration was water, which in room temperature of 20°C, has kinematic viscosity $\nu = 1.004 \times 10^{-6}$ m^2/s and density $\rho = 998.20$ kg/m^3.

It should be noted that we used tap water, and although we were unable to determine the surface tension of the tap water in the laboratory, we will consider a surface tension of $\gamma = 0.06$ N/m.

3.1.2 Parameter variation

The rotation rate is the most important parameter. The range of rotation rates for spinning disk experiments was decided in correlation to the operational speeds in the VFD. As explained in section 1.2, the performance of the VFD varies significantly from 1,000 to 9,000 rpm, while the best performance is achieved at speeds between 7,000 and 8,000 rpm. Therefore, every set of experiments was tested for a range of rotation rates, from 1,000 to 10,000 rpm with a step of 1,000 rpm. In order to explain the optimum performance of the VFD, the results mostly focused between 5,000 rpm and 9,000 rpm.

Two pipettes with outlet diameter of 5 mm and 2.5 mm produced droplet of 80 μl and 40 μl respectively. The droplet volume was estimated by measuring the average size of 1,000 droplets from each pipette, with the use of the Ohaus SP-602 Scout Pro Digital Balance, with precision of 0.01 g corresponding to 0.01 ml. In both cases the flux was controlled by the syringe pump SPLG-200, which was set at 0.8 ml/sec and with accuracy of $\pm 0.5\%$.

The pipette released the droplet above the already rotating disk and the droplet experienced a free fall under the force of gravity. The height of release, measured from the surface of the disk to the lower end of the pipette, was varied from 5 mm to 15 mm with a step of 5 mm. Several groups of experiments were conducted with the droplet released on the axis of rotation. The axial landing caused axisymmetric spreading, very similar to the one expected for an axial landing in the VFD. The alignment of the pipette with the axis was confirmed by the resulting pattern of spreading. Small variations away from the axis were seen to lead to early formation of a single finger, guiding most of the fluid through that finger, towards the rim of the disk.

One set of experiments for each category, was conducted with the pipette positioned 10 mm off the axis. The early stage of the off-axis landing is similar to the droplet landing on the rotating wall of the VFD. The spreading evolution on the surface of the glass disk was compared to the spreading evolution on the surface of the painted brass disk, exploring the effect of surface smoothness on the onset of instabilities. By pre-coating the disk with water we allowed investigations of the spreading, removing contact line effects. Finally, in order to understand the possible connection of the tilting with the fluid mechanics in spinning disks, experiments were conducted with the set-up secured at various tilting angles.

To organise the experiments according to the parameter under investigation, a unique code is attributed to every case and every set of realisations. For example, the base case has the code FB5000H10V80, which stands for a Flat Brass disk which rotates at 5,000 rpm (FB5000), a droplet released at a height of 10 mm above the disk (H10), of 80 μl volume (V80). A set of experiments, implies the investigation of the total range of rotation rates (1,000 to 9,000 rpm) and the code becomes FB-H10V80. The experiments conducted on the class of the flat disks are presented in Table 3.1.

Utilising the experimental measurements for a range of a control parameters, the main characteristics of the flow can be described using dimensionless diagnostic parameters. The diagnostic parameters are indicative of the forces that have a weak effect in the spreading

pattern and can be factored out. To express the importance of the forces applied Reynolds, Weber, Froude, Rossby and Péclet numbers are used, defined as,

$$Re = \frac{\text{centrifugal force}}{\text{viscous force}} = \frac{uh}{\nu},$$
$$We = \frac{\text{centrifugal force}}{\text{capillary force}} = \frac{\rho u^2 h}{\gamma},$$
$$Fr = \frac{\text{centrifugal force}}{\text{gravitational force}} = \frac{u}{\sqrt{gh}},$$
$$Ro = \frac{\text{centrifugal force}}{\text{Coriolis force}} = \frac{u}{\omega h},$$
$$Pe = \frac{\text{advective transportation rate}}{\text{diffusive transportation rate}} = \frac{uh}{D}.$$

The Bond number, as defined in section 2.2.3, has been used in literature relating γ and ω with the onset of instability, assuming a uniform film of volume V. However, for the range of rotation rates in this project, as we will see in chapter 4, that the thickness of the film and the ring evolve in a way that has not been described in the literature. The volume distribution varies significantly between the film and the ring, thus all dimensionless numbers are calculated for both areas. Therefore, when comparing centrifugal and capillary forces, we prefer to use the Weber number, which contains the film thickness. Specific definition for each diagnostic parameter is given in each chapter and depends on the symbols used to characterise the flow in each device.

Table 3.1: Experiments on flat rotating disks.

Code	**Explanation**
	Base case
FB5000H10V80	Flat brass disk, rotating at 5,000 rpm, with a pipette positioned 10 mm above the axis of rotation, releasing a droplet volume of 80μl. Camera: IDT, fps: 5,000, lens: Nikkor 60 mm, f/2.8D, shutter speed: 1/5,000 s.
	PIV case
FG5000H10V80	Flat black glass disk, rotating at 5,000 rpm, with a pipette positioned 10 mm above the axis of rotation, releasing a droplet volume of 80μl. Camera: IDT, fps: 6,000, lens: Nikkor 60 mm, f/2.8D, shutter speed: 1/36,000 s.
	Parameter: film thickness
FB-H10V80	Flat brass disk, rotating from 1,000 to 10,000 rpm, with a pipette positioned 10 mm above the axis of rotation, releasing a droplet volume of 80μl. Camera: Photron, fps: 5,000, lens: Nikkor 60 mm, f/3.5D, shutter speed: 1/17,000 s.
	Parameter: height of release
FB-H05V80	Flat brass disk, rotating from 1,000 to 10,000 rpm, with a pipette positioned 5 mm above the axis of rotation, releasing a droplet volume of 80μl. Camera: IDT, fps: 5,000, lens: Nikkor 60 mm, f/2.8D, shutter speed: 1/5,000 s.

Table 3.1: Experiments on flat rotating disks.	
Code	**Explanation**
Parameter: height of release	
FB-H10V80	Flat brass disk, rotating from 1,000 to 10,000 rpm, with a pipette positioned 10 mm above the axis of rotation, releasing a droplet volume of 80μl. Camera: IDT, fps: 5,000, lens: Nikkor 60 mm, f/2.8D, shutter speed: 1/5,000 s.
FB-H15V80	Flat brass disk, rotating from 1,000 to 10,000 rpm, with a pipette positioned 15 mm above the axis of rotation, releasing a droplet volume of 80μl. Camera: IDT, fps: 5,000, lens: Nikkor 60mm, f/2.8D, shutter speed: 1/5,000 s.
Parameter: droplet volume	
FB-H10V40	Flat brass disk, rotating from 1,000 to 10,000 rpm, with a pipette positioned 10 mm above the axis of rotation, releasing a droplet volume of 40μl, compared to the set FB-H10V80. Camera: IDT, fps: 5,000, lens: Nikkor 60 mm, f/2.8D, shutter speed: 1/5,000 s.
Parameter: surface smoothness	
FG-H10V80	Flat black glass disk, rotating from 1,000 to 10,000 rpm, with a pipette positioned 10 mm above the axis of rotation, releasing a droplet volume of 80μl, compared to the set FB-H10V80. Camera: IDT, fps: 5,000, lens: Nikkor 60 mm, f/2.8D, shutter speed: 1/5,000 s.
Parameter: wet disk	
FB-H10V80W	Flat brass disk, rotating from 1,000 to 10,000 rpm, with a pipette positioned 10 mm above the axis of rotation, releasing a droplet volume of 80μl, with a flux of 20 ml/min, compared to the set FB-H10V80. Camera: IDT, fps: 5,000, lens: Nikkor 60 mm, f/2.8D, shutter speed: 1/5,000 s.
Parameter: pipette position	
FB-H10V80OFF10	Flat brass disk, rotating from 1,000 to 10,000 rpm, with a pipette positioned 10 mm above the axis and 10 mm off the axis of rotation, releasing a droplet volume of $V = 80\mu$l. Camera: IDT, fps: 5,000, lens: Nikkor 60 mm, f/2.8D, shutter speed: 1/5,000 s.
FG-H10V80OFF10	Flat glass disk, rotating from 1,000 to 10,000 rpm, with a pipette positioned 10 mm above the axis and 10 mm off the axis of rotation, releasing a droplet volume of 80μl. Camera: IDT, fps: 5,000, lens: Nikkor 60 mm, f/2.8D, shutter speed: 1/5,000 s.

Table 3.1: Experiments on flat rotating disks.	
Code	**Explanation**
Parameter: tilted set-up	
FB-T45V80A10	Flat brass disk tilted at 45°, rotating from 1,000 to 10,000 rpm, with a pipette positioned so that the droplet lands 10 mm above the axis of rotation, releasing a droplet volume of 80μl. Camera: IDT, fps: 5,000, lens: Nikkor 60 mm, f/2.8D, shutter speed: 1/5,000 s.
FB-T45V80ON	Flat brass disk tilted at 45°, rotating from 1,000 to 10,000 rpm, with a pipette positioned so that the droplet lands on the axis of rotation, releasing a droplet volume of 80μl. Camera: IDT, fps: 5,000, lens: Nikkor 60 mm, f/2.8D, shutter speed: 1/5,000 s.
FB-T45V80B10	Flat brass disk tilted at 45°, rotating from 1,000 to 10,000 rpm, with a pipette positioned so that the droplet lands 10 mm below the axis of rotation, releasing a droplet volume of 80μl. Camera: IDT, fps: 5,000, lens: Nikkor 60 mm, f/2.8D, shutter speed: 1/5,000 s.

The spreading at the hemispherical base of the VFD was tested by replacing, in the same set-up, the flat disk with the hemispherical brass disk. The parameters under investigation are the rotation rate, the height of the release and the effects of gravity due to the curved geometry. Single droplets of 80 μl, landing on an already rotating hemispherical disk, are investigated for the understanding of the VFD under CF. The base case is designated with the code HB6000H10V80, which stands for the hemispherical brass disk that rotates at 6,000 rpm (HB6000), with a droplet released 10 mm above the disk (H10), of 80 μl volume (V80). The experiments on the hemispherical disk are presented in Table 3.2.

Table 3.2: Experiments on a hemispherical disk.	
Code	**Explanation**
Base case	
HB6000H10V80	Hemispherical brass disk, rotating at 6,000 rpm with the pipette positioned 10 mm above the axis of rotation, releasing a droplet volume of 80 μl. Camera: IDT, fps: 5,000, lens: Nikkor 60 mm, f/2.8D, shutter speed: 1/5,000 s.
Parameter: height of release	
HB-H05V80	Hemispherical brass disk, rotating from 1,000 to 10,000 rpm with the pipette positioned 5 mm above the axis of rotation, releasing a droplet volume of 80 μl. Camera: IDT, fps: 5,000, lens: Nikkor 60 mm, f/2.8D, shutter speed: 1/5,000 s.

Table 3.2: Experiments on a hemispherical disk.	
Code	**Explanation**
Parameter: height of release	
HB-H10V80	Hemispherical brass disk, rotating from 1,000 to 10,000 rpm with the pipette positioned 10 mm above the axis of rotation, releasing a droplet volume of 80 μl. Camera: IDT, fps: 5,000, lens: Nikkor 60 mm, f/2.8D, shutter speed: 1/5,000 s.
HB-H15V80	Hemispherical brass disk, rotating from 1,000 to 10,000 rpm with the pipette positioned 15 mm above the axis of rotation,releasing a droplet volume of 80 μl. Camera: IDT, fps: 5,000, lens: Nikkor 60 mm, f/2.8D, shutter speed: 1/5,000 s.
Parameter: pipette position	
HB-H10V80OFF10	Hemispherical brass disk, rotating from 1,000 to 10,000 rpm, with a pipette positioned 10 mm above the axis and 10 mm off the axis of rotation, releasing a droplet volume of $V = 80\mu$l. Camera: IDT, fps: 5,000, lens: Nikkor 60 mm, f/2.8D, shutter speed: 1/5,000 s.
Parameter: Tilted hemispherical disk	
HB-T45V80A10	Hemispherical brass disk, rotating from 1,000 to 10,000 rpm with the pipette positioned so that the droplet lands 10 mm above the axis of rotation, releasing a droplet volume of 80 μl. Camera: IDT, fps: 5,000, lens: 60mm, f/2.8D, shutter speed: 1/5,000 s.
Parameter: Tilted hemispherical disk	
HB-T45V80ON	Hemispherical brass disk, rotating from 1,000 to 10,000 rpm with the pipette positioned so that the droplet lands on the axis of rotation, releasing a droplet volume of 80 μl. Camera: IDT, fps: 5,000, lens: Nikkor 60 mm, f/2.8D, shutter speed: 1/5,000 s.
HB-T45V80B10	Hemispherical brass disk, rotating from 1,000 to 10,000 rpm with the pipette positioned so that the droplet lands 10 mm below the axis of rotation, releasing a droplet volume of 80 μl. Camera: IDT, fps: 5,000, lens: Nikkor 60 mm, f/2.8D, shutter speed: 1/5,000 s.

3.1.3 Flow visualisation techniques

Two high–speed cameras were used in the spinning-disk experiments. An IDT OS4-S3, with $1,024 \times 1,024$ pixel image size, 12-bit monochrome with 8 GB memory capable of 6,000 frames per second (fps), was placed above the axis of rotation. A Micro Nikkor lens was used to record the total area of spreading with maximum focal length at 60 mm and maximum aperture at f/2.8D. The distance between the outer face of the lens and the disk surface was 20 cm. A

Photron Fastcam SA1.1, with $1,024 \times 1,024$ pixel image size, that can capture up to $5,400$ fps, was placed on the side. A Tamron macro lens was used, for the detailed recording of the landing area. The macro lens had a fixed focal length of 180 mm and maximum aperture at f/3.5D. The distance between the outer face of the lens and the axis of rotation was 15 cm. The minimum working distance, using the macro lenses, was short enough to allow a 1:1 magnification. The lens aperture was dependent on the shutter speed, which was selected to prevent over-illumination. The positions of the cameras and the lights are shown in Figure 3.4.

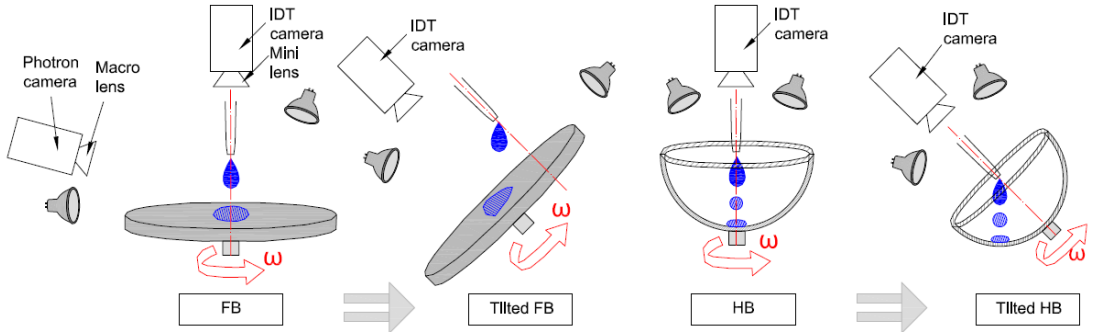

Figure 3.4: Positions of cameras for spinning disk experiments.

Two 250 W halogen lamps were used, that had ellipsoidal dichroic reflectors, forming an optical axis targeting the centre of the disk. For the flat disk experiments, one of the lamps was placed above the disk with the optical axis vertically targeting the disk and the other lamp was placed on the side with the optical axis immediately above the disk surface. This placement of lamps produced a uniform illumination on the film with minimal shadows while maximising the reflections at the crests of the surface waves, allowing a better visualisation of the pattern.

To enhance the contrast between the disk and the liquid, water soluble dyes were used. For every syringe of 100 ml approximately 4 ml of blue food dye was introduced to the sample (i.e. 4% wt). Liquid volumes were measured with a Pipetman Classic P2 pipette with a precision of 0.2 μl and an error of 0.03 μl. Especially for the glass disk, a fluorescent dye was needed for the visualisation of the film, thus 6 g of fluorescein sodium were diluted in 300 ml of water (i.e. 2% wt). The same fluorescent solution was used for the measurement of the film thickness in combination with a monochromatic blue laser FP-MVnano-488-40M-45-F, which was incident from the top. The wavelength of the laser, was 488 nm and the thickness of the line was 1 mm. The Powell lens had a fan angle at 45°. The experiment was conducted in a dark room. The Photron high–speed camera with the macro lens attached, was placed on the side, facing the beam, collecting the 2D patterns of reflections. The distance from the outer face of the lens to the axis of rotation was 15 mm. Two rays of enhanced intensity within the beam, one from the tangential projection of the free surface of the liquid and one from the tangential projection of the interface between the liquid and the rotating disk, as shown in Figure 3.5, were brought to coincidence on the camera.

The film thickness variation was recorded over the radius of the brass disk. The optical path of the reflected light produced by the rotating disk surface (green line) was subtracted from each image. The remaining line (blue line) was the free surface and required calibration. In every cross–section, along the r direction, of the remaining line the pixel intensity was assumed to

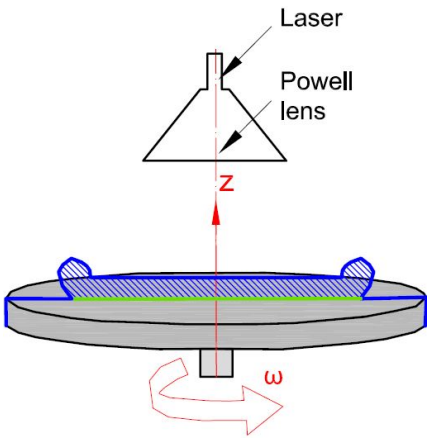

Figure 3.5: Experimental set-up of the film thickness experiment using a laser beam.

follow a Gaussian distribution as

$$I = I_{max} e^{-\frac{(z-z_{I_{max}})^2}{\sigma^2}},$$

where z represents the pixel coordinates of the free surface, I_{max} is the maximum intensity, $z_{I_{max}}$ is the position of maximum intensity and σ is the standard deviation. The value of $z_{I_{max}}$ can be determined by taking the log of the above expression of I and the differentiation $\frac{d\ln(I)}{dz} = 0$. The intensity of each cross–section along the line can be approximated by a quadratic curve ($\sim -az^2 + bz + c$) of the $\ln I$. Taking the derivative of each curve we determine the $z_{I_{max}} = -\frac{b}{2a}$ in each cross–section. The collection of $z_{I_{max}}$ of the distributions along the laser ray, formed the free surface of the spreading droplet.

Particle Image Velocimetry (PIV) was also attempted to determine the velocity profile in the spreading film. PIV is based on fundamentals of pattern matching and measures the displacement of an ensemble of particles. Any particle motion therefore appears as a moving pattern superimposed on the apparent motion of the background pattern (Sveen and Dalziel, 2005). While fluorescent and food dyes can assist in the visualisation of the bulk of the fluid, pearlessence and particles can indicate possible cross–flow instabilities in the pattern.

In a typical PIV experiment strong reflections from the pearlessence and the particles are obtained in regions of high shear. This experiment was restricted by the very small time scale and the film thickness. Therefore, to optimise the spacial velocity resolution, the camera was focused only to half of the black glass disk, giving uniformly spaced images at 6,000 fps with a shutter speed at 1/36,000 s. The pixel size was 0.03 mm, while a typical pixel size in experimental recordings covering all the disk area was 0.07 mm. The determination of the velocity profiles was based on interrogation areas of 25 × 25 pixels with 50% overlapping.

The PIV experiment followed the methodology of Landel et al. (2015), through the addition of particles to the dyed solution. Landel et al. used a solution of 4 litres of water, dyed with 40 g methylene blue (i.e. 1% wt) and with the addition of 20 g artificial pearlescence (i.e. 0.5% wt, made of titanium-dioxide coated mica particles, size: 5 to 25 μm). Similarly in this experiment, the liquid solution consisted of 200 ml of water, dyed with 2 ml of blue (i.e. 1% wt), red (i.e. 1% wt) and green (i.e. 1% wt) food dyes respectively. The purpose of this almost black mixture of dye was to render the film opaque for the camera so that only the particles at the surface of the film could be seen. Furthermore, 1 g of artificial pearlescence (i.e. 0.5% wt, made of

titanium-dioxide coated mica particles, size: 5 to 25 μm) was added and was well mixed in the water solution. The large aperture of the lens, used due to the lack light, resulted to a small depth of field, thus pearlescence particle could not be traced for most of the recorded area. Therefore, several solutions using the same concentration of water, dyes and pearlescence but with the addition of particles of different sizes were attempted. The particle combination that gave the most detailed velocity profile consisted of 4 g (i.e. 2% wt, made of Polyamid seeding particles, size: 20 μm) and 4 g (i.e. 2% wt, made of Iriodin 119 polar white particles, size: 5 to 25 μm). The pearlescence tracers and the particles produced a non-uniform reflecting texture of light intensity at the surface of the film, from which the surface velocity could be computed using the 2017a PIV algorithm of DigiFlow. The results focus mostly on the spreading before and right after the front reaches the critical radius r_c.

3.2 Experiments with the VFD

Experiments with the VFD in CM mainly focused on the spin–up, the development of the film and the thickness of the film at steady state. The film thickness experiments were conducted with the use of neutron imaging at ANSTO, funded by the Australian Government's Super-Science Initiative. Access to the radiography apparatus was provided at ANSTO, as part of our collaboration on the VFD with Flinders University.

Experiments with the VFD in CF, investigated the volume capacity of the tube for a range of rotation rates, reaction rate variations and the landing and spreading of droplets on a tube with a film already at steady state. Part of the reaction experiment was conducted at Flinders University in Adelaide, in collaboration with the Raston laboratory. The experiments were conducted both with the use of miscible and immiscible solutions.

3.2.1 Basic experimental set–up

The VFD was provided by the lead inventor and senior Flinders University research scientist Prof. Colin Raston. The device was constructed in the same workshop that created all VFDs at the School of Chemical and Physical Sciences, Flinders University. The VFD is driven by a Faulhaber 4490 024 B K1155 DC Motor, which can reach rotation rates up to 9,000 rpm. The motor shaft is connected to the lower bearing of the device. The tube is secured between the lower and the upper bearing, as shown in Figure 3.6. The upper bearing follows the rotation of the tube caused by the lower bearing. Each bearing secures the tube with the use of two O Rings made of Nitrile Butadiene Rubber (NBR). A metallic frame holds the two bearings, keeping them aligned. A cylindrical lid is attached to the higher end of the frame, securing the top of the set–up and the positioning of the pipettes. The lid is important in CF, collecting the product expelled from the tube. The lid is connected to the housing unit with 6 plastic screws and the housing unit is connected to the frame with another 6 screws.

3.2.2 Parameter variation

Several VFD tubes were tested but only two tubes were used for all the experiments reported in this thesis. The tubes are custom–made in Adelaide, either from blown glass (GT) or from

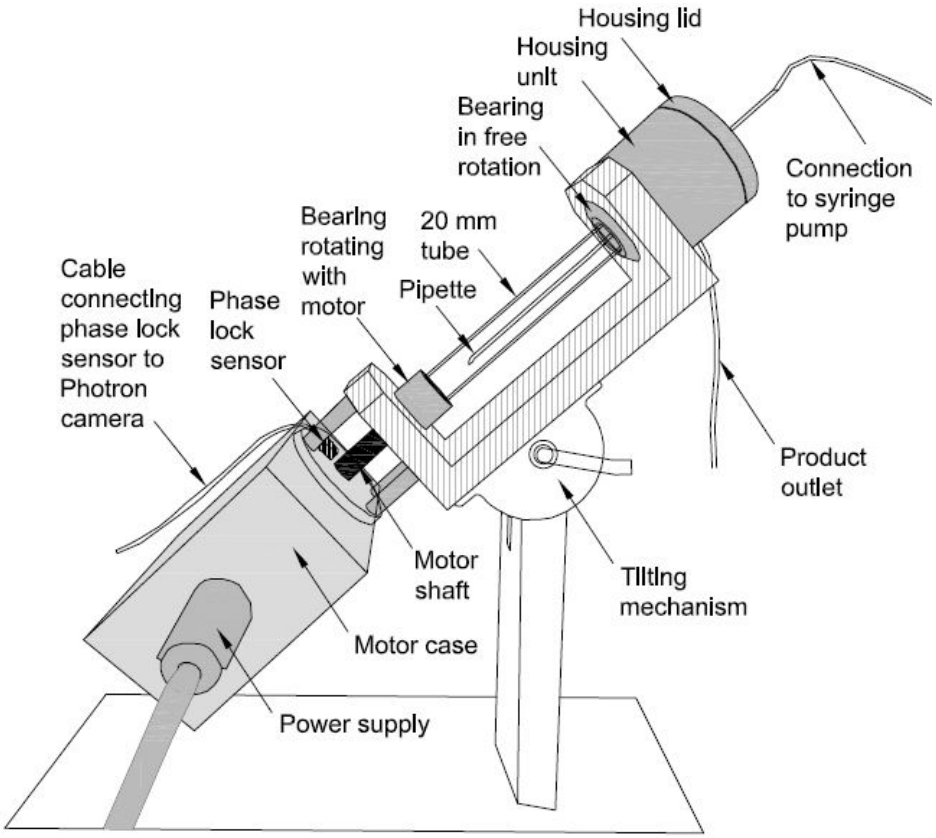

Figure 3.6: Experimental set-up using the VFD.

quartz glass (QT). In the course of this work it was found that every tube has unique geometrical imperfections, which lead to an inhomogeneous contact line. Given this unique characteristic, two tubes one from blown glass and one from quartz glass, were measured geometrically in detail and were used for all the experiments. It is expected that the two glasses will form films of different surface energy. The QT was used for the neutron imaging experiments at ANSTO, due to its increased transparency compared to the GT. Therefore the QT became the primary tube of testing. Both tubes were cleaned before every realisation, using acetone and were dried out with a spray duster (containing Butane, Isopropane and Propane).

Mixing was explored by using miscible and immiscible liquids. As immisible we consider two liquids with low solubility. The two almost immiscible fluids were water (at 20 C°, $\nu = 10^{-6}$ m^2/s, $\rho = 1,000$ kg/m^3 and $\gamma = 7 \times 10^{-2}$ N/m) and toluene (at 20 C°, $\nu = 7 \times 10^{-7}$ m^2/s and $\rho = 871$ kg/m^3, $\gamma = 3 \times 10^{-2}$ N/m). The solubility of toluene in water, in room temperature and ignoring evaporation, is $\sim$ 0.52 g/l. For comparison the solubility of glucose, which is miscible to water, is $\sim$ 900 g/l. For immiscible liquids, droplets of dyed water were released on a film of toluene at steady state. For experiments using miscible liquids, droplets of dyed water were released in the VFD while a colorless water film was already rotating at steady state. The dyed water solution had the same concentration of food dye as in the spinning disk experiments.

The spin–up was tested from 1,000 to 9,000 rpm, with 1 ml of water, and the VFD tilted, from the horizontal axis, at 85° and at 45°. The spin-up was also tested for immiscible liquids, using 0.3 ml of toluene and 0.7 ml of water for the same range of rotation rates and inclination angles. The film thickness was determined, with the technique of neutron imaging, from 1,000 to 9,000 rpm, for 1 ml of toluene.

In order to determine the reaction rate in the VFD, the aim was to find a reaction that would require a substantial amount of time in a static flask, compared to the time needed in the VFD. The reaction should be characterised by intense colour changes that could be captured by the high–speed camera. Several attempts were made in order to find the most suitable reaction. In order to secure that the film is uniformly developed in the VFD, 3 ml of the one reactant were placed inside the tube. After the spin–up and once the film reached steady state, one droplet of 40μl of the second reactant was released close to the base of the tube, through a pipette as in CF. The evolution of colour change was recorded by the high–speed camera. Every solution gave different qualitative and quantitative observations all of which, along with the specifics of the reactions, are discussed in section 6.3.6.

The list of experiments conducted in the VFD is presented in Table 3.3.

Table 3.3: List of experiments in the VFD - 20 mm tube

Code	**Explanation**
	Base case - CM
CM45GT85000W1	Spin-up and steady state of 1 ml of water dyed with methylene blue, in blown glass tube, inclined at 45°, rotating at 5,000 rpm. Camera: Photron, fps: 500, lens: Nikkor 60 mm, f/3.5D, shutter speed: 1/2,000 s.
	VFD Capacity - CF
CF85GT-W	Steady state of water in a blown glass tube, inclined at 85°, at rotation rates from 1,000 to 9,000 rpm. Camera: Photron, fps: 1,000, lens: Nikkor 60 mm, f/3.5D, shutter speed: 1/2,000 s.
CF45GT-W	Steady state of water in a blown glass tube, inclined at 45°, at rotation rates from 1,000 to 9,000 rpm. Camera: Photron, fps: 500, lens: Nikkor 60 mm, f/3.5D, shutter speed: 1/2,000 s.
	Spin up - CM
CM85GT-W1	Steady state of 1 ml of water in a blown glass tube, inclined at 85°, at rotation rates from 1,000 to 9,000 rpm. Camera: Photron, fps: 500, lens: Nikkor 60 mm, f/2.8D, shutter speed: 1/2,000 s.
CM45GT-W1	Steady state of 1 ml of water in a blown glass tube, inclined at 45°, at rotation rates from 1,000 to 9,000 rpm. Camera: Photron, fps: 500, lens: Nikkor 60 mm, f/2.8D, shutter speed: 1/2,000 s.
CM45GT-T1	Steady state of 1 ml of toluene in a blown glass tube, inclined at 45°, at rotation rates from 1,000 to 9,000 rpm. Camera: Photron, fps: 500, lens: Tamron 180 mm, f/3.5D, shutter speed: 1/30,000s .
CM45QT-W1	Steady state of 1 ml of water in a fussed quartz tube, inclined at 45°, at rotation rates from 1,000 to 9,000 rpm. Camera: IDT, fps: 500, lens: Nikkor 60 mm, f/2.8D, shutter speed: 1/2,000s .

Table 3.3: List of experiments in the VFD - 20 mm tube	
Code	**Explanation**
Spin up - CM	
CM85GT-W7T3	Steady state of 0.7 ml of water and 0.3 ml of toluene in a blown glass tube, inclined at 85°, at rotation rates from 1,000 to 9,000 rpm. Camera: Photron, fps: 1,000, lens: Nikkor 60 mm, f/2.8D, shutter speed: 1/2,000 s.
CM45GT-W7T3	Steady state of 0.7 ml of water and 0.3 ml of toluene in a blown glass tube, inclined at 45°, at rotation rates from 1,000 to 9,000 rpm. Camera: Photron, fps: 1,000, lens: Nikkor 60 mm, f/3.5D, shutter speed: 1/2,000 s.
Film thickness - inclination at 45° (ANSTO)	
CM45QT-T1	Film of 1 ml of toluene at steady state, in a quartz tube, inclined at 45°, at rotation rates from 1,000 to 9,000 rpm. Camera: Andor, lens: Zeiss 100 mm, f/2D, shutter speed: 90 s.
Diffusion rate - CM	
CTBS	Control experiment, using a capillary tube of 1 mm diameter, placed vertically, filled with 1 ml bromothymol blue touching at the lower edge for 1 s, at the initiation of the experiment a sample of sulfuric acid. Camera: Nikon D5000 Digital SLR, lens: Nikon 30 mm f/4.5D, shutter speed: 30 s.
Reaction rate	
IN45GTS8N2	Indigo dye processing, using a solution of Sodium hydroxide 0.8 ml and 0.2 ml 0-Nitrobenzaldehyde, in a blown glass tube, inclined at 45°, at rotation rates form 1,000 to 9,000 rpm. Camera: IDT, fps: 1,000, lens: Nikkor 60 mm, f/2.8D, shutter speed: 1/2,000 s.
D-QT45B3S40	Solution of 3 ml of bromothymol blue with a droplet of 40 μl of sulfuric acid in a quartz tube, inclined at 45°, at rotation rates from 1,000 to 9,000 rpm. Camera: IDT, phase locked to rpm, lens: Nikkor 60 mm, f/2.8D, shutter speed: 1/2,000 s.
Vapour effects - tube inclination at 45° - CM	
V-QT45B3A40	Solution of 3 ml of bromothymol blue with a droplet of 40 μl of acetic acid in a quartz tube, inclined at 45°, at rotation rates from 1,000 to 9,000 rpm. Camera: IDT, phase locked to rpm, lens: Nikkor 60 mm, f/2.8D, shutter speed: 1/2,000 s.
Immiscible liquids - CF	
CFGT45T2W1	Film of 2 ml of toluene at steady state, with dyed water released in the form of droplets of 40 μl with a flux of 1 ml/min, in a blown glass tube, inclined at 45°, at rotation rates from 5,000 to 9,000 rpm. Camera: Photron, fps: 1,000, lens: Tamron 180 mm, f/3.5D, shutter speed: 1/30,000 s.

Table 3.3: List of experiments in the VFD - 20 mm tube	
Code	**Explanation**
Miscible liquids - CF	
CFGT45W2W1	Film of 2 ml of colorless water at steady state, with dyed water released in the form of droplets of 40 μl with a flux of 1 ml/min, in a blown glass tube, inclined at 45°, at rotation rates from 5,000 to 9,000 rpm. Camera: Photron, fps: 1,000, lens: Tamron 180 mm, f/3.5D, shutter speed: 1/30,000 s.

3.2.3 Flow visualisation techniques

The experiments in the VFD were recorded primarily with the IDT camera or the Photron camera, using the 60 mm Nikkor lens when recording the total length of the tube and the 180 mm Tamron macro lens when recording zoomed parts of the tube. The time scale of the recordings varied significantly depending on the experiment. The spin–up, for example, is complete in a few seconds, while a diffusion experiment requires 3 to 20 minutes. There were cases where the recording time was greater than the maximum frame storage available on the high–speed camera. However, the IDT camera had the option to be phase locked with the tube. Therefore the camera was phase locked with the tube by placing a sensor adjacent to the motor shaft. A reflecting indicator was attached to the motor shaft which was captured by the sensor after every exact rotation. The sensor was connected to the camera. The camera captured a frame after every sensor signal, i.e. at the same position azimuthally, after every rotation. For the experiments using edge detection, a solution of dyed water was used as in the spinning–disk experiments.

3.2.3.1 Neutron imaging

The film thickness in the VFD can be determined experimentally with the use of neutron imaging. While X-rays are preferred at seeing dense materials inside light materials (e.g., bone in flesh), neutron radiography has traditionally been used to see hydrogenous materials inside metallic or ceramic objects. The experiments are conducted at ANSTO's Open Pool Australian Lightwater (OPAL) reactor, a 20 Megawatt reactor that uses low enriched uranium fuel for several research and industrial applications. For the neutron imaging experiment, the reactor produces neutrons which are guided to the instrument DINGO. The neutrons pass through the collimator and are guided towards the sample through the flight tubes, as shown in Figure 3.7. The neutrons pass through the sample and are scattered by atoms in the material being probed. The scattering pattern reveals the sample's structure and dynamics.

The detector records the attenuation of neutrons passing through the object. The portion of the beam transmitted through the sample is converted into visible light using a 20 μm, thick Gadox scintillator. The light is then reflected via a mirror to an Andor Neo 5.5 sCMOS camera, as shown in Figure 3.8, with a $2,560 \times 2,160$ (5.5 Megapixel) pixels sensor. A Carl Zeiss lens is attached to the camera with fixed focal length at 100 mm. The distance between the VFD and the scintillator is 15 cm.

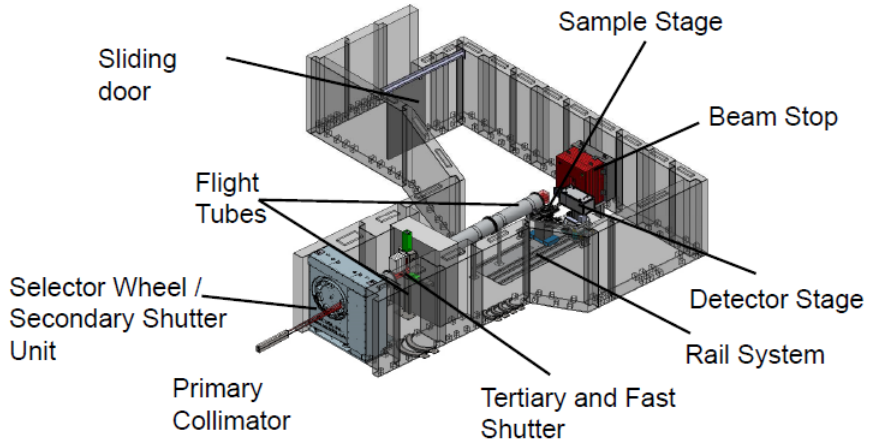

Figure 3.7: The general assembly of the instrument DINGO (Garbe et al., 2015).

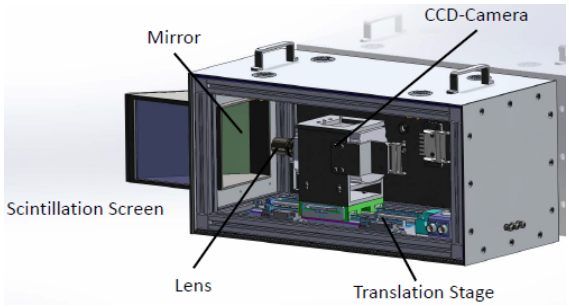

Figure 3.8: Configuration of the camera set-up (Garbe et al., 2015).

The outcome of the process is an image with pixel intensity directly related to the properties of the materials in the sample. With the camera used at ANSTO, the exposure time is 90 s. The method works better for rigid objects, as a high signal–to–noise ratio is preferable. In the VFD case, depending on the rotation rate, the final image is a time average of tube revolutions that range form $1,500$ to $13,500$ rotations per picture. The rotating VFD is a challenging sample and it is the first neutron imaging attempt on a moving frame at ANSTO.

The image resolution depends on the collimator geometry (length and aperture) on the side facing the source. For that reason, we use the highest flux available on DINGO at 4.75×10^7 neutrons/(s cm^2). The spatial resolution is also maximised (with the ratio of collimator-detector length to inlet collimator diameter equal to 1,000), corresponding to a pixel size of 13 μm. In this configuration, the size of the neutron beam available on the machine permits a region of interest of 30×35 mm^2 to be studied at one time. Hence for a sensor of 10 cm^2 we get 4.75×10^8 neutrons/s, i.e. 80 neutrons/s per pixel. Given the small region of study per radiography, for every experiment, 11 radiographies are necessary to image the entire length of the tube. The exposure time to the neutron beam, for each of the 11 steps, is 90 s, equal to the exposure time of the camera. Thus, a 90 s exposure time captures a maximum of 7,200 neutrons per pixel.

In comparison the publication by Solheim et al. (2019) refers to neutron imaging experiments with the ratio of collimator-detector length to inlet collimator diameter equal to 500, corresponding to a pixel size of 67 μm. The exposure time to the neutron beam was 1 s. Assuming maximum flux of neutrons, the neutron imaging result corresponds to approximately 80 neutrons per pixel.

The IDT camera, although available for the ANSTO experiments, was not used, due to concerns regarding possible damages caused by the neutrons. Using the IDT camera, we could be able to capture several pictures per revolution. However shorter exposure time would mean less neutrons per pixel per second, resulting to reduced brightness variations in the final image.

The static VFD is also captured in 11 radiographies, which are considered the background images of the experiment. The radiographies are corrected with the software Octopus. The static background field is subtracted both from the rotating and the stationary radiographies. The rotating radiographies is divided by the stationary radiographies. Thus each image contains the resulting neutron transmission. Finally AVISO 9.1, an image processing software available at ANSTO, is used for the stitching of the 11 radiographies.

The processing for the estimation of the time average film thickness requires a new methodological approach. The novel methodology consists part of the results of this project and therefore is analysed in detail in paragraph 6.3.5.

3.3 Summary

The methodology is developed according to the modes of operation in the VFD. Three classes of experiments are formed, one for each device, i.e. flat, hemispherical disk and the VFD.

The rotating disks are used to investigate the film formation caused by single droplets in rotating surfaces. The single droplet experiments are motivated by the feeding of droplets in the VFD under CF. The radial evolution and the onset of instabilities are explored for variations in rotation rate, droplet volume, height of release and surface smoothness.

In the VFD, experiments are conducted under CM, exploring the film development over time, the film thickness and the reaction rate. Experiments in CF are also attempted, mainly to explain the dynamics of droplet landing in an already developed and rotating liquid film.

The range of rotation rates under investigation is decided based on the chemical performance of the VFD. The VFD performs best, both in CM and in CF, at approximatelly 7,000 to 8,000 rpm, with the maximum rotation rate limit of the VFD motor being at 9,000 rpm. Therefore the range of rotation rates is set in all devices from 1,000 to 9,000 rpm with a special focus from 5,000 to 9,000 rpm.

Mathematical approximations are developed to describe the experimental observations both in the rotating disks and in the VFD. The time scale of the spreading pattern of single droplets in the flat disk is found to be different that the time scale suggested in section 2.2.2. Therefore, new models, suitable to our results, describing the evolution of the wet area are developed in this thesis, both for the flat and the hemispherical disk. Models for the film shape, in the VFD, at steady state and during the spin–up are also formed. The models consider a rotating frame so that inertia can be neglected. In addition, the lubrication approximation is deployed for the spin–up problem in the VFD. Azimuthal motion is considered negligible simplifying a three–dimensional to a two–dimensional problem. The mathematical formulations and the experimental results are presented in the following chapters.

Chapter 4

Flat disks

This chapter explores the formation of thin films caused by single droplets landing on already rotating surfaces. The experiments focus on the dynamics of droplet landing, the spreading evolution and the presence of instabilities both at the contact line and at the interface with the air boundary layer. The results indicate an unexpected pattern of spreading which has not been documented previously in the literature.

The stages of film formation define the important parameters of investigation. The droplet is released from a pipette at a specific height over the disk, falls under the force of gravity and lands on the already rotating substrate. During early times after landing, the droplet experiences shape oscillations due to the inertia of the free fall and the rotating substrate (section 4.1.1). After the transient stage, the centrifugal force, which is the dominant factor of spreading, drags the fluid outwards. The droplet occupies two distinct areas, the film and the ring. As the front propagates, perturbations develop near the contact line, evolving into contact–line and free–surface instabilities (section 4.6).

This chapter attempts to address a number of questions that vary according to the parameter under investigation. The experiments explore the spreading pattern and the onset of instabilities changing the rotation rate (section 4.4), the height of the release, the volume of the droplet and the substrate roughness (section 4.5). Each variation is investigated by measuring the evolution of the radius of the wet area $r_r(t)$ and the critical radius r_c at the onset of the instabilities. The thickness of the ring is measured to determine the volume distribution between the film and the ring (section 4.3), with the volume distribution being a very critical factor for the onset of the contact line instabilities.

4.1 Basic spreading characteristics

In this section we analyse the basic characteristics of axisymmetric droplet spreading. The transient stage is investigated in section 4.1.1. The number of experiments and the variety of parameters investigated make it necessary to establish a base case experiment to which all the other experiments would be compared.

The base case, determined in section 4.1.2, is chosen in order to represent a typical spreading pattern, satisfying specific requirements: (a) the inertia from the free fall should be minimised, (b) the rotation rate should be high enough to achieve axisymmetric spreading but low enough

to be captured in detail by the camera and (c) the droplet volume should be sufficient for all the instabilities to be developed. In this section we set the foundations for the determination of parameters for the base case.

4.1.1 Transient stage

The inertia of the droplet landing is explored by setting heights of release at 5 mm, 10 mm and 15 mm, as shown in Figure 4.1. When the droplet is released 5 mm above the disk (Figure 4.1a), the liquid touches the disk before a droplet is fully formed (Figure 4.1d). The landing is smooth but the spreading pattern is very sensitive to the alignment of the pipette with the axis of rotation (Figure 4.1g). The bottom of the droplet is already in rotation while the droplet is still attached to the pipette. The interaction of the droplet with the von Kármán layer expelling liquid outwards, explained in section 1.4, might be different in this case compared to the free falling droplets.

The increased sensitivity for the axial alignment is also due to the reduced liquid volume in each droplet. When the height of release is set at 5 mm above the centre of the disk, for constant flux of 0.8 ml/s and within a time scale of 10 min, more frequent droplet discharges are observed, compared to a height of release at 10 and at 15 mm. When the pipette is placed 5 mm above the disk, 120 discharges are observed of approximately 67 μl each. When the pipette is placed 10 mm and 15 mm above the disk, the number of discharges is 100 and the volume of each droplet is approximately 80 μl. As a result, a height of release at 5 mm reduces the volume of the droplet by 13 μl and therefore is not comparable with the other heights of release. An important factor for the reduced droplet size is the time scale of the flow rate in the pipette which is much larger in comparison with the time scale of the flow rate from the expelled liquid which reaches the disk. Thus, increasing the flux at the pipette could lead to increased volume of liquid per discharge for the height of release at 5 mm, while the other two pipette positions would have more frequent discharges of approximately the same droplet volume.

When the droplet is released at 10 mm above the disk, the droplet has just about enough space to form. The droplet touches the disk at the moment of detachment from the pipette (Figure 4.1b). The detachment from the pipette causes the formation of capillary waves, which propagate downwards. During the free fall, the capillary waves reach the lower part of the droplet and are reflected upwards, repeating that phenomenon until the droplet reaches the rotating disk (Figure 4.1e). Immediately after the impact, the droplet experiences shape oscillations, for 30 ms (approximately 26% of the total time of spreading), due to the collision with the rotating surface (Figure 4.1h).

When the droplet is released 15 mm above the disk, the droplet has enough time to form a sphere (Figure 4.1c). During the detachment from the pipette, capillary waves form and move across the surface of the droplet causing shape oscillations. The droplet lands on the rotating disk and capillary waves propagate upwards due to the impact (Figure 4.1f). The droplet experiences shape oscillations during the transient stage, for 40 ms (approximately 40% of the total spreading time), due to the collision with the rotating surface (Figure 4.1i). The extended spreading time, for a height of release at 15 mm, is due to the extended shape oscillations at early times. Thus, the height of the release affects, not only the early times of landing but also alters the total spreading time.

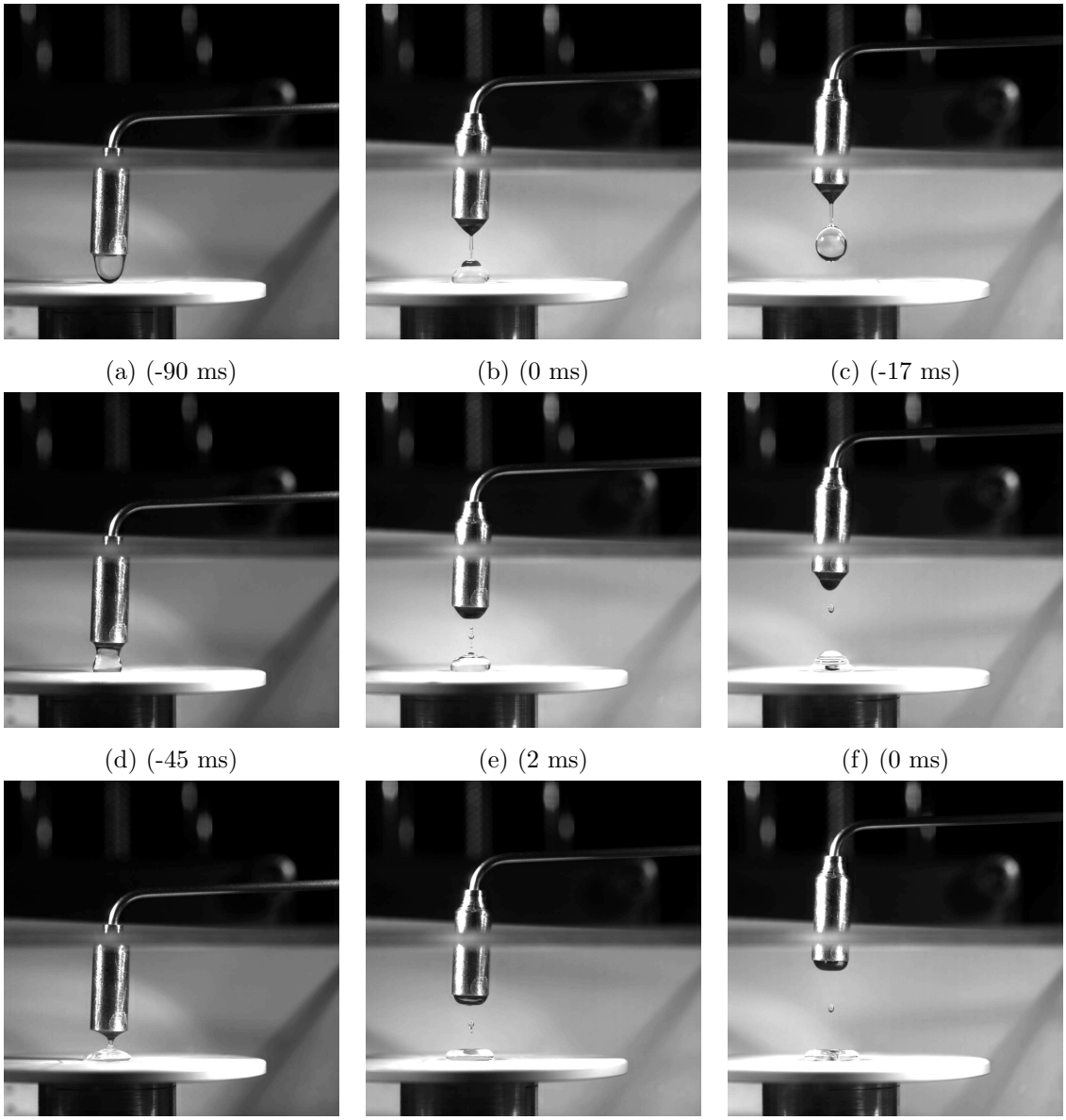

(a) (-90 ms) (b) (0 ms) (c) (-17 ms)

(d) (-45 ms) (e) (2 ms) (f) (0 ms)

(g) (0 ms) (h) (15 ms) (i) (17 ms)

Figure 4.1: Detachment, free fall and landing of droplets, where $t = 0$ s is the time that the edge of the droplet is beyond the perimeter of the pipette, i.e visible to the camera. The droplet is released at 5 mm (a,d,g), 10 mm (b,e,h) and 15 mm above the disk (c,f,i) – cases FB5000H05V80, FB5000H10V80 and FB5000H15V80 respectively.

The total spreading time for heights of release at 5 mm and at 15 mm is increased compared to the spreading time for a height of release at 10 mm, as shown in Figure 4.2. For a droplet release at 5 mm, the spreading is slower due to the smooth landing and the reduced volume of liquid discharged. For a droplet released at 15 mm, the spreading is slower due to the more pronounced shape oscillation at early times after landing. Thus, the radius at early times after the fall and before centrifugal force becomes the main driving force of motion, affects the pattern of spreading. Therefore, the most appropriate height of release, for the base case, with minimised inertia effects, is chosen to be at 10 mm above the disk. To understand the effect of H, we explore the magnitude of the maximum radius in the transient stage after the impact (defined in the following section).

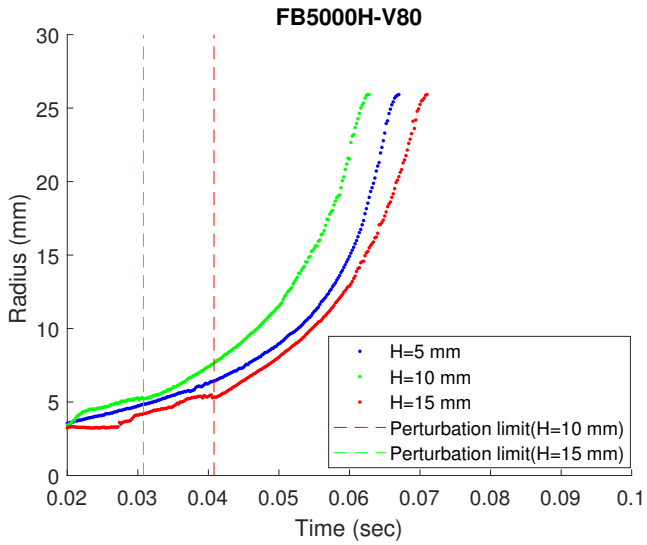

Figure 4.2: Radial evolution with respect to release heights at 5, 10 and 15 mm above a disk, rotating at 5,000 rpm (cases FB5000H05V80, FB5000H10V80 and FB5000H15V80). Detachment and free fall of droplets, setting $t = 0$ s when the edge of the droplet is beyond the perimeter of the pipette, i.e visible to the camera.

4.1.1.1 Transient radius after landing

The radius of a droplet landing onto a rotating disk evolves due to the inertia of the fall and the interaction with the rotating disk. For a stationary surface, the transient radius is the maximum radius achieved after the impact and before the droplet retracts to its sessile shape. For a droplet landing on a rotating disk at low rotation rates, provided that the impact velocity is not too large, the droplet extends to its transient radius and then retracts to its sessile shape. The sessile shape in this case has increased surface energy compared to the first case. At low rotation rates and high impact velocity the droplet spreads far enough for centrifugal force to dominate the flow and allow the droplet to continue spreading. At high rotation rates and high impact velocity, the droplet reaches the transient radius and centrifugal force dominates the flow, spreading the liquid further out axisymmetrically. Although the existence of the aforementioned cases is acknowledged, we focus on the last case. Thus, rather than observing a retracting droplet we assume a quasi–static radius at the time when centrifugal force dominates the flow, which from now on will be called 'transient radius' (r_t). The stage between the first contact with the

disk at the 'contact time' and the time the droplet reaches the transient radius at the 'transient time' is called 'transient stage' and is characterised by shape oscillations which will be named as 'impact effects'. A sketch describing the transient stage is shown in Figure 4.3.

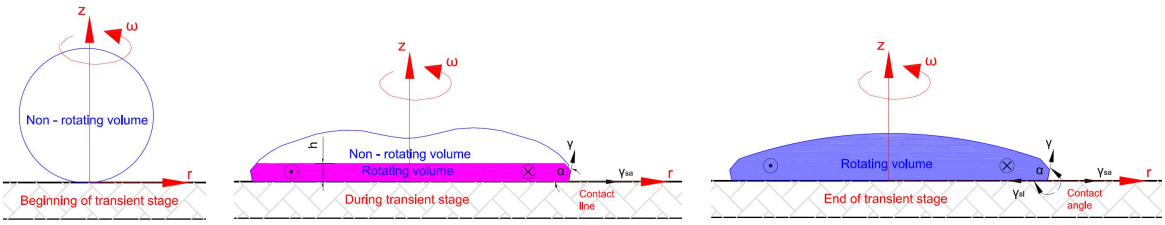

(a) (b) (c)

Figure 4.3: (a) The beginning of the transient stage is determined at the first instance of the contact of the droplet with the disk. (b) During the transient stage the von Kármán layer has formed (pink layer), setting the lower part of the droplet into rotation, while the top of the droplet remains essentially irrotational as it reshapes above the rotating boundary layer. (c) At the end of the transient stage centrifugal force dominates the flow while the bulk of the fluid is already in rotation.

In order to understand the initial stages of spreading, we define the transient radius by using an energy balance in the frame of reference rotating with the disk, using a cylindrical polar coordinate system (r, ϕ, z). As the time origin, we define the instant immediately after the droplet is detached from the pipette, which from now on will be referred to as 'release time'. Immediately after the detachment, the droplet is approximated as a sphere of volume $V = \frac{4}{3}\pi r_0^3$, where r_0 is the initial radius of the droplet. The height of release, H, is the height between the solid surface and the centre of the mass of the droplet. Using the energy balance between the release and the transient time, we determine the transient radius, after which centrifugal force dominates the flow.

The energy equation, based in the equation of landing on a stationary substrate analysed in section 2.2.1, but modified for a rotating frame of reference, axial landing and axisymmetric spreading is

$$\underbrace{E_k + E_g + E_c + E_s}_{\text{release time}} = \underbrace{E_k'' + E_g'' + E_c'' + E_s'' + E_\nu''}_{\text{transient time}}, \tag{4.1}$$

where E_g is the gravity potential energy, E_c is the centrifugal potential energy at the release time and E_ν'' is the integral of the energy dissipated between the release and the transient time. Double prime is used for the expressions of energy referring to the transient time. The initial kinetic energy in the frame rotating with the disk is

$$E_k = \int_V \frac{1}{2}\rho u_\phi^2 dV = \int_{-\pi}^{\pi}\int_{H-r_0}^{H+r_0}\int_0^{r_0} \frac{1}{2}\rho\omega^2 r^2 r dr dz d\phi \sim \pi\rho\omega^2 r_0^2 V. \tag{4.2}$$

The final kinetic energy is considered negligible under the assumption that at the transient time the droplet is momentarily at rest in the rotating frame, hence $E_k'' \sim 0$. The initial surface energy is

$$E_s = 4\pi r_0^2 \gamma. \tag{4.3}$$

At the transient time momentarily we assume a quasi–static droplet, in the rotating frame of reference, which sustains the advancing contact angle, as shown in Figure 4.3. Taking into con-

sideration Young's equation for a static contact line (Bonn et al., 2009), modified to incorporate the advancing contact angle, we get

$$\gamma_{sa} + \gamma \cos\alpha = \gamma_{sl} \rightarrow \gamma_{sa} - \gamma_{sl} = -\gamma \cos\alpha. \tag{4.4}$$

Assuming asymptotically that the droplet is already nearly flat, the area of the gas-liquid surface is close to the area of the liquid-solid surface ($\sim \pi r_t^2$). The surface energy at the transient time, for a droplet nearly flat, making use of equation 4.4, can be approximated as

$$E_s'' \sim (\text{area of the cap})\gamma + (\text{area of the base})(\gamma_{sa} - \gamma_{sl}) \sim \pi r_t^2 \gamma (1 - \cos\alpha). \tag{4.5}$$

The gravitational potential energy at the release time is

$$E_g = \rho g V H. \tag{4.6}$$

The gravitational potential energy, at the transient time, is negligible assuming that the droplet takes a cylindrical shape of thickness h, $E_g'' = \rho g V h \approx 0$, for $h \ll H$. The centrifugal potential energy at the release time is assumed $E_c \sim 0$. The centrifugal potential energy at the transient time, refers to the potential in which the body will accelerate in one dimension, along r, in the frame rotating with the disk, expressed as

$$E_c'' = -\int_V \frac{1}{2}\rho\omega^2 r^2 dV = -\frac{1}{2}\rho\omega^2 \int_{-\pi}^{\pi}\int_0^h \int_0^{r_t} r^2 r dr dz d\phi \sim -\pi\rho\omega^2 r_t^2 V. \tag{4.7}$$

The scaling of viscous dissipation is analysed in the literature review in paragraph 2.2.1. To determine viscous dissipation we consider the thickness of the boundary layer equal to the von Kármán thickness, $\delta \sim \left(\frac{\nu}{\omega}\right)^{\frac{1}{2}}$, and assume that the spreading is axisymmetric. Thus, the viscous dissipation function can be approximated as

$$E_\nu'' = \int_0^{t_t}\int_0^V \Phi dV dt, \tag{4.8}$$

where Φ is the viscous dissipation function and t_t is the time between the contact time and the transient time. Let us assume that the time between the contact and the transient time is approximately the time that the droplet takes to transform from a spherical shape to almost a flat film, scaling as the vertical distance from the centre of the mass of the droplet to the surface of the disk at the contact time ($\sim r_0$) over the velocity $u_{z(t=0)}$ of the droplet at the contact time, $t_t \sim \frac{r_0}{u_{z(t=0)}}$. This simplification is based on the assumption that at the early times of the transient stage, the droplet falls as on a stationary substrate. It was observed experimentally, during the PIV experiment, that at the early times of the transient stage the particles spread radially, without any indication of azimuthal motion, similar to the impact on a stationary substrate. The velocity u_z at the contact time can be determined by the energy balance between the release time and the contact time. Assuming a spherical droplet, under constant rotation rate, we can ignore surface energy as $E_s = E_s'$ and centrifugal potential energy $E_c = E_c'$, while E_k' is defined, using equation 4.2, as

$$E_k' = E_k + \frac{1}{2}\rho V u_{z(t=0)}^2, \tag{4.9}$$

thus

$$\underbrace{E_k + E_g}_{\text{release time}} \sim \underbrace{E_k'}_{\text{contact time}} \rightarrow \rho g V H \sim \frac{1}{2}\rho V u_{z(t=0)}^2 \rightarrow u_{z(t=0)} \sim \sqrt{2gH}. \tag{4.10}$$

The viscous dissipation function, in cylindrical polar coordinates, was obtained from the publication of Cloutman, (2001), and assuming that during the transient stage $u_\phi \ll u_r$, maximum $u_r \sim u_{z(t=0)}$ and $r_0 > \delta$, scales as

$$\Phi \sim \mu \left(\frac{u_r}{\delta}\right)^2, \tag{4.11}$$

where u_r is estimated in the following section (equation 4.21). By replacing equation 4.10 and 4.11 to equation 4.8, the viscous dissipation becomes

$$E_\nu'' = \int_0^{t_t} \int_0^V \Phi dV dt \sim \Phi V t_L = \mu \left(\frac{u_r}{\delta}\right)^2 V \frac{r_0}{u_{z(t=0)}} = \rho\omega r_0 \frac{u_r^2}{u_{z(t=0)}} V. \tag{4.12}$$

Replacing equations 4.2 - 4.7 and 4.12 to 4.1, an expression of the transient radius can be obtained as

$$r_t^2 \sim \frac{\rho\omega^2 r_0^2 V + \rho g V H + 4\pi r_0^2 \gamma - \rho\omega r_0 \frac{u_r^2}{u_{z(t=0)}} V}{\pi\gamma(1-\cos\alpha) - \rho\omega^2 V}. \tag{4.13}$$

In order for $r_t \, \epsilon \, \mathbb{R}$, equation 4.13 requires $\pi\gamma(1-\cos\alpha) > \rho\omega^2 V$, which means that the almost stationary shape of the droplet depends on the final surface energy and the final centrifugal potential energy (E_s'' and E_c''). Also, the maximum transient radius after the impact and before the centrifugal acceleration, depends on the excess of energy above the final surface and the potential energy, reduced by viscous dissipation. Thus, the transient radius depends on the height of the release, the impact velocity, the rotation rate of the substrate, the droplet volume and the way the capillary waves travel along the liquid body.

4.1.1.2 Transient velocity after landing

The behaviour of the spreading front is affected by the conditions of landing. The evolution of the radius at early times is affected by the transient stage, between the instant of the first contact of the droplet with the disk and the instant reaching the transient radius. The shape oscillations at this stage are observed due to the inertia of the fall and before centrifugal force spreads the fluid further away from the axis. The evolution of the radius is defined in the rotating frame, during the transient stage and ignoring viscous dissipation by the energy balance

$$\underbrace{E_k' + E_g' + E_c' + E_s'}_{\text{contact time}} = \underbrace{E_k'' + E_g'' + E_c'' + E_s''}_{\text{transient time}} \rightarrow E_c'' = E_s' + E_k' - E_s'', \tag{4.14}$$

where E_k' is determined by equation 4.9, assuming a spherical droplet, by the energy balance between the release and the contact time. The energy components $E_g',\ E_c', E_k'' \sim 0$, as explained in the section 4.1.1.1, $E_s' = E_s$ determined by equation 4.3 and E_s'' is defined by equation 4.5. Ignoring contact line effects and assuming uniform thickness, the thickness of the droplet can be expressed as

$$V = \pi r_t^2 h \rightarrow h = \frac{V}{\pi r_t^2} \rightarrow \frac{\partial h}{\partial t} = \frac{-2V}{\pi r_t^3} \frac{\partial r_t}{\partial t}, \tag{4.15}$$

where r_t it the radius of the wet area at the contact line. The centrifugal potential energy E_c'', at the transient time is a function of the spreading rate defined by equation 4.7 as

$$E_c'' \sim -\frac{1}{2}\rho V u_r^2. \tag{4.16}$$

To define u_r as a function of r_t and t, assuming $r_r \gg h$, where $u_\phi \ll u_r$ and $u_z \ll u_r$ and using volume conservation from equation 4.15, continuity equation becomes

$$\frac{\partial h}{\partial t} + \nabla \cdot (hu) = 0 \rightarrow \frac{\partial h}{\partial t} + \frac{1}{r}\frac{\partial}{\partial r}(u_r r h) = 0 \rightarrow \frac{\partial u_r}{\partial r} = \frac{2}{r_t}\frac{dr_t}{dt} - \frac{u_r}{r}, \tag{4.17}$$

where

$$u_r = \frac{B}{r} \rightarrow \frac{\partial u_r}{\partial r} = \frac{\frac{\partial B}{\partial r} r - B}{r^2}, \tag{4.18}$$

and $B(r,t)$ is a function that can be determined by using variations of parameters. Replacing equation 4.18 to equation 4.17 we get

$$\frac{2}{r_t}\frac{dr_t}{dt} - \frac{\cancel{B}}{\cancel{r^2}} = \frac{\frac{\partial B}{\partial r} r - \cancel{B}}{r^2} \rightarrow \frac{\partial B}{\partial r} = r\frac{2}{r_t}\frac{dr_t}{dt}. \tag{4.19}$$

Integrating equation 4.19 over r,

$$B(r,t) = \frac{1}{r_t}\frac{dr_t}{dt}r^2 + C(t) \rightarrow u_r = \frac{C(t)}{r} + \frac{1}{r_t}\frac{dr_t}{dt}r,$$

where using the boundary condition at the contact time with the solid substrate, at $t = 0$ s, $r_t = 0$ m and $u_r = 0$ m/s then $C = 0$, and u_r is defined as

$$u_r = \frac{1}{r_t}\frac{dr_t}{dt}r. \tag{4.20}$$

By placing equation 4.20 into equation 4.16

$$E_c'' \sim -\rho V \left(\frac{dr_t}{dt}\right)^2. \tag{4.21}$$

Replacing equations 4.3, 4.5, 4.9 and 4.21 to equation 4.14 we get the radial velocity

$$u_r \sim (L_1 - L_2 r_t^2)^{1/2}, \tag{4.22}$$

where

$$L_1 = \frac{\pi r_0^2 \gamma + \rho g H V + \rho \omega^2 r_0^2 V}{\rho \pi V} \text{ and } L_2 = \frac{\pi\gamma(1-\cos\alpha)}{\rho\pi V}.$$

Integrating over r_t with the boundary condition that at $t = 0 \rightarrow r_t = 0$, we get the evolution of the radius during the transient stage expressed as,

$$r_t \sim \left(\frac{L_1}{L_2}\right)^{1/2} \sin\left(\sqrt{L_2}t\right). \tag{4.23}$$

The time dependence of r_t presented in equation 4.23 will be compared to the evolution of the radius at the early times of spreading. The development of r_t at early times is expected to scale as $\sqrt{L_1}t + \mathcal{O}(t^3)$. In our experiments the droplet lands and spreads due to the inertia of the fall. Then centrifugal force acts on the liquid and the droplet spreads further outwards.

4.1.2 Axisymmetric spreading

First we explore the lower limit of rotation rate under which a droplet, initially in sessile shape rotating with the disk, spreads outwards. Consider a droplet of 80 μl, landing at the centre of a stationary flat disk. The disk is set into rotation, which increases from 50 rpm, with a step of 10 rpm, every 30 s. The droplet breaks into a single rivulet and moves towards the rim of the disk

only above 340 rpm. For free falling droplets, landing on an already rotating disk, the break into a single rivulet is observed up to 3,000 rpm, as shown in Figure 4.4. In the single rivulet case, the centrifugal force is not strong enough to form an axisymmetric film. As a result a finger is formed instantly, which guides most of the fluid outwards more rapidly. Small variations in the position of the pipette above the axis of rotation might affect the subsequent behaviour and so pipette movements were avoided between runs.

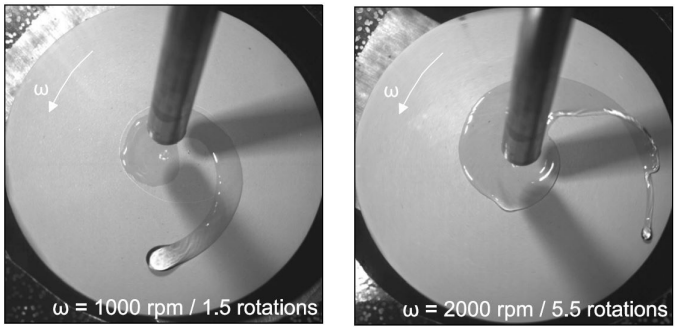

(a) (b)

Figure 4.4: Spreading on axis at (a) 1,000 (90 ms) and (b) 2,000 rpm (165 ms) (cases FB1000H10V80 and FB2000H10V80).

At 4,000 rpm, as shown in Figure 4.5, an axisymmetric film begins to form, with a single rivulet moving away from the axis faster than the rest of the film. At 5,000 rpm, the film spreads axisymmetrically until the contact line becomes unstable. Thus, beyond 4,000 rpm, the regime of axisymmetric spreading is met, with contact line instabilities forming at the critical radius r_c, leading to a fingering instability as explained in section 2.2.3. Axisymmetric spreading starts at 4,000 rpm and r_c is maximised at 5,000 rpm, while at 6,000 rpm, r_c is significantly reduced. Nevertheless, for the base case, the aim is to maximise the film area, before the onset of instabilities, thus we consider the base case rotation rate at 5,000 rpm.

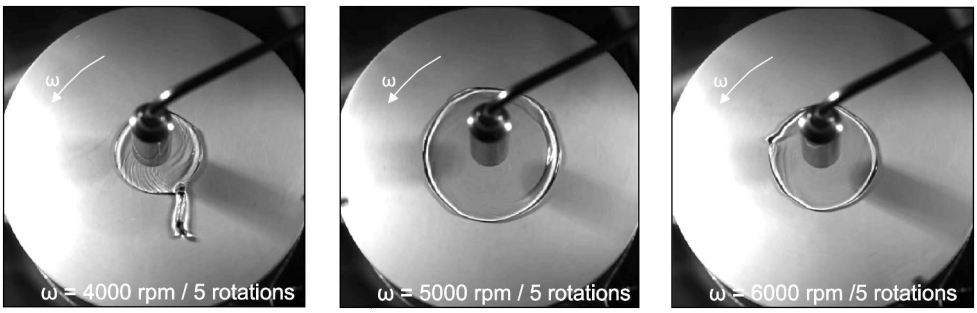

(a) (b) (c)

Figure 4.5: Critical radius in axisymmetric spreading, on a flat disk, at (a) 4,000 rpm (75 ms), (b) 5,000 rpm (r_c = 11mm - 72 ms) and (c) 6,000 rpm (r_c = 8mm - 60 ms) - cases FB4000H10V80, FB5000H10V80 and FB6000H10V80.

For axisymmetric spreading, the evolution of the radius is measured using edge detection with the measurement starting once the droplet is outside the perimeter of the pipette. The position of r_c is carefully acquired using two different methods. Firstly, the axisymmetric edge of the film, measured from the top view, is compared to a perfect circle. When the deviation from a perfect circle, becomes more than 10% ($\sim$ 1.5 mm), the edge of the film is considered

unstable and this radius is measured as critical. Secondly, the measurement of r_c is verified, using the observations from the film thickness experiment, which is analysed in section 4.3. To determine an error for these measurements we consider the representation of the rim of the disk in the images. From the images captured by the camera looking vertically down, the rim should be represented by approximately 2 pixels. In reality, the camera is defocusing in that area and the rim of the disk is blurred out, represented by 4 pixels. Hence we set the error to be ± 2 pixels, i.e. all measurements have an error of ± 0.14 mm.

The evolution of the film follows the same pattern up to 10,000 rpm with r_c decreasing as ω increases. Above 8,000 rpm, as shown in Figure 4.6, perturbations start earlier. While fingers form faster and the tip of the fingers is obvious very early, the fluid accelerates faster with increasing ω and the fingers are caught back up by the main flow.

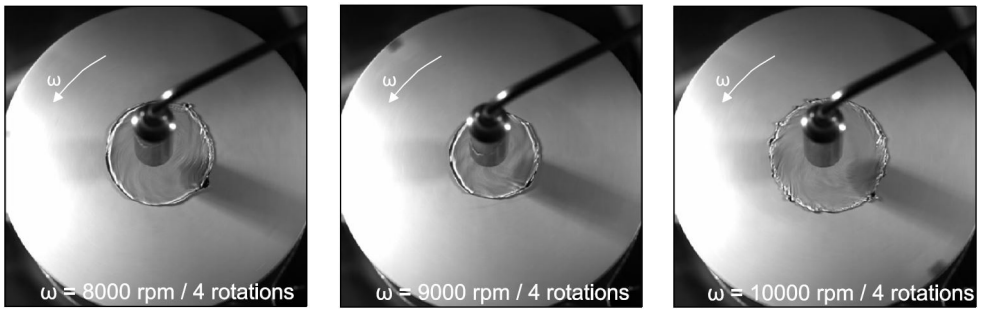

(a) (b) (c)

Figure 4.6: Critical radius in axisymmetric spreading, on a flat disk, at (a) 8,000 rpm (r_c = 7.7mm - 30 ms), (b) 9,000 rpm (r_c = 7.5 mm - 33 ms)and (c) 10,000 rpm (r_c = 7.3 mm - 22 ms) - cases FB8000H10V80, FB9000H10V80 and FB10000H10V80.

4.2 Base case

The base case is a droplet of 80 μl, released 10 mm above the painted brass disk, which rotates at 5,000 rpm (FB5000H10V80), as shown in Figure 4.7. The droplet spreads axisymmetrically outwards and once the front reaches r_c, perturbations are visible at the contact line.

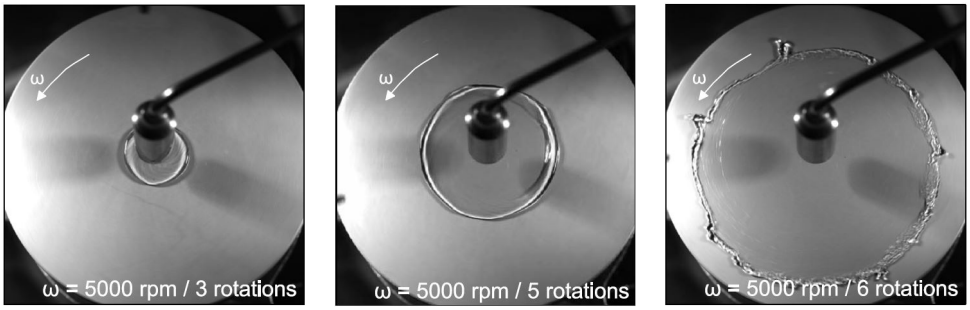

(a) (b) (c)

Figure 4.7: Axisymmetric spreading stages, for the base case (FB5000H10V80), where (a) initially the film is uniform with waves developing at the free surface (36 ms), (b) the ring forms near the contact line (60 ms) where capillary pressure gradients lead to (c) fingering instability (72 ms).

4.2.1 Radial evolution

As we were unable to find existing literature on the radial evolution of droplets in rotation rates over 5,000 rpm, a comparison with the Nusselt approximation, widely used at lower rotation rates is warranted. According to the Nusselt film approximation, for a single droplet, the radius of the film contact line scales as $r_r \sim t^{1/4}$ (Fraysse & Homsy, 1994), and the comparison with the base case is shown in Figure 4.8.

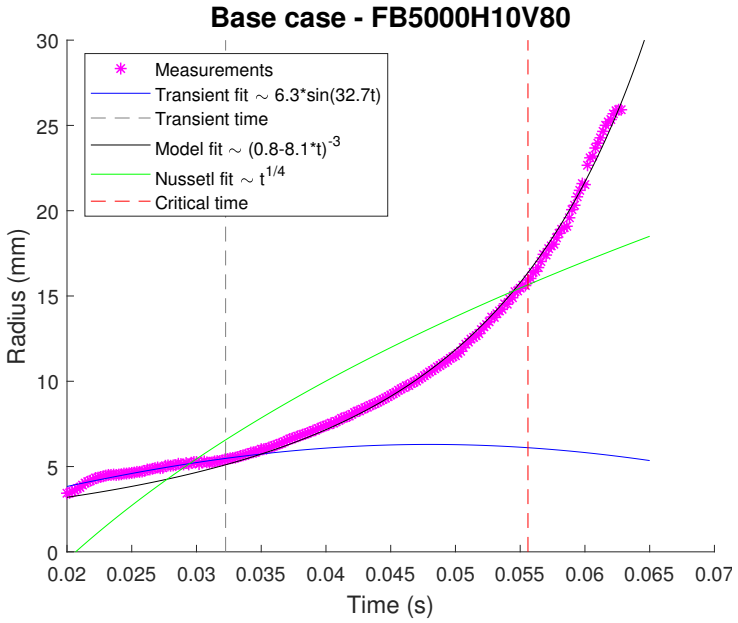

Figure 4.8: Example of radius evolution for the base case (FB5000H10V80). The spreading is characterised at early times by the transient stage (up to the grey dashed line). When centrifugal force dominates the flow, the radius depends on time as $r_r \sim (C_0 - C_\omega t)^{-3}$. At the third stage (beyond red dashed line) the contact line becomes unstable and the data are more scattered. The measurements stop at the rim of the disk, with radius of 25 mm.

There are three visible stages of spreading, divided by the grey dashed line and the red dashed line. First is the transient stage at the early times of spreading, affected mostly by the height of the release (kinetic energy before the impact), volume, viscosity and the way the capillary waves travel along the liquid body. The plot shows the extent of the oscillations during the transient stage and the fit of the relevant time dependence determined in section 4.1.1.2 (blue line).

The second stage is observed after the transient stage, when the centrifugal force dominates the flow (interval between the grey and the red dashed lines). The time of transition between the first two stages had to be carefully determined. In order to differentiate the two stages, the side camera, was used to capture the ending of shape oscillations at the transient time. The end of shape oscillations is distinguished with a change of slope in the spreading pattern, and the limit is indicated by the grey dashed line. The red dashed line represents the critical radius r_c, beyond which the spreading is not axisymmetric. After the droplet has reached $r_r = r_c$ at the critical time, $t = t_c$, where r_r is the radius at the edge of the ring near the contact line, the capillary pressure gradient across the ring creates the conditions for the formation of fingers. The experimental measurements beyond r_c, towards the rim of the disk, is another indication of the unstable contact line.

The Nusselt film scaling ($\sim t^{1/4}$) is indicated by the green line and is not a good fit for the experimental result as it predicts $\frac{\partial^2 r}{\partial t^2} < 0$ rather than $\frac{\partial^2 r}{\partial t^2} > 0$, at all times after the transient stage. Instead, using the least squares power law fit to the data between the end of the transient stage and r_c, the pattern has a dependence of $r_r \sim (C_0 - C_\omega t)^{-3}$, with $C_\omega < 0$, and the root–mean square (RMS) deviation at 0.32 mm. The fit, indicated as a black line, is in good agreement with the experimental measurements even beyond r_c. The parametrisation of the coefficients C_0 and C_ω follows in section 4.2.2.

The deviation from the Nusselt approximation can be explained as the droplet does not follow the predicted uniform film. In fact, there is a ring forming very early. Before the front reaches r_c, the ring is continuously fed with liquid, increasing in volume, while beyond r_c and as the front moves towards the rim of the disk, the ring gradually loses its volume. Thus, there are two fluid motions identified between the transient time and the end of spreading at the rim of the disk. After the transient time and until the critical time t_c at r_c, an important amount of liquid volume is guided to the ring. The entrainment of liquid to the ring makes its semi–circular cross–section constantly increasing and this stage will be referred to as 'ring growing stage'. Beyond r_c the liquid, already in the ring, is left behind, coating the disk. During that stage the semi–circular cross–section of the ring is constantly decreasing and this stage will be referred to as 'ring shrinking stage'. A sketch of this idea is presented in Figure 4.9.

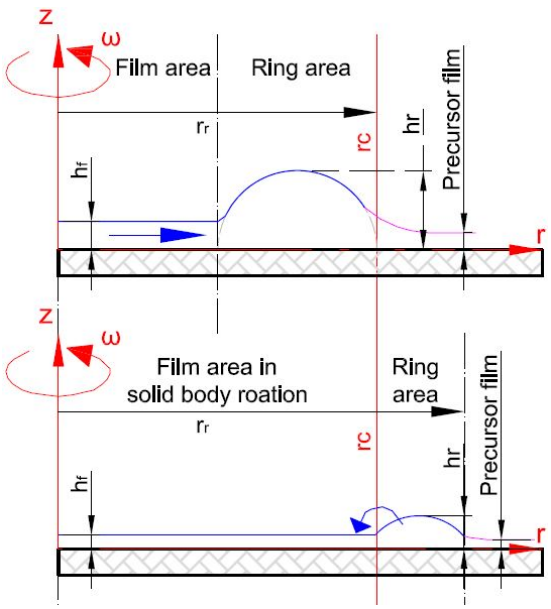

Figure 4.9: Hypothesis for the two stages of liquid flow on a flat disk. A significant volume of liquid is entrained in the ring before the front reaches r_c (ring growing stage) and beyond r_c the liquid, already gathered in the ring, is left behind coating the disk (ring shrinking stage).

Given that the Nusselt scaling is not a good fit for the experimental measurements, a mathematical approximation is developed in section 4.2.2, that describes the spreading pattern, taking into consideration the ring growing stage. The hypothesis and the distribution of volume between the film and the ring has not been found in existing literature, and is investigated further with the PIV experiment (section 4.2.3) and the film thickness experiment (section 4.3).

4.2.2 Mathematics of radial evolution

As explained in section 4.2.1, the Nusselt film approximation, which assumes uniform thickness, is not in good agreement with the experimental results and a new mathematical approach is required. The Nusselt film approximation for a single droplet is analysed in section 2.2.2.2 and the time evolution of the radius is defined in equation 2.17. Motivated by the form of the Nusselt approximation, we attempt a correlation of a fit with the general form $r \sim (a + bt)^c$ that would be in good agreement with the experimental results. Using least square regression analysis, to the experimental results, a good fit is expressed as

$$r_r \sim \frac{1}{(C_0 - C_\omega t)^3} \rightarrow u_r \sim r_r^{4/3}, \tag{4.24}$$

where r_r is the radius at the contact line. A subset of other functions were also explored, including an exponential, but the resulting fit was less satisfactory, with the RMS deviation exceeding twice that of the power law. One of the first observations is that for $r_r < r_c$, a substantial amount of liquid is entrained in the ring which grows in volume. In this section we explore a mathematical approximation for the determination of the coefficients C_0 and C_ω.

First, the droplet is divided in two separate areas, the film and the ring, as shown in Figure 4.9. Consider the ring of fluid as a growing semi–toroid of a semi–circular cross–section with radius h_r, propagating outwards. Provided that $h_r \ll r_r$, we introduce a scaling for the height of the ring as

$$h_r \sim h_0 \left(\frac{r_r}{r_0}\right)^p, \tag{4.25}$$

where r_0 and h_0 are the radius and the thickness of the film immediately after the contact with the disk and p is a parameter that will be defined by this scaling. The expression is chosen so that h_r increases as r_r increases for $p > 0$ and when $r_r = r_0$ then $h_r = h_0$. Assuming that most of the liquid is gathered in the ring and that V is constant, then

$$V \sim \underbrace{\pi^2(r_r - h_r)h_r^2}_{\text{ring volume}} + \underbrace{\pi(r_r - 2h_r)^2 h_f}_{\text{film volume}},$$

where h_f is the film thickness. However, for $r_r h_r^2 \gg r_r^2 h_f$, the volume becomes

$$V = \pi^2(r_r - h_r)h_r^2 \rightarrow dV = \pi^2 h_r^2 dr, \tag{4.26}$$

which implies that for $r_r \gg h_r$, then h_r decreases as

$$h_r \sim \left(\frac{V}{r_r}\right)^{\frac{1}{2}}. \tag{4.27}$$

Comparing the powers in equation 4.25 and 4.27, for $p = -1/2$, the ring decreases in volume. The only way for $p > -\frac{1}{2}$ is when the ring volume is increasing, i.e. when the film feeds liquid to the ring.

Ignoring contact line dynamics and using equation 4.25, the net radial centrifugal force acting on the ring is

$$F_c = \pi^2 \int_{r_r - 2h_r}^{r_r} \rho\omega^2 r h_r^2 dr \sim \pi^2 \rho\omega^2 h_r^3 r_r. \tag{4.28}$$

Viscous drag at a point, using the Nusselt film approximation of a parabolic profile for the velocity $\hat{u}_r \sim z^2$ is

$$\tau = \mu \frac{\partial \hat{u}_r}{\partial z},$$

which at the solid surface $z = 0$ scales as

$$\tau_0 \sim \mu \frac{u_r}{h_r}.$$

Knowing τ_0, the net viscous force at the bottom is

$$F_\nu = 2\pi \int_{r_r - 2h_r}^{r_r} \tau_0 r dr \sim \pi \mu u_r r_r. \tag{4.29}$$

So balancing the two forces $F_c \sim F_\nu$, the velocity at the front is expressed as

$$u_r \sim \frac{\pi \omega^2}{\nu} \frac{h_0^3}{r_0^{3p}} r_r^{3p}. \tag{4.30}$$

Balancing the powers between equation 4.30 and the experimental result, $u_r \sim r_r^{4/3}$, then $p = \frac{4}{9}$. As $p > 0$ the film must feed liquid to the ring and the ring must increase in volume. In contrast if the droplet was spreading as a Nusselt film scaling, $r_r \sim t^{1/4} \rightarrow u_r \sim r^{-3}$, then $p = -1$, indicating a shrinking ring.

From the velocity at the front and with the boundary condition at $t = 0 \rightarrow r = r_0$, this model suggests that the radius at the front of the ring behaves as

$$r_r = \frac{1}{(C_0 - \frac{\omega^2}{\nu} \frac{h_0^3}{r_0^{4/3}} t)^3},$$

with $C_0 = r_0^{-1/3}$ or

$$\frac{r_r}{r_0} = \frac{1}{(1 - C_\omega t)^3}, \tag{4.31}$$

where

$$C_\omega = \frac{\omega^2 h_0^3}{\nu r_0}. \tag{4.32}$$

Although contact line effects are not included in the calculations, it was shown in the previous section that a model of the form $r_r \sim (C_0 - C_\omega t)^{-3}$ is a good fit for the total duration of spreading. To verify the scaling of C_0 and C_ω determined above, we will test the model for variations in rotation rate (section 4.4), height of release, droplet volume and disk smoothness (section 4.5). The coefficient C_ω, is descriptive of the flow characteristics, will be treated as the main parameter of investigation and therefore will be used for comparisons between sets of experiments. There is a singularity giving $r_r \rightarrow \infty$ at

$$t = \frac{C_0}{C_\omega} = \frac{r_0 \nu}{\omega^2 h_0^3}.$$

This time scale is related to infinite radius. However in that case the droplet is no longer on the disk. Even if the disk had a larger radius then the ring would have been drained out. The contact line would have been unstable leading to the formation of fingers, thus the thin film approximation that have been considered for the formation of the model would not be valid.

4.2.3 Film velocity

Based on experimental observations on the evolution of the spreading, the droplet was divided in the film and the ring area. The model described in the previous section, provides a scaling for the spreading pattern, taking into consideration that the film feeds liquid to the ring. The PIV experiment investigates whether the film feeds liquid to the ring and if there is an instant in time where the fluid motion changes, with the ring leaving fluid behind. These two different stages are explored by following the motion of particles. We expect that as the ring grows, the film moves radially faster than the ring and as the ring shrinks, the film reaches the angular velocity of the disk so no more liquid is entrained in the ring. For this experiment, instead of the brass disk we used the glass disk. Although the spreading pattern is qualitatively similar, the glass disk has smoother surface and r_c is increased, extending the duration of liquid entrainment in the ring. A comparison between the spreading in a brass and a glass disk follows in section 4.5.3.

Given the small time scale of the experiment, this modification was beneficial for the PIV measurements. To maximise the spreading time, the rotation rate was set at 5,000 rpm, the height of release at 10 mm and the droplet volume at 80 μl (FG5000H10V80). In order to optimise the video recording, the camera was focused only on half of the disk, using minimum available exposure time at 0.04 ms and maximum available frame rate at 6,000 fps.

Examples of the particles' velocity evolution are shown in Figure 4.10, with (a), (c) and (e) showing the raw particle images as captured by the camera before the film reaches r_c, at r_c and beyond r_c. While the droplet lands, the bottom of the droplet starts rotating with the disk. The top of the droplet lands in an already wet area and instead of sinking towards the solid surface, it spreads radially over the wet area. On the right hand side images (b), (d) and (f) show the velocity profile obtained by the PIV algorithm for the same frame.

In the first raw image (a), the ring grows in volume as it is fed by fluid. The second raw image (c), shows the frame right before r_c, where the particles in the film area are close to reaching the angular velocity of the disk, and the ring reaches its maximum volume. The third raw image (e), shows the ring beyond r_c, where its volume is decreasing, leaving fluid behind. The fluid left behind has almost zero inertia and immediately reaches the angular velocity of the disk. The visibility of particles close to the ring, during the third stage, is very restricted and does not produce reliable results.

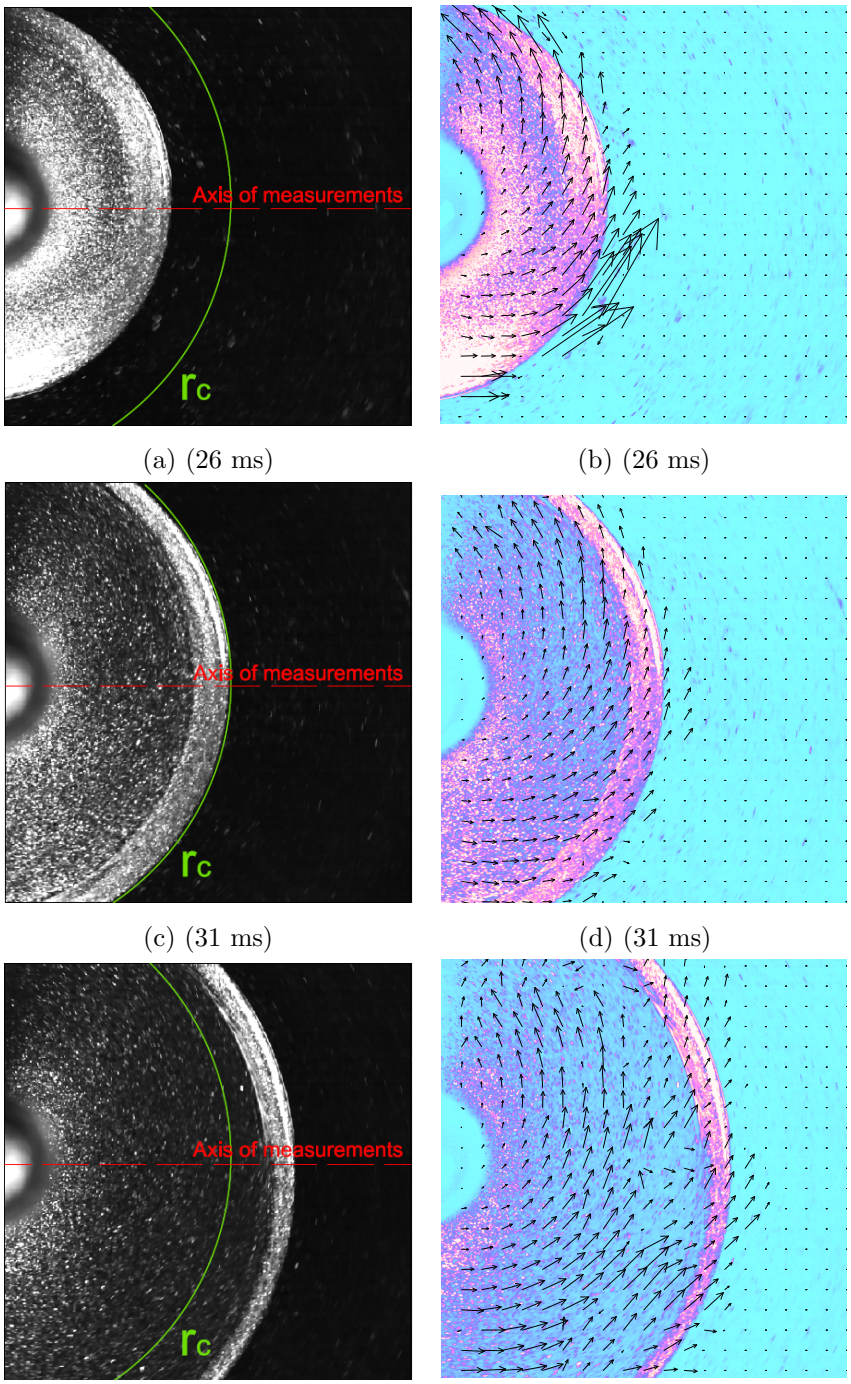

(a) (26 ms) (b) (26 ms)

(c) (31 ms) (d) (31 ms)

(e) (34 ms) (f) (34 ms)

Figure 4.10: PIV experiment, using a glass flat disk, rotating at 5,000 rpm (FG5000H10V80) with examples of raw particle images (a), (c) and (e) and the obtained velocity profiles for the same frame (b), (d), and (f). In (a-b) the film feeds the ring with liquid. In (c-d) the ring is at its maximum volume, before r_c, while the film marginally reaches the angular velocity of the disk. In (e-f) the ring is decreasing in volume, after r_c. The velocity profiles were collected along the horizontal radius (red dashed line).

The velocity of the particles is indicative of the fluid motion. The local time-averaged surface velocity of the film and the ring in the radial and azimuthal direction are shown in Figures 4.11 a and b respectively. The velocity profiles are collected along the red dashed line, indicated in Figure 4.10. The radial and the azimuthal velocity profiles were determined taking into consideration the average of 20 interrogation points.

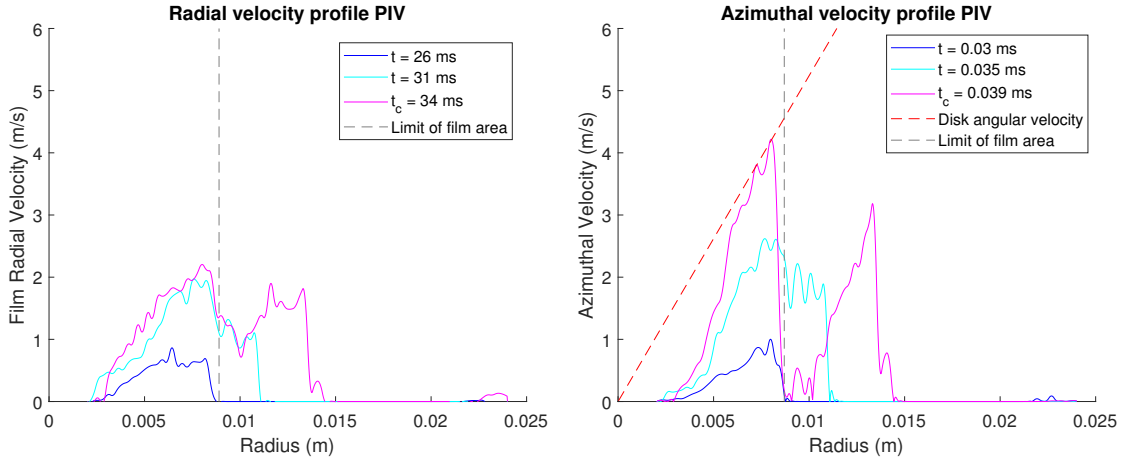

(a) (b)

Figure 4.11: Velocity profile of the PIV experiment (FG5000H10V80). The diagrams show the radial (a) and the azimuthal (b) velocities, in three different times. The radial surface velocity (a) shows that the film moves faster than the ring $u_r \sim r_r^{4/3}$. The azimuthal surface velocity in (b), shows that the film angular velocity increases and approximately at r_c, reaches the angular velocity of the disk.

The blue and cyan lines shows the evolution of velocities before the ring radius reaches r_c. The film has increased velocity compared to the ring, hence most of the liquid is guided form the film towards the ring. The magenta line shows the profile immediately after r_c. Both the radial and the azimuthal velocity have a consistent sharp drop at the point where the particles enter the ring. The sharp decrease in both components of velocity near the ring is due to the fact that the film thickness at approximately r_c is of $\mathcal{O}(10^{-5})$ m, similar to the size of the particles. Hence the entrainment of particles in the ring might be stopped and is represented as a discontinuity in the velocity profiles. Experimental measurements of the film thickness are analysed in section 4.3.

Beyond r_c and as the film thickness decreases, the movement of particles might be restricted within the film. The azimuthal profiles in (b) indicate that the film moves approximately with the velocity of the disk. The lack of particles close to the ring, constrains the PIV measurements at the stage immediately after r_c, hence the sharp drop of the pink line. Thus, with this experiment we confirmed the hypothesis of the growth of the ring. The volume of the ring over time is another relevant measurements and follows in section 4.3.

4.3 Film thickness

During the droplet spreading, the thickness of the film and the ring are important variables that characterise the flow. Having determined the scaling of the spreading pattern, it is important to measure the film thickness and the distribution of volume between the film and the ring, exploring the validity of the assumption that the ring grows in volume for $r_r < r_c$ and decreases in volume for $r_r > r_c$. Experiments measuring the thickness of the spreading droplet were conducted, with the laser set-up (explained in section 3.1.3), for the set FB-H10V80. The example of the ring evolution, for the base case, is shown in Figure 4.12. The plot shows the ring thickness before and after r_c with a time step of 3 ms. The results indicated that when $t \to t_c$ the ring reaches its maximum thickness.

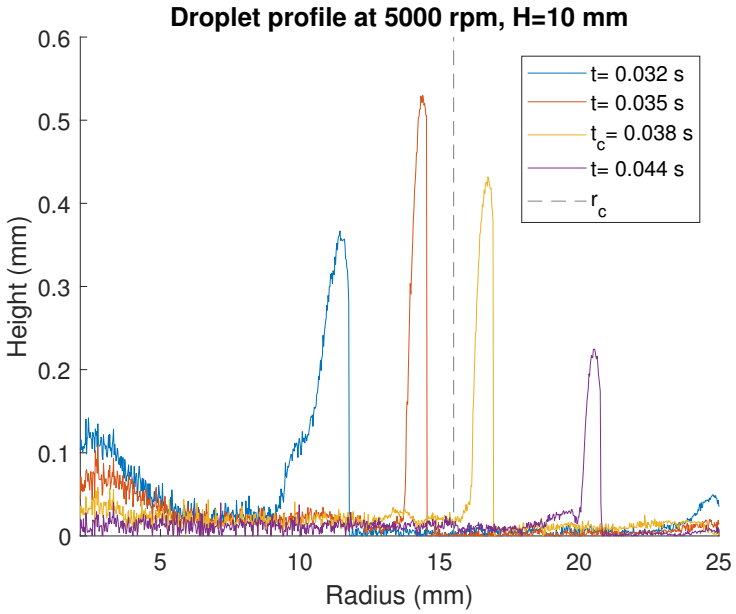

Figure 4.12: Example of raw data for the ring evolution for the base case (FB5000H10V80). The maximum ring thickness is met just before the r_c. The maximum ring volume is approximately 55 μl.

The experiment gave insights to the behaviour of the contact angle during the evolution of the film and the ring. During the early times of spreading, the contact angle is large as the front moves outwards. At r_c, the contact angle and the angle at the intersection between the ring and the film seem to be similar at almost 90°, as shown in Figure 4.13.

Both sides of the ring experience perturbations, while within the ring there is redistribution of liquid in the azimuthal direction. Beyond r_c, fingers are formed near the contact line while at the intersection with the film, the ring leaves fluid behind. With the instabilities well established on both sides of the ring, the contact angle increases again while the angle at the intersection with the film decreases.

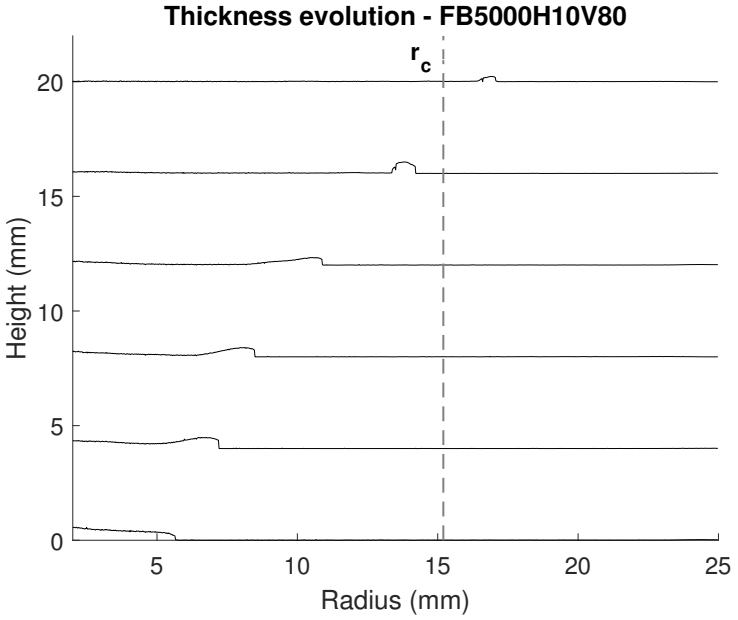

Figure 4.13: Visualisation of the contact line evolution for the base case (FB5000H10V80). Each profile is shifted by 4 mm, to show the evolution of the profile with time. Before the front reaches r_c, both the inner and the outer limits of the ring are unstable, indicated by the angle at the intersection with the film and the contact angle, which are both approximately 90°.

The PIV experiment investigated the film velocities, from the ring growing stage before r_c, to the ring shrinking stage beyond r_c, verifying the hypothesis about the ring growing and shrinking stages. The transition, between the growing and the shrinking stages, can be identified by visualising the volume of the ring throughout the spreading, as shown in Figure 4.14. Before r_c, the ring volume increases almost linearly in time.

At approximately r_c, and for an almost fixed time scale of 2 ms, the ring maintains the same volume of liquid but experiences azimuthal perturbations that result to the instabilities mentioned above. The film characteristics right before r_c are important for the description of fluid motion. The ring thickness is also important characterising the flow and determining whether Coriolis force is an important factor in the spreading pattern and in the ring evolution.

In order to compare the experimental result at the growing stage with the best fit, we consider the expression of the ring volume as defined in section 4.2.2, incorporating equations 4.25 and 4.32 in equation 4.26. Thus the volume of the ring can be expressed as

$$V_{ring} \sim r_r h_r^2 = r_r h_0^2 \left(\frac{r_r}{r_0}\right)^{\frac{8}{9}} \rightarrow \frac{V_{ring}}{V_{droplet}} \sim \frac{1}{(1-\frac{\omega^2 h_0^3}{\nu r_0} t)^{\frac{17}{3}}}. \tag{4.33}$$

The resulting fit (indicated as a dotted line) is compared with the experimental results in Figure 4.14. It should be noted that t_c is not a fitted parameter but was obtained from experimental observations. The fit coefficient indicates that

$$\frac{\omega^2 h_0^3}{\nu r_0} t \sim 0.029\omega t \rightarrow h_0 \sim 0.029 r_0^{\frac{1}{3}} \left(\frac{\nu}{\omega}\right)^{\frac{1}{3}}.$$

This length scale is reduced compared to the von Kármán layer thickness, $\delta \sim \left(\frac{\nu}{\omega}\right)^{1/2}$, and could be considered as a representative length scale of the initial thickness that is set into

rotation immediately after landing. Assuming that r_0 has small variations for different ω and that ν is constant, then h_0 varies with $\omega^{-\frac{1}{3}}$, resulting in decreased h_0 for increased ω. Although measurements of the thickness of the rotating liquid at early times is not possible, we will proceed under the condition that this is a realistic scaling for h_0 and test the fit's compatibility with experimental results varying other parameters, such as H and V. Overall, the fit is in good agreement with the experimental results indicating that the scaling introduced in section 4.2.2 is a good approximation for the growing stage of the ring.

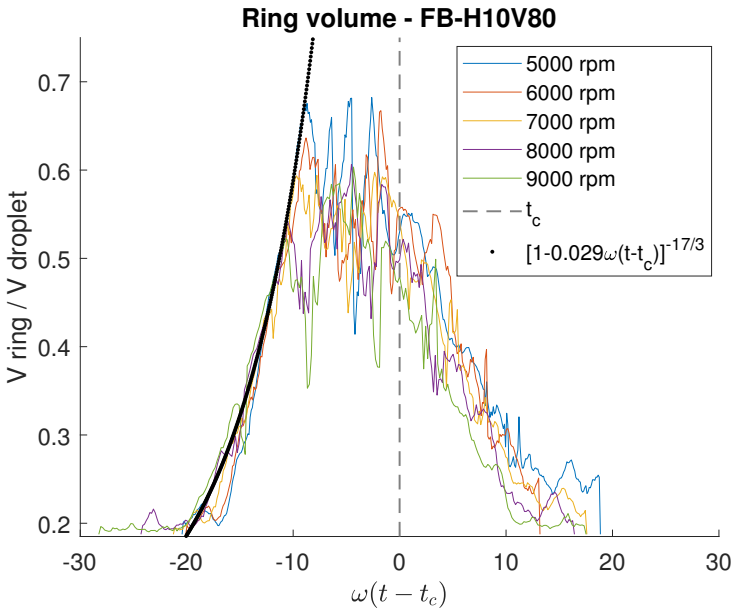

Figure 4.14: Evolution of the volume of the ring for the set FB-H10V80. The volume of the ring increases until the front reaches r_c and beyond that point the ring volume shrinks leaving fluid behind and coating the disk.

Knowing the thickness and the volume of the ring, from volume conservation, the volume and the thickness of the film can be extracted. All the data are available at this stage to determine the dimensionless numbers that characterise the flow both for the film and the ring.

The diagnostic dimensionless numbers first introduced in section 3.1.2, are redefined according to the symbols used to describe the droplet profile in Figure 4.9. For example, velocity at the ring area scales as $\sim \omega r_r$ while at the film as $\sim \omega(r_r - 2h_r)$, following the geometrical approach in Figure 4.9. Knowing h_r the thickness in the film can be defined as

$$h_f \sim \frac{(V_{\text{droplet}} - V_{\text{ring}})}{\pi r_f^2},$$

where $r_f \sim r_r - 2h_r$ is the radius of the film at the intersection with the ring. For example, for the base case, the maximum height of the ring is $h_r = 5.5 \times 10^{-4}$ m and assuming a semi–circular cross–section and a semi–toroidal ring shape, the volume of the ring is 55 μl. With the droplet volume being $V = 80$ μl and using volume conservation, the volume of the film must be 25 μl. Assuming uniform thickness of the film area and the radius at the beginning of the ring at $r_f = 15$ mm, the film thickness is about $h_f = 4 \times 10^{-5}$ m.

Following the aforementioned approach, the diagnostic parameters can be determined and the results for $r_r = r_c$, indicating the main flow characteristics, are presented in Table 4.1.

Table 4.1: Main flow parameters at r_c from 5,000 to 9,000 rpm					
rpm	$5,000$	$6,000$	$7,000$	$8,000$	$9,000$
rad/s	524	628	733	838	942
r_c (mm)	15.5	14.4	13.7	13.0	12.6
Volume ring (μl)	55	53	49	48	47
Volume film (μl)	25	27	31	32	33
Thickness ring (m)	6×10^{-4}	6.1×10^{-4}	6.0×10^{-4}	6.2×10^{-4}	6.2×10^{-4}
Thickness film (m)	3×10^{-5}	4×10^{-5}	5×10^{-5}	6×10^{-5}	6×10^{-5}
Re ring = $\frac{\omega r_r h_r}{\nu}$	4854	5545	6054	6703	7399
Re film = $\frac{\omega r_f h_f}{\nu}$	274	370	527	646	755
Re Nusselt = $\frac{\omega r_r h}{\nu}$	831	1111	1363	1642	1905
We ring = $\frac{\rho(\omega r_r)^2 h_r}{\gamma}$	564	398	331	261	199
We film = $\frac{\rho(\omega r_f)^2 h_f}{\gamma}$	31	57	66	72	80
Ro ring = $\frac{\omega r_r}{\omega h_r}$	26	23	23	21	20
Ro film = $\frac{\omega r_f}{\omega h_f}$	460	352	261	219	198
Fr ring = $\frac{\omega r_r}{\sqrt{g h_r}}$	1385	1254	1214	1192	1080
Fr film = $\frac{\omega r_f}{\sqrt{g h_f}}$	24570	18814	13957	11705	10574
Pe ring = $\frac{\omega r_r h_r}{D}$	4.9×10^6	3.7×10^6	3.2×10^6	2.8×10^6	2.3×10^6
Pe film = $\frac{\omega r_f h_f}{D}$	2.7×10^5	5.3×10^5	6.4×10^5	7.7×10^5	9.2×10^5

The difference in the Reynolds number, between the ring and the film, means that inertia is more important in the ring. The value of $Re > 500$ in the ring and for the Nusselt approximation indicates possibly a transition to an unstable environment. The Weber number shows that surface tension becomes more important at the ring, as ω increases, and more important in the film, as ω decreases. The Rossby number ($Ro > 1$), indicates that Coriolis force might be important within the ring but less important in the film. The Coriolis force could be responsible for the redistribution of liquid in the azimuthal direction and could affect the direction of the fingers produced due to contact line instabilities. Regarding chemical reactivity, diffusion dominates the reaction rate but might be enhanced due to the decreased film thickness. However, Pe is increased within the ring which means that the flow field in the ring could be an important factor enhancing advection and contributing to the reaction rate.

As the rotation rate is increased, r_c and h_r decrease, while h_f increases. However, in every case, the ring gathers at least half of the droplet volume. When ω is increased, Re is increased, We is decreased in the ring but increased in the film, Ro and Fr are decreased and Pe is increased.

4.4 Rotation rate variations

One of the most important parameters of investigation is the angular velocity of the disk as it is strongly coupled with the spreading time and the onset of instabilities. Given that initial axisymmetric spreading starts at 5,000 rpm, the range of rotations under investigation is between 5,000 and 10,000 rpm. The radial evolution for the set FB-H10V80 with respect to angular velocity is shown in Figure 4.15.

The raw data, in Figure 4.15a, show that the impact effects initially dominate the spreading, especially at lower rotation rates, i.e. at 5,000 rpm, while the impact effect vanishes as ω increases. After r_c the data are more scattered, indicating perturbations near the contact line. The onset of instabilities, indicated by the value of r_c (black continuous line), is decreased with increased ω.

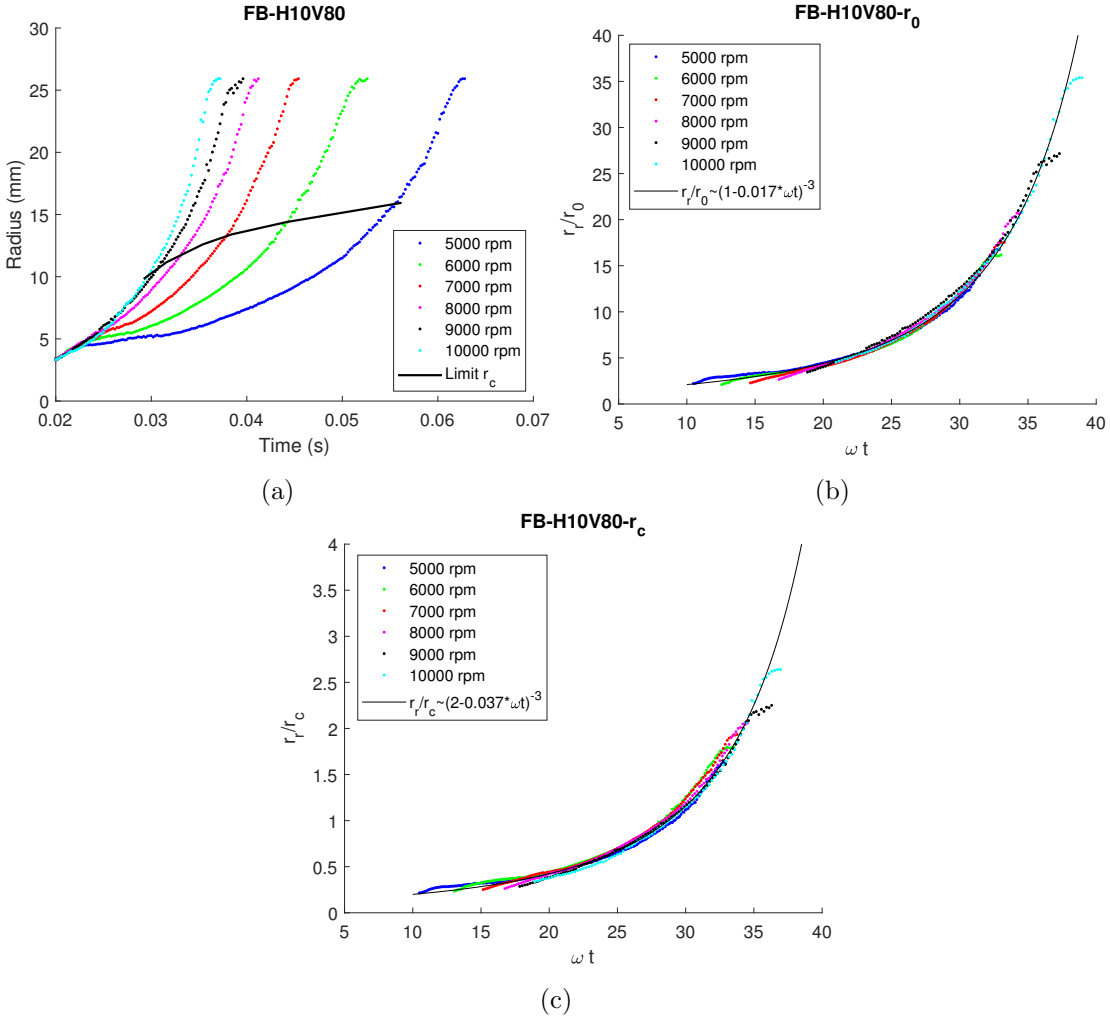

Figure 4.15: (a) Radius evolution for a range of rotation rates (5,000 - 10,000 rpm) - set FB-H10V80. (b) Correlation of the radius evolution with the model predictions, normalised with r_0 and (c) radius evolution normalised with r_c.

The non–dimensional radius $\frac{r_r}{r_0}$, as measured from the experimental results, is plotted in Figure 4.15b against the dimensionless time ωt. The plot shows the correlation of the experimental results to the evolution of the dimensionless radius, discussed in section 4.2.2 and determined in equation 4.31. Thus, considering water with $\nu = 1.004 \times 10^{-6}$ m^{2}s^{-1} and r_0 of $\mathcal{O}(10^{-3})$ m, following the analysis of the fit in Figure 4.14, the scaling of h_0 can be obtained, from 5,000 to 10,000 rpm, as

$$\frac{\omega^2 h_0^3}{\nu r_0} t = 0.017\omega t \rightarrow h_0 \sim 0.017 r_0^{\frac{1}{3}} \left(\frac{\nu}{\omega}\right)^{\frac{1}{3}}.$$

This length scale is reduced compared with the von Kármán layer thickness, $\delta \sim \left(\frac{\nu}{\omega}\right)^{1/2}$, and could be considered as a representative length scale of the initial thickness that is set into rotation immediately after landing. Assuming that r_0 has small variations for different ω and

that ν is constant, then h_0 varies with $\omega^{-\frac{1}{3}}$, resulting in decreased h_0 with increased ω. Although measurements of the thickness of the rotating liquid at early times is not possible, we will proceed under the condition that this is a realistic scaling for h_0 and test for the model's compatibility with the experimental results for other parameters, such as H and V.. In addition, the dimensionless plot, in Figure 4.15c, introduces a new non–dimensional variable $\frac{r_r}{r_c}$ and shows the correlation to the experimental results. The RMS deviation in (b) is 0.47 and in (c) 0.09. Considering that the ration $\frac{r_r}{r_0} \sim \mathcal{O}(10)$, both fits are in good agreement with the experimental results, with the difference in deviations being very small. This result indicates that another mathematical approximation, incorporating the r_c limit, would be beneficial for the description of the droplet spreading.

4.5 Other parameters

Focusing on the base case FB5000H10V80, we described the basic flow characteristics for the film and the ring evolution. A mathematical approximation was formed to describe the spreading pattern during the ring growing stage. Additional experiments were conducted to explore the spreading pattern by altering the height of release, the droplet volume and the disk smoothness. Altering one parameter each time, the results are compared to the base case and are correlated to the mathematical approximation.

4.5.1 Height of release

The effect of the height of release, H, is investigated for the sets FB-H5V80, FB-H10V80 and FB-H15V80 respectively. The height of release affects the transient radius and the spreading at early times. A comparison of the base case FB5000H10V80, varying the height of release from 5 to 15 mm, with the spreading for the experiments FB5000H5V80 and FB5000H15V80 is shown in Figure 4.16. For a height of release at 5 mm above the centre of the disk, the droplet lands smoothly and shape oscillations after the impact are reduced.

The oscillations from the impact affect the spreading up to the transient time. However, as explained in section 4.1.1, this is the only case of non-free falling droplet, with reduced liquid volume in each discharge, thus a small variation in the spreading pattern could be expected. When the droplet is released 10 mm above the centre of the disk, the experiment is essentially the base case, analysed in detail in section 4.2. The droplet lands on the disk at the instance of detachment from the pipette, hence the free fall is minimised. The effect of the impact in the spreading is more prominent when the droplet is released 15 mm above the centre of the disk. For comparison, the RMS deviation of the fit in FB5000H10V80 is 0.32 mm while for FB5000H15V80 is 0.42 mm, both in good correlation with the experimental results. The oscillations at early times, represented in the plot by deviations from the fitted line, are repeated for all angular velocities and for increased height of release. However, as the rotation rate increases, the influence of the early time oscillations is minimised as centrifugal force acts faster on the liquid. Due to the rotating surface, the von Kármán layer is formed faster, thus the liquid is set faster into rotation. For completeness, the experimental results in the form of graphs are shown in the Appendix A for the sets FB-H5V80, FB-H10V80, FB-H15V80.

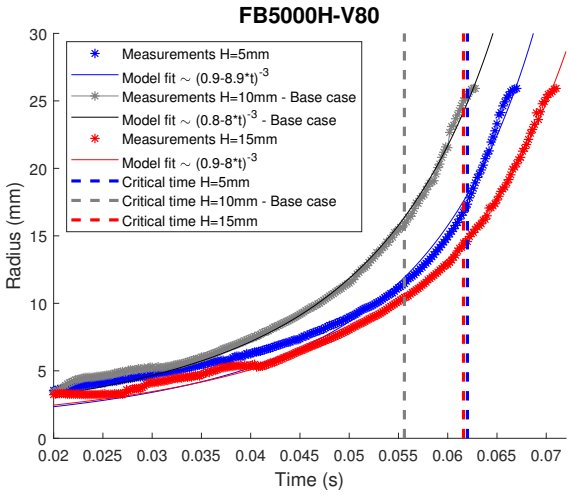

Figure 4.16: Examples of radius evolution, with height of release at 5, 10 and 15 mm, for the cases (a) FB5000H05V80, (b) FB5000H10V80 and (c) FB5000H15V80 respectively. When centrifugal force dominates the flow, after the transient stage, the radius depends on time as $r_r \sim (C_0 - C_\omega t)^{-3}$. Beyond r_C (dashed lines), the contact line becomes unstable and the data are more scattered, following approximately the same time dependence. The deviation from the base is indicative of the effect of the height of release to the time evolution of r_r.

The spreading in all sets follows the pattern of the base case, which can be represented by a non–dimensional plot and in accordance with the model in section 4.2.2 for all heights of release and for all the rotation rates that allow axisymmetric spreading ($\omega \geq 5,000$ rpm), as shown in Figure 4.17.

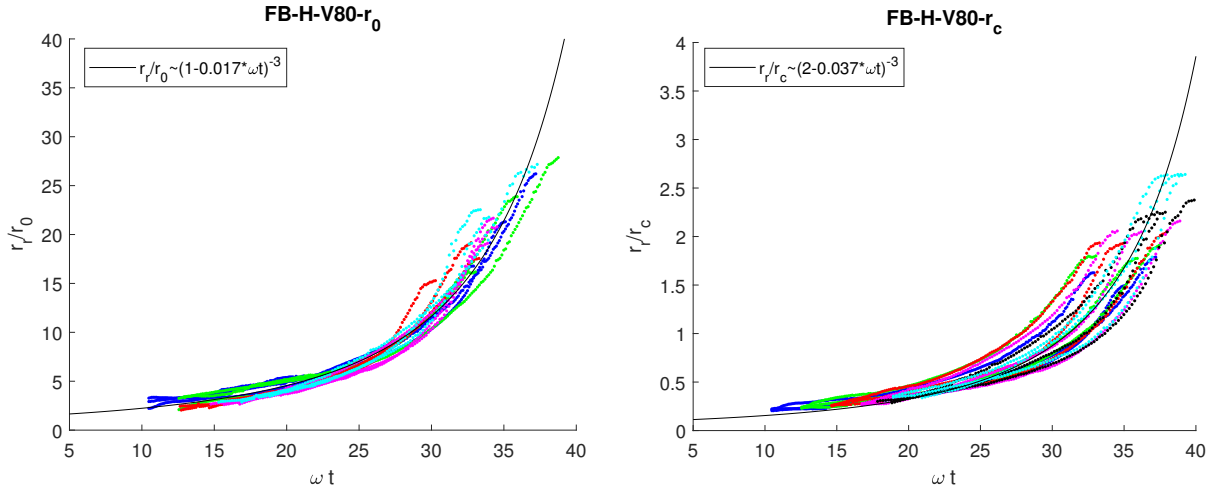

(a) (b)

Figure 4.17: Correlation of the radius evolution (a) with the model predictions normalised with r_0 and (b) radius evolution normalised with r_c, for the sets FB-H5V80, FB-H10V80 and FB-H15V80 respectively.

The effect of H is indirectly related with the model, by incorporating in C_ω the values of the initial radius and thickness after the impact, r_0 and h_0 respectively. Normalising r_r with r_0 in (a), the results are in good correlation with the model and with the maximum RMS deviation at 1.12. Although there is still good agreement with the experimental results, the increased deviation compared to section 4.4, is due to the oscillations of the droplet at early times, which

vary for different heights of release. The non–dimensional plot in (b), shows a similar pattern related to r_c, but not as close to the base case fit with the RMS deviation reaching 0.16. The deviation indicates that the height of release has an impact in the onset of instabilities.

In order to visualise this effect of H to the onset of the contact–line instability, r_c and t_c are plotted for the three sets, as indicated in Figure 4.18a and Figure 4.18b respectively. As a general observation, when the rotation rate is increased the contact line becomes unstable faster, thus r_c and t_c are decreased. Second, when the height of release is decreased, r_c is increased while t_c is decreased.

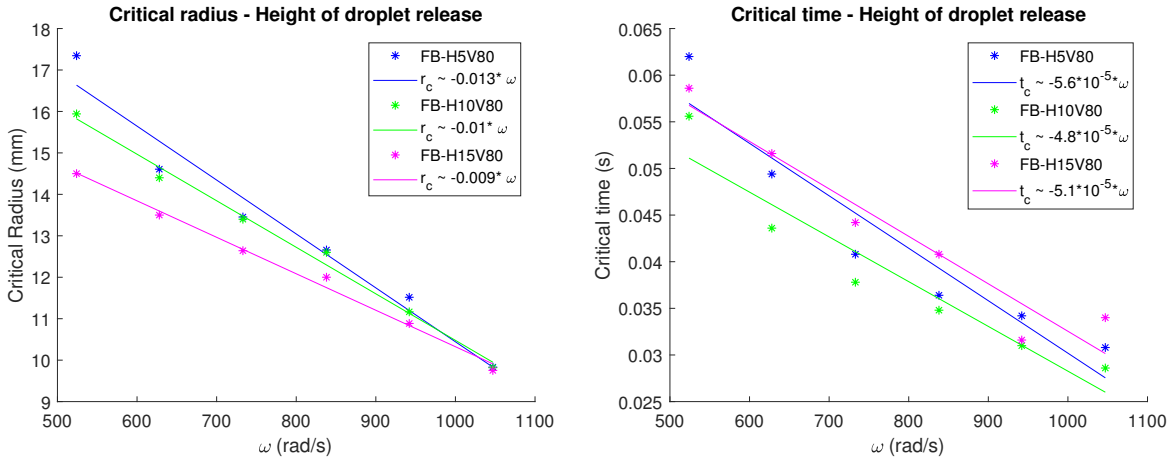

(a) (b)

Figure 4.18: Onset of (a) critical radius and (b) critical time for the sets FB-H5V80, FB-H10V80 and FB-H15V80 respectively.

The data for $H = 5$ mm are more scattered and as explained in section 4.1.1 the released volume is slightly reduced, thus this set of experiment might not give a representative pattern for the onset of instabilities. These observations would require validation through additional sets of experiments for various heights of release.

The observations could be related with the flow rate feeding the ring. When ω is decreased, the spreading time is increased and more liquid is entrained in the ring. We already showed that the maximum ring volume is decreased with increased ω in section 4.3. When H is decreased, r_c is increased as the landing is smooth and centrifugal force becomes the dominant factor of spreading faster. Thus the process of liquid entrainment in the ring could have a stabilising effect at the contact line. However, the difference between the fitted lines decreases as ω increases. Although it is clear that H affects r_c, the effect is reduced when the rotation rate is increased. To investigate whether the droplet volume could affect the volume in the ring and the onset of instabilities, the following section explores the spreading pattern for droplet volume variations.

4.5.2 Droplet volume

The effect of the droplet volume, V, is investigated for the sets FB-H10V80 and FB-H10V40, with droplet volumes of 80 μl and 40 μl respectively. For a droplet volume of 40 μl, axisymmetric spreading starts at 6,000 rpm. Therefore, an exception was made only for this variable and the base case is FB6000H10V80 compared to FB6000H10V40. The experimental results are in good

agreement with the model, as shown in Figure 4.19. The main difference in the plots is the duration of the transient stage, which is extended for the smaller droplet, shown as a deviation from the blue fitted line. As the volume is reduced, the initial radius r_0 after the contact with the disk is smaller, i.e. the centrifugal force scaled as $\rho\omega^2 r$ is reduced at early times. The difference during the transient stage is observed for all the tested rotation rates (6,000 - 9,000 rpm). For completeness, the experimental results of the set FB-10V40 in the form of graphs are shown in the Appendix A.

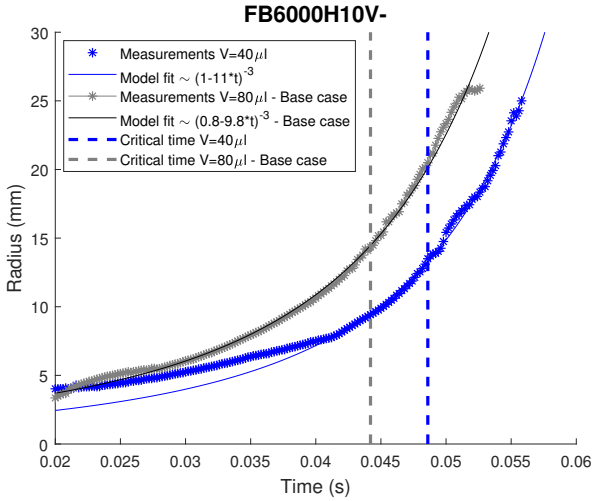

Figure 4.19: Examples of radius evolution, varying the droplet volume from 40 to 80 μl, for the cases FB6000H10V80 and FB6000H10V40 respectively. Beyond the transient stage, when centrifugal force dominates the flow, the radius depends on time as $r_r \sim (C_0 - C_\omega t)^{-3}$. Beyond r_c (dashed lines), the contact line becomes unstable and the data are more scattered, following approximately the same time dependence. The main difference between the two liquid volumes is the duration of the landing effect which is extended for the smaller droplet.

The spreading pattern is in good agreement with the model's time dependence $r_r \sim (C_0 - C_\omega t)^{-3}$, with the RMS deviation for FB6000H10V40 being 0.28 mm, while for FB6000H10V80 is slightly increased at 0.42 mm. The effect of V is indirectly related with the model of section 4.2.2 by incorporating in C_ω the values of the initial radius and thickness after the impact, r_0 and h_0 respectively. The validity of the model was tested for all the rotation rates that allow axisymmetric spreading ($\omega \geq 6,000$ rpm), as shown in Figure 4.20a, with the RMS deviation being 0.72. A second non–dimensional plot is shown in Figure 4.20b, which incorporates r_c and the RMS deviation is 0.11. The deviation from the fit indicated that V in an important factor to the onset of contact line instabilities.

The onset of the contact line instabilities is already connected with the volume distribution and is another parameter than can be affected by volume variations. To visualise the effect of V, the values of r_c and t_c are compared for the two sets (FB-H10V80 and FB-H10V40), as shown in Figure 4.21. The main observation is that for reduced V, the variation of r_c is minor, as shown in Figure 4.21a. In the case of the 40 μl droplet, the onset of the instability happens approximately at the same radius for all rotation rates. We showed for the set FB-H10V80 in Table 4.1 in section 4.3, that as ω increases the volume in the ring is reduced at t_c. Assuming that the volume distribution follows a similar pattern for the set FB-H10V40, then minor variations in r_c indicate that r_c is increased while the ring is fed with liquid by the film. In support of this

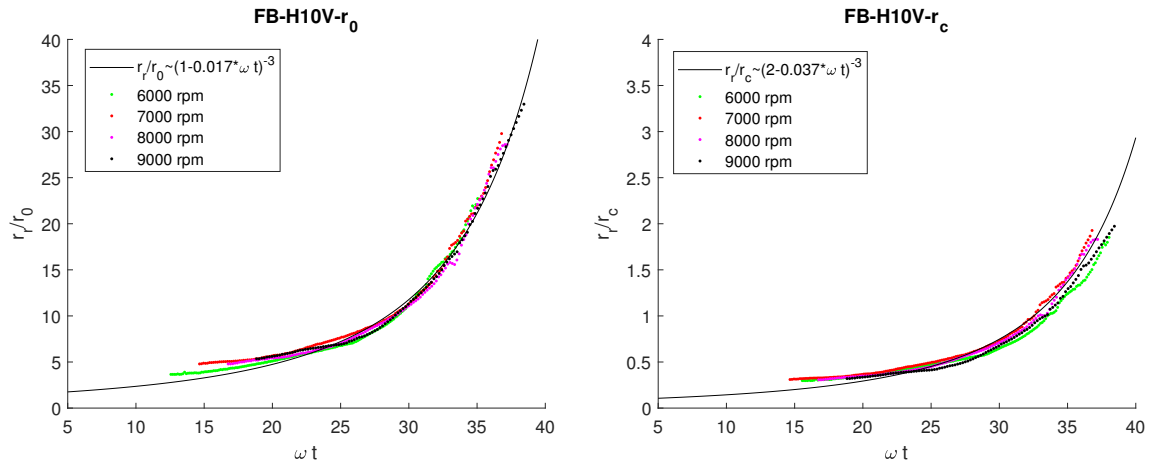

(a) (b)

Figure 4.20: Correlation of radius evolution (a) with the model predictions normalised with r_0 and (b) radius evolution normalised with r_c, for the set FB-H10V40.

argument t_c is also delayed for a droplet of $40\mu l$ at all rotation rates, as shown in Figure 4.21b. The decrease of t_c with ω indicates that the feeding stops earlier.

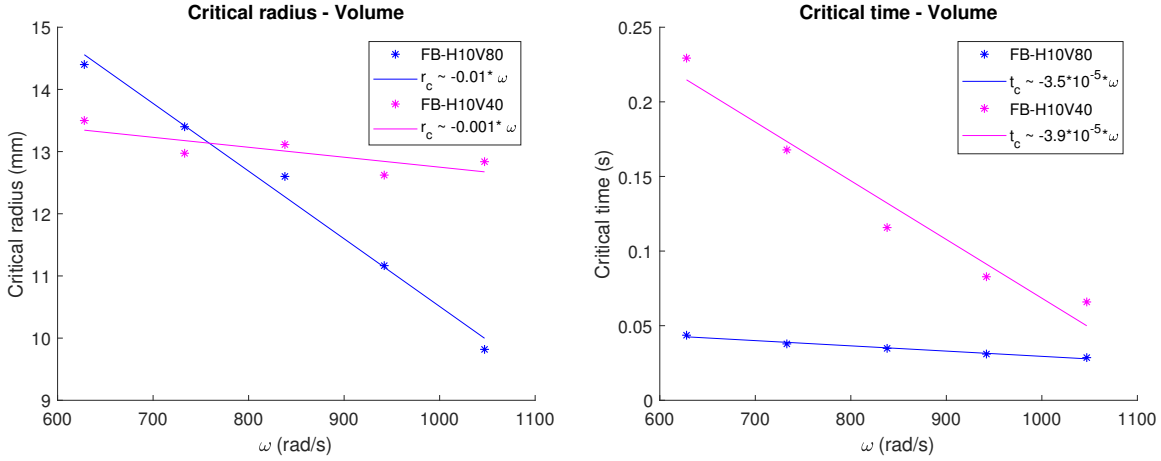

(a) (b)

Figure 4.21: Onset of (a) critical radius and (b) critical time for the sets FB-H10V80 and FB-H10V40.

4.5.3 Disk smoothness

In order to explore the effect of the disk smoothness to the spreading, experiments were conducted using the brass and the glass disk for the sets FB-H10V80 and FG-H10V80 respectively. For the brass disk, water was dyed with methylene blue, while for the glass disk water was dyed with fluorescein. Once again, the experimental results are in good agreement with the model, as shown in Figure 4.22.

The main difference is the duration of the spreading, which is shorter for the glass disk, as shown in Figure 4.22b, compared to the base case, as shown in Figure 4.22a. Reduced spreading times were observed on the glass disk for all rotation rates (5,000 – 9,000 rpm). The painted brass disk has a surface that is characterised of micro-structures due to the brass and the paint

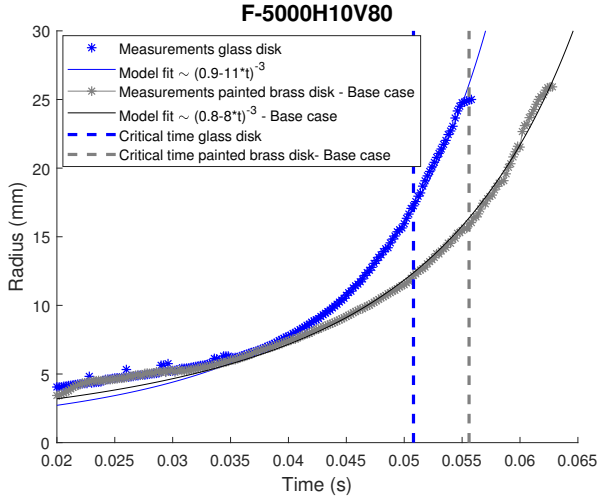

Figure 4.22: Examples of radius evolution on the brass and the glass disk, at 5000 rpm (cases FB5000H10V80 and FG5000H10V80). The main difference is the duration of the spreading, which is shorter for the glass disk.

of automotive primer. The contact line effects are reduced in the glass disk where the surface is smoother. For completeness, the experimental results of the set FG-10V80 in the form of graphs are shown in the Appendix A.

The spreading pattern is in good agreement with the model's time dependence $(C_0 - C_\omega t)^{-3}$, with the RMS deviation at 0.31 mm, similar to the the RMS deviation of the base case (0.32 mm), indicating that the disk smoothness has little effect on the functional form and hence, by inference, on the spreading mechanism.

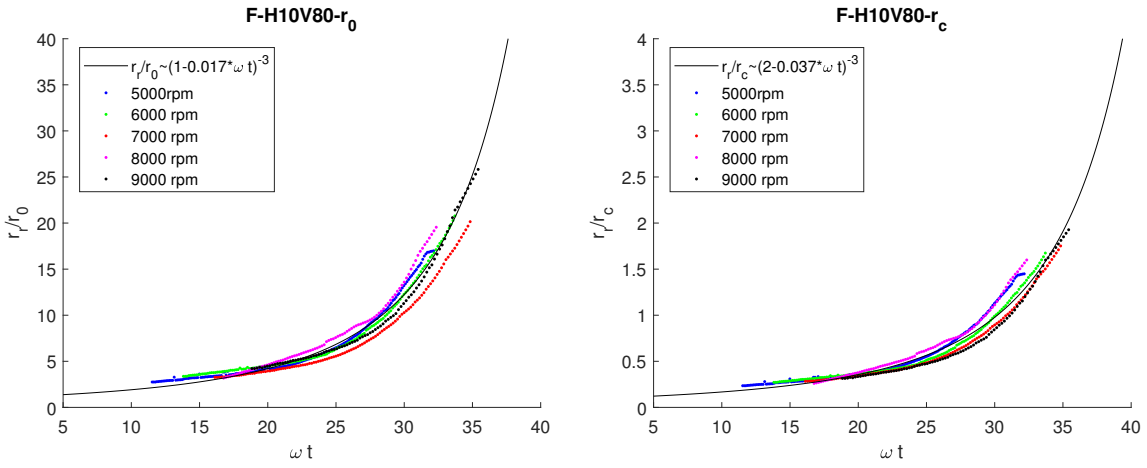

(a) (b)

Figure 4.23: Correlation of radius evolution (a) with the model predictions normalised with r_0 and (b) radius evolution normalised with r_c, for the set FG-H10V80.

The effect of surface smoothness is indirectly related with the model of section 4.2.2, by incorporating in C_ω the values of the initial radius and thickness after the impact, r_0 and h_0 respectively. The validity of the model was tested for the brass and the glass disk and for all the rotation rates that allow axisymmetric spreading (5,000 - 9,000 rpm). The results are presented in the dimensionless plot in Figure 4.23a and shows that all experiments are in good agreement with the model, with the RMS deviation at 0.94. The deviations from the base case fit (black

line), are towards the end of the spreading and might be indicative of the perturbations near the contact line. Another dimensionless plot is introduced in Figure 4.23b, incorporating r_c, which shows a similar evolution and deviation from the fitted line for most of the experimental results and with the RMS deviation being 0.08. This deviation indicates that the surface smoothness is a factor affecting the onset of the contact–line instability. Further investigation measuring the contact angle is required for more robust results.

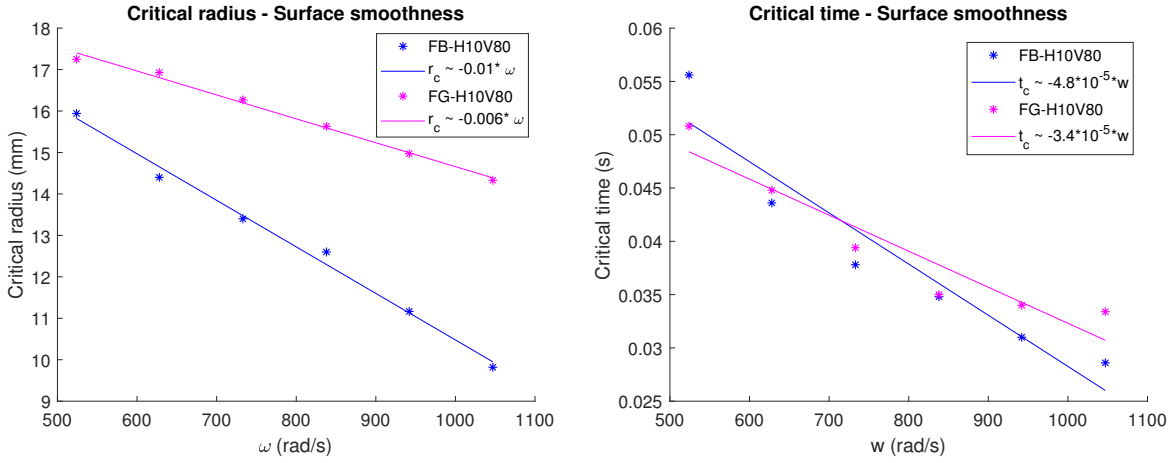

(a) (b)

Figure 4.24: Onset of (a) critical radius and (b) critical time for a brass and a glass disk, for the sets FB-H10V80 and FG-H10V80.

The brass disk has microscopic variations in its texture that could lead to increased perturbations. Additionally the sprayed paint on the brass disk may lead to macroscopic variation on top of the microscopic structure and hence, lead to longer length scale perturbations. The onset of the contact–line instability is investigated by comparing r_c for the two sets of experiments. The perturbations at the contact line are suppressed when the substrate is smoother and so r_c is increased, as shown in Figure 4.24a. This deviation is more prominent at higher rotation rates. Also the spreading is faster on the glass disk, however t_c is similar for the two disks, as shown in Figure 4.24b, leading probably to increased volume in the ring before r_c.

4.6 Instabilities/Spiral waves

So far we have described the spreading pattern until the contact line becomes unstable, once the front reaches r_c. Beyond r_c two instabilities develop. The first instability is at the contact line, where the unstable ring forms fingers. The fingers unfold in a direction opposite to the disk rotation and from now on will be referred to as 'retrograde' fingers. The second instability starts at the intersection between the film and the ring. As the ring moves beyond r_c, spiral waves start forming within the film area. The waves are visible from r_c and outwards ($r \geq r_c$), for 1 to 2 revolutions and eventually disappear as they are dissipated in the film. The spiral waves unfold in the same direction with the disk rotation and from now on will be referred to as 'prograde' spirals. Thus, the fingers and the spirals fold in opposite directions, as shown in Figure 4.25. The fingers at the higher end of rotation rates, instead of propagating ahead of the droplet ring forming proper rivulets, are caught back up by the main flow. We will also see, in chapter 6, that for the range of parameters under investigation, there is no contact–line

instability observed during the film development in the VFD, leading to fingers. Therefore finger formation due to contact line instabilities will not be investigated further.

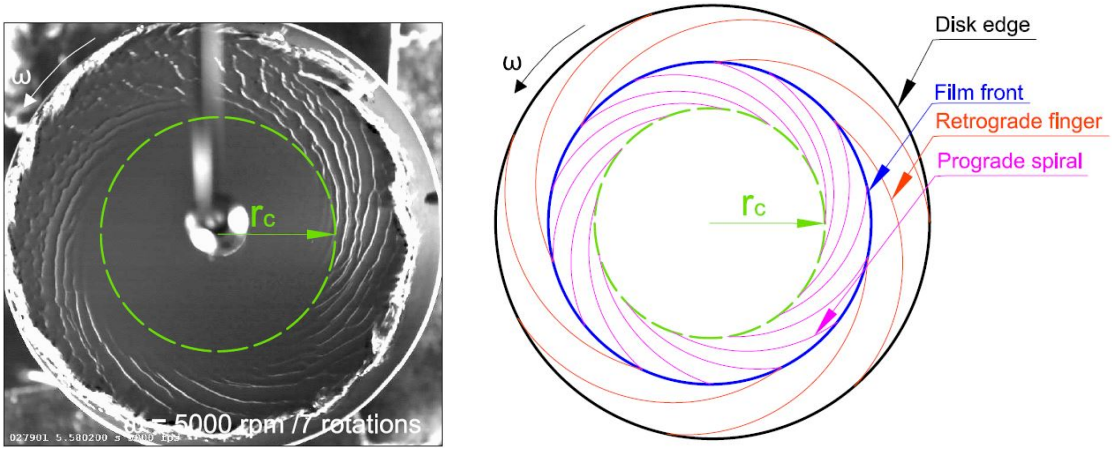

(a) (b)

Figure 4.25: Spreading on axis for the base case FB5000H10V80 (524 rad/s, $t = 54$ ms). The disk rotates anticlockwise. The fingers beyond the contact line unfold in the opposite direction to the rotation of the disk (retrograde fingers). The spiral waves in the film unfold in the direction of the disk rotation (prograde spirals).

On the other hand, retrograde spiral waves have been documented in boundary layer instabilities for rotating films of constant flux, as mentioned in section 2.2.4. However, there is no evidence of retrograde spirals but instead prograde spirals are visible. Such prograde spirals, due to the spreading of single droplets, are not documented in detail. Therefore, in this project we focus on the spiral waves, measuring the wave characteristics for the set FB-H10V80.

The transition from laminar to the wavy film appears beyond r_c. The wave crests become more irregular as they propagate outwards. These irregularities occur on a smaller length scale than the distance between successive fronts. The transition to irregular fronts is not easily distinct. The wavelength between spirals is slightly decreased as ω increases, with the wave crests appearing more irregular.

We also explore whether these waves are stationary in the disk frame of reference, indicating a boundary layer instability as described in section 2.2.4, or they are similar to roll waves, as described in section 2.2.5. To understand the formation of the waves, we focus on the measurement of the wavelength and the velocity of the spirals. Due to the moving set-up, light reflections are constantly changing and the visualisation of the spirals, adequate for image processing, is limited to approximately 1 to 2 revolutions. Thus, in order to measure the wavelength of the spirals, we choose 1 frame from each realisation. The frame with the most prominent reflections is processed in Matlab. The image is transformed to a binary format and overlapping polar spirals are imposed over the binary image. The spiral step, at the polar plot, was chosen in order for the additional spirals to collapse with the experimental spirals. An example of this processing is shown in Figure 4.26. The image in (a) shows the spiral development for the experiment FB7000H10V80. The critical radius is indicated by the white circle beyond which spiral waves are visible. The image in (b) shows the collapse of the additional spirals with the experimental spirals.

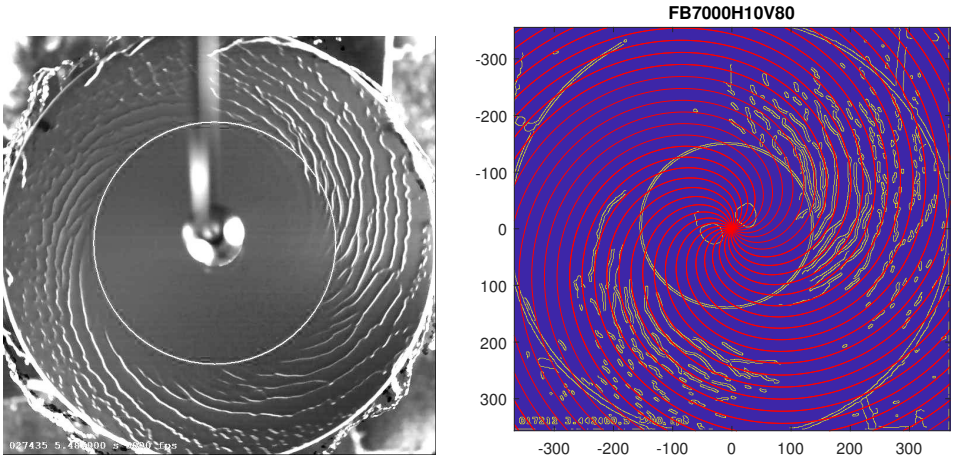

(a) (b)

Figure 4.26: (a) Spiral wave development for the case FB7000H10V80, starting from the critical radius (yellow circle) and (b) additional spirals overlapping with the experimental spirals (units in pixels).

The wavelength of the spirals is $\sim$ 1 mm for all rotation rates with a small decrease for increased ω. The experimental spiral tends to deviate from the overlapping spiral towards the rim of the disk. The spiral angle is not constant, indicating that the phase propagation of each spiral is outwards and retrograde, normal to the crest of the spirals. Although measurements of the azimuthal velocity proved challenging, the measurement of the radial velocity of the spirals in the rotating frame of reference was feasible for the base case, using the data from the PIV experiment, and the results are presented in Figure 4.27. Experiments on inclined planes have determined a ratio between the wave velocity of roll waves and the mean velocity at approximately 2.3 (see section 2.2.5). It appears that the velocity of the spirals in the spinning disk scales as $2.6\omega r$, and the mechanism might be similar to roll waves.

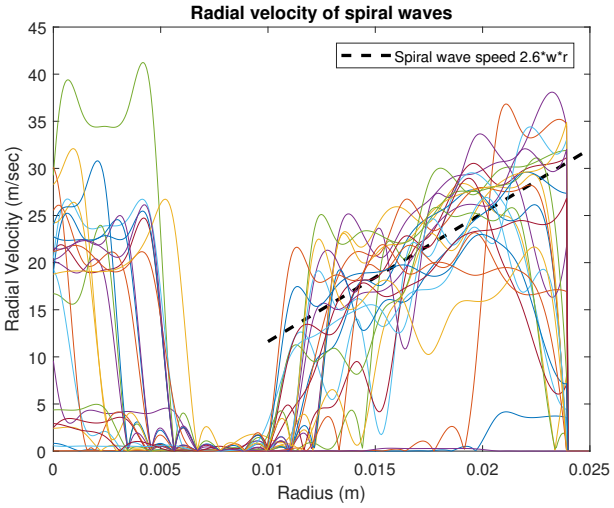

Figure 4.27: Radial velocity of the spiral waves, in the rotating frame of reference, for the base case (FB5000H10V80).

A plausible mechanism for the formation of the spirals, suggested in the current section, is based on the azimuthal perturbations developed in the ring when it reaches r_c. The suggested mechanism was motivated by the work of Moisy et al. (2004) that investigated shear flow

instabilities in the flow between counter–rotating disks. When the distance between the two disks was small and the top disk was rotating with increased angular velocity compared to the lower disk, Moisy et al. observed the formation of spirals on the top disk, similar to the ones observed in the current experiment.

In the counter–rotating disk regime, spiral waves result from the interaction of the shear layer primary instability pattern in the bulk of the flow with the centrifugal Ekman boundary layer over the faster disk. The Ekman layer advects the perturbation outwards, resulting to the observed prograde spirals. In our case, we can consider the spinning disk as the top disk in the counter–rotating regime. Our case differs from the counter–flow regime, as the air rotates in the same direction of the disk, at a mean rotation rate lagging behind the disk's. However, as the ring is no longer uniform, in the azimuthal direction, the liquid left behind from the ring also varies in the same direction, causing disturbances to the film flow. The expelled liquid interacts with the von Kármán layer, causing the formation of well-defined spiral waves. Thus, the formation of the spirals is more likely to be a shearing–induced instability.

Boundary layer instabilities form stationary, in the rotating frame of reference, retrograde spiral waves. The Reynolds number over which the growth of stationary vortices saturates is defined as $Re = {}^{r\omega\delta}/_{\nu} \sim 507$, where δ is the von Kármán thickness $({}^{\nu}/_{\omega})^{1/2}$ (Lingwood & Alfredsson, 2015). This is a scaling frequently documented in the literature describing the unstable spiral regime and therefore it is used for comparison with our regime. Although the scaling takes into consideration the von Kármán thickness, the film thickness in our experiments varies significantly with ω. Therefore, a comparison of Re as defined by Lingwood & Alfredsson, with Re at r_c, taking into account the actual film thickness, measured by the experiment in section 4.3, is shown in Figure 4.28.

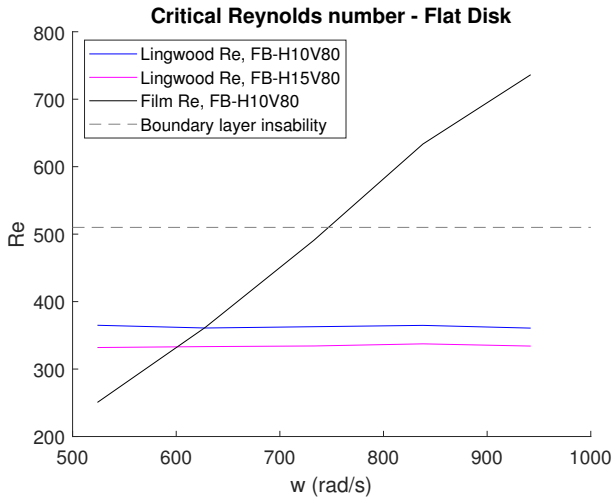

Figure 4.28: Reynolds number at r_c and comparison to the Lingwood & Alfredsson limit, [2015], for for the sets FB-H10V80 and FB-H15V80.

The blue line indicated Re of the film for the set FB-H10V80 and the pink line for the set FB-H15V80. The deviation between the blue and the pink line is due to the variation in r_c. The resultant Re for the two sets of experiments is lower than the Lingwood & Alfredsson threshold. However, in reality the film thickness and consequently Re increase with ω, hence using the experimental measurements of h, Re exceeds the Lingwood & Alfredsson limit beyond 7,000 rpm, indicated as a black continuous line. The wave formation is present even for $\omega < 7,000$

rpm and the mechanism requires further investigation both theoretically and experimentally as it has the potential to enhance chemical reactions.

At this stage we identified the main characteristics of fluid flow and tested the behaviour of the fluid development under a range of parameters. Given the complexity of the problem, several other considerations were taken into account and were tested. The observations were transformed mostly into qualitative analysis of fluid behaviour and are presented in the following section.

4.7 Other considerations

Many other variations of parameters could be investigated on the flat disk. In the current section we restrict our attention to a small number of additional parameters, that are related to how the VFD is operated in practice. In this section the focus is on the wetting properties of the disk, the spreading pattern when the droplet lands away from the axis of rotation, and the pattern when the disk is tilted. Although each variation was a separate set of experiments, the observations are mainly qualitative. The sets are described in this section to give a broader idea of the fluid motion but they could consist individual research projects. All sets of experiments were conducted with the painted brass disk and for a droplet volume of 80 μl.

4.7.1 Wet spinning disk

The aim is to observe the spreading pattern when the disk is already wet, thus removing the contact line dynamics. It is observed during the PIV experiment that the film becomes very thin and rotates almost with the angular velocity of the disk, within a time scale of approximately 50 ms, long enough for a droplet to land and spread onto the wet area. Thus, to achieve the landing of the droplet on a wet disk, experiments are conducted with droplets landing on shorter intervals. Several flow rates are tested and monitored with the high–speed camera. By increasing the flow rate from 0.8 to 20 ml/min, every droplet lands after the spreading of the previous droplet and before the disk is dried out.

For this flow rate, one could argue that landing happens on the film while it is effectively in solid body rotation. Although the thickness of coating is not monitored, the consistent results from repetitive experiments indicate that the thickness of the coating does not vary significantly. Based on the film thickness experimental results, after the ring reaches the rim of the disk, i.e. similar thickness with the current experiment, a rough estimation of the thickness is of $\mathcal{O}(10^{-5})$ m.

Compared to the base case at 5,000 rpm (FB5000H10V80), in the wet disk experiment (FB5000H10V80W), capillary waves form at the front even at early times, and travel along the free surface of the film, as shown in Figure 4.29. The capillary waves seem to suppress the ring formation, compared to the dry brass disk, creating a more uniform film. An important component for the spreading is the film thickness, which seems to be increased due to increased uniformity. Compared to the base case where the film thickness at r_c was of $\mathcal{O}(10^{-5})$ m, the film thickness for the wet disk could be of $\mathcal{O}(10^{-4})$ m, much larger than the film thickness defining Re of the spiral waves on a dry disk.

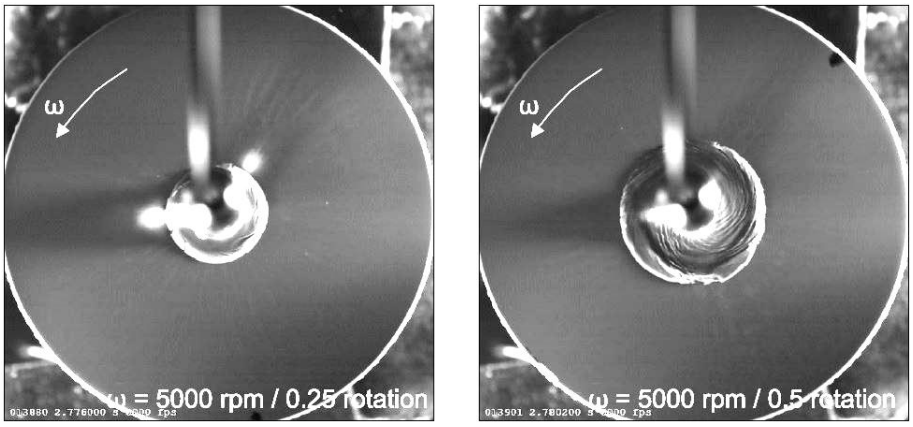

(a) 6 ms (b) 12 ms

Figure 4.29: (a) At early times, capillary waves developed at the front of the ring. The capillary waves travel towards the axis of rotation, forming free surface spirals. (b) The spirals are fully developed and visible throughout the spreading (case FB5000H10V80W).

The front of the spreading droplet forms a ring which looks much smaller than the ring formed in the base case. Eventually the front breaks into fingers outwards and spiral waves inwards, as shown in Figure 4.30. The prograde spirals are similar to the spiral instability described in section 4.6. The retrograde fingers have decreased wavelength and are thinner than in the base case.

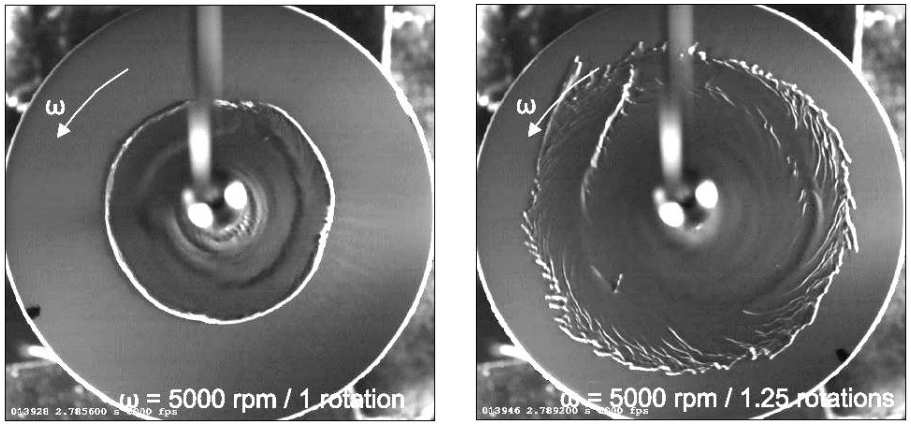

(a) 18 ms (b) 21 ms

Figure 4.30: (a) The droplet loses its axisymmetric shape at r_c. (b) The retrograde fingers and the prograde spirals are visible with smaller wavelength than on the dry disk (case FB5000H10V80).

A wavy shape is also identified along the crest of each spiral wave, as shown in Figure 4.31. The instability along the crest causes the formation of small fingers, indicating the presence of an additional instability occurring locally. The time scale of spreading varies, with the spreading being faster as ω increases.

An illustration of the radius evolution with respect to time at 5,000, 7,000 and 9,000 rpm is presented in Figure 4.32. The fit used in the previous experiments, could potentially be applicable, although it should be noted that RMS deviation is 0.89 mm, relatively increased

compared to the base case indicated in the Figure with colour black (RMS = 0.32 mm). The fit assumes a growing ring and the deviation of the radius evolution from the fit must be due to the different ring dynamics.

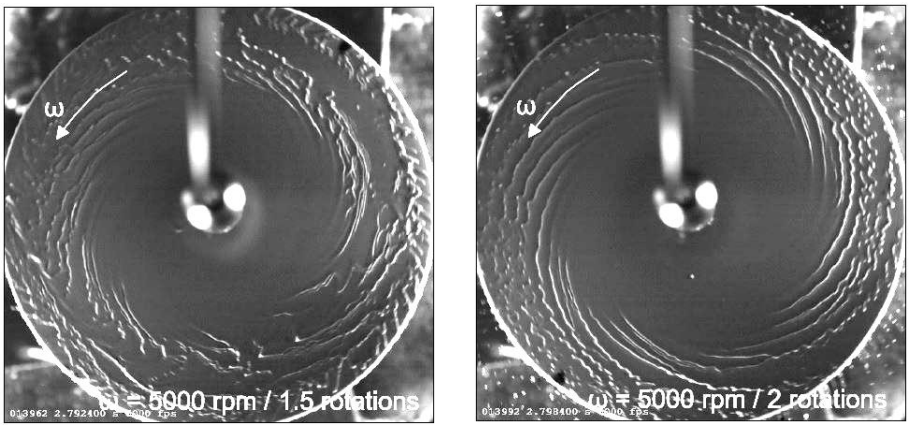

(a) 24 ms (b) 30 ms

Figure 4.31: (a) The front reaches the rim of the disk. The spiral waves become unstable and small fingers form along the crest of each spiral (case FB5000H10V80W).

For $r < r_c$, the data coincide for different ω. The scatter within each experiment represents the perturbations at the front, present throughout the spreading. The value of r_c varies with ω and appears to be slightly increased at 5000 rpm (red dashed line) when compared to the base case (grey dashed line). Overall, the wet substrate leads to the reduction of surface tension effects. Reduced surface tension effects make the spreading faster and suppress the formation of the ring. Therefore, the time dependence at early times for the wet disk, could be approximated by the Nusselt film scaling (green line).

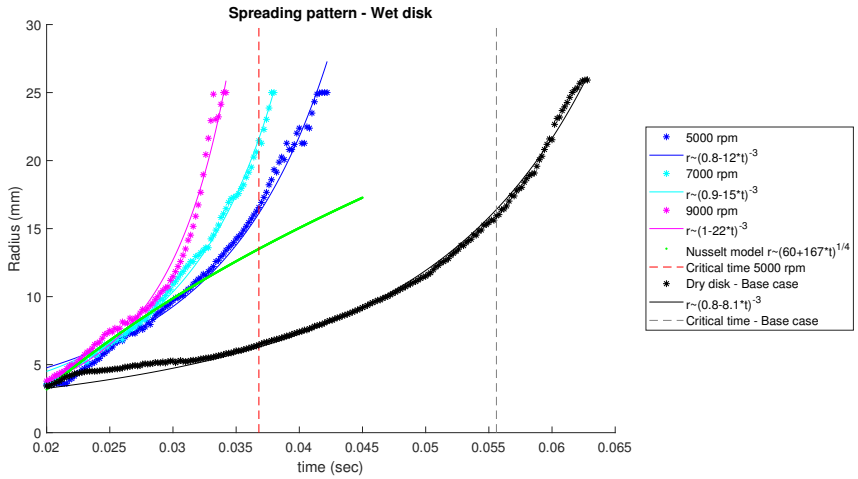

Figure 4.32: Comparison of radius evolution on a wet brass disk for rotation rates at 5,000, 7,000 and 9,000 rpm (cases FB5000H10V80W, FB7000H10V80W and FB9000H10V80W) with the base case at 5,000 rpm and on a dry disk (FB5000H10V80).

4.7.2 Off–axis spreading

Another set of experiments investigates the spreading pattern when the droplet lands away from the axis of rotation. The pipette is positioned 10 mm away from the axis and 10 mm above

the rotating disk. The brass disk is used and the experiment is conducted from 1,000 rpm to 9,000 rpm for the set FB-H10V80OFF10. An example of the spreading at 1,000 rpm is shown in Figure 4.33. In the laboratory frame of reference, after one rotation period at 1,000 rpm, the bottom of the droplet is carried away by the rotating disk while the bulk of the remaining droplet moves slightly radially and azimuthally.

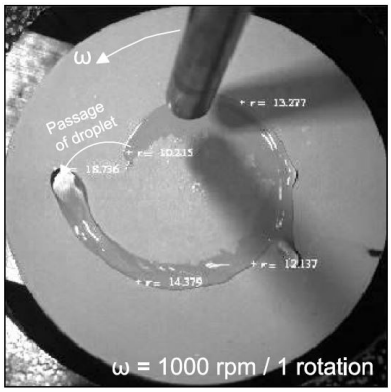

Figure 4.33: Spreading after landing off axis, on a flat disk, at 1,000 rpm - case FB1000H10V80OFF10.

From 2,000 rpm to 9,000 rpm the angular velocity is high enough so that the disk accelerates only the bottom of the droplet, while the rest of the droplet is still landing. One revolution after the droplet touches the disk, the film which rotates with the disk, returns to the point of release and meets the remaining droplet. The film mixes with the droplet and from this point and on, the solid surface is pre-wetted, the tip of the droplet becomes wider and spreads rapidly in every direction as shown in Figure 4.34.

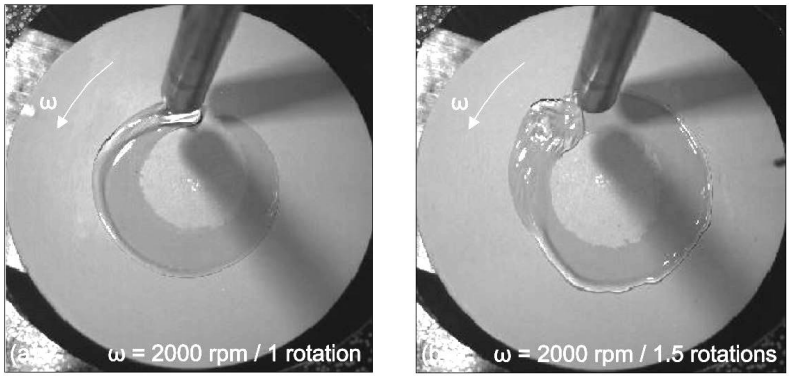

(a) 30 ms (b) 45 ms

Figure 4.34: Spreading after landing off axis, on a flat disk, at 2,000 rpm (case FB2000H10V80OFF10).

The duration of spreading is approximately the same as for the on–axis landing. However, the duration varies significantly for different rotation rates. At 2,000 rpm, after one revolution a capillary ridge is created at the outer edge of the angular wet area, which eventually becomes unstable and leads to the formation of fingers. At 5,000 rpm, as shown in Figure 4.35, after the first revolution only a few thin stripes are visible.

The air boundary rotates faster, with increased ω, creating a barrier which works as a cushion for the droplet. A continuous film line is visible after the second revolution. After

four revolutions most of the volume is stripped out of the droplet and only a small portion of liquid still remains in the landing area. Even from the second revolution, fingering instability is prominent at the contact line at the outer edge of the angular film.

In an attempt to estimate the thickness of the film, let us assume that the feeding of liquid from the droplet after the first contact with the disk is constant. Knowing that the spreading requires more than 4 revolutions, it appears as less than 40μl have coated the disk. Suggesting that this is an overestimation, let us assume that the liquid coated on the disk is approximately half of the droplet volume, i.e. $4 \times 10^{-8}\text{m}^3$. The wet area after the second revolution is approximately 4×10^{-3} m^2 and assuming a uniform film, the thickness must be $(4 \times 10^{-8})/(4 \times 10^{-3}) \sim 10^{-5}$m. This is the length scale that surface tension becomes important and fingering instabilities are expected.

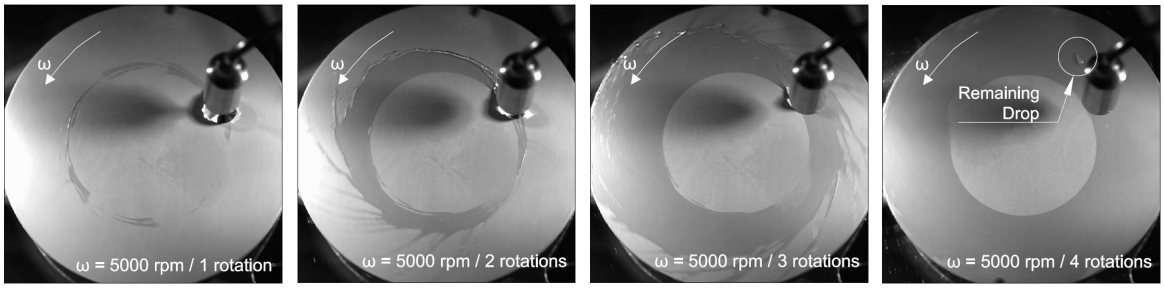

(a) 12 ms (b) 24 ms (c) 36 ms (d) 48 ms

Figure 4.35: Spreading after landing off axis, on a flat disk, at 5,000 rpm (case FB5000H10V80OFF10).

As the rotation rate increases, the air boundary makes the formation of the film slower at early times. The air rotating with the disk works against the landing of the droplet. The early times of the droplet contact appear with some stripes of wet areas on the dry disk. As ω increases there is an increasing number of revolutions with visible wet stripes before a continuous angular film is formed, as shown in Figure 4.36.

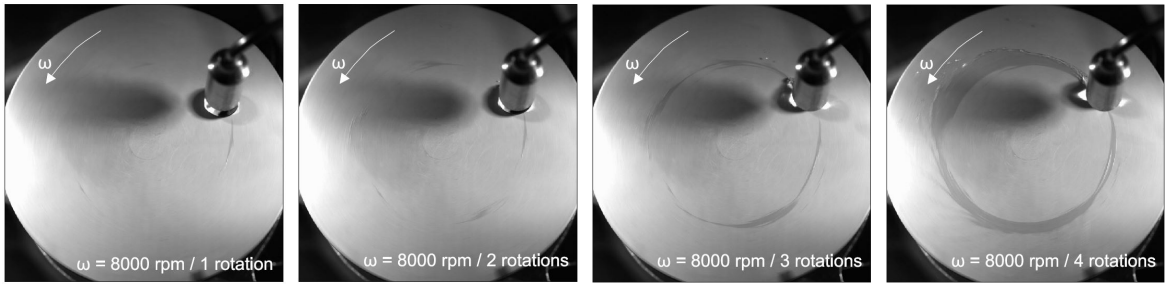

(a) 7.5 ms (b) 15 ms (c) 30 ms (d) 60 ms

Figure 4.36: Spreading after landing off axis, on a flat disk, at 8,000 rpm (case FB8000H10V80OFF10).

The effect of the air boundary layer, the initiation of the instability, the rate of the droplet drainage, the thickness of the film and the fingers are mechanisms that are worth further future investigation. Whether these phenomena affect chemical reactions in spinning disks is unclear. As the VFD presents optimum performance when the device is tilted, the droplets in CF land at the walls of the tube and not at the axis of rotation. The off–axis landing in the flat disk is

very similar to the landing of droplets in CF at the walls of the VFD. As we will see in chapter 6, the glass tube in the VFD, in combination with the already coated area, minimise the surface tension effects and no fingering phenomena are observed in the device.

4.7.3 Tilted disk

The experimental set–up is tilted in order to investigate the spreading pattern under the effect of the component of gravity tangential to the disk. Experiments are conducted for a droplet of 80 μl landing on the brass disk that is tilted at a range of inclination angles. We shall however restrict our attention to a single inclination angle of 45°, that illustrates the dominant effects of the spreading. Also, it has been reported that this is the inclination at which the VFD works best and possible correlations to the VFD film formation could be useful. A representative example at 8,000 rpm, with an inclination angle of 45°, is analysed to explain the film formation onto the inclined flat disk. The rotation rate was chosen at 8,000 rpm, which is high enough to produce a film for more than one revolution even when the droplet lands close to the lower rim of the disk. Three different landing points are investigated. First the droplet lands 10 mm above the axis of rotation (set FB-T45V80A10), as shown in Figure 4.37.

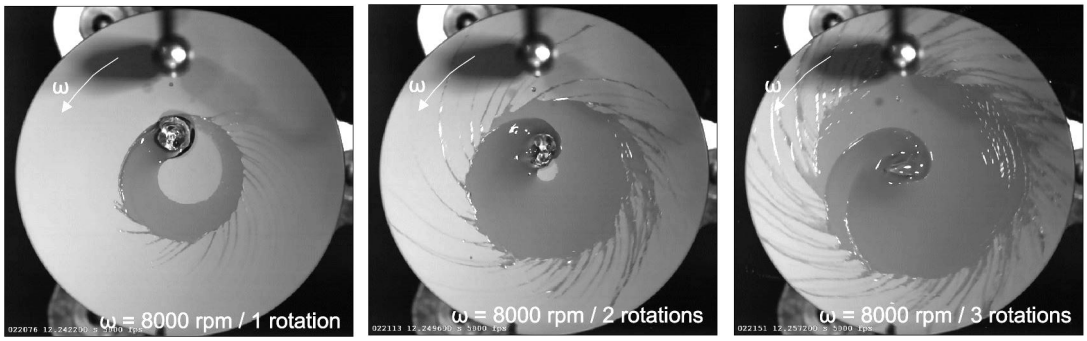

(a) 7.5 ms (b) 15 ms (c) 23 ms

Figure 4.37: During landing, the droplet forms a film azimuthally due to the rotating frame and radially, towards the axis of rotation, due to gravity (case FB8000T45V80A10).

The bottom of the droplet is stripped away by the moving surface while the bulk of the droplet moves down towards the axis of rotation due to gravity. The distance that the droplet has slid down the inclined surface due to gravity, after one revolution, is approximately the droplet diameter. At the beginning of the third revolution the droplet reaches the axis of rotation. Fingering instabilities are present at the contact line from the first revolution similarly to the horizontally placed disk for an off–axis release.

In the second case (FB-T45V80ON), the droplet lands close to the axis of rotation, as shown in Figure 4.38. The film forms almost axisymetrically and the bulk of the droplet, not yet rotating, moves radially to lower parts of the disk. The distance that the bulk makes in one revolution is again similar to the diameter of the droplet.

In the third set (FB-T45V80B10), the droplet lands below the axis of rotation as shown in Figure 4.39. The pattern is very similar to the first set, with the droplet landing above the axis of rotation. The main difference is that the droplet moves, due to gravity, downwards and due to centrifugal force always radially outwards, thus the centre of the disk remains dry at all

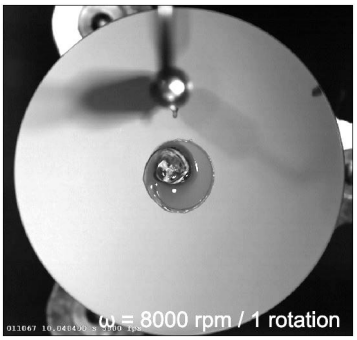

(a) 7.5 ms

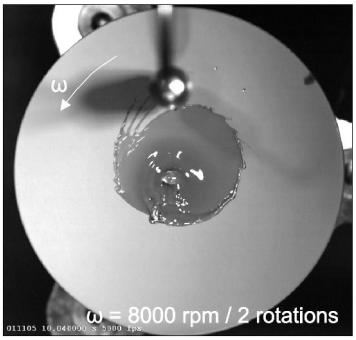

(b) 15 ms

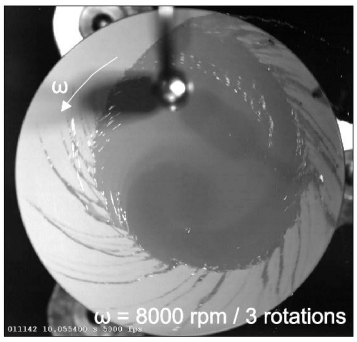

(c) 23 ms

Figure 4.38: The droplet lands approximatelly at the centre of the disk and the spreading is initially axisymmetric. The radial distance covered, due to gravity, in one rotation is approximately equal to the diameter of the droplet (case FB8000T45V80ON).

times.

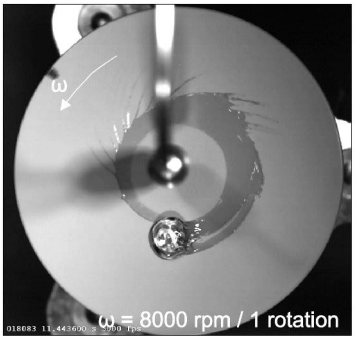

(a) 7.5 ms

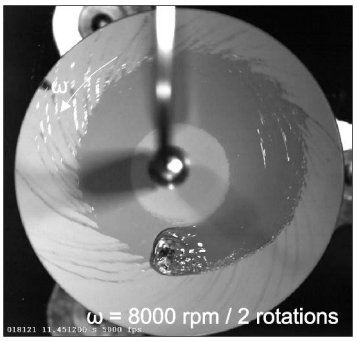

(b) 15 ms

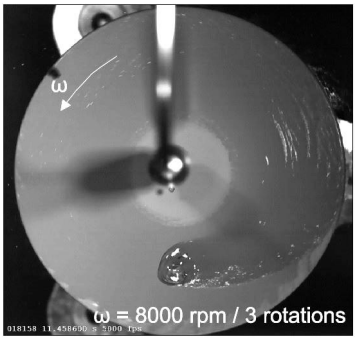

(c) 23 ms

Figure 4.39: The droplet lands below the axis of rotation and the pattern is very similar to the FB8000T45V80OFF10. The main difference is the faster coating due to the radial downwards movement of the droplet (case FB8000T45V80B10).

In all cases, the liquid is stripped from the base of the droplet and contact–line instabilities cause the formation of fingers at the front of the film, very similar to the ones observed for an off-axis landing on a horizontally placed disk. In combination with the downwards movement, due to gravity, the droplet presents intense capillary waves in the bulk that is not yet rotating. Overall, it seems that when the droplet lands above the axis of rotation, the centrifugal force guiding liquid radially outwards in combination with the tangential component of gravity guiding the liquid downwards, form a slightly wider film than in the almost axisymmetric case, with possible benefits in shearing and chemical reactivity.

4.7.4 Collision rate

One of the aims of this project is the connection of the fluid mechanics characteristics with the collision rate of the molecules as mentioned in section 2.1. According to the main hypothesis, the rate of increase of the product [C] can be achieved due to enhanced diffusion and advection. Advection is related to the collision coefficient Z, proportional to shearing, due to the velocity gradient normal to the direction of the flow. The Nusselt approximation is broadly incorporated

when spinning disks are used as flow chemistry devices both under constant flux and under constant volume. In this section we define Z, assuming a Nusselt film either for constant flux Q or for constant volume V.

The shearing in the droplet can be expressed proportionally to the mean averaged velocity as

$$Z \propto \frac{\bar{u}_{(z=h)}}{h}. \tag{4.34}$$

For a Nusselt film of uniform thickness h, the velocity profile $\hat{u}$, balancing viscosity and the centrifugal force, is

$$\mu\frac{\partial^2\hat{u}}{\partial z^2} = \rho\omega^2 r \rightarrow \hat{u}(z) = \frac{\rho\omega^2 r}{\mu}\int_z^h (h-z)dz = \frac{\rho\omega^2 r}{2\mu}z(2h-z),$$

as explained in section 2.2.2.1, and at $z = h$, the surface velocity is

$$U = \frac{\rho\omega^2 r}{2\mu}h^2. \tag{4.35}$$

So the velocity profile expressed in reference to U is

$$\hat{u} = \frac{U}{h^2}z(2h-z)$$

and the depth-averaged velocity is

$$\bar{u} = \frac{1}{h}\int_0^h \frac{U}{h^2}z(2h-z)dz = \frac{2}{3}U. \tag{4.36}$$

Replacing equation 4.35 to equation 4.36, the collision rate of equation 4.34 becomes

$$Z \propto \frac{\omega^2 r}{3\nu}h. \tag{4.37}$$

By considering a continuous flow mode with constant flux Q and using equation 4.36, the thickness of the film is

$$Q = 2\pi r h\bar{u} \rightarrow h = \left(\frac{3Q\nu}{2\pi\omega^2 r^2}\right)^{\frac{1}{3}}. \tag{4.38}$$

The radius for a fluid element changes as

$$\frac{dr}{dt} = \bar{u} \rightarrow r = \left(\frac{\omega^2 Q^2}{\nu\pi^2}\right)^{\frac{1}{4}} t^{\frac{3}{4}} \rightarrow t = \left(\frac{\nu\pi^2}{\omega^2 Q^2}\right)^{\frac{1}{3}} r^{\frac{4}{3}}. \tag{4.39}$$

Replacing equations 4.38 and 4.39 to equation 4.37, and integrating over the time, the concentration of the product with respect to fluid mechanics is predicted to follow

$$\Delta C \sim \int_0^t Z dt \sim \left(\frac{\omega^2 r^5}{Q\nu}\right)^{\frac{1}{3}}. \tag{4.40}$$

The above relation indicates that there is enhanced shear stress when the angular velocity and the axisymmetric spreading are maximised ($\omega^2 r^5 \rightarrow \max$).

Considering the definition of Z for constant volume V we take into consideration volume conservation with a uniform film so that

$$V = 2\pi r^2 h \rightarrow h = \frac{V}{2\pi r^2}. \tag{4.41}$$

The radius for a fluid element changes as

$$\frac{dr}{dt} = \bar{u} \rightarrow \frac{dr}{dt} = \frac{\rho\omega^2 r}{3\mu}h^2 \rightarrow r = \left(\frac{\omega^2 V^2}{3\pi^2\nu}t\right)^{\frac{1}{4}} \rightarrow t = \frac{3\pi^2\nu}{\omega^2 V^2}r^4. \tag{4.42}$$

Replacing equations 4.41 and 4.42 to equation 4.37, and integrating over the time, the concentration of the product with respect to fluid mechanics is predicted to follow

$$\Delta C \sim \int_0^t Z dt \sim \frac{r^3}{V}. \tag{4.43}$$

The above relation indicates that there is enhanced shear stress when the axisymmetric spreading is maximised and the droplet volume is reduced. The implication here is that the axisymmetric radius is increased with ω and the droplet volume should be large enough to achieve axisymmetric spreading. Thus, the ratio of axisymmetric spreading and volume should be explored further in flow chemistry experiments taking into consideration reaction rates. Interestingly, although the fluid experiences high shear as ω increases. However, increased ω leads to reduced residence time. Thus, if the dynamics of advection were governed by the Nusselt film scaling, we would expect small variations in chemical reactivity with respect to rotation rate.

The scaling of Z could be also correlated to the growing and shrinking ring and the spiral waves, as the velocities and pressure gradients in these areas could enhance reactivity. In order to validate this scaling and further developments of this approximation, a correlation should be made to experiments exploring the performance of chemical reactivity.

4.8 Summary

This chapter explores the fluid motion caused by single droplets landing on already rotating horizontal and inclined surfaces, at rotation rates from 1,000 to 10,000 rpm. Apart from the rotation rate, the height of release, the droplet volume and the smoothness of the disk are parameters of variation that altered the spreading pattern and the onset of instabilities. The experiments investigate the dynamics of droplet landing, the film development and the presence of instabilities at the contact line and along the free surface of the film.

The droplet is released from a pipette at a specific height over the disk, falls under the force of gravity and lands on the already rotating substrate. Immediately after landing, the von Kármán layer forms where the centrifugal force, which is the dominant factor for spreading, drags the fluid outwards. The droplet is divided in two different areas, the film and the ring. The ring forms very early and is fed with liquid by the film. The volume within the ring reaches its maximum just before the front reaches r_c. At r_c, the thickness of the film ($\sim 10^{-5}$ m) is around 10 times smaller than the thickness of the ring ($\sim 10^{-4}$ m). This unexpected pattern of spreading, i.e. the growing and shrinking ring, has not been documented previously in the literature. Thus, fits of the general form $r \sim (a+bt)^c$ were explore as descriptions of the growth of the ring. This form was motivated by the Nusselt approximation. A good correlation to the experimental observations was found using a two parameter fit $r_r \sim (C_0 - C_\omega t)^{-3}$, both for the brass and the glass disk. It should be noted that the best fit exponent is negative, predicting a singularity at a finite time. However, the ring becomes unstable before the singularity is reached. Future developments should explore other fits and scaling for the mathematical problem, taking into consideration the contact line instabilities.

Beyond r_c, perturbations at the contact line lead to fingering instability, with the fingers unfolding retrograde to the rotating disk. While the front moves away from r_c, the ring leaves liquid behind coating the disk. The initially growing and later shrinking in volume ring is described for the first time in this thesis. In parallel, spiral waves appear at the free surface of the film. The spiral waves are visible from r_c and outwards and unfold prograde to the rotating disk. The spiral waves seem to behave as roll waves and they eventually dissipate in the film. The radial velocity of the spiral waves, in the rotating frame of reference, was determined by the PIV experiment and is approximately $2.6\omega r$.

Experiments altering the height of the release indicate that shape oscillations after the impact not only affect the initiation of spinning, but have a long lasting effect which is represented by the value of r_c. The volume of the droplet can affect the onset of the instability, with larger droplets ($\sim$ 80 μl) forming thicker rings, while smaller droplets ($\sim$ 40 μl) form thinner rings and delay the onset of instability. Thus, by altering the droplet volume we suppress or enhance the ring formation and the onset of instabilities. From our observations it seems as the feeding of liquid to the ring works as a stabilising factor. When the feeding stops the contact line becomes unstable. The volume limit under which the ring forms instabilities should be investigated further. By switching the brass disk with the glass disk we observed a qualitatively similar spreading pattern with the onset of contact line instabilities being delayed. The correlation of each parameter to the onset of instabilities is indicated by the experimental measurements of r_c and t_c, as shown in Table 4.2.

Table 4.2: Onset of contact line instabilities

Parameter	r_c	t_c
$\omega \uparrow$	$\downarrow$	$\downarrow$
$H \uparrow$	$\downarrow$	$\uparrow$
$V \uparrow$	$\downarrow$	$\downarrow$
Smoothness $\uparrow$	$\uparrow$	$\uparrow$

Experiments on the wet disk alter the contact line dynamics. Spiral waves develop at the free surface of the droplet at early times, which suppressed the formation of the ring. In contrast to the dry disk, r_c seems to be very similar for rotation rates from 5,000 to 9,000 rpm. The instability pattern is expressed with fingers at the contact line and mini fingers along the crest of the spiral waves.

When the droplet is released away from the axis of rotation, the bottom of the droplet is dragged by the rotating surface while the rest of the volume is still landing. The film in rotation is immediately exposed to greater centrifugal force and fingers form at the contact line. The fingers drive the fluid faster outwards. The fingering instabilities could reduce the processing time and be a disadvantage for a potential chemical reaction. However the rate of drainage of the droplet during the landing could lead to increased shearing within the film. In order to be more conclusive on the benefits of the off-axis landing, the rate of drainage at the interface with the disk should be investigated further.

When the set–up is tilted, the lower part of the landing droplet is dragged away by the disk, while the rest of the volume follows a radial motion downwards, due to gravity. The interface with the disk is increased, thus the film area formed by the drained liquid is increased. The rate of drainage is altered due to the tilting of the disk.

Whether the spreading before or after the onset of instabilities is more beneficial for the chemical reactions is unclear. The correlation between fluid mechanics and molecular reactions is explored with the definition of the dimensionless variable Z, proportional to the averaged depth velocity. This scaling is based on assumptions that can be representative of the flow conditions. The variable Z was defined for a Nusselt film of constant flux. The particles in the film move under laminar flow. Their radial velocity is increased, which in combination with diffusion could increase their collision probability. Experiments, with respect to chemical reactivity, could give an insight to the reliability of the assumptions made for the determination of Z.

Overall, the onset of instabilities seems to be related to the rate the ring is being fed by liquid and the total accumulation of volume in the ring. The correlation between the value of r_c and the ring volume should be investigated further. The experimental observations of the spreading droplets and the instabilities are useful for the understanding of the landing of droplets in CF in the VFD. In the next chapter, the pattern of spreading is investigated on a hemispherical surface, a geometry more relevant to the hemispherical base of the VFD.

Chapter 5

Hemispherical disk

This chapter explores the formation of thin films, caused by single droplets, landing on an already rotating hemispherical disk. The experiments focus on the dynamics of droplet landing, the film development and the presence of instabilities at the contact line and along the free surface of the film. Having explored the spreading pattern on a flat disk, the same approach is used for the hemispherical disk.

The stages of film formation are very similar to the formation on the flat disk. The droplet is released from a pipette at a specific height over the disk, falls under the force of gravity and lands on the already rotating substrate. After the impact, during early times, the droplet experiences shape oscillations. The centre of the disk is considered locally flat, with the centrifugal force nearly tangential to the surface of the disk. The centrifugal force, which is the dominant factor of spreading, drags the fluid outwards. As the fluid begins to rise up the curved surface, the centrifugal force adopts a component normal to the surface of the disk, increasing as the tangential component decreases. Similarly to the flat disk, the spreading is divided in two different areas, the film and the ring. As the front propagates, perturbations develop near the contact line. The perturbations evolve into fingering instabilities at the front and spiral waves at the free surface of the film.

This chapter attempts to address a number of questions regarding the effect of the curvature of the disk to the spreading pattern and the onset of instabilities. One important component is that the centrifugal force, normal to the disk, might suppress the formation of fingers, thus extend the axisymmetric spreading. Another important characteristic is the component of gravity tangential to the main direction of flow, delaying the spreading and the normal component working along with the component of the centrifugal force normal to the disk.

The changing curvature of the disk surface made the light attenuation obtained by the camera inadequate for the range of experiments explored in the flat disk. Thus, the measurements in this chapter focus on the spreading pattern and the onset of the contact line instabilities for a range of rotation rates and heights of release. Having already detailed results for the same characteristics on a flat disk, a comparison is made with the hemispherical disk.

5.1 Basic spreading characteristics

In this section we analyse the basic characteristics of axisymmetric droplet spreading in a hemispherical disk. The number of experiments and the variety of parameters made it necessary to establish a base case experiment to which all the other experiments would be compared.

The base case is chosen in order to represent a typical spreading pattern, satisfying specific requirements: (a) the inertia from the free fall should be minimised, (b) the rotation rate should be high enough to achieve axisymmetric spreading but low enough to be captured in detail by the camera and (c) the droplet volume should be sufficient for all the instabilities to be developed. The droplet volume is fixed at 80 μl. In this section we set the foundations for the determination of parameters for the base case.

5.1.1 Transient stage

As the centre of the hemispherical disk is considered locally flat, the shape oscillations after the impact are similar to the flat disk. Thus, the radial evolution during the transient stage can be described by the analysis in section 4.1.1.2. The time dependence retrieved from equation 4.23 is compared to the experimental results during the early times of spreading.

5.1.2 Axisymmetric spreading

First we explore the lower limit of rotation rates, under which a droplet of 80 μl, lands at the centre of an initially stationary hemispherical disk and spreads out as a single rivulet. The disk is set into rotation, which increases from 50 rpm with a step of 10 rpm every 30 s. The droplet breaks into a single rivulet only above 500 rpm. The observation is very similar to the flat disk, where the droplet breaks at approximately at 340 rpm. The deviation is related to the curvature of the hemispherical disk that reduces the magnitude of the centrifugal force and enhances the influence of gravity. For a free falling droplet, onto an already rotating disk, the break into a single rivulet is observed up to 3,000 rpm, as shown in Figure 5.1.

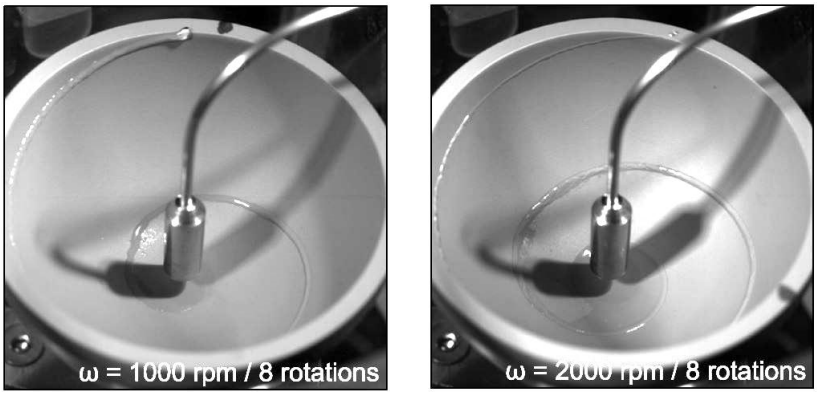

(a) (b)

Figure 5.1: Spreading on axis at (a) 1,000 rpm (480 ms) and (b) 2,000 rpm (240 ms) (cases HB1000H10V80 and HB2000H10V80).

In the single rivulet case, centrifugal force is not strong enough to form an axisymmetric film. As a result, a finger is formed instantly, which guides most of the fluid outwards more rapidly. Small variations in the position of the pipette above the axis of rotation might affect the subsequent behaviour and so pipette movements were avoided between runs. From 5,000 rpm to 8,000 rpm, the spreading is axisymmetric, with the duration of spreading being slower than on a flat disk, indicating that the reduction of the centrifugal force in combination with gravitational forces are crucial components. The critical arc length, L_c, is defined similarly to r_c as the arc length after which the contact line becomes unstable. The value of L_c is very similar at 5,000 and 6,000 rpm and decreases at 7,000 rpm, as illustrated in Figure 5.2, indicating that maximum axisymmetric spreading occurs between 5,000 rpm and 7,000 rpm. Thus, for the hemispherical disk, the base case is set at 6,000 rpm.

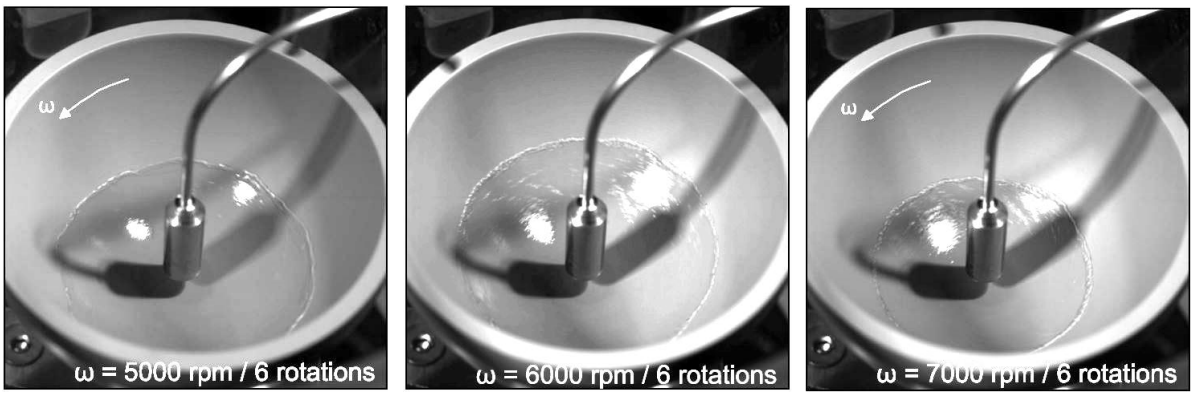

(a) (b) (c)

Figure 5.2: Critical arc length in axisymmetric spreading, on a curved disk, at (a) 5,000 rpm (L_c = 28.4 mm − 72 ms), (b) 6,000 rpm (L_c = 29.4 mm − 60 ms) and (c) 7,000 rpm (L_c = 22.6 mm − 51 ms) (cases HB5000H10V80, HB6000H10V80 and HB7000H10V80).

The unstable contact line is defined as the circumference of the spreading which is 10% or more, deviated from a perfect circle. To determine an error for these measurements, we consider the representation of the rim of the disk in the images. From the images captured by the camera looking vertically down, the rim should be represented by approximately 2 pixels. In reality, the camera is defocusing in that area and the rim of the disk is blurred out, represented by 4 pixels. Hence we set the error to be ±2 pixels, i.e. all measurements have an error of ±0.16 mm.

The evolution of the film follows the same pattern up to 10,000 rpm, with L_c decreasing as ω increases. Above 8,000 rpm, as shown in Figure 5.3, perturbations start earlier. In contrast with the flat disk, where fingers cannot develop and are caught back up by the flow, on the hemispherical disk fingers form at all rotation rates.

5.2 Base case

The base case is a droplet of 80 μl, released 10 mm above the painted brass hemispherical disk, which rotates at 6,000 rpm (HB6000H10V80). The droplet spreads axisymmetrically outwards and once the front reaches L_c, perturbations are visible near the contact line. The film length evolution is measured using edge detection, with measurements starting once the droplet is

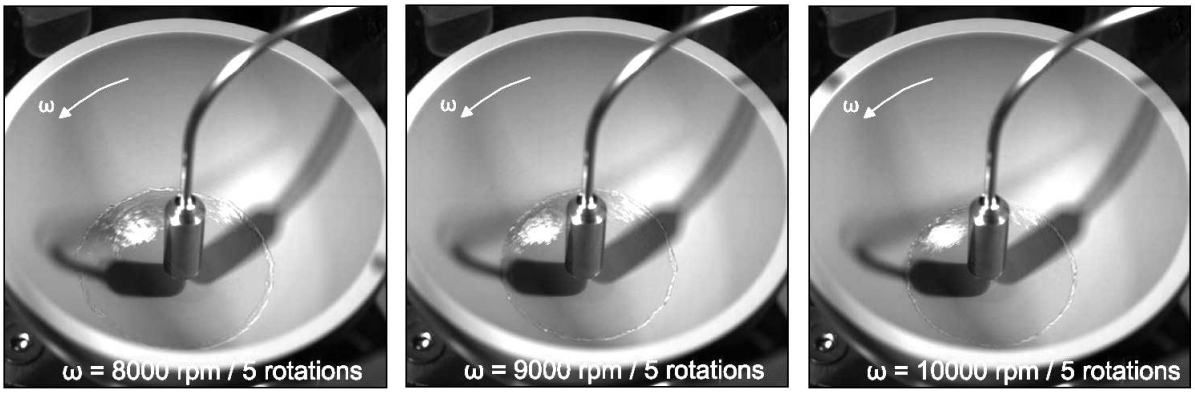

(a) (b) (c)

Figure 5.3: Critical arc length in axisymmetric spreading, on a curved disk, at (a) 8,000 rpm ($L_c = 20.7$ mm $-$ 38 ms), (b) 9,000 rpm ($L_c = 19.9$ mm $-$ 33 ms) and (c) 10,000 rpm ($L_c = 19.5$ mm $-$ 30 ms) (cases HB8000H10V80, HB9000H10V80 and HB10000H10V80).

outside the perimeter of the pipette. The different stages of the spreading pattern are shown in Figure 5.4.

After the transient stage, the fluid is expelled by centrifugal force and climbs the curved walls forming a thin film. The spreading is divided in two areas, the film and the ring. The value of L_c is increased, in comparison to r_c in the flat disk, as the instability at the contact line is delayed.

The delayed instability is due to centrifugal and gravitational forces normal to the main direction of the flow, which suppress the capillary pressure gradients within the ring. At the same time, the tangential component of gravity has a direction that works against the main direction of the flow, delaying the formation of the ring and reducing the volume gathered in the ring. When the contact line becomes unstable, fingers develop and unfold retrograde to the rotation of the disk. The deflection of the fingers is significant, making Coriolis force an important component of the fingering instability analysis.

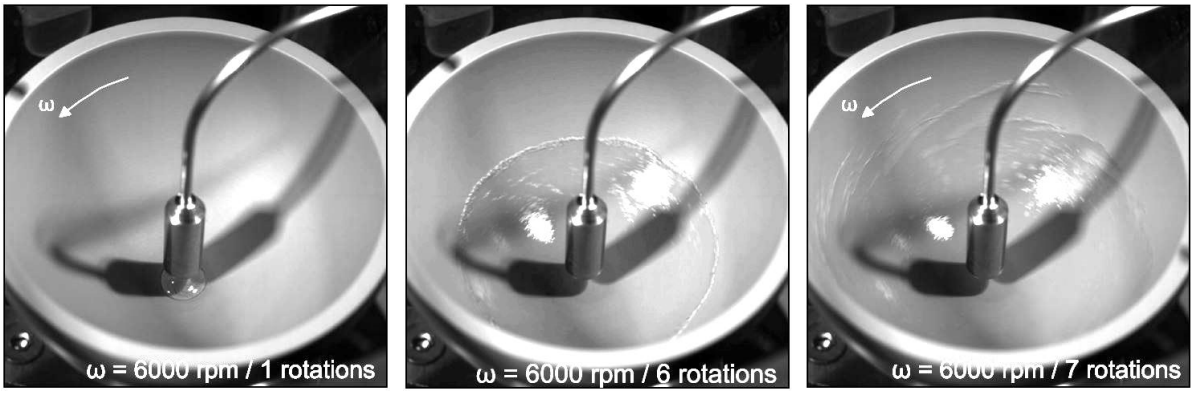

(a) 10 ms (b) 60 ms (c) 70 ms

Figure 5.4: Axisymmetric spreading stages, on a hemispherical disk, at 6,000 rpm. (a) The film is initially uniform while (b) the ring forms later near the contact line where capillary pressure gradients lead to (c) fingering instabilities (case HB6000H10V80).

5.2.1 Film evolution

The time dependence of the evolution of the arc length L with time was explored, following the methodology in the flat disk. The evolution of L was determined by measuring the coordinate $r = R\sin\theta$ and then calculating the arc length as $L = \theta R$. It should be noted that for $0 < \theta < \frac{\pi}{2}$, we could not provide good measurements towards the upper limit of angles due to the curved surface and the defocusing of the camera. The arc length evolution for the base case and a comparison with the equivalent radius evolution on the flat brass disk is shown in Figure 4.8.

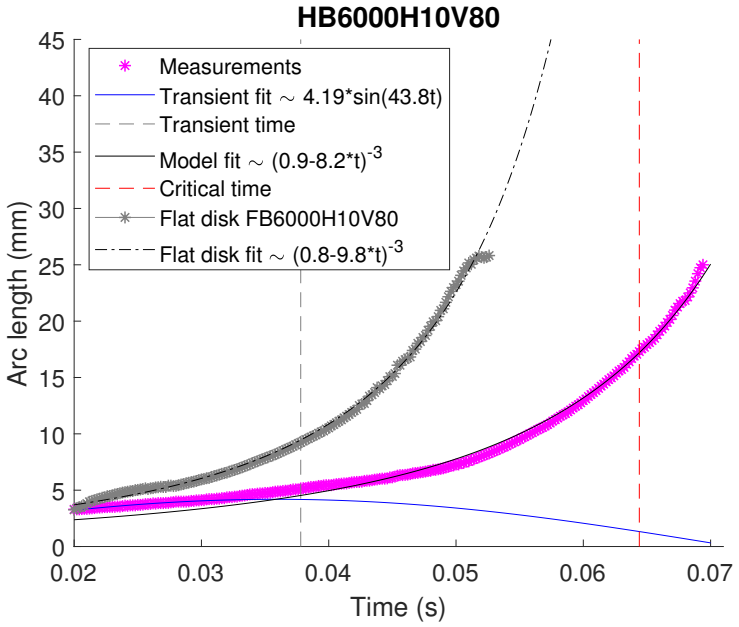

Figure 5.5: Example of film length evolution for the base case HB6000H10V80. The spreading is characterised at early times by the transient stage (up to the grey dashed line). When centrifugal force dominates the flow, the radius depends on time as $L \sim (C_0 - C_\omega t)^{-3}$. At the third stage (beyond red dashed line), the contact line becomes unstable and the data are more scattered. The flat disk is presented as a comparison of the radius evolution due to the geometry of the tube.

There are three visible stages of spreading, as in the flat disk base case. The first part shows the effect of the inertia of the landing at the early times of spreading, which is affected mostly by the height of the release (kinetic energy before the impact), volume, viscosity and the way capillary waves travel along the liquid body. The pattern is in good agreement with the time dependence determined in section 5.1.1 (blue line). The second stage is observed right after the transient stage, when centrifugal force dominates the flow (area between the grey and the red dashed lines). The time of transition between the first two stages is defined by a change of slope in the spreading pattern, separated by a dashed grey line. The red dashed line represents the critical arc length (L_c). The capillary pressure gradient around the ring creates the conditions for the formation of fingers. The scattered data in the measurements towards the rim of the disk is another indication of the unstable contact line.

Overall, the evolution of the radius is slower compared to the evolution on the flat disk, with the maximum delay observed between the two dashed lines. The slower spreading is due to the component of the centrifugal force in the direction of the flow which is reduced compared to the flat disk and the tangential component of the gravitational force parallel and opposite to

the main direction of the flow, as shown in Figure 5.6. The fit follows the same pattern as in the flat disk experiment, $L \sim (C_0 - C_\omega t)^{-3}$, indicated as a black line. The RMS deviation is 0.42 mm, slightly increased compared to the flat disk RMS deviation at 0.32 mm. A mathematical model correlated to the best fitted line is analysed in the next section.

5.2.2 Mathematics of film spreading

As explained in section 5.2.1, the Nusselt film approximation, which assumes uniform thickness, is not in good agreement with the experimental results, and a new mathematical approximation is required. As with the flat disk, we find that the expression

$$L \sim \frac{1}{(C_0 - C_\omega t)^3} \rightarrow u_\theta \sim L^{4/3}, \tag{5.1}$$

is a good fit to the experimental results, Here $L \sim R\theta_r$ is the arc length of the film, R is the radius of the hemispherical disk and θ_r is the polar angle forming from the axis of rotation until the edge of the ring, as shown in Figure 5.6.

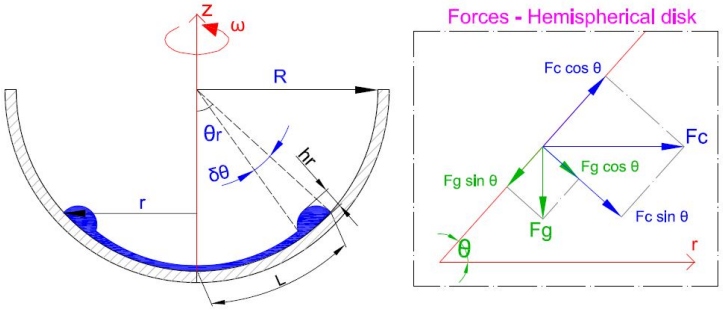

Figure 5.6: Coordinate system in the hemispherical disk, using spherical polar coordinates. The forces applied on the hemispherical disk are analysed as on an inclined plane, where F_c is the centrifugal force and F_g is the force of gravity. The direction of Coriolis force is normal to the plane r–z to the paper and consequently not visible in this sketch.

In order to define the variables C_0 and C_ω, consider, as on the flat disk, a ring growing in semi–toroidal ring shape, which propagates outwards. For $r \sim R\sin\theta_r$, and assuming that most of the liquid is gathered in the ring and that V is constant, provided that $Lh_r^2 \gg L^2 h_f$, the volume becomes

$$V \sim \pi^2(r - h_r)h_r^2 \rightarrow dV = \pi^2 R \sin\theta_r h_r^2 d\theta,$$

Provided that the ring thickness is much smaller than the arc length, $h_r \ll L$, then the h_r scales as

$$h_r \sim h_0 \left(\frac{L}{r_0}\right)^p, \tag{5.2}$$

where r_0 and h_0 are the initial radius and the initial thickness of the film immediately after the impact and p is a parameter that will be defined by the scaling. The expression is chosen so that when $L = r_0$, $h_r = h_0$ and h_r increases as L increases. Ignoring contact line dynamics and using equation 5.2, the net tangential centrifugal force acting on the ring is

$$F_c = \pi^2 \int_{(\theta_r - \delta\theta)}^{\theta_r} \rho\omega^2 h_r^2 R^2 \sin\theta\cos\theta d\theta \sim \pi^2 \rho\omega^2 h_r^2 R^2 \delta\theta \sin\theta_r \cos\theta_r. \tag{5.3}$$

Viscous drag at a point, using the Nusselt film approximation of a parabolic profile for the velocity $\hat{u}_\theta \sim z^2$, is

$$\tau = \mu \frac{\partial \hat{u}_\theta}{\partial z},$$

which at the solid surface $z = 0$, scales as

$$\tau_0 = \mu \frac{u_\theta}{h_r}.$$

Replacing h_r with equation 5.2 and integrating over L, the net viscous force becomes

$$F_\nu = 2\pi \int_{(\theta_r - \delta\theta)}^{\theta_r} \tau_0 R^2 \sin\theta d\theta \sim -\pi\mu \frac{u_\theta}{h_r} R^2 \delta\theta \sin\theta_r. \tag{5.4}$$

The tangential component of gravity is

$$F_g = \pi^2 \int_{(\theta_r - \delta\theta)}^{\theta_r} \rho g h_r R^2 \sin^2\theta d\theta \sim -\pi^2 \rho g h_r^2 R \delta\theta \sin^2\theta_r. \tag{5.5}$$

The forces F_c, F_ν and F_g were determined by using Taylor's expansions and linearising over $\delta\theta$. So balancing the forces $F_c \sim F_\nu + F_g$, as expressed in equations 5.3, 5.4 and 5.5, we get the velocity in the main direction of the flow

$$u_\theta = (\omega^2 \cos\theta_r - g \sin\theta_r) \frac{h_0^3}{\nu r_0^{3p}} L^{3p}.$$

Making use of the experimental result so that $u_\theta \sim L^{4/3}$, then

$$3p = \frac{4}{3} \rightarrow p = \frac{4}{9},$$

and the velocity becomes

$$u_\theta = (\omega^2 \cos\theta_r - g \sin\theta_r) \frac{h_0^3}{\nu r_0^{4/3}} L^{4/3}. \tag{5.6}$$

The first term on the right hand-side of equation 5.6 is of higher order and includes the tangential centrifugal component, the main force responsible for the initiation of motion. Therefore, the second term can be ignored if $\omega^2 \cos\theta_r \gg g \sin\theta_r$. Then the arc length evolution can be defined as

$$\frac{d\theta}{dt} = \frac{\omega^2 \cos\theta}{\nu} \frac{h_0^3}{r_0^{4/3}} (R\theta)^{4/3} \rightarrow \frac{\nu r_0^{4/3}}{\omega^2 R^{4/3} h_0^3} \int_0^{\theta_r} \frac{1}{\theta^{4/3} \cos\theta} d\theta = \int_0^t dt + c. \tag{5.7}$$

If θ is small, then $\cos\theta \sim 1$, and the integral is simplified to

$$\frac{\nu r_0^{4/3}}{\omega^2 R^{4/3} h_0^3} \int_0^{\theta_r} \frac{1}{\theta^{4/3}} d\theta = \int_0^t dt + c. \tag{5.8}$$

To explore the validity of this approximation we consider the evolution of the arc length with θ for the equations 5.7 and 5.8, as shown in Figure 5.7. The approximation is in good agreement with the actual arc length evolution up to an angle $\sim 45°$, corresponding to an arc length of 17.7 mm, which is approximately the limit beyond which contact–line instability develops.

Thus for the arc length evolution, $L \sim R\theta_r$, we consider

$$-\frac{\nu r_0^{4/3}}{\omega^2 R^{4/3} h_0^3} \frac{1}{\theta_r^{1/3}} = t + c \rightarrow -\frac{\nu r_0^{4/3}}{\omega^2 R h_0^3} \frac{1}{L^{1/3}} = t + c$$

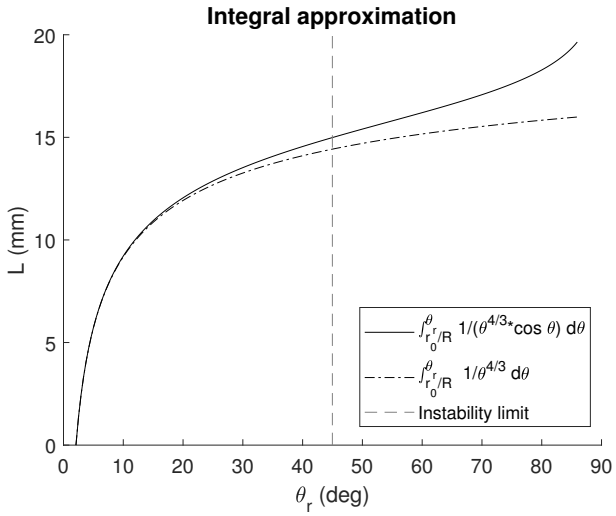

Figure 5.7: Integral approximation for the arc length evolution with θ. The simplified approximation is good agreement with the arc length evolution up to the instability limit.

and using the boundary condition at $t = 0 \rightarrow L = r_0$,

$$c = -\frac{r_0 \nu}{\omega^2 h_0^3}.$$

The model suggests that the arc length evolution scales as

$$L = \frac{1}{\left(C_0 - \frac{\omega^2}{\nu}\frac{h_0^3}{r_0^{4/3}}t\right)^3},$$

with $C_0 = r_0^{-1/3}$, or

$$\frac{L}{r_0} = \frac{1}{(1 - C_\omega t)^3}, \tag{5.9}$$

where

$$C_\omega = \frac{\omega^2}{\nu}\frac{h_0^3}{r_0}.$$

The final approximation uses the same scaling as in the flat disk model (equation 4.31). The centrifugal force is reduced as $\cos\theta$ increases, hence we expect C_ω to be reduced in the hemispherical disk. This implication has already been expressed in Figure 5.5. Although the force of gravity and contact line effects are not included in the calculations, it was shown in the previous section that a model of the form $L \sim (C_0 - C_\omega t)^{-3}$ is a good fit for the total duration of spreading. To verify the scaling, we test the model for variations in rotation rate (section 5.3) and heights of release (section 5.4). The coefficient C_ω, which is descriptive of the flow characteristics, will be treated as the main parameter of investigation and therefore will be used for comparisons between sets of experiments. The singularity at

$$t = \frac{\nu}{\omega^2}\frac{r_0}{h_0^3},$$

leading to $L \rightarrow \infty$, is not possible in our case as the disk is limited by the internal radius and more importantly contact–line instabilities will evolve before that limit.

5.3 Rotation rate variations

One of the most important parameter of investigation is the angular velocity of the disk as it is strongly coupled with the spreading time and the onset of instabilities. Given that axisymmetric spreading starts at 5,000 rpm, the range of rotations under investigation, for the hemispherical disk, is between 5,000 and 10,000 rpm. The evolution of L for the set HB-H10V80 with respect to angular velocity is shown in Figure 5.8a. The raw data show that the transient stage is more prominent at lower rotation rates, i.e. at 5,000 rpm, while the duration of the stage decreases as ω increases. The onset of instabilities, i.e. the value of L_c (indicated by the black continuous line), decreases with increased ω.

The non–dimensional arc length $\frac{L}{r_0}$, in Figure 5.8b, shows the correlation of the experimental results to the model, discussed in section 5.2.2 and determined in equation 5.9. The RMS deviation is 0.77 and slightly increased compared to the flat disk RMS deviation at 0.47. The red line represents the relevant fit on the flat disk.

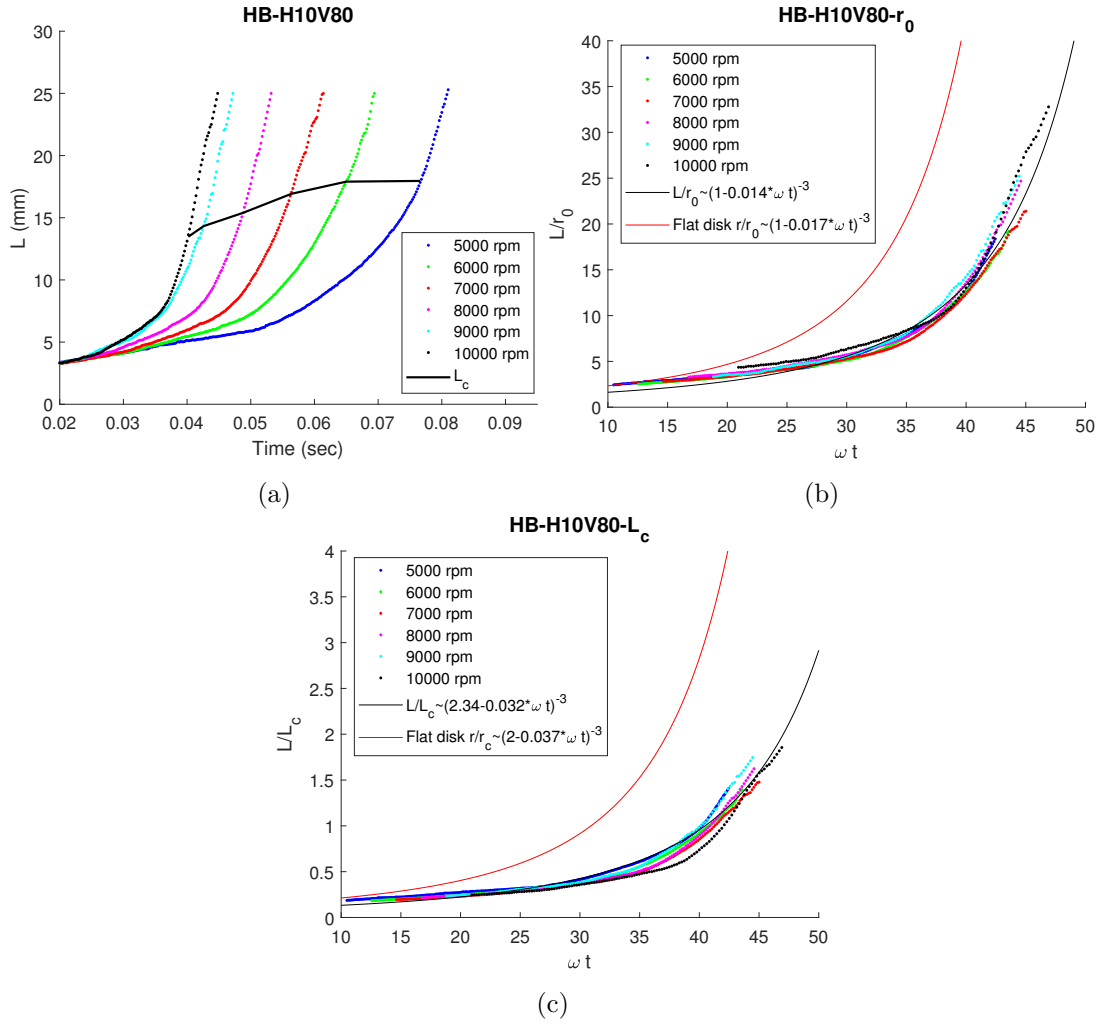

Figure 5.8: a) Evolution of L for a range of rotation rates (5,000 - 10,000 rpm) - set FB-H10V80. (b) Correlation of L with the model predictions normalised with r_0. (c) Evolution of L normalised with L_c.

In order to correlate the fit with the model approximation we Consider water with $\nu = 1.004 \times 10^{-6}$ m^{2}s^{-1} and r_0 of $\mathcal{O}(10^{-3})$ m. The scaling of h_0 can be obtained, from 5,000 to

10,000 rpm, as

$$\frac{\omega^2 h_0^3}{\nu r_0} t = 0.014\omega t \rightarrow h_0 \sim 0.014 r_0^{\frac{1}{3}} \left(\frac{\nu}{\omega}\right)^{\frac{1}{3}}.$$

This length scale is reduced compared to the von Kármán layer thickness $\sim \left(\frac{\nu}{\omega}\right)^{1/2}$, and could be considered as a representative length scale of the initial thickness that is set into rotation immediately after landing. Assuming that r_0 has small variations for different ω and ν is constant, then h_0 varies with $\omega^{-\frac{1}{3}}$, resulting to decrease in h_0 with ω. Although measurements of the thickness of the rotating liquid at early times is not possible we will proceed under the condition that this is a realistic scaling for h_0 and test for the model's compatibility with the experimental results. Thus, although this approximation is descriptive of the arc length evolution, further modelling is required to give consistent results for disks of different geometries.

In addition, the plot in Figure 5.8c, introduces a new non–dimensional variable $\frac{L}{L_c}$ and shows the correlation to the experimental results, with the RMS deviation at 0.13 and slightly increased compares to the flat disk RMS deviation at 0.09. Considering that the ratio $\frac{L}{r_0} \sim \mathcal{O}(10)$, both fits are in good agreement with the experimental results, with the difference in deviations being very small.

The deviations determined for the non–dimensional plots in the hemispherical disk are slightly larger than the deviation on the flat disk. Although the scaling is descriptive of the spreading rate, the role of gravity and the reduced centrifugal force in the direction of the flow could be important factors. Another model could be more appropriate and could constitute future work in this area of research.

5.4 Height of release

The height of release affects the transient stage, the spreading at early times and the onset of fingering instabilities on the flat disk. The effect of the height of release, H, is investigated in the hemispherical disk, for heights of release at 5, 10 and 15 mm (sets HB-H5V80, HB-H10V80 and HB-H15V80 respectively). A comparison of the base case HB6000H10V80 with the spreading for the experiments HB6000H05V80 and HB6000H15V80 is shown in Figure 5.9.

For a height of release at 5 mm above the centre of the disk, the droplet lands smoothly and shape oscillations are reduced, as shown in Figure 5.9a. However, as explained in section 4.1.1, this is the only case of non-free falling droplets, with reduced liquid volume in each discharge, thus a small variation in the spreading pattern could be expected. When the droplet is released 10 mm above the centre of the disk, the experiment is essentially the base case, analysed in detail in section 5.2. The droplet touches the rotating disk at the instance of detachment from the pipette. Hence the free fall is minimised, with the end of the transient stage indicated as a dashed grey line. The transient stage is more prominent when the droplet is released 15 mm above the centre of the disk, shown in Figure 5.9c. For comparison, the RMS deviation of the fit in HB6000H10V80 is 0.45 mm, while in the flat disk 0.42 mm. The RMS deviation for the case HB6000H5V80 is 0.49 mm, while for the case FB6000H15V80 is 0.62 mm. The oscillations at the transient stage, are observed at all angular velocities and for increased height of release. However, as the rotation rate increases, the influence of the early time oscillations is minimised as the centrifugal force acts faster on the liquid, thus the liquid is set faster into rotation. For

completeness, the experimental results, for the sets HB-H5V80, HB-H10V80, HB-H15V80, in the form of graphs are shown in the Appendix B.

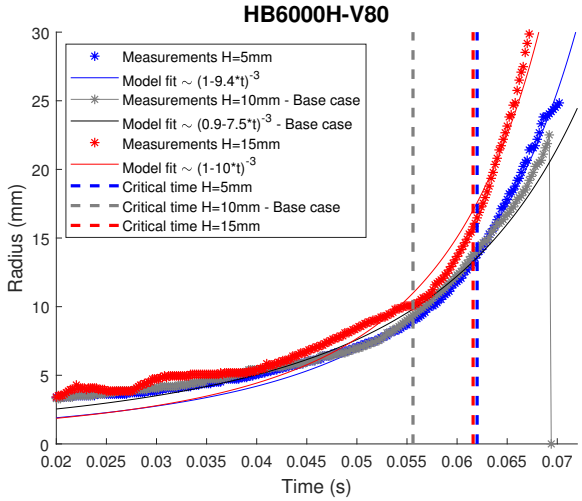

Figure 5.9: Examples of L evolution on a hemispherical disk rotating at 6,000 rpm, for heights of release at 5, 10 and 15 mm (cases HB6000H05V80, HB6000H10V80 and HB6000H15V80 respectively). The spreading is characterised at early times by the transient stage (up to the grey dashed line). When centrifugal force dominates the flow, the arc length depends on time as $L \sim (C_0 - C_\omega t)^{-3}$. At the third stage (beyond red dashed line), the contact line becomes unstable and the data are more scattered.

The spreading in all cases follows the pattern of the base case, which can be represented by a non–dimensional plot and in accordance with the model in section 5.2.2, for all heights of release and for all the rotation rates that allow axisymmetric spreading ($>$ 5,000 rpm), as shown in Figure 5.10a.

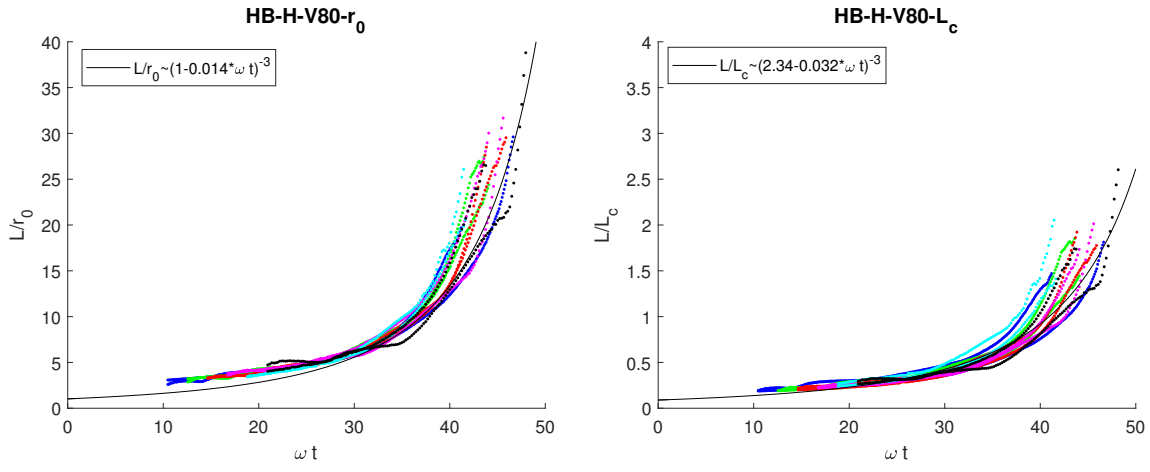

(a) (b)

Figure 5.10: (a) Correlation of L with the model predictions normalised with r_0 and (b) evolution of L normalised with L_c, for the sets HB-H5V80, HB-H10V80 and HB-H15V80.

The effect of H is indirectly related to the model, by incorporating in C_ω the values of the initial radius and thickness after the impact, r_0 and h_0 respectively. The experimental results are in good agreement with the model's time dependence, with the RMS deviation at 2.76, indicating that the landing oscillations have significant effect to the main spreading rate.

For comparison, the RMS deviation in the flat disk is 1.12. Also, the non–dimensional plot in Figure 5.10b shows a similar pattern related to L_c, which is even more deviated from the base case fit with the RMS deviation at 0.51. The RMS deviation in the flat disk is 0.16. This deviation indicates, as in the flat disk case, that the height of release has an impact in the onset of instabilities.

In order to visualise this effect of H to the onset of the contact–line instability, L_c and t_c were plotted for the three sets, as indicated in Figure 5.11a and Figure 5.11b respectively. As a general observation, when the rotation rate is increased the contact line becomes unstable faster, thus L_c and t_c are decreased. Secondly, when the height of release is decreased, L_c is increased while t_c is decreased. The data for $H = 5$ mm are more scattered and as explained in section 4.1.1, the released volume is slightly reduced, thus this set of experiment might not give a representative pattern for the onset of instabilities. In contrast to the flat disk, the deviation between the fitted lines for L_c, is almost constant for different H, while for t_c the fitted lines almost coincident. These observations would require validation through additional sets of experiments for various heights of release.

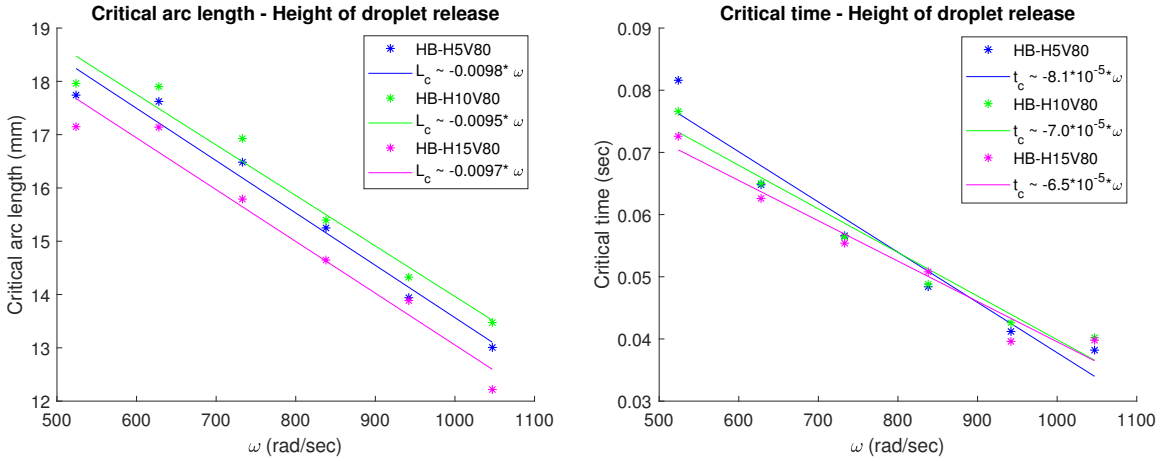

(a) (b)

Figure 5.11: Onset of (a) critical arc length L_c and (b) critical time t_c for the sets HB-H5V80, HB-H10V80 and HB-H15V80 respectively.

5.5 Instabilities/Spiral waves

So far we have described the spreading pattern until the contact line becomes unstable, once the front reaches L_c. Beyond L_c, two instabilities develop, similar to the flat disk. The first instability is at the contact line and grows into the formation of fingers. The fingers unfold in a direction opposite to the disk rotation (retrograde fingers). The second instability starts at the intersection between the film and the ring. As the ring moves beyond L_c, spiral waves form within the film area. The waves are visible from L_c and outwards ($L \geq L_c$) and eventually disappear as they are dissipated within the film. The spiral waves unfold in the same direction with the disk rotation (prograde spirals). Thus, the fingers and the spirals fold in opposite directions, as shown in Figure 5.12.

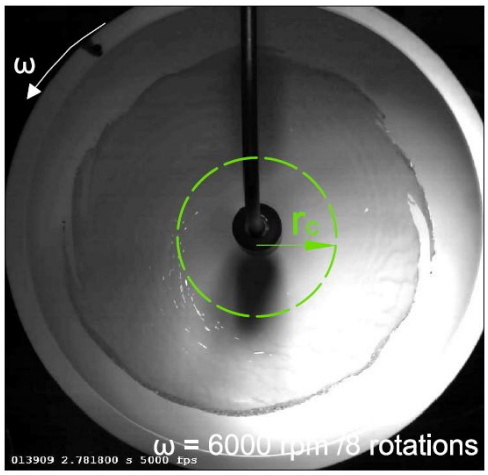

Figure 5.12: Spreading on axis for the base case HB6000H10V80 (80 ms). The disk rotates anticlockwise. The fingers beyond the contact line unfold in opposite direction to the rotation of the disk (retrograde fingers). The spiral waves in the film unfold in the direction of the disk rotation (prograde spirals).

In the hemispherical disk, and in contrast to the flat disk, the contact–line instability leads to distinct fingers that are not caught back up by the main flow. According to the scaling of Fraysse & Honsy, 1994, analysed in the section 2.2.3, the number of fingers for the Nusselt film approximations beyond 5,000 rpm, is expected to be approximately 50 fingers. In reality, there are approximately 10 fingers and as the spreading evolves smaller fingers develop between the already developed fingers. Thus, the role of the curvature altering the direction and the magnitude of centrifugal and gravitational forces should be investigated further with respect to fingering instability.

We will also see, in chapter 6, that there is no contact–line instability leading to fingers in the VFD. One of the reasons for the lack of fingering in the VFD is the fact that the radius of the tube is 10 mm while the radius of the hemispherical disk is 27.5 mm. The centrifugal force in the VFD, which scales as $\rho\omega^2 R$, is reduced in magnitude compared to the centrifugal force at the walls of the hemispherical disk. Therefore further investigation at this point would be irrelevant to the main aim of the project which is the optimisation of the VFD. However the fingering instability in the VFD would be an important factor when considering scaling up the device. A tube with radius close to the one of the hemispherical disk would probably cause the formation of fingers and would require a separate research project.

On the other hand, retrograde spiral waves have been documented in boundary layer instabilities for rotating films, as mentioned in section 2.2.4. However, we see no evidence of retrograde spirals but instead we observe prograde spirals. The spirals follow a similar pattern as in the flat disk and were analysed in detail in section 4.6. The stationary light sources in combination with the changing curvature of the hemispherical disk caused constantly changing light reflections. Several alterations in the set–up were attempted in order to achieve an attenuation pattern that would allow measurements. Unfortunately, the reflections in the recordings were inadequate for image processing. Therefore the presence of the two instabilities is acknowledged but further investigation is required with respect to experimental methods and image processing. However, it should be noted that the spirals seem to have similar wavelength and angle to the spirals on the flat disk.

5.6 Other consideration

5.6.1 Off–axis spreading

Another set of experiments investigates the spreading pattern when the droplet lands away from the axis of rotation. The pipette is positioned 10 mm away from the axis and 10 mm above the rotating disk. The experiment is conducted from 1,000 rpm to 9,000 rpm for the set HB-H10V80OFF10. The motion in the hemispherical disk, of a droplet landing off axis, is similar to the motion on a flat disk. The bottom of the droplet is carried away by the rotating disk while the remaining droplet moves slightly radially and azimuthally. The radial and azimuthal displacement is obvious in Figure 5.13. At 1,000 rpm, the droplet lands and spreads azimuthally with the the main bulk of the droplet being slightly deviated as a single finger from the circumference of the film after one revolution.

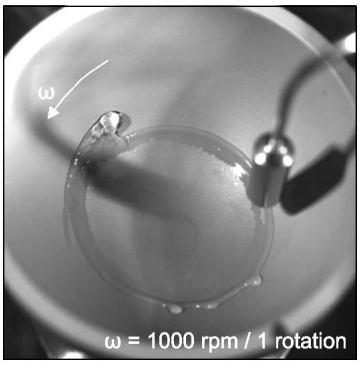

Figure 5.13: Spreading after landing off axis, on a hemispherical disk, at 1,000 rpm (60 ms) (case HB1000H10V80OFF10).

From 2,000 rpm to 10,000 rpm the angular velocity is high enough so that one rotation period after the droplet touches the disk, the film returns to the point of the release and mixes with the droplet. The main body of the droplet, which is still at the area of the landing, moves radially towards the centre of the disk due to gravity. Despite the fact that centrifugal force is reduced and the influence of gravity is significant, allowing a downwards motion of the liquid, the centre of the disk remains dry, as shown in Figure 5.14.

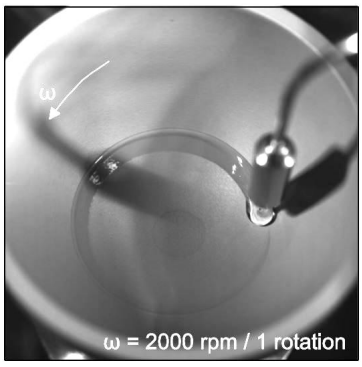

(a) 30 ms

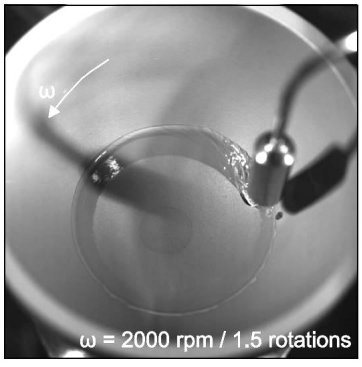

(b) 45 ms

Figure 5.14: Spreading after landing off axis, on a hemispherical disk, at 2,000 rpm (case HB2000H10V80OFF10).

The duration of spreading varies significantly for different rotation rates. Another indicative example is shown in Figure 5.15, where after 6 revolutions at 8,000 rpm, the remaining droplet is still draining into the film with the main bulk positioned slightly deviated from the point of landing.

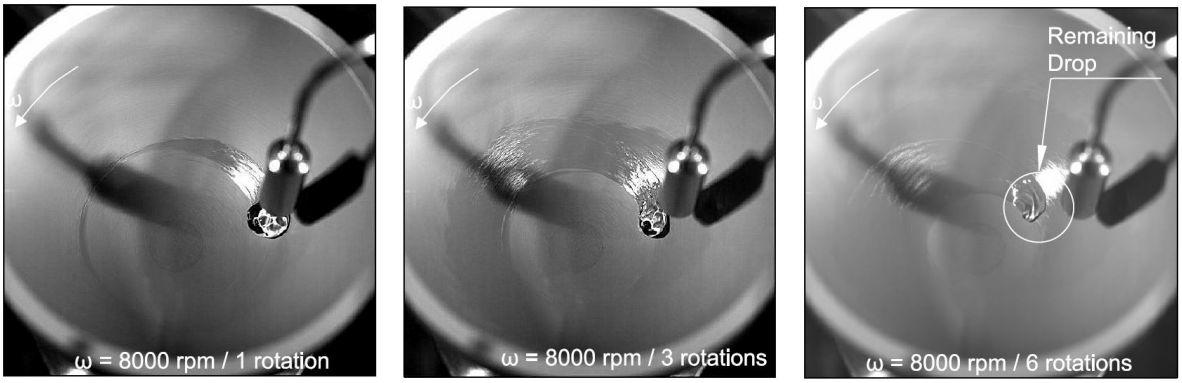

(a) 7.5 ms (b) 22.5 ms (c) 45 ms

Figure 5.15: Spreading after landing off axis, on a hemispherical disk, at 8,000 rpm (case HB8000H10V80OFF10).

The effect of the air boundary layer, the initiation of instabilities, the rate of the droplet drainage, the thickness of the film and the fingers are mechanisms that worth further investigation. Whether these phenomena affect chemical reactions in spinning disks is unclear. As the VFD presents optimum performance when the device is tilted, the droplets in CF land at the walls of the tube and not at the axis of rotation. The off–axis landing in the curved disk is very similar to the landing of droplets in CF at the walls of the VFD. As we will see in chapter 6, the glass tube in the VFD, in combination with the already coated area, minimise the surface tension effects and no fingering phenomena are observed for an off–axis landing.

5.6.2 Tilted disk

The case of droplets falling on an inclined hemispherical disk, over a range of rotation rates, inclination angles and droplet landing points is explored. We shall however restrict our attention to a single inclination angle of 45°, that illustrates the dominant effects of the spreading. Also, it has been reported that this is the inclination at which the VFD works best and possible correlations to the VFD film formation could be useful. A representative example at 8,000 rpm, for a droplet of 80 μl, is analysed to explain the film formation onto the inclined hemispherical disk. This experiment is chosen as it is representative of all the interesting dynamics of spreading in the set HB-T45V80A10. Each of the images shows the first three revolutions after the droplet contacts the disk.

First, the aim is to understand whether the spreading is axisymmetric for a droplet landing at the centre of the disk. In order to achieve centred landing, the pipette is displaced considerably above the axis of rotation, as shown in Figure 5.16. Due to the inclination, the axis is not the lowest point in the hemisphere, consequently the droplet after the first contact continues to run down the hemisphere, while the fluid is stripped off the bottom of the droplet. This stripping of the bottom occurs at a gradually increasing radius, leading to the development of a wide film. Initially the droplet migrates radially outwards (downwards) faster than the film, thus the

droplet continues to interact with a dry boundary. The remnant of the droplet is still clearly visible at the lower edge of the growing film. Eventually the growing film catches up with the droplet and the outer edge of the film has already gone unstable forming fingers, as seen on the flat disk. However, the instability occurs at a slightly larger radius. Spiral waves appear, which are marginally visible in the Figure 5.16c. They are very similar to the spirals observed in the axisymmetric spreading on a flat disk. However, the curvature of the disk changes the light attenuation captured by the camera and does not allow proper measurements of the spiral angle.

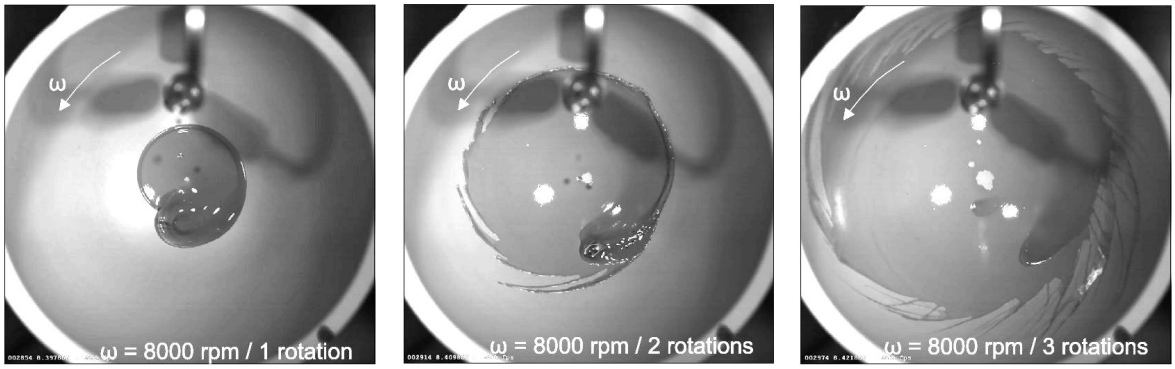

(a) 7.5 ms (b) 15 ms (c) 22.5 ms

Figure 5.16: Droplet landing nearly on axis and followed by a downwards motion due to gravity (case HB8000T45V80A10).

For a pipette positioned on the axis, the droplet lands off the axis, as shown in Figure 5.17. The bulk of the droplet continues its downward movement, corresponding to a radial outward displacement comparable with the droplet diameter. The dynamics are similar to the first case, but the film overtakes the droplet at an earlier stage. However, with the landing of the droplet is occurring at larger radius, the velocity difference between the droplet and the surface is greater, and so the film stripped off is potentially thinner. During the next 2 revolutions the film area is significantly increased forming an azimuthally almost axisymmetric film. The area covered by the film in the two cases is similar, but the distribution looks somewhat different with the inner edge of the annular region that has been wet starting to dry out. The image after one revolution shows that the film is much thinner than in the first case.

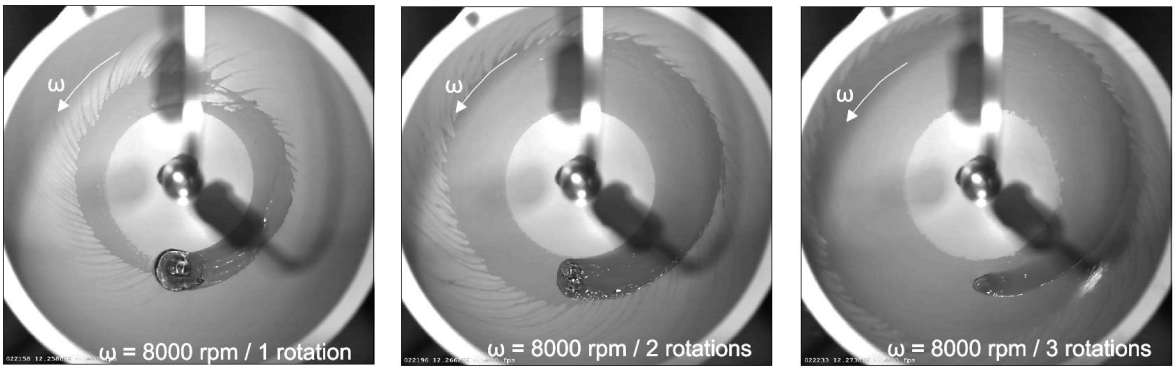

(a) 7.5 ms (b) 15 ms (c) 22.5 ms

Figure 5.17: Droplet landing below the axis, with reduced downwards motion due to the disk curvature (case HB8000T45V80ON).

When the droplet lands at a radius greater than the lowest point in the hemisphere, there is an inward migration of the droplet, as shown in Figure 5.18. However, far more important is the much greater relative velocity between the surface and the droplet. Specifically, the air in contact with the hemisphere is moving very rapidly and acts as a cushion for the droplet, causing it to 'bounce' rather than stick to the surface. Consequently, the pattern of wetting is very different and three rotations after first contact, as shown in Figure 5.18c, the disk remains dry over part of its circumference, even though in other parts the film has gone unstable. The precise pattern of wetting is likely to depend in part on potential resonances between the droplet and the surface, resonances driven by capillary waves changing the shape of the droplet. Both the thinner layer and the bouncing mean that the droplet volume is drained out on a slower rate.

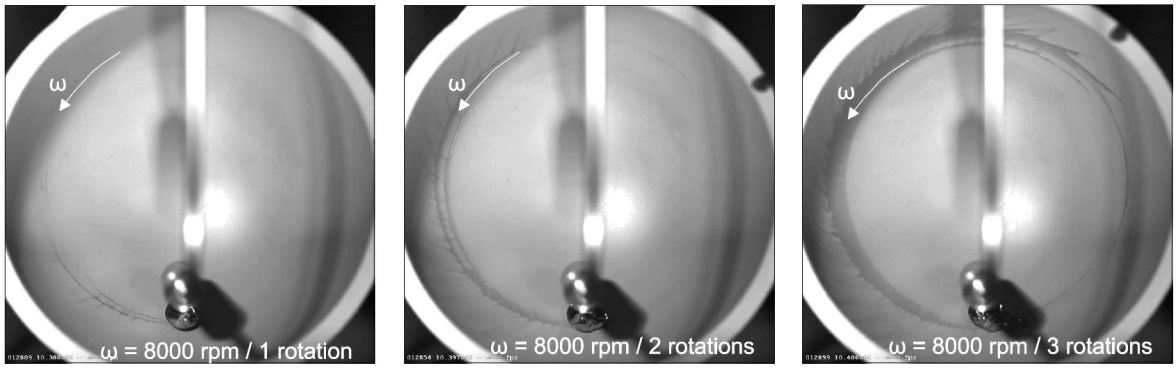

(a) 7.5 ms (b) 15 ms (c) 22.5 ms

Figure 5.18: Droplet landing close to the rim of the disk (case H8000T45V80B10),

Between the three landing points there are qualitative differences in the droplet behaviour. These are three characteristic behaviours that could be met in CF in the VFD. The fluid behaviour that produces the best results, from the chemical perspective is unclear, but the 'bouncing' introduces a possible resonance mechanism. Whether this pattern has implications in the chemical reactions is unclear. From a fluid mechanics perspective, similar experiments were conducted in the VFD and are presented in the next chapter.

5.7 Summary

This chapter explores the fluid motion caused by single droplets landing on an already rotating hemispherical disk. The hemispherical disk is used to understand (a) the effect of the disk geometry to the spreading pattern in comparison to the flat disk and (b) the fluid motion at the hemispherical base of the VFD.

The experiments investigate the dynamics of droplet landing, the film development and the presence of instabilities at the contact line and along the free surface of the film. One of the most prominent observations is that the evolution of the radius is slower than in the flat disk and the onset of the instability is delayed. The delayed instability is due to the components of the centrifugal and the gravitational forces normal to the solid surface, which suppress the capillary pressure gradients within the ring, in combination with the tangential component of gravity, which delays the formation of the ring.

The droplet is released from a pipette at a specific height over the disk, falls under the force of gravity and lands on the already rotating substrate. Immediately after landing, the von Kármán layer forms where centrifugal force, which is the dominant factor of spreading, drags the fluid outwards. The droplet is divided in two different areas, the film and the ring. The ring forms very early and it was assumed, as in the flat disk, that it is fed with liquid by the film.

Beyond L_c, perturbations at the contact line lead to fingering instability, with the fingers unfolding retrograde to the rotation of the disk. In parallel, spiral waves appear at the free surface of the film. The spiral waves form from L_c and outwards and unfold prograde to the rotation of the disk. The spirals seem to have similar wavelength to the spirals observed on the flat disk experiments. Due to the changing curvature, light attenuation restricts the experimental measurements. However, the similarities to the observations on the flat disks allow the qualitative description of the spreading pattern even when measurements on the hemispherical disk are not feasible. Further developments in the experimental set–up could give an insight to the wavelength of the spirals.

The rate of spreading is described by a mathematical approximation, $L \sim (C_0 - C_\omega t)^{-3}$, very similarly to the flat disk and focusing mostly to the growth of the ring. Although the mathematical approximation is a good fit to the experimental results, future development of the model should incorporate the role of gravity, contact line dynamics and the finger development.

The rotation rate and the height of release are the parameters of variation that alter the spreading time and the onset of instabilities. Increasing the rotation rate leads to faster spreading and decreased L_c. Experiments altering the height of the release indicate that shape oscillations during the transient stage not only affect the initiation of droplet spreading but have a long lasting effect that is reflected in the value of L_c. Volume variations could provide further information regarding the volume distribution between the ring and the film, indicating the importance of curvature to the onset of instabilities. The correlation of the rotation rate and the height of release to the onset of contact line instabilities is indicated by the experimental determination of L_c and t_c, as shown in Table 5.1.

Table 5.1: Onset of contact line instabilities

Parameter	L_c	t_c
$\omega \uparrow$	$\downarrow$	$\downarrow$
$H \uparrow$	$\downarrow$	$\uparrow$

However, we shall see in the next chapter that there is no relevant fingering instability in the VFD. One of the reasons for the lack of fingering in the VFD is the fact that the centrifugal force, which scales as $\rho\omega^2 R$, is decreased in the VFD, due to the smaller internal tube radius. Fingering instabilities could be relevant to the VFD when considering the scaling up of the device. A tube with radius close to the hemispherical disk would probably cause the formation of fingers.

When the droplet is released off-axis the bottom of the droplet is dragged by the rotating surface while the rest of the volume is still landing. The film in rotation is immediately exposed to greater centrifugal force and fingers form at the contact line. The fingers allow the fluid to move outwards faster, which could reduce the processing time and be a disadvantage for a potential chemical reaction. However the drainage of the droplet during the landing could lead

to increased shearing within the film. In order to be more conclusive on the benefits of the off-axis landing, the rate of drainage at the interface with the disk should be investigated further in correlation to shearing in the film.

Whether the spreading before or after the onset of instabilities is more beneficial for the chemical reactions is unclear. After establishing the spreading rate and the instabilities observed for single droplets on a flat and a hemispherical disk we move to investigate the fluid motion in the VFD. In the next chapter, the pattern of spreading is investigated in the VFD both in CM and in CF.

Chapter 6

The Vortex Fluidic Device

This chapter explores the formation of thin films in the VFD. The stages of film formation define the important parameters of investigation. In confined mode (CM), the liquid is initially stationary at the bottom of the tube. Once the VFD is set into rotation, the moving substrate drags the liquid which is consequently set in motion. The fluid climbs the walls forming a thin film, and eventually reaches a steady state of rotation.

Under continuous flow (CF), the droplet is released from a pipette, fixed on the axis of rotation at a specific height in the tube. The droplet falls under the force of gravity and lands on the already rotating substrate. The bottom of the droplet is dragged out of the bulk by the rotating substrate forming azimuthally a thin film. After the spreading of the first droplet, each droplet lands on an already rotating thin film, is absorbed by the film, increasing the total length, thickness and volume of the film.

The chapter is structured according to two discrete areas of investigation, the steady state of a fully developed film and the time-dependent spin-up. The VFD experiments in CM focus on the time-dependent spin-up velocity of an initially stationary liquid and on the total length and film thickness at the steady state of processing. In CF, the focus is on a sequence of droplets that fall on an already developed thin film. The results indicate the shape, length and thickness of the film, and the reaction rate in the device.

The Raston group (Flinders University, Adelaide, Australia) finds that the performance of the VFD is optimised when the tube is inclined at an angle $\beta = 45°$, at approximately 7,000 to 8,000 rpm, both in CM and in CF. As we shall see in section 6.3.1, the shape of the film is largely controlled by the radial component of the centrifugal force and the axial component of gravity, which is captured by the dimensionless parameter, broadly used in this chapter, $C_M = \frac{\omega^2 R}{g \sin \beta}$, where R is the internal radius of the tube. The leading order implication of C_M is that the film has a paraboloidal shape.

The thickness of the thin film is a very critical parameter for the hydrodynamic conditions, defining the chemical reaction with respect to enhanced diffusion and advection in the device. A thinner film could achieve more uniform distribution of reactants, which could be beneficial for the performance of the chemical reaction.

The technique of neutron imaging is used for the measurement of film thickness at steady state. The neutron imaging experiments were conducted in collaboration with the Raston group. The film thickness experiments were conducted using the facility at the Australian Nuclear

Science and Technology Organisation in Sydney, Australia. The reaction experiments were initiated while visiting the Raston laboratory in Adelaide, Australia and continued in the GK Batchelor laboratory at the University of Cambridge.

6.1 Base case

The base case is an experiment in CM, of 1 ml of water placed initially in a stationary tube. The tube is tilted at 45°, and the rotation rate is set at 5,000 rpm. The tube is set into rotation and with motor acceleration at 203 rad/s^2, reaches 5,000 rpm at approximately 2 s. The experiment is conducted both for the glass tube (CM45GT5000W1) and the quartz tube (CM45QT5000W1). When the tube is set into rotation, the fluid climbs the walls, forms a thin film and eventually reaches a steady state. Pictures of the film at steady state are shown for the GT in Figure 6.1a and for the QT in Figure 6.1b. Measurements of the film development focus on the evolution of the leading edge of the film, referred to as the 'film front'. The film front measurements start once the fluid is outside of the aluminium hub of the lower bearing, along the axis indicated in red in Figure 6.1. The film front is measured in the azimuthal direction from a sequence of frames, using the high–speed camera, recording at 500 fps. For example, at 5,000 rpm, 6 frames are captured by the camera over one rotation and equal number of lengths are measured for the film front, both for the GT and the QT. The error of the measurements is defined by considering the tangential projection of the tube edge, represented by 5 pixels, thus the error is ±0.28 mm.

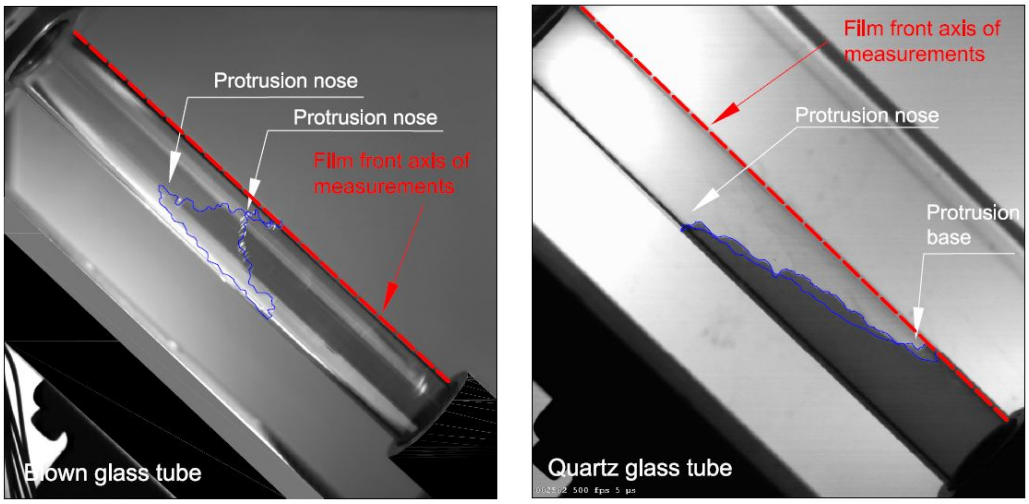

(a) (b)

Figure 6.1: (a) Film at steady state in the blown glass tube (GT), forming two protrusions. (b) Film at steady state in the fuzzed quartz tube (QT), forming one protrusion - cases CM45GT5000W1 and CM45QT5000W1 respectively.

The results for the film front evolution are shown in Figure 6.2a for the glass tube (GT) and in Figure 6.1b for the quartz tube (QT). The liquid reaches a steady state in less than 1 s. The film front does not progress uniformly, hence the plot shows both the minimum (black line) and the maximum (blue line) edge of the film front, during the spin-up and at steady state. Initially, for 0.3 s, in both tubes the fluid rises almost linearly with time $L \sim t$, where L is the length of the film. However, the motor increases the angular velocity of the tube for approximately 2 s. Thus, the linear spin–up although relevant to the film spin–up in section 6.4, is more correlated

to the acceleration of the motor. Immediately after this initial stage, protrusions start forming and keep growing for almost 1 s. The deviation from a linear spin-up is increasing and the oscillating values of the film front measurements are due to the development of the protrusions. The periodicity in the measurements, presented in the zoomed plot, in the GT is due to the formation of two protrusions almost opposite to each other, while there is only one protrusion in the QT.

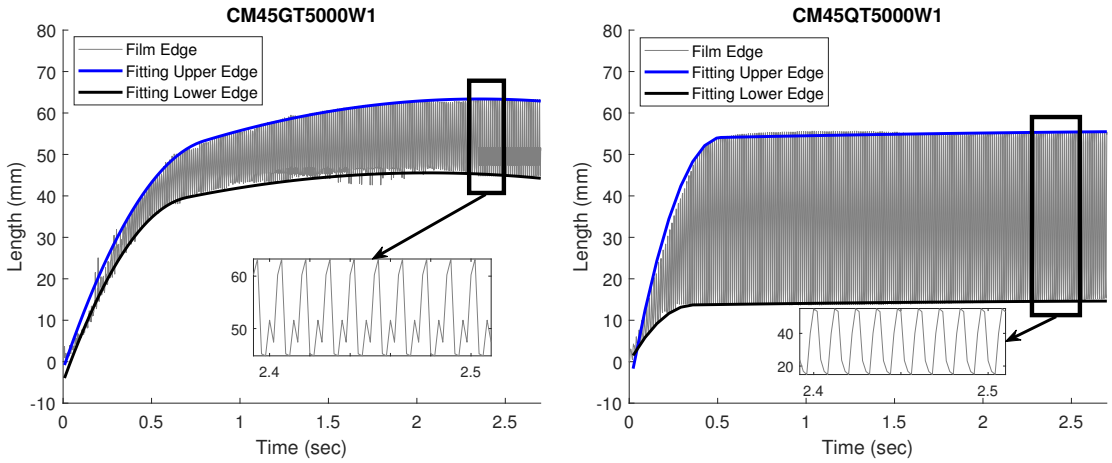

(a) (b)

Figure 6.2: Evolution of 1 ml of water film, developing in a tube rotating at 5,000 rpm tilted at 45°. This is the base case experiment and was conducted both (a) in the blown glass tube (GT) and (b) in the fuzzed quartz tube (QT) - cases CM45GT5000W1 and CM45QT5000W1 respectively. The periodicity of the film front measurements at steady state indicated the formation of two protrusions in the GT and one protrusion in the QT.

Once the protrusions reach their maximum length, the film is at steady state. The protrusions are fully developed, approximately after 1 s and the recording is stopped after 3 s. Then 2 min later, a new recording is obtained, the film front is measured again and is found at the same protrusion length as 3 s after the spin-up. The protrusion formation alters the film thickness locally in the tube and might be a significant factor for the chemical processing and therefore comparable chemistry experiments should be conducted with the same tube.

The formation of protrusions could be caused by fluid mechanics instabilities or due to tube imperfections. The position of the protrusions in opposite sides, in the GT, could indicate a contact–line instability, with the most unstable wavelength scaling as πR. However, the azimuthal position of the two protrusions is the same for different realisations of the experiment, pointing to the possibility of tube imperfections, such as eccentricity. The hypothesis of tube imperfections is explored by examining the tube for elliptical parts.

6.2 Tube imperfections

Each tube develops the same pattern of protrusions in the same azimuthal locations for different realisations. The tubes are tested for possible deviations from a circular internal radius, under the hypothesis that the unique geometric imperfections of each tube could cause protrusions in the film. The two tubes, used for all the experiments reported in this thesis, develop different

protrusion pattern, thus both tubes are examined for eccentricity. The test explores whether the tubes have a curved shape along the z axis or they develop internally cross–sectional shapes that are not circular. The measurements are compared to the film formation recorded by the high–speed camera. The high–speed camera recording indicates two protrusions azimuthally opposite to each other in the GT and a single protrusion in the QT, as shown in Figure 6.1.

In both tubes, protrusions form above 2,000 rpm with the distance between the base and the tip of the protrusion increasing with increased rotation rates. In order to compare the protrusions with possible imperfections in the tube, a Dial Test Indicator is used. The aim is the measurement of the internal radius of the tube. The nose of the Indicator is placed initially, from the top, 35 mm inside the tube, as indicated in Figure 6.3a. Given that the nose of the Indicator cannot reach internally lower parts of the tube, measurements are taken externally at 4 positions along the tube. A specific azimuthal position is pitched as zero along the tube. At every position, 4 measurement are taken azimuthally, as indicated in Figure 6.3b.

The imperfections measured internally at the top of the tubes verify the hypothesis of geometric ellipticity for the GT and eccentricity for the QT. The internal measurement matches all the external measurements. For the QT, there is a maximum outward deviation of 0.17 mm, consistent along the length of the tube, at the side where the protrusion is developed. For the GT, there are two larger sides opposite to each other, forming the major axis of an elliptical cross–section, with maximum deviation from a circular cross–section of 0.15 mm, corresponding to the two protrusions. The results of the measurements are shown in Figure 6.3c and the correlation with the protrusions in the film are denoted by colour red.

The tubes are mounted on the device via two pairs of O rings at the base and at the top of the device. If the O rings were not aligned, there would be consistent measurements of deviation towards one side for both tubes. Thus the protrusions' alignment would be consistent with the eccentric hub. However the protrusions are developed at the same sides of the tubes even for random phasing between the hub and the tubes. Also the curvature of the upper end of the tube makes the measurements for possible tube curvature against a flat surface impossible. Given that the protrusions form along the sides where we measure the radial deviations, we conclude that the internal circumference of the GT is ellipsoidal, while the QT, with only one side deviated, is eccentric.

This test verifies the hypothesis that the protrusions are correlated to the imperfection of the tube. Once the fluid reaches the ellipsoidal (GT) or the eccentric circumference (QT), the potential energy, along the circumference of the free surface is constant, while along the circumference of the surface of the tube it is not constant. Under the assumption of constant volume, the protrusion keeps growing until the fluid reaches a new energy equilibrium, minimising $E_g + E_c$. Given that $\omega^2 R \gg g$, the film is very sensitive to axisymmetry, i.e. even minor variations in the shape of the tube could alter the wet area. Although there have been no explicit tests, from a chemistry point of view, the imperfection of the tube could affect the performance of the chemical reaction. An extended protrusion could mean reduced processing time and restriction of the film area. The film thickness, taking into consideration of the protrusions, is analysed further in section 6.3.5.

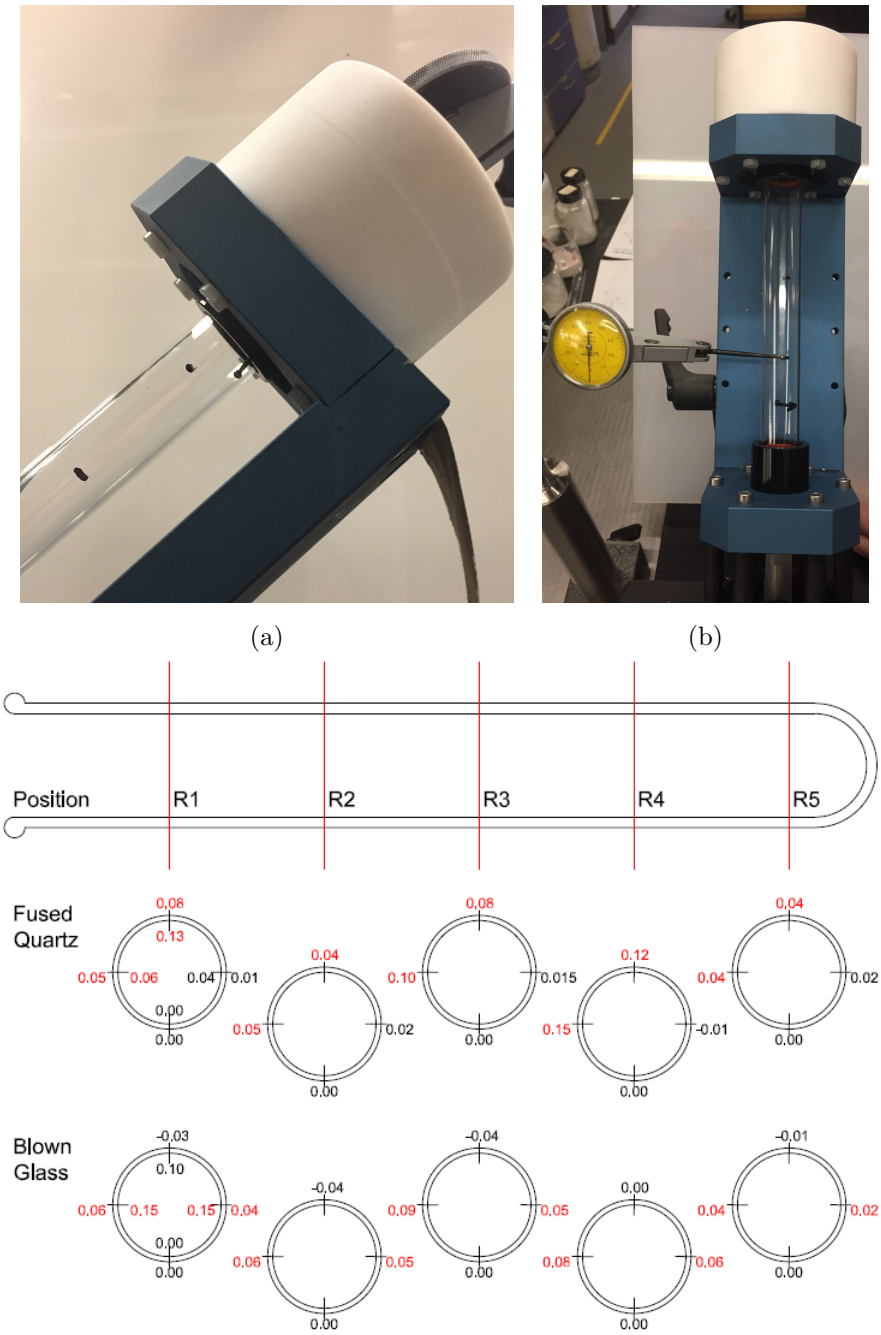

Figure 6.3: Dial Test Indicator set-up, taking (a) the internal measurement where the nose of the Indicator is visible and placed as far as possible in the tube and (b) the external measurements in 4 different positions along the tube. (c) The measured deviations from a circular shape showes that the QT is eccentric - forming one protrusion and the GT has ellipsoidal shape - forming two protrusions. The measured imperfections are in accordance with the observations from the high-speed camera recordings.

6.3 Steady state

Most of the processing time in the VFD happens when the film is at steady state. The film thickness at steady state defines the hydrodynamic environment of the chemical reaction, indicating whether the film moves within the boundary layer under conditions of laminar flow. In order to determine the film thickness, we first derive the shape of the film at stead state.

Consider a finite volume of liquid at steady state, rotating in an inclined VFD. The fluctuating gravitational force, in the rotating frame, could cause a weak motion in the azimuthal direction. Due to the fixed position of the protrusions, observed in the experiments, the motion in the azimuthal direction is relatively small. Especially above the base of the protrusions, the azimuthal velocity must be very small, as the protrusions maintain their shape at all times. Therefore the shape of the film is approximated as if the film is in solid body rotation. Using the simplification of solid body rotation, the shape of the film can be determined, correlating the thickness and the length of the film. A range of rotation rates and inclination angles is tested to determine the experimental values of the film length L. The predicted film shape is compared to the results of the film length and the neutron imaging experiments.

6.3.1 Film shape

A fully developed thin Newtonian incompressible liquid film, of density ρ, is predominantly rotating in its equilibrium shape of solid body rotation in a tube of internal radius R, spinning around its axis, with angular velocity ω. The shape of the free surface of the film $Z_s(r, \phi, z_0)$, of thickness $h(\phi, z)$, is assumed paraboloidal, subject to a fixed volume of liquid V. This model is referred to as the 'shape model'. A rotating cylindrical coordinate system, (r, ϕ, z), is introduced to formulate the mathematical model describing the dynamics of the film bounded by the free surface at $r = R - h$ and the underlying solid substrate at $r = R$. We also assume that the thickness of the film vanishes at the contact line, i.e. $h = 0$ at $Z_s = L_{max}$. As the base of the tube contains a small portion of liquid at steady state, for this approximation we assume a flat base, as shown in Figure 6.4, where z_0 is the intersection between the parabola Z_s and the z axis. Evaporation, condensation and mechanical vibrations are considered negligible. The volume of liquid is fixed so that

$$V = \iiint dV = \int_0^{2\pi} \int_{r_b(\phi)}^{R} \int_0^{Z_s} r dz dr d\phi.$$

The shape profile of the film can be determined by the Potential Energy (PE), ignoring surface energy and assuming a flat base, as

$$PE = E_g + E_c.$$

For a vertically positioned tube, as shown in Figure 6.4, E_g is defined as

$$E_g \sim \int \int \int \rho g z dV.$$

Thus the gravity potential energy is expressed as

$$E_g = \int_0^{2\pi} \int_{r_b}^{R} \rho g \frac{Z_s^2}{2} r dr d\phi.$$

Similarly, E_c is

$$E_c \sim -\int\int\int \frac{1}{2}\rho\omega^2 r^2 dV$$

$$E_c = -\frac{1}{2}\rho\omega^2 \int_0^{2\pi}\int_{r_b}^{R}\int_0^{Z_s} r^3 dz dr d\phi$$

$$E_c = -\frac{1}{2}\rho\omega^2 \int_0^{2\pi}\int_{r_b}^{R} r^3 Z_s dr d\phi,$$

where r_b is a the distance between the z axis and the free surface of the film at the base of the tube where $Z_s = 0$.

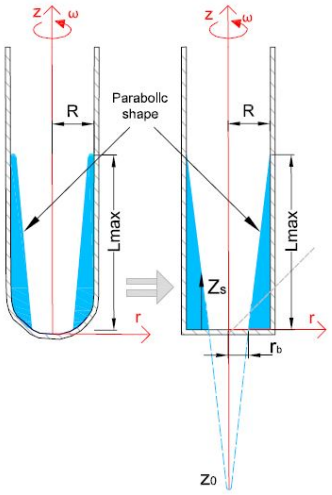

Figure 6.4: Sketch representing the main parameters defining the film shape in a vertically rotating tube.

If the surface of the film does not correspond to a surface of constant PE, then the total PE of the volume is going to be greater than the minimum. Thus, the excess of PE is converted to motion enabling the film to adjust to a new equilibrium as the excess energy is dissipated. At steady state, PE is minimised thus $\frac{\partial PE}{\partial S} = 0$. For

$$PE = \int_0^{2\pi}\int_{r_b}^{R}\left(\rho g\frac{Z_s^2}{2} - \frac{1}{2}\rho\omega^2 r^2 Z_s\right) r dr d\phi,$$

the shape Z_s can be determined as

$$Z_s = \frac{1}{2}\frac{\omega^2}{g}r^2 + z_0, \tag{6.1}$$

Considering the base of the tube, where $Z_s = 0$ and a thin film developed at the walls where $z_0 < 0$, the expression of r_b can be obtained as

$$r_b = \sqrt{\frac{-2z_0 g}{\omega^2}}.$$

Then volume conservation can be expressed as

$$V = 2\pi\int_{r_b}^{R} Z_s r dr d\phi = \pi\left[\frac{\omega^2}{2g}\frac{R^4 - r_b^4}{2} + z_0(R^2 - r_b^2)\right]$$

and

$$z_0 = -\frac{\omega^2 R^2}{2g} + \sqrt{\frac{\omega^2 V}{\pi g}}. \tag{6.2}$$

Thus by replacing equation 6.2 to equation 6.1 we get

$$Z_s = \frac{1}{2}\frac{\omega^2}{g}r^2 + -\frac{\omega^2 R^2}{2g} + \sqrt{\frac{\omega^2 V}{\pi g}}. \tag{6.3}$$

By setting the film length $Z_s = L_{max}$ equal to the length of the tube and $r = R$, the volume capacity of the tube can be determined, using equation 6.6 as

$$V \sim \frac{\pi g L_{max}^2}{\omega^2}. \tag{6.4}$$

If the aim is the development of a film at the walls of the tube, i.e. $z_0 < 0$, then

$$\frac{\omega^2 R}{g} > \frac{V}{R^3}, \tag{6.5}$$

setting the limit for thin film formation with an almost dry tube base. We proceed using the same approach to define the film shape in an inclined tube, as shown in Figure 6.5.

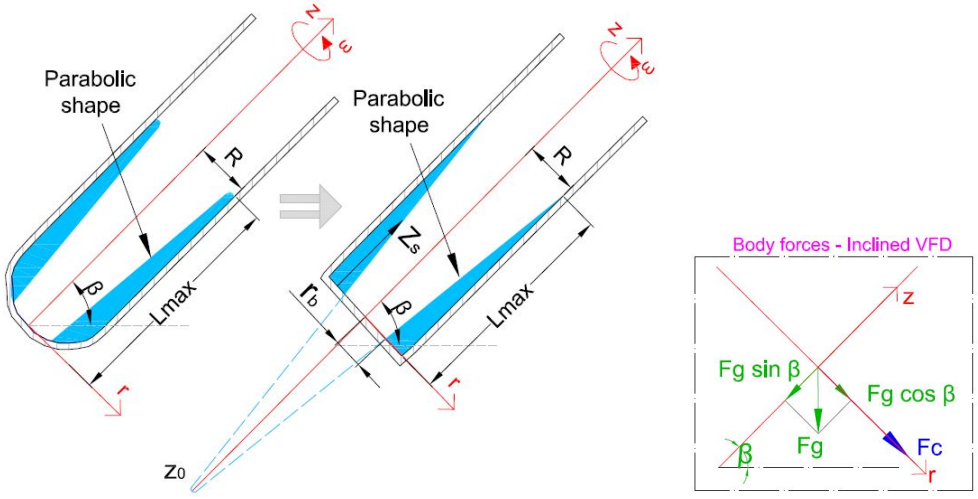

(a) (b)

Figure 6.5: Sketch representing the main parameters defining the film shape in an inclined rotating tube.

When the axis of the tube is inclined by an angle β from the horizontal axis, E_g is defined as

$$E_g \sim \int\int\int \rho g(z\sin\beta - r\cos\phi\cos\beta)dV.$$

Thus the gravity potential energy is expressed as

$$E_g = \int_0^{2\pi}\int_{r_b(\phi)}^{R} \rho g\left(\frac{Z_s^2}{2}\sin\beta - rZ_s\cos\phi\cos\beta\right)rdrd\phi.$$

Similarly, E_c is

$$E_c \sim -\int\int\int \frac{1}{2}\rho\omega^2 r^2 dV$$

$$E_c = -\frac{1}{2}\rho\omega^2\int_0^{2\pi}\int_{r_i(\phi)}^{R}\int_0^{Z_s} r^3 dzdrd\phi$$

$$E_c = -\frac{1}{2}\rho\omega^2\int_0^{2\pi}\int_{r_b(\phi)}^{R} r^3 Z_s drd\phi,$$

where r_b is a the distance between the z axis and the free surface of the film at the base of the tube where $Z_s = 0$.

If the surface of the film does not correspond to a surface of constant PE, then the total PE of the volume is going to be greater than the minimum. Thus, the excess of PE is converted to motion enabling the film to adjust to a new equilibrium as the excess energy is dissipated. At steady state, PE is minimised thus $\frac{\partial PE}{\partial S} = 0$. For

$$PE = \int_0^{2\pi} \int_{r_b(\phi)}^{R} \left[\rho g \left(\frac{Z_s^2}{2} \sin\beta - r Z_s \cos\phi \cos\beta \right) - \frac{1}{2} \rho \omega^2 r^2 Z_s \right] r dr d\phi,$$

the shape Z_s can be determined as

$$Z_s = \frac{1}{2} \frac{\omega^2}{g \sin\beta} r^2 + r \cos\phi \cot\beta + z_0, \tag{6.6}$$

Considering the base of the tube, where $Z_s = 0$ and a thin film developed at the walls, the expression of r_b can be obtained as

$$r_b = \frac{-\cos\phi \cot\beta + \sqrt{\cos^2\phi \cot^2\beta - 2 z_0 \frac{\omega^2}{g \sin\beta}}}{\frac{\omega^2}{g \sin\beta}}.$$

Then r_b can be expressed as

$$r_b = -2 z_0 \frac{-C_2 + \left(1 + C_2^2\right)^{1/2}}{C_1}, \tag{6.7}$$

where

$$C_1^2 = -2 \frac{z_0}{R} C_M \text{ and } C_2 = \frac{\cos\phi \cot\beta}{C_1}, \tag{6.8}$$

while C_M is a dimensionless coefficient, which will be later compared to many of the experimental results and is defined as

$$C_M = \frac{\omega^2 R}{g \sin\beta}. \tag{6.9}$$

Volume conservation can be expressed as

$$V = \int_0^{2\pi} \int_{r_i}^{R} Z_s r dr d\phi = \int_0^{2\pi} \left(\frac{\omega^2}{2g \sin\beta} \frac{R^4 - r_i^4}{4} + \cos\phi \cot\beta \frac{R^3 - r_i^3}{3} + z_0 \frac{R^2 - r_b^2}{2} \right) d\phi.$$

For $z_0 < 0$ and $-2 z_0 C_M \gg R$, then $C_1 \gg 1$. If the VFD can be inclined so that $\cot\beta \ll C_M$ then $C_2 \ll 1$. Using the binomial expansion of equation 6.7 and linearising for C_2, we get

$$r_b = \frac{-2 z_0 \left(1 - C_2\right)}{C_1},$$

and V becomes

$$V = \int_0^{2\pi} \left(\frac{-C_1^4 R^4 - 16 z_0^4 + 8 R^2 C_1^2 z_0^2}{16 C_1^2 z_0} + C_2 \frac{-24 z_0^3 + 2 R^3 C_1^3 - 8 z_0^3}{C_1^2} \right) d\phi. \tag{6.10}$$

Since $C_2 \sim \cos\phi$ and assuming symmetric spreading $\int_0^{2\pi} \cos\phi \; d\phi = 0$, then all the terms linear in C_2 vanish. For z_0 being independent of ϕ, we integrate so that

$$V = \pi \frac{-C_1^4 R^4 - 16 z_0^4 + 8 R^2 C_1^2 z_0^2}{8 C_1^2 z_0}.$$

Replacing C_1 with the expression defined in equation 6.8, V becomes

$$V = \frac{\pi R}{4 C_M} \left(4 z_0^2 + 4 R z_0 + C_M^2 R^2 \right). \tag{6.11}$$

For a thin film we consider $z_0 < 0$, so

$$z_0 \sim -\frac{C_M R}{2} + \sqrt{\frac{C_M V}{\pi R}}$$

and for an axisymmetric film, equation 6.6 becomes

$$Z_s \sim \frac{1}{2} C_M \frac{r^2}{R} - \frac{C_M R}{2} + \sqrt{\frac{C_M V}{\pi R}}. \tag{6.12}$$

By setting the film length $S = L_{max}$ equal to the length of the tube and $r = R$, the volume capacity of the tube can be determined, using equation 6.6 as

$$V \sim \frac{\pi L_{max}^2 R}{C_M}. \tag{6.13}$$

If the aim is the development of a film at the walls of the tube, i.e. $z_0 < 0$, then

$$C_M > \frac{V}{R^3}, \tag{6.14}$$

setting the limit for thin film formation with an almost dry tube base.

Both equations 6.13 and 6.14 are compared to the volume capacity experiments in the following section 6.3.4. As the solution is independent of ϕ and $R - r_b \ll R$, the base of the tube can be considered either flat or hemispherical. Keeping ϕ in S, we can also determine an asymmetric film in a flat base tube. Overall, a ϕ independent solution is a good approximation when ω is large, i.e when the condition in equation 6.14 is satisfied.

This simplified approximation could be useful for the scaling of the device, which is repeatedly requested by several industries. It should be noted that the determination of the film shape takes into consideration volume conservation, but ignores surface tension. Although the approximation ignores asymmetries in the azimuthal direction, in the following sections we attempt to test the model by comparing C_M, defined in equation 6.9, with experimental results varying only ω (section 6.3.2) and β (section 6.3.3).

6.3.2 Rotation rate variations

The film front evolution during the spin-up and the length of the film at steady state are investigated, for a fixed volume of liquid, varying only the rotation rates. The experiment is conducted both for the GT (set CM45GT-W1) and the QT (set CM45QT-W1). The film front evolution is shown in Figure 6.6. The continuous lines show the tip of the protrusions and the dashed lines show the base of the protrusions. The lines were generated by the fits following the lower and the upper end of the film front (black and blue lines respectively in the base case - Figure 6.2).

The film front initially propagates linearly and uniformly in both tubes. The time dependence of the film length evolution is related to the motor acceleration (203 rad/s^2), which takes approximately 2 s to reach the predetermined angular velocity ($\sim$ 5,000 to 10,000 rpm). This time is approximately the time required for the film to reach a new equilibrium shape. Thus the slope of the acceleration which seems similar in both tube is related to the acceleration of the motor. Then, as explained in section 6.1, in the GT, two protrusions develop quadratically until they reach a maximum length and the film reaches a steady state. In the QT, only one protrusion forms, with the base of the protrusion forming significantly lower than in the GT.

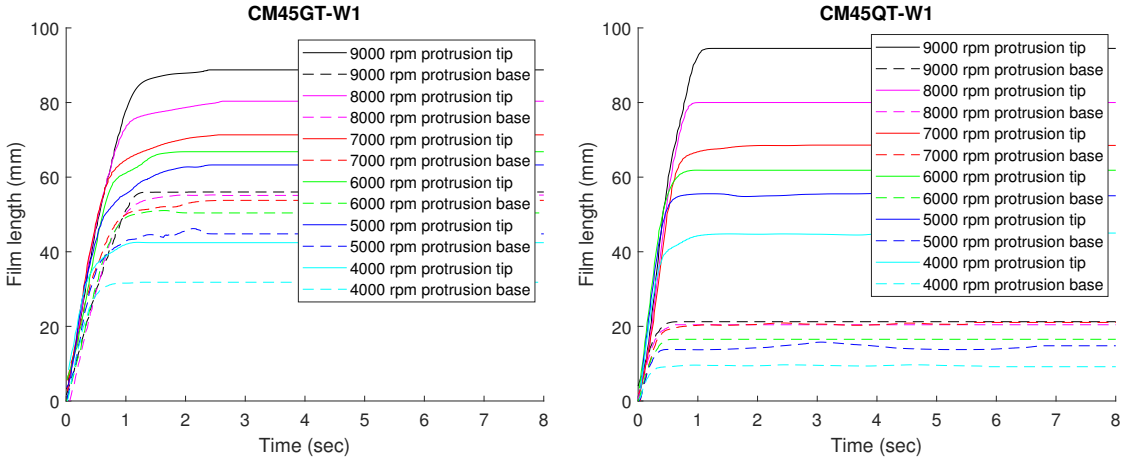

(a) (b)

Figure 6.6: Film evolution of 1 ml of water for a range of rotation rates (4,000 to 9,000 rpm) with (a) the GT (set CM45GT-W1) and (b) the QT (set CM45QT-W1), both inclined at 45°. Overall, the protrusion in the QT is larger in length than the two protrusions in the GT.

The protrusions in each tube, form at the same azimuthal location for different realisations and for all the variations of ω. The centrifugal force scales as $\rho\omega^2 R$ and is the dominant factor for the film development. Thus, even small variations in R alter the film development, due to the imperfections of the tubes. More importantly, at a given length along the z axis, if the PE at the free surface is constant, the PE at the walls varies due to the tube imperfections. Around the areas of increased PE, the total length of the protrusion is increased with increased ω. This correlation is in accordance with the experimental observations both in the GT and in the QT, as shown in Figure 6.6a and 6.6b respectively. For completeness, the experimental results in the form of plots are shown in the Appendix C for the sets CM45GT-W1 and CM45QT-W1.

6.3.3 Tube inclination

The film thickness and the position of the base and the tip of the protrusions are correlated to the inclination of the tube. To investigate the effect of gravity on the film formation, the sets CM45GT-W1 and CM85GT-W1 are compared. The recording follows the development of the film front, until the film reached a steady state. Measurements are taken at the steady state for the lower edge of the film front (i.e. the base of the protrusions), and the upper edge of the film front (i.e. the tip of the protrusion). The results, correlating the non–dimensional maximum length $\frac{R^2 L_{max}}{V}$ with $C_M = \frac{\omega^2 R}{g \sin\beta}$, are presented in Figure 6.7. The normalised L_{max} exhibits a correlation with C_M as predicted by equation 6.13 of the shape model. The shape model is developed for a horizontal tube base and the predictions are valid for large ω, according to the condition in equation 6.14.

The circles and the stars indicate the base and the tip of the protrusion respectively, for an inclination at 45° (blue symbols) and at 85° (pink symbols). The tip of the protrusion is considered as the maximum film length and is used for the correlation of the experimental results to the shape model, represented in the plot by a blue dashed line for $\beta = 45°$ and by a pink dashed line for $\beta = 85°$. Comparing for each tested ω the maximum length for the two

inclinations, we observe that the deviation does not exceed 10 mm (dimansionless 1). Thus, the two fitted lines almost overlap, indicating a good agreement with the film shape model.

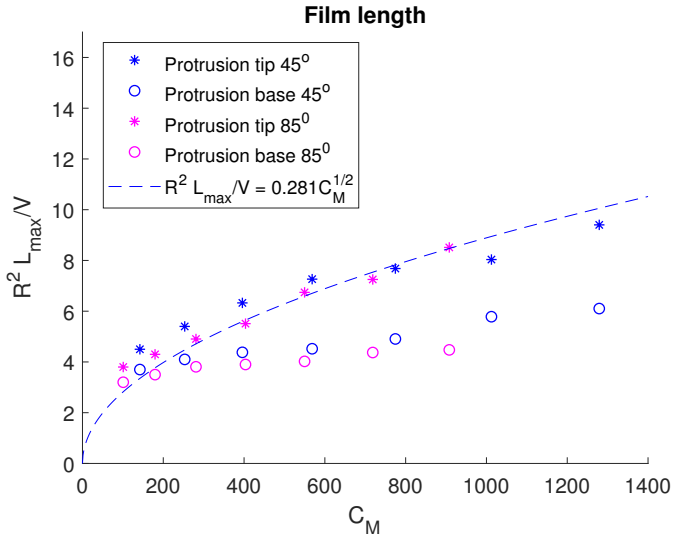

Figure 6.7: Film length and protrusion development at steady state of 1 ml of water, for a range of rotation rates (4,000 to 9,000 rpm) with the GT inclined (a) at 45° (set CM45GT-W1) and (b) at 85° (set CM85GT-W1). The fitted lines represent a correlation between the average length of the film (averaging the base and the tip of the protrusion) with the film shape coefficient $C_M = \frac{\omega^2 R}{g \sin\beta}$.

Between the two inclination angles, the tip of the protrusion is observed further away from the bottom of the tube at an inclination angle of 45°. In general for decreased β, the length of the protrusion increases. For increased β, the gravitational force, that works against the upwards flow, is increased. Therefore for a more vertically positioned tube the base and the tip of the protrusion are always formed closer to the base of the tube. For completeness, the experimental results in the form of plots are shown in the Appendix C for the sets CM45GT-W1 and CM85GT-W1.

For a given volume of liquid in CM and assuming a perfectly shaped tube, a longer and thinner film (decreased β) is more uniform in thickness, resulting in similar hydrodynamic conditions along the film. In reality, due to tube imperfections, a longer film results to longer protrusions. A more extended protrusion means that the fluid is guided faster, via the protrusion, towards the upper end of the tube. In this scenario, the azimuthal displacements are very limited and only within the protrusion. In CF, a thinner and more uniform film could be achieved at the cost of reduced residence time. Whether a longer film is beneficial for the chemical reaction is unclear as it comes with the cost of the protrusion formation and reduced residence time. In order to explore the film uniformity, it is important to determine the film thickness. To determine the appropriate volume for the film thickness experiments, first the capacity of the tube for the rotation rates under investigation should be defined.

6.3.4 Volume capacity

The capacity of the tube at different rotation rates can play an important role on the film thickness, the residence time and the scalability of the device. Moreover, for the neutron imaging

experiments, in the following section 6.3.5, the determination of the maximum volume of liquid that remains in the VFD under the highest ω was necessary.

In order to measure the capacity of the tube, experiments are conducted in continuous flow. The flux is fixed at 1 ml/min and is stopped when the first drop is extracted from the device. To measure the capacity under steady state, the device is stopped a minute after the extraction of the first drop. After bringing the tube at rest, the volume left in the tube is extracted using the pipette. The volume extracted from the pipette is cross-checked with the expected volume calculated by the flow rate. For example, at 2,000 rpm and with the device tilted at 45° the first drop was extracted after 23 min while at 9,000 rpm the first drop was extracted after 2 min.

The variation of tube capacity is explored using the GT, for a range of rotation rates (1,000 - 9,000 rpm). The volume capacity is tested with the tube inclined at 45° and at 85° respectively (sets CF45GT-W and CF85GT-W), as shown in Figure 6.8. At 1,000 rpm the tube is almost full, reaching 34 ml. From 2,000 to 4,000 rpm there is a quadratic decay in volume, while over 5,000 rpm it seems that variations in capacity are significantly smaller. The plot shows that when ω is increased, the capacity of the tube is decreased, reaching asymptotically a value of 2 ml. The capacity of the tube varies for different inclination angles, with the more vertically positioned tubes having increased capacity. For example, at 9,000 rpm, the volume capacity is approximately 2.5 ml when the tube is tilted at 85° and 2 ml at 45°.

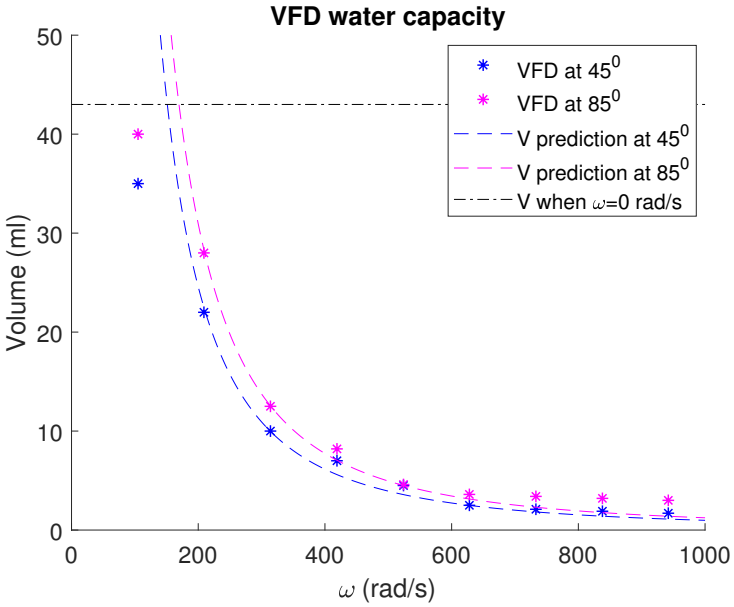

Figure 6.8: Tube water capacity at steady state using GT inclined at 45° - blue lines (set CFGT45-W) and at 85° - pink lines (set CFGT85-W). The dashed lines indicate a quadratic decay which is in agreement with the film shape model.

It was observed that at rotation rates greater than 4,000 rpm, most of the liquid developed at the walls as a thin film. At low rotation rates, below 4,000 rpm, volume capacity was significantly higher, leading to swirling flow. Swirling flows is a fluid mechanics research area that is not investigated in this thesis, thus the investigation is focused on rotation rates greater than 4,000 rpm.

The results can be compared to the film shape model, using the volume prediction, for L_{max} equal to the length of the tube, as expressed in equation 6.13. The model was developed for

a horizontal tube base and the predictions are valid for large ω, according to the condition in equation 6.14. The predictions show a similar decays with the experimental results, although towards the asymptotic values of V ($\sim$ 2 ml), a deviation from the experimental results of 0.5 ml is significant.

Having explored the volume capacity of the tube for different rotation rates, taking into consideration tube imperfections, the appropriate volume for the film thickness experiment can be defined. The volume should be enough to form a thin film, but low enough so the liquid remains in the tube even at high rotation rates. The inclination of the tube affects the volume remaining in the tube. The component of gravity, that resists the main direction of the flow, is increased at the inclination angle of 85°, and consequently the volume in the tube is increased.

6.3.5 Film thickness using neutron imaging

The volume capacity experiment, in section 6.3.4, showed that a water volume of approximately 2 ml is the maximum capacity of the VFD tilted at 45° and rotating at 9,000 rpm. In order to compare the film thickness for a range of rotation rates, the volume of the liquid is fixed at 1 ml. The film thickness is initially measured for toluene with viscosity of 6.3×10^{-7} m^2/s and surface tension of 3×10^{-2} N/m.

The thickness of the film, at steady state, is investigated using the technique of neutron imaging. Although this technique is predominantly used for stationary objects, the measurement of the film thickness is achieved by developing a new mathematical framework describing the neutrons' scattering as they pass through the rotating tube. The detector records the attenuation of neutrons passing through the object and the portion of the beam transmitted through the sample is converted into visible light. Details of the experimental set-up are presented in section 3.2.3.1.

As explained in chapter 3, with the camera used at ANSTO, the exposure time is 90 s, thus each radiography is captured in over 90 s. The final image, covering the total length of the tube, is compiled from 11 radiographies. Depending on the rotation rate, each radiography is a time average of tube revolutions ranging form $1,500$ to $13,500$ rotations. An example of the final neutron imaging product is shown in Figure 6.9. Both pictures represent the same experimental conditions. The difference in the two images, is the result of the resolution and the exposure time of the two cameras.

The resolution in Figure 6.9a is 100 MP, while the resolution in Figure 6.9b is 1 MP. The picture in Figure 6.9b is taken with a camera capturing 500 fps with exposure time at 1/2,000 s. The colour intensity variations inside the tube, observed in Figure 6.9a, indicate the variations in film thickness, as reflected by the neutrons' attenuation passing through the tube. The red colour indicates the maximum distance travelled by neutrons in the film. The same QT, used in both cases, is eccentric and forms a single protrusion.

The comparison of the neutron imaging radiographies in (a) and the high–speed camera recording in (b), motivated the development of a new methodology. The aim of the method is to understand the way the neutron images describe the film and the protrusion area over an average of more than 1,000 rotations.

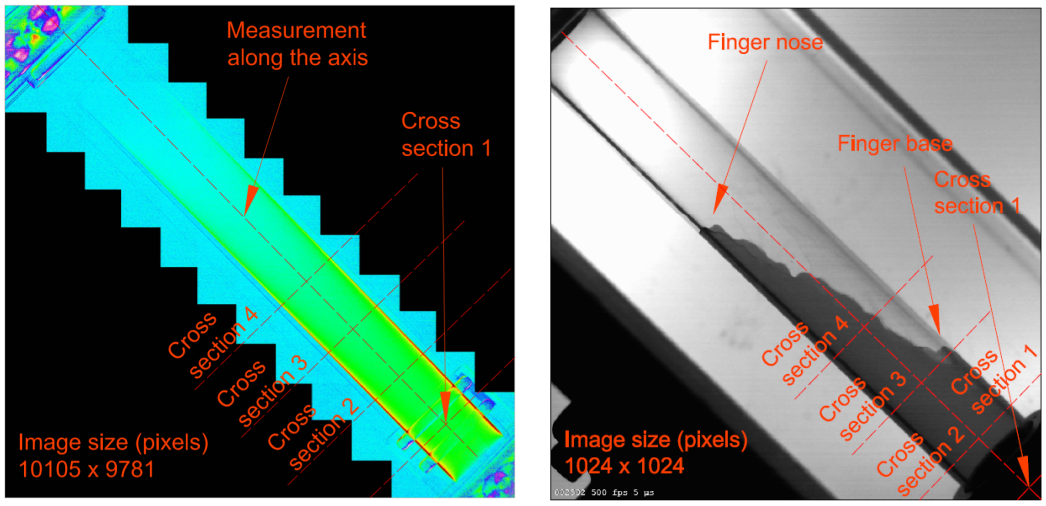

(a) (b)

Figure 6.9: (a) Neutron attenuation as obtained from the camera at ANSTO (resolution 100MP and exposure time 90 s), with the red colour indicating the maximum distance travelled by neutrons in the film. (b) The same tube is examined using the high–speed camera (resolution 1 MP and 500 fps). The comparison between the two images (with (b) showing the protrusion) motivated the development of a new methodological approach.

6.3.5.1 Mathematical framework for neutron imaging in the VFD

We propose a new framework for neutron imaging experiments using rotating objects. The film thickness can be determined, from the side view available. The pixel intensity is monotonically related to the length in which neutrons travelled through the film. The distance travelled by the neutrons within the film is referred to as 'optical depth' D_f.

We explore the optical depth in two different areas to determine the shape and the thickness of the film. One measurement is obtained along the axis of rotation, referred to as 'axis measurement', in order to capture the attenuation as an average of wet and dry areas. The second measurement is obtained close to the walls, referred to as 'wall measurement', to capture the attenuation produced by the maximum distance travelled by neutrons as they pass through the film. The method was initially tested at 4 cross–sections along the tube, with different wetting characteristics, as shown in Figure 6.9.

The neutron attenuation I is transformed to D_f, following the governing equation by the Beer-Lambert law:

$$I = I_0 e^{-\Sigma D_f},$$

where I_0 is the attenuation by the incident beam and $\Sigma = \Sigma_a + \Sigma_s$ is the sum of the absorbed (Σ_a) and the scattered neutrons (Σ_s). The ratio between I and I_0 is called transmission. Hence, the optical depth according to the Beer-Lambert law is

$$D_f = -\frac{1}{\Sigma} \ln \frac{I}{I_0}.$$

Thus, a logarithmic decay in pixel intensity is expected, along the axis of the tube. A comparison of the predicted D_f according to the Beer-Lambert law (black line) and the measurement of D_f along the axis of the tube (red line) is presented in Figure 6.10, for the case QT45QT5000T1.

The optical depth is increased close to the base, as it is an average of wet areas only and decreases as it moves away from the base and the film becomes thinner. The optical depth has an inflection point, approximately at the base of the protrusion. Beyond the inflection point, D_f is an average of wet and dry areas, decreasing more rapidly, giving a more linear apparent thickness profile. Overall, the sequence of pixels along the axis of rotation indicates the shape profile of the film and not the thickness of the film. Knowing the shape of the film, a calibration coefficient can be used to address the volume of the liquid in the tube.

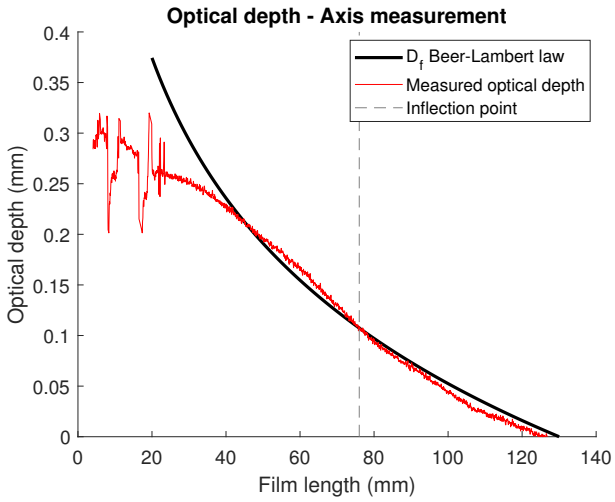

Figure 6.10: Measured pixel intensity along the axis of rotation and comparison with the Beer-Lambert expected optical thickness (case QT45QT5000T1).

For the wall measurements, we consider the almost axisymmetric case as a first example. Cross–section 1 is placed between the O rings and before the formation of the protrusion. The optical depth of cross–section 1 is shown in Figure 6.11. The maximum distance travelled by neutrons, as they pass through the film, is along the tangential projection of the free surface, as shown in Figure 6.11a. Thus, the projection of the free surface is described with the pixel of maximum D_f.

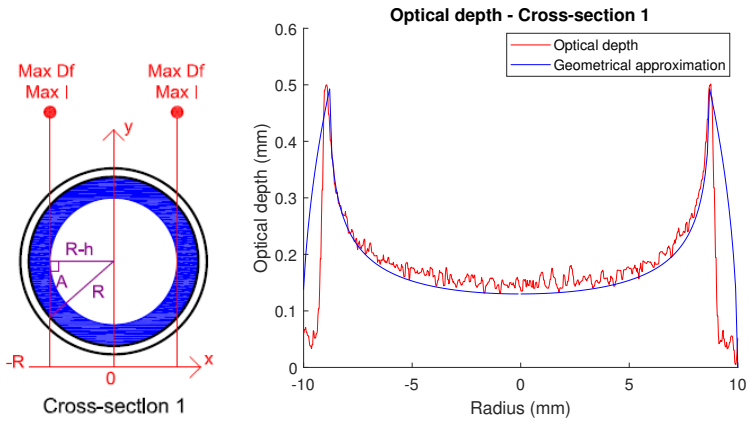

(a) (b)

Figure 6.11: Comparison of a) the geometrical approach and (b) optical depth of cross–section 1, obtained by the neutron imaging experiment. The maximum D_f is met at the maximum route of neutrons passing through the film, i.e in the tangential projection of the free surface (case QT45QT5000T1).

The optical depth of cross–section 1 is shown in Figure 6.11b. In this cross–section the film is almost axisymmetric, as both sides give almost the same D_f at the same distance from the walls. The red line represents the D_f obtained from the experiment. The blue line represents the expected D_f based on the geometrical approach of an axisymmetric film, which is in good agreement with the experimental results. Starting from the wall of the tube and as long as $x < R - h$, the optical thickness is

$$D_f = 2\sqrt{R^2 - (R-x)^2} = 2\sqrt{x(2R-x)}.$$

For $x > R - h$, the optical thickness is

$$D_f = 2\left(\sqrt{R^2 - (R-x)^2} - \sqrt{(R-h)^2 - (R-x)^2}\right) = 2\left(\sqrt{x(2R-x)} - \sqrt{(x-h)(2R-(x+h)}\right).$$

We assumed here that the distance travelled by the neutrons is divided in 2 equal parts by the horizontal radius. In reality, these two parts are not equal due to the internal asymmetries of the tube. The deviation at the beginning and the end of the plot in Figure 6.10b, between the predicted and the experimental D_f, is due to the eccentricity of the QT.

For a given position in the tube, the tube axis is in constant distance with the internal walls of the tube, while the free surface is in constant distance from the axis of rotation. Thus, the axis of rotation must be different than the axis of the tube. A sketch representing this deviation is shown in Figure 6.12a, taking into consideration the measured eccentricity. The sketch of cross–sections, in Figure 6.12b, shows the azimuthal development of the film at 4 different positions, determined in Figure 6.9. In all cases the film is thicker in the protrusion area and the deviation between the axis of rotation and the axis of the tube is of $\mathcal{O}(10^{-5})$ m and in accordance with the measurements of the Dial Test Indicator in section 6.2.

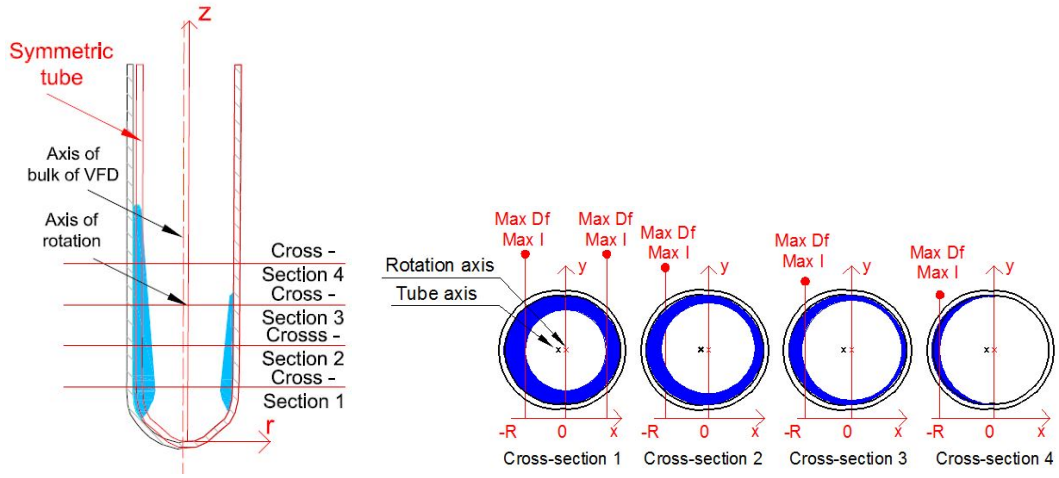

(a) (b)

Figure 6.12: (a) Example of the deviation between the axis of the tube and the axis of rotation. (b) Examples of film thickness at the cross–sections, due to tube eccentricity.

The sequence of pixels of maximum D_f, near the wall along the z direction, can define the free surface of the film, which in greater lengths is the thickness of the protrusion only. Although this is useful for the measurement of the thickness of the protrusion, it is not a reliable measurement, as the thickness varies along the azimuth. For example the method shows a film thickness along the protrusion as if the tube is fully coated until the tip of the protrusion. This

bias would lead to an overestimation of the thickness and the volume of the film. For that reason the second measurement along the axis of rotation is obtained and compared to the wall measurement.

After exploring D_f in cross–section 1, more asymmetric cross–sections can be investigated. A representative example is cross–section 4, as shown in Figure 6.13. At the wall, the maximum D_f is indicated by the darkest pixel and represents the free surface, therefore indicates the maximum film thickness. The axis measurement is an average of dry and wet areas, with D_f indicating the presence of wet areas.

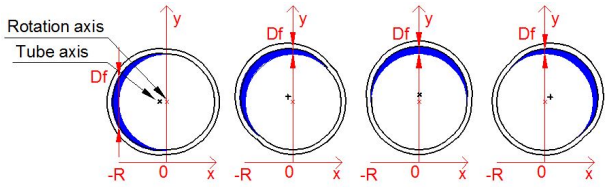

Figure 6.13: Qualitative representation of the optical thickness D_f captured near the wall and along the axis of rotation within one rotation at cross–section 4. Maximum pixel intensity is expected near the wall at the maximum route of neutrons through the film, i.e. in the tangential projection of the free surface.

A comparison of D_f for the 4 cross–sections, is shown in Figure 6.14. Each cross–section has a distance of one internal diameter ($\sim$ 18 mm) from the previous one, as indicated in Figure 6.9. The dashed lines are the expected D_f for each cross–section, as determined by the geometrical approach assuming a symmetric film.

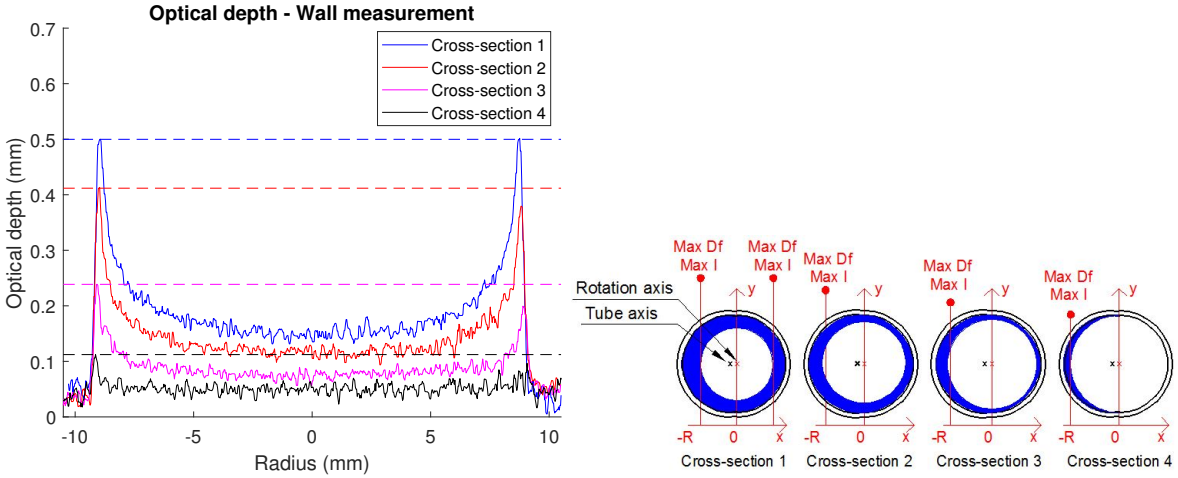

Figure 6.14: Examples of D_f at the 4 cross–sections. Cross–section 1 represents the pixel intensity at the area between the O rings of the lower bearing where the film thickness is almost symmetric. Cross–section 2 shows a more asymmetric D_f for the two wall measurements, where the tube is already eccentric. Cross–section 3 shows D_f at the base of the protrusion where part of the tube is marginally wet. Cross–section 4 shows D_f at the protrusion where part of the tube is dry. The deviation from the maximum D_f of each cross–section, indicated as a dashed line, is indicative of the film thickness differences in the azimuthal direction. The sketch is a qualitative representation of the film thickness for the cross–sections, indicating the maximum route of neutrons through the film, which is met always in the tangential projection of the free surface.

6.3.5.2 Neutron imaging results

Following the approach analysed in the previous section, measurements of D_f are taken along the axis of the tube and along the walls. The axial and the wall measurements are tested for 1 ml of toluene, from 1,000 to 9,000 rpm, with the QT inclined at 45° (set CM45QT-T1). The results are presented in Figure 6.15. For the axial measurement, we collect the average intensity along a thin column, i.e. average of 10 pixels normal to every point of the axial line and we make use of the Beer-Lambert law. The results are presented in Figure 6.15a. Along the wall and in order to determine the wall interface, we collect one row of pixels with values at the limit of the background intensity. Along the wall and in order to determine the free surface of the film, we collect one row of pixels with maximum intensity. The measurement along the wall appears much noisier than the measurement along the axis. The results are presented in Figure 6.15b.

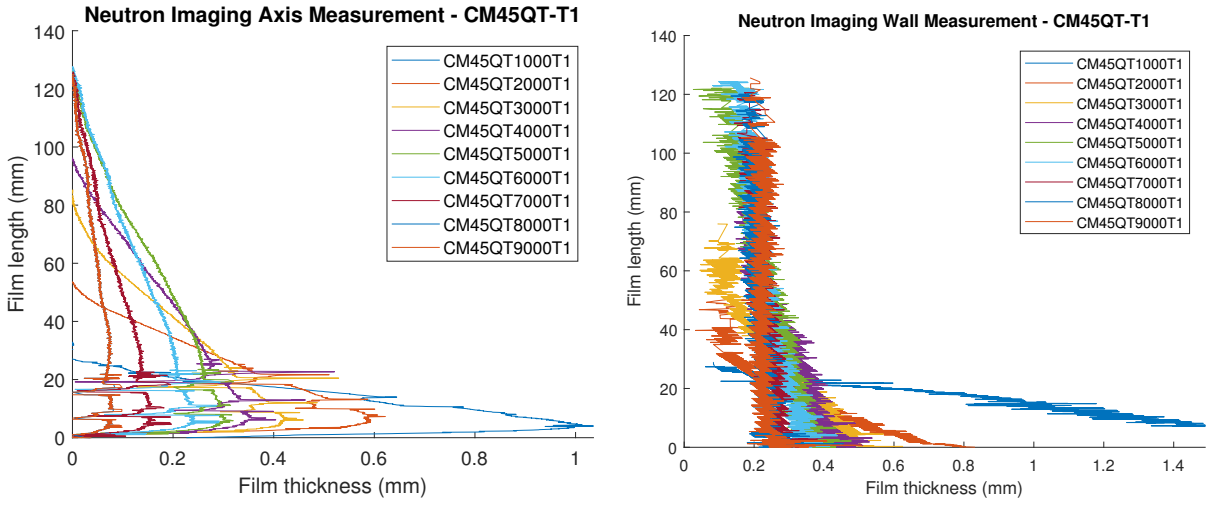

(a) (b)

Figure 6.15: Film thickness obtained by neutron imaging experiments of 1 ml of toluene, rotating for a range of rotation rates (1,000 - 9,000 rpm), at steady state in QT, inclined by 45° (set CM45QT-T1). Film thickness was measured (a) along the axis of rotation, indicating an average azimuthal thickness and (b) near the wall, indicating the maximum thickness of the film, met in the tangential projection of the free surface.

The noise of the wall measurements is related with the determination of the film surface and the wall limit. The tangential projection of the free surface should be the only reliable limit to be compared to noise, as it is at a constant distance from the axis of rotation. The interface between the tube and the film, i.e. the edge of the solid surface, is supposed to be a straight line for a perfectly circular tube. In reality, the eccentric shape of the tube, forces the tangential projection of the wall position and the film thickness to vary within every rotation.

To determine the error in the measurements we explore the number of pixels that represent the free surface and the wall respectively. An example of a zoomed image is shown in Figure 6.16. At every point along the wall, 2 to 4 pixels appear with the maximum intensity, representing the free surface, as shown in Figure 6.16b. The neuron image, averaging more than 1,000 rotations, shows the edge of the walls by 4 to 7 pixels, normal to the hypothetical linear wall interface, as shown in Figure 6.16c. The deviation of the eccentric side of the tube ($\sim \mathcal{O}(10^{-4})$ m - section 6.2) is in accordance with the measured 7 pixels. As the oscillating wall limit cannot be

considered as noise, we set the error of the measurements equal to 4 pixels, based on the noise at the free surface. Each side of the square pixel is 13 μm and the diagonal is 18.4 μm. Thus, all the measurements less than 73.6 μm should be considered unreliable. It is expected that at high rotation rates the film thickness close to the contact line is approximately $\mathcal{O}(10^{-5})$ m. This length scale is within the error limit and therefore the thickness near the contact line cannot be measured.

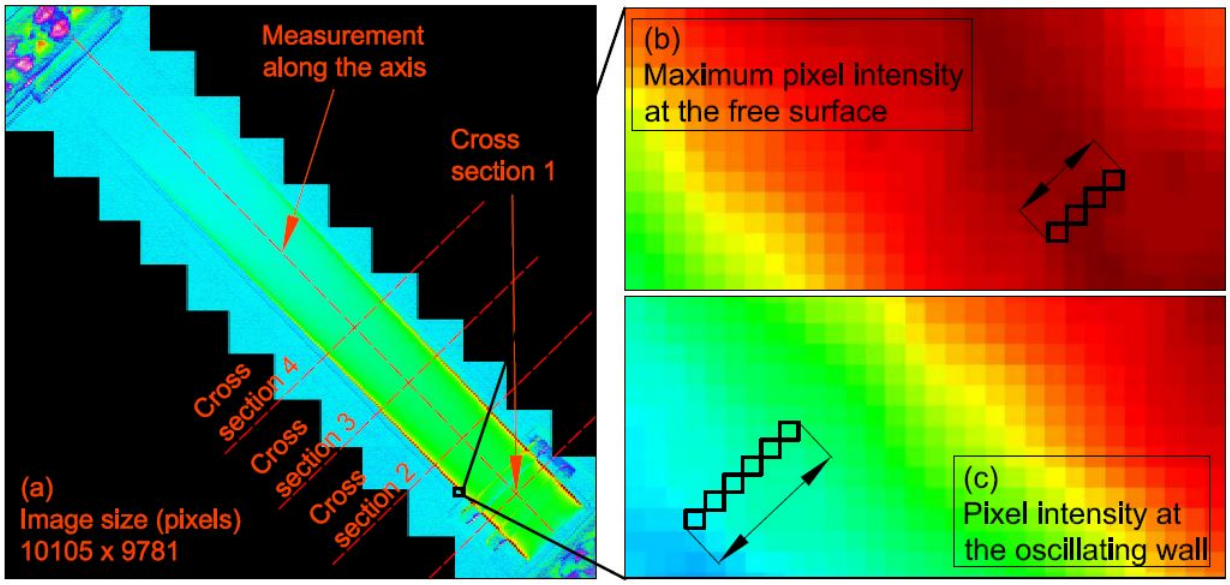

Figure 6.16: The maximum pixel intensity (dark red pixels) represents the free surface of the film. The free surface is represented by 2 to 4 pixels. The oscillating wall (green to blue pixels) is represented by 4 to 7 pixels.

Solheim et al. 2019 treated the first round of experiments by measuring the film thickness only in two–cross sections normal to the axis of rotation at 7,8 and 18,7 mm from the base of the tube. The error, for their ANSTO configuration, was set at 10 pixels, resulting at $\pm$ 667μm. According to the measurements presented in Figure 6.15, the film thickness is below the Solheim et al. error limit, for all rotation rates beyond 2,000 rpm. The significant deviation from the Solheim et al. measurements is due to the difference in resolution, exposure time and advanced image processing techniques used in this thesis.

For measurements of thickness greater than the error limit, we conduct regression analysis, applying a fitted quadratic curve based on the film shape model, determined in section 6.3.1. An example of the results for the axial and the wall measurement for 1 ml toluene at 7,000 rpm (CM45QT7000T1), is shown in Figure 6.17, with the fitting being almost linear due to the very thin film.

Volume conservation is a validation test for the method. From the axial measurement only the shape of the film is obtained. The average pixel intensity is an average over space (average of 10 pixels normal to the axis) and over time (average over 90 s). During a time frame of 90 s, the film thickness traversed by the neutron beam is fluctuating. As the relationship between the film thickness and the pixel intensity is not linear, we must take into account the effect of these fluctuations on the perceived film thickness. By considering how this impacts the axis measurements, we see that the variance in the film thickness will be represented by an additive constant, if we compute the thickness purely from the averaged images.

The shape is adjusted, with the use of a coefficient (ranging from 0.1 to 0.15), to account for a liquid volume from 0.9, to 1.1 ml, assuming symmetric coating up to the base of the protrusion in a tube with a circular cross–section. The result is represented by the black continuous line. The area between the wall limit and the free surface at the wall, is also used for the determination of the volume in the tube. The wall measurement leads to an overestimation of the volume, ranging from 1.1, to 1.5 ml. In this particular experiment, the liquid volume is estimated 0.98 and 1.31 ml, for the axial and the wall measurement respectively.

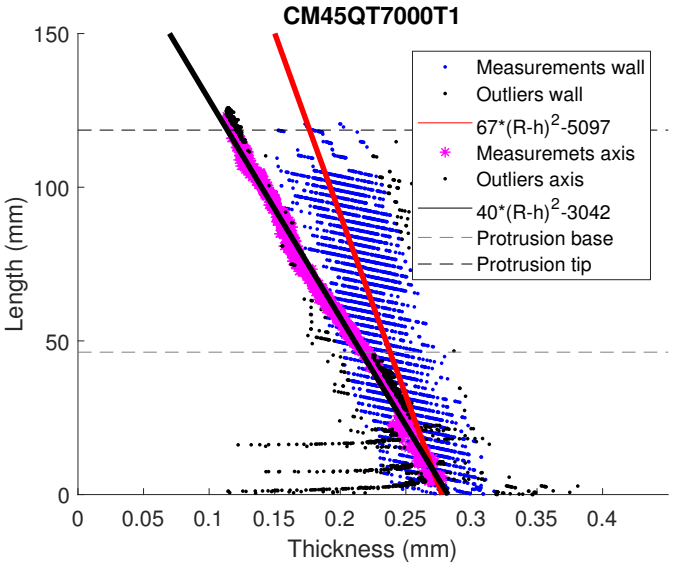

Figure 6.17: Example of film thickness measurement at the the wall and along the axis of rotation, obtained by neutron imaging for 1 ml of toluene rotating at 7,000 rpm in a QT, inclined at 45° (case CM45QT7000T1). The axis measurement indicates the average film thickness along the circumference at each point along the z axis, while the wall measurement indicates the maximum film thickness. The axis measurement uses an adjustment coefficient to account for the fixed liquid volume.

Given the noisy measurement at the wall, we could argue that obtaining the film shape from the axis and adjusting to account for volume conservation is a more robust approach. However, the wall measurement until the base of the protrusion is shaped by the edge of the free surface, which is the only fixed length from the axis of rotation. The deviation of the two measurements at the lower parts of the tube is small.

The wall measurement is the best representation of the maximum film thickness around the circumference in each position along the tube. Although neither measurement can directly determine the imperfections of the tube, they can be compared to indicate the different shapes of the film before and after the protrusion base. The combination of the noise at the free surface with the oscillating wall, makes the definition of the wall limit challenging. Although the error is estimated at 73.6 μm, in reality we are unable to measure film thickness less than 0.2 mm. The magnitude of eccentricity of the QT significantly restricts the lower limits of measurements. The imperfections could be random for different tubes and further analysis including scenarios of imperfect rotating shapes could be investigated in the future.

Repeating the axial and the wall measurement for the set CM45QT-T1, we determine the film profile from 1,000 to 9,000 rpm. For completeness, the experimental results for the set

CM45QT-T1 in the form of plots are shown in Appendix C. The deviation between the two measurements is consistent at all rotation rates. The shape of the film is parabolic with the thicker area of the film at the lower part of the tube. Measuring the thickness between the O rings (cross–section 1), we can determine the maximum thickness of the film, h, and compare it to the scaling of the boundary layer thickness, $\delta \sim \left(\frac{\nu}{\omega}\right)^{1/2}$. The results are presented in Table 6.1.

Table 6.1: Film thickness cross–section 1

rpm	1,000	2,000	3,000	4,000	5,000	6,000	7,000	8,000	9,000
δ (mm)	0.083	0.059	0.048	0.042	0.037	0.034	0.031	0.029	0.028
h (mm)	1.521	0.663	0.456	0.391	0.346	0.318	0.271	0.234	0.232

The main observation in Table 6.1 is that for $\omega \geq 7,000$ rpm the thickness of the film, at the O rings is very close to the scaling of the boundary layer thickness. Beyond the O rings the film is decreased in thickness, thus part of the film moves within the boundary layer. The exact point of transition to the boundary layer cannot be determined due to the protrusion. It is likely that beyond the O rings, the film is thinner than 0.2 mm at higher rotation rates. The very thin film at the higher parts of the tube, within the protrusion, could be of $\mathcal{O}(10^{-5})$ m. Given that the VFD performance is found to be optimal between 4,000 to 8,000 rpm, the focus is at this range of rotation rates. Each profile is characterised mainly by the coefficient of the quadratic term of the fitted line and can be compared to the constant C_M determined for the parabolic shape of the film in section 6.3.1. A comparison of the dimensional coefficient of the fit with the adjusted coefficient $\frac{C_M}{R}$ is shown in Figure 6.18.

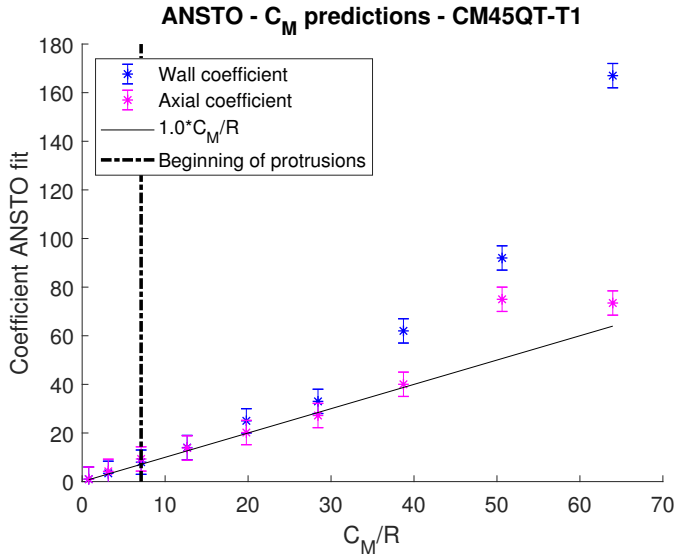

Figure 6.18: Comparison of the shape model predictions to the neutron imaging results of the wall and the axis measurement, indicating that the shape model is in good agreement with the experimental results up to 6,000 rpm. Beyond 6,000 rpm, the film is likely to be thinner than the measurements and the slope of the film shape less steep. At high rotation rates the protrusion length is increased and a deviation from the shape model predictions is expected.

The correlation between the experimental and the predicted thickness is linear with the model being very close to the axil measurements. The error was determined taking into account the average deviation between the coefficients produced by the fittings (~ 5 mm^{-1}). The model

coefficient is in good agreement with both measurements up to 6,000 rpm. Taking into account only the quadratic term of the film shape model of equation 6.6 in section 6.3.1, is similar to accounting only for the maximum axisymmetric spreading with a flat tube base and without any protrusions. The curvature of the wall measurement is affected by the protrusion, hence the deviation from the model predictions, beyond 6,000 rpm.

The wall measurement takes into account the protrusion and extends the fitted line up to the tip of the protrusion as in an axisymmetrically coated tube. Thus, the very thin film along the protrusion alters the coefficient of the wall measurement. Beyond 7,000 rpm, the protrusion covers a significant length in the tube while the shape model assumes symmetric coating. The measurements of thickness beyond 7,000 rpm, are very close to the minimum measurements that could be obtained (0.2 mm) and therefore it is likely that the film is thinner, the slope of the film shape is less steep and the coefficient of the quadratic term closer to the model prediction.

6.3.6 Reaction rate

Neutron images defined the film thickness in the VFD. Film thickness is related to the pressure that the molecules experience in the film. The maximum film thickness is met near the base of the tube between the O rings of the device. Beyond the O rings, pressure is in a quadratic decay correlated with the decrease in thickness. Knowing the film thickness for each case of sets, the pressure at the wall can be estimated. The pressure gradient between the wall and the free surface, at each point along the z direction can be approximated using only the higher order term of P, as defined by the analytical solution of the Navier–Stokes equations, explained in the following section 6.4 (equation 6.27). Thus $\Delta P \sim \rho\omega^2 Rh$, where h is the film thickness. Knowing h from the neutron imaging experiment, we can determine the pressure difference across the thickness of the film, ΔP. For example, between the lower O rings of the tube, ΔP goes from 1,050 N/m^2 at 5,000 rpm to 2,230 N/m^2 at 9,000 rpm. Thus, increased ω leads to a film of increased length and decreased thickness, experiencing increased ΔP.

Increased ΔP could be altering the diffusion coefficient D. Indicative measurements of optimum P for maximum D are mentioned in section 2.1, with maximum D in water at 10^8 Pa. While P obtained from the experiments as an absolute value is relatively small $\sim 10^3$ Pa, ΔP might work in favour of increased reactivity. Pressure gradients are experienced in the film along the r and the z direction. Especially in the r direction, the pressure gradients might be even more important due to the significantly shorter travel path. Experiments attempting to measure D and reaction rates in the VFD are analysed in the next section.

In order to visualise the chemical processing in the VFD, several chemical reactions of intense colour change are attempted. The aim is to measure the time scale of the propagation of the chemical reaction and conclude on the contribution of advection and diffusion to enhanced reactivity.

6.3.6.1 Chemical reactions

The first attempt is the production of the dye indigo ($C_{16}H_{10}N_2O_2$), prepared according to the Pfleger's synthesis (1901). The reaction undergoes more than 10 steps, within which the solution turns from green to blue and at the final stage to bright orange. Using a test tube the

reaction requires (depending on the motion of the tube) 10 minutes (manual shaking) to one day (stationary tube). In contrast, in CM with the VFD tilted at 45° (case IN45GTS8N2) the solution turns almost instantly to bright orange.

Aiming to control and monitor the reaction as much as possible, another reaction is introduced, combining CM and CF. A bromothymol blue solution is prepared by diluting 4 mg bromothymol blue, in 1 ml of 2wt% Sodium Hydroxide, which is then added in a solution of 2 ml of Ethanol filled to 50 ml with water. In every run, 3 ml of the bromothymol blue solution is initially placed in the stationary tube. After the initiation of motion in the VFD, a waiting time of 1 min is set in order for the liquid to reach steady state. Once the film is at steady state, a droplet of 40 μl of sulfuric acid (8M), of pH 1, is released near the base of the tube (set D-QT45B3S40). Excluding the initial stage of advection, the colour change is caused by the ionic diffusion of hydrogen: $H_2SO_4 \xrightarrow{H_2O} HSO_4^- \xrightarrow{H_2O} SO_4^{2-}$.

6.3.6.2 Diffusion coefficient and advection

The diffusion coefficient D can vary depending on the chemical potential gradient as mentioned in section 2.1. The length in which reaction is observed due to diffusion scales as $l_R \sim (Dt)^{\frac{1}{2}}$. Therefore in our experiments, we assume that a reaction length evolution with time dependence of $t^{1/2}$, is an indication that reaction was achieved mainly due to diffusion. The reaction rate in the VFD is determined for a bromothymol blue solution in full capacity in the QT, inclined by 45°, rotating from 5,000 to 9,000 rpm (set D-QT45B3S40). This set of experiments has intense colour change and in a time scale convenient for the camera recording. The intense colour change occurs due to the ionic diffusion and advection of hydrogen.

In order to determine D in the VFD, a control experiment is conducted in a non-rotating capillary tube. The tube contains approximately 1 μl of the bromothymol blue solution. The tube is constantly closed from the top and marginally touches, for 1 s, a plate covered with sulfuric acid. The camera takes a picture every 2 minutes. The experiment lasts for more than 30 hours with the length of the test tube under which reaction occurs covering, at the end of the experiment, almost half of the bromothymol blue solution, as shown in Figure 6.19a. The length of diffusion evolved with a time dependence scaled as $l_D \sim (Dt)^{1/2}$, where $D \sim 4 \times 10^{-8} \mathrm{m}^2/\mathrm{s}$. The results are presented in Figure 6.19b.

The coefficient D estimated in the control experiment, is considered the D for a stationary solution and is compared to the coefficients obtained from experiments of the same reaction in the VFD, varying the rotation rate (set D-QT45B3S40). During each realisation, immediately after the landing of the sulfuric acid droplet, there was a rapid initial spreading due to advection caused by the landing droplet and then the colour change became slower and followed a time dependence of $t^{1/2}$.

An example for the evolution of the reaction at 7,000 rpm, (case D7000QT45B3S40) is presented in Figure 6.20. The picture in Figure 6.20a shows the raw image at the point in time after which reaction occurs due to diffusion (40 s after droplet landing). The darker grey downwards tip is due to the eccentricity of the QT, with the reaction propagating faster in areas where the film is thicker. The same point in time is indicated as $t = 0s$ (dashed grey line) on the plot in Figure 6.20b, which overall presents the reaction evolution. Beyond that point in time,

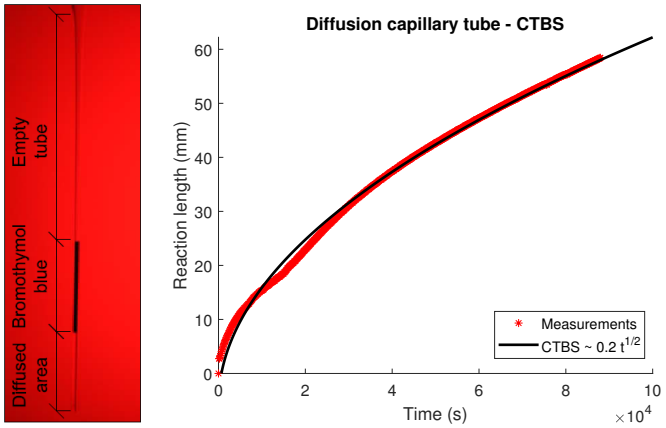

(a) (b)

Figure 6.19: Evolution of diffusion, lasting for 30 hours, in a capillary tube filled with 1 ml of bromothymol blue and marginally touching a plate covered with sulfuric acid, only for 1 s, at the initiation of the experiment (case CTBS). (a) Capillary tube at the end of the control experiment with distinction between the diffused and the unprocessed area. (b) Evolution of diffusion for the experiment CTBS, for more than 24 hours.

the time dependence is $t^{1/2}$. Excluding the initial advection time (due to the droplet landing), the fact that the time dependence follows the diffusion law, would suggest that diffusion dominates the chemical reaction. Taking into consideration that the rate of the reaction covering a length l_R, might be a combination of diffusion and advection, we set a new 'reaction coefficient' D_m. For completeness, the experiments for the set D-QT45B3S40 are presented in Appendix C.

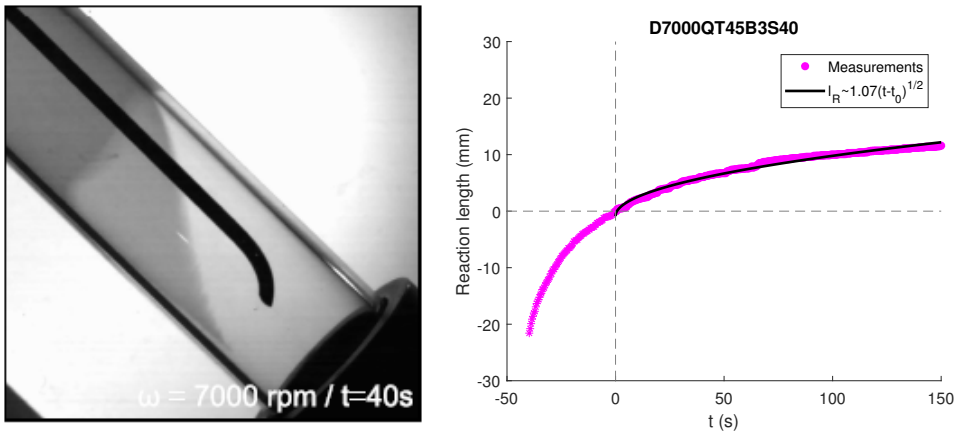

(a) (b)

Figure 6.20: Example of reaction evolution in a QT, tilted by 45°, rotating at 7,000 rpm, in full capacity with bromothymol blue and with the addition of a droplet of 40 μl of sulfuric acid (case D7000QT45B3S40). (a) Raw image of the reaction evolution, after 40 s, in the VFD. (b) Reaction evolution, with the dashed line indicating the same point in time as the raw image in (a) (t= 40 s from the droplet landing, t=0 s for the time scale of the reaction rate of $t^{1/2}$.)

Pressure variations are significant along the r directions. The two liquids have different densities at $20°C$, with sulfuric acid having a density $\sim 1,840$ kg/m^3 and bromothymol blue having a density $\sim 1,000$ kg/m^3. Due to the centrifugal force, the denser liquid tends to form a layer between the walls and the lighter liquid. Thus, sulfuric acid creates a front similar to

the sketch in Figure 6.21. It is plausible that shearing and diffusion are present at the interface between the two liquids but also due to the density difference we have vorticity ζ generated at the interface.

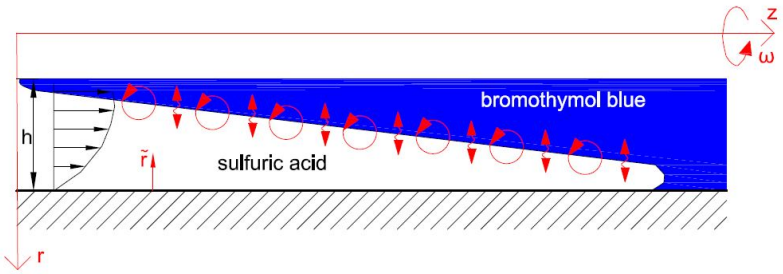

Figure 6.21: Sketch of the denser liquid, going underneath the lighter liquid and forming a layer between the walls and the lighter liquid. At the interface of the two liquids, there is a combination of diffusion and advection.

We attempt to form a scaling connecting diffusion and vorticity, in order to determine the reaction coefficient. Assuming that we have significant flow only in the z direction so that $\frac{\partial u_r}{\partial z} \ll \frac{\partial u_z}{\partial r}$, vorticity is defined as

$$\zeta = -\frac{\partial u_z}{\partial r}.$$

The advection–diffusion equation for the concentration of bromothymol blue $C_b(r, z)$ can be expressed as

$$\frac{\partial C_b}{\partial t} + u_z \frac{\partial C_b}{\partial z} = D\left(\frac{\partial^2 C_b}{\partial r^2} + \frac{\partial^2 C_b}{\partial z^2}\right). \tag{6.15}$$

In a variable density two-dimensional flow the vorticity equation has an additional term describing the baroclinic generation of vorticity (Thoroddsen & Van Atta, 1996), i.e.

$$\frac{D\zeta}{Dt} = -\frac{1}{\rho_b^2}\nabla\rho \times \nabla P + \frac{1}{\rho_b}\nabla\rho \times \mathbf{g} + \nu\nabla^2\zeta.$$

In this problem centrifugal force is the main driving force, hence we proceed by replacing the gravitational acceleration with $\omega^2 R$, assuming a thin film where $\omega^2 r \sim \omega^2 R$. Noting that this acceleration acts on the density gradient due to the concentration gradient, we get the scaling

$$\frac{1}{\rho_b}\nabla\rho \times \mathbf{g} \to \frac{\Delta\rho}{\rho_b}\omega^2 R\frac{\partial C_b}{\partial z}.$$

Thus, the rate of change of vorticity, assuming that there is no significant motion normal to the walls of the tube, is

$$\frac{\partial \zeta}{\partial t} = -\frac{\Delta\rho}{\rho_b}\omega^2 R\frac{\partial C_b}{\partial z} + \nu\frac{\partial^2 \zeta}{\partial r^2}, \tag{6.16}$$

where $\Delta\rho$ is the density difference between bromothymol blue and surfuric acid and ρ_b is the density of bromothymol blue. Ignoring the time rate of change of vorticity, under the assumption that $D \ll \nu$, so that $\frac{\partial \zeta}{\partial t} \sim 0$, equation 6.16 becomes

$$\frac{\partial^3 u_z}{\partial r^3} = \frac{\Delta\rho}{\rho_b \nu}\frac{\partial C_b}{\partial z}\omega^2 R,$$

leading to the velocity field, parallel with the walls of the tube,

$$u_z = \frac{1}{6}\frac{\Delta\rho}{\rho_b \nu}\frac{\partial C_b}{\partial z}\omega^2 R\tilde{r}^3 + \frac{a}{2}\tilde{r}^2 + b\tilde{r} + c, \tag{6.17}$$

where $\tilde{r} = R - r$, and a, b, c are coefficients that will be determined in the following steps. Imposing the no–slip boundary condition where at $\tilde{r} = 0 \rightarrow u = 0$, from equation 6.17 we get $c = 0$. Then at $\tilde{r} = h \rightarrow \frac{\partial u_z}{\partial r} = 0$, so from equation 6.17 we get

$$b = -\frac{\Delta\rho}{\rho_b \nu}\frac{\partial C_b}{\partial z}\omega^2 R\frac{h^2}{2} + ah. \tag{6.18}$$

Then by considering the depth–averaged velocity $\bar{u}_z = 0$,

$$\bar{u}_z = \frac{1}{h}\int_0^h u_z = 0 \rightarrow b = -\frac{\Delta\rho}{\rho_b \nu}\frac{\partial C_b}{\partial z}\omega^2 R\frac{h^2}{12} - \frac{a}{3}h. \tag{6.19}$$

Defining a and b from equations 6.18 and 6.19, the velocity profile of equation 6.17 becomes

$$u_z = \frac{\Delta\rho}{\rho_b \nu}\frac{\partial C_b}{\partial z}\omega^2 R\left(\frac{1}{6}\tilde{r}^3 + \frac{5}{32}\tilde{r}^2 h - \frac{9}{48}\tilde{r}h^2\right). \tag{6.20}$$

Putting equation 6.20 into equation 6.15 we get

$$\frac{\partial C_b}{\partial t} + \frac{\Delta\rho}{\rho_b \nu}\left(\frac{\partial C_b}{\partial z}\right)^2 \omega^2 R\left(\frac{1}{6}\tilde{r}^3 + \frac{5}{32}\tilde{r}^2 h - \frac{9}{48}\tilde{r}h^2\right) = D\left(\frac{\partial^2 C_b}{\partial r^2} + \frac{\partial^2 C_b}{\partial z^2}\right) \tag{6.21}$$

As initial condition we consider at $z = 0 \rightarrow C_b = 0$ and at $z = l_R \rightarrow C_b = 1$, then

$$\frac{\partial C_b}{\partial z} \sim \frac{1}{l_R}.$$

At the interface, diffusion alone is trying to make the concentration contours 'vertical' (in the orientation of Figure 6.21, i.e. along the r direction), while the density differences are trying to drive them towards 'horizontal' (along the z direction) through advection. Thus, assuming that $\frac{\partial C_b}{\partial z} \sim \frac{\partial C_b}{\partial r}$, then

$$\frac{\partial C_b}{\partial r} \sim \frac{1}{l_R}$$

and

$$\frac{\partial C_b}{\partial t} \sim \frac{\partial C_b}{\partial l_R}\frac{\partial l_R}{\partial t} = \frac{1}{l_R}\frac{\partial l_R}{\partial t}.$$

Then equation 6.21 becomes

$$\frac{1}{l_R}\frac{\partial l_R}{\partial t} + \frac{\Delta\rho}{\rho_b \nu}\omega^2 R\left(\frac{1}{6}\tilde{r}^3 + \frac{5}{32}\tilde{r}^2 h - \frac{9}{48}\tilde{r}h^2\right)\frac{1}{l_R^2} \sim D\frac{1}{l_R^2}.$$

Integrating, using the boundary condition at $t = 0 \rightarrow l_R = 0$, we can define the length of the reaction as

$$l_R \sim \left[D - \frac{\Delta\rho}{\rho_b \nu}\omega^2 R\left(\frac{1}{6}\tilde{r}^3 + \frac{5}{32}\tilde{r}^2 h - \frac{9}{48}\tilde{r}h^2\right)\right]^{1/2} t^{1/2}. \tag{6.22}$$

According to equation 6.22, the reaction coefficient is a combination of advection and diffusion. For example at the free surface of the film where $\tilde{r} = h$, and assuming that the diffusion coefficient is constant and similar to the control experiment ($D \sim 0.45$ mm^2/s), equation 6.22 becomes

$$l_R \sim (D_m t)^{1/2} \tag{6.23}$$

where

$$D_m \sim D + 0.14\frac{\Delta\rho}{\rho_b \nu}\omega^2 R h^3.$$

In this case the reaction coefficient is defined by a combination of vorticity and diffusion with advection having a strong effect when

$$\frac{\Delta\rho}{\rho_b \nu D}\omega^2 R h^3 \gg 1.$$

The mathematical approximation of equation 6.23 was compared to the experimental coefficients of the set D-QT45B3S40, as shown in Figure 6.22. The thickness of the film was assumed constant and equal to h immediately before the base of the protrusion, as determined by the neutron imaging experiments (black continuous line). Although we would expect a parabolic increase due to ω^2, the terms $\omega^2 h^3$ define the dependence of D_m to the rotation rate, which seems to be almost linear to *omega*. As ω is decreased, D_m moves towards values that represent a stationary environment, reaching for $\omega \sim 0 \rightarrow D_m \sim D$, the coefficient of the control experiment.

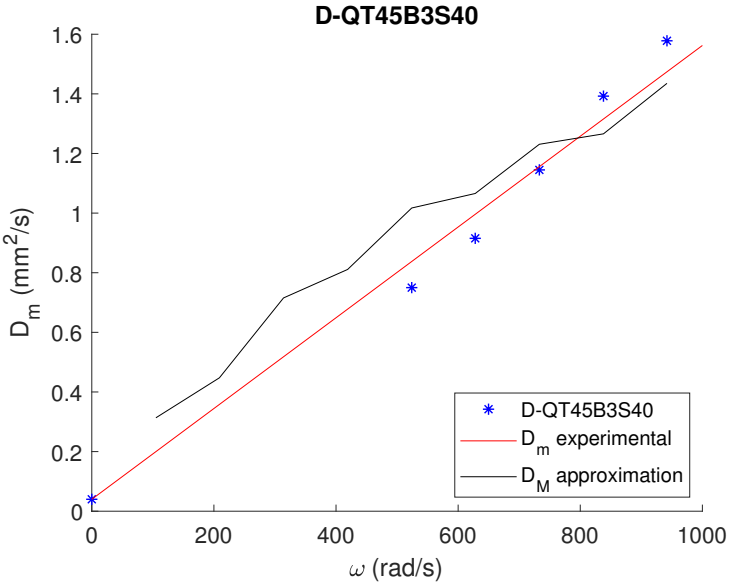

Figure 6.22: Reaction coefficients for a QT, inclined by 45°, rotating from 5,000 rpm to 9,000 rpm, with a film of bromothymol blue already developed in the tube and with the addition of a single droplet of 40 μl of surfuric acid (set D-QT45B3S40). The reaction coefficient D_m increases almost linearly with increased ω. The projection of the trend line towards a non-rotating tube reaches D determined by the control experiment. The mathematical approximation, using the film thickness from the neutron imaging results (black continuous line) is almost linear and is in good agreement with the experimental results indicating the presence of a advection–diffusion reaction mechanism.

The term $\omega^2 R$ is generated due to the centrifugal force ($F_c \sim \rho\omega^2 r$), which is the main driving force creating pressure gradients and triggering motion in the z direction in the VFD. A similar scaling for the growing stage of the ring was also generated for the flat disk, by balancing centrifugal force with viscous stresses and in the hemispherical disk by balancing centrifugal force, gravitational force and viscous stresses. For the scaling of the spreading on a rotating disk, the term h^3 accounts for the liquid volume in the ring, while for the reaction front in the VFD the centrifugal force is acting to drive a counter flow due to density differences within an otherwise static layer. Therefore, h^3 in the VFD is related to the density gradients. Thus, although the form $\omega^2 R h^3$ is similar in the disk and the VFD scaling, the dynamics that lead to

h^3 are fundamentally different and the similarity between the forms is a dimensional necessity. The similar scaling both for the enhanced diffusion and the growth of the ring, in the flat disk, leads to an almost linear dependence with ω.

Given that $\omega^2 R \gg g$, then pressure gradients, along the r direction, trigger motion that tends to homogenise density differences along the film through advection rather than just diffusion. Although these factors could affect chemical reactivity, it is unclear whether they have an enhanced effect in the VFD, compared to other devices. Having already defined the main characteristics of the film at steady state we conclude that the formation of the thin film, the extended residence time achieved at steady state, and the enhanced ΔP leading to increased l_R, could be a unique characteristic in the VFD, enhancing mass transfer even at molecular level.

6.4 Film progression during spin–up

When exploring the steady state, we suggested a mechanism of pressure gradients, driven by density differences and for $\omega^2 R \gg g$, that potentially enhances chemical reactions in the VFD. The gradual evolution of the film, although represents a small portion of processing time, it is still important for the film formation and fluid shearing. In this section, we consider the evolution of the film where the tube rotates with constant ω and the fluid is already predominantly rotating and is spreading along the length of the tube towards its equilibrium shape. The approach focuses on the upwards motion of the film in the tube, which is treated as an inclined plane.

The liquid forms a thin Newtonian incompressible film, of thickness h, length L, kinematic viscosity ν and density ρ, flowing along the inside of a solid impermeable tube of internal radius R, spinning around its axis, with angular velocity ω. We consider the case of a perfectly cylindrical tube, with its symmetry axis coincident with the axis of rotation. A rotating cylindrical coordinate system, (r, ϕ, z), shown in Figure 6.23, along with the velocity field (u_r, u_ϕ, u_z), are introduced to formulate the mathematical model describing the dynamics of the film, bounded by the free surface at $r = R - h$ and the underlying solid substrate at $r = R$.

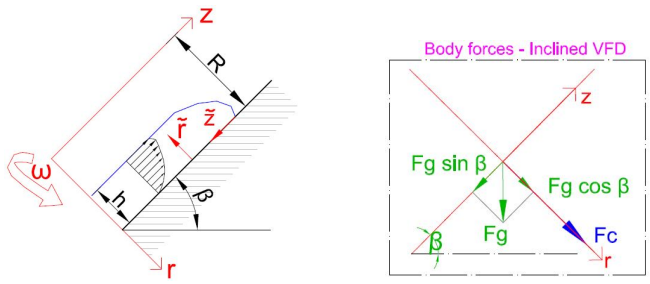

(a) (b)

Figure 6.23: (a) Coordinate system in the VFD using cylindrical polar coordinates. (b) Body forces applied to the fluid with Coriolis force being normal to the plane r–z. The film propagates upwards due to the pressure gradient created mainly by the centrifugal force which is applied along the r direction.

The base state describes the evolution of the film as it propagates along the walls. The film eventually reaches a new equilibrium, reaching a steady state. The flow is governed by the continuity equation, Navier–Stokes equations and an appropriate set of boundary conditions:

– No slip ($u_z = 0$ and $u_\phi = 0$ at $r = R$) boundary condition.

– No penetration at the tube surface ($\mathbf{u} \cdot \mathbf{n} = 0$ at $r = R$).

– The kinematic boundary condition at the surface ($u_r = \frac{Dh}{Dt}$) ensures that no fluid passes through the liquid air interface.

– The dynamic boundary condition, where the pressure of air is considered constant so that normal and shear stress balances at the film surface $\left(\left[\underline{\underline{\sigma}} \cdot \mathbf{n} \right]_{h^-}^{h^+} = -\gamma_{la}(\nabla^2 h + \frac{1}{R-h})\mathbf{n} \right)$ where $\underline{\underline{\sigma}}$ is the stress tensor. We assume that the effects of evaporation, condensation and mechanical vibrations are negligible.

– The contact line dynamics are ignored, the thickness of the film vanishes at the contact line and the velocities of the liquid particles must equal the velocity at the tip of the film, which gives the boundary condition $h = 0$ at $z = L$.

For the following solutions all boundary conditions are applied and hence, fulfilled. The centrifugal force acts normal to the z direction, forming a pressure gradient in the r direction. The thin film is formed when the pressure gradient is strong enough to make the fluid drain the hemispherical base and develop a film along the walls. The role of gravity on the cylindrical walls of the tube varies according to the inclination β of the tube from the horizontal axis. When the tube rotates vertically, with $\beta = 90°$, gravity acts against the main direction of the flow. When the tube rotates horizontally, with $\beta = 0°$, gravity acts opposite to the centrifugal force at the upper side and in the same direction to centrifugal force at the lower side, opposite to the azimuthal flow at the upwards side and in the same direction to the azimuthal flow at the downwards side. Thus, in the rotating frame, for all $\beta < 90°$, the gravitational force is a function of t and ϕ, fluctuating within each rotation period. The fluctuating direction of gravity could work in favour of an azimuthal motion which would lead to a more uniform film. Film uniformity could work beneficially for the chemical processing, although the processing time is reduced for decreased inclination.

The Navier–Stokes equation for the VFD in the rotating frame is

$$\rho \frac{D\mathbf{u}}{Dt} = -\nabla P + \mu \nabla^2 \mathbf{u} - 2\rho\, \boldsymbol{\omega} \times \mathbf{u} - \rho\, \boldsymbol{\omega} \times (\boldsymbol{\omega} \times \mathbf{r}) + \rho \mathbf{g}. \tag{6.24}$$

Assuming that the film is thin so that $h \ll R$ and using continuity equation, $\nabla \cdot \mathbf{u} = 0$, the relative magnitudes of the velocity components can be approximated. For example, for a thin film $h \ll L$,

$$\frac{u_r}{h} \sim \frac{u_z}{L} \rightarrow u_r \ll u_z.$$

A lubrication approximation model in ϕ and z, incorporating centrifugal force and gravity, can reproduce the main features of the film development in the VFD. In the rotating frame, the body forces, excluding Coriolis force, acting on the fluid element of mass m can be expressed as the Cartesian vector

$$\mathbf{F} = m\ (g\cos\beta + \omega^2 r, g\cos\beta e^{i(\phi - \omega t)},\ -g\sin\beta),$$

where the complex exponential encapsulates both the varying direction of gravity around the tube and the variations due to the rotation of the tube.

The lubrication approximation is valid, provided that inertia is small, relative to centrifugal force and viscous forces. Compared to centrifugal force, using a scaling from equation 6.24, this approximation holds when

$$\frac{u_z^2}{L} \ll \omega^2 r,$$

while compared to viscous forces the approximation holds when

$$\rho\omega u_\phi \ll \mu\frac{u_\phi}{h^2}.$$

If we assume that the Coriolis force is negligible, we need to validate the approximation by proving that $u_\phi \ll u_z$. To determine u_ϕ, the Nusselt film approximation, introduced in section 2.2.2, is used under the condition that the film thickness is less than the boundary layer scaling, satisfying

$$h < \left(\frac{\nu}{\omega}\right)^{1/2}.$$

The magnitude of u_ϕ can be determined by balancing the gravitational force with viscosity as

$$\mu\frac{\partial^2 u_\phi}{\partial r^2} = \rho g \cos\beta e^{i(\phi-\omega t)}.$$

Using the no slip boundary condition and the kinematic boundary condition we get

$$u_\phi = U_\phi\left[\frac{R}{h}\left(\frac{r}{h} - \frac{R}{2h} + 1\right) - \frac{r}{h}\left(1 + \frac{r}{2h}\right)\right], \tag{6.25}$$

where U_ϕ is the velocity at the free surface ($r = R - h$), determined as

$$U_\phi = \frac{g\cos\beta}{\nu}h^2 e^{i(\phi-\omega t)}.$$

The time that viscous dissipation requires to act on the fluid is smaller compared to one rotation period

$$\frac{h^2}{\nu} \ll \frac{1}{\omega},$$

and consequently U_ϕ reacts instantly to variations in the direction of gravity. Thus, we hypothesis at this point that the component of gravity in the ϕ direction is only a weak effect and u_ϕ is expected to be small relative to u_z, with the exception of when $u_z \to 0$ as the film reaches asymptotically its maximum length. Assuming that there are small variations in the film thickness in the ϕ direction, and neglecting variations in the z direction, the thickness variations in ϕ can be determined using continuity equation as

$$\frac{\partial h}{\partial t} + \frac{1}{r}\frac{\partial}{\partial\phi}(\bar{u}_\phi h) = 0, \tag{6.26}$$

where $\bar{u}_\phi$ is the depth-averaged velocity and the film thickness can be expressed adding a perturbations as

$$h = h_0 + h_1 e^{i(\phi-\omega t)},$$

where h_0 is the mean value of film thickness, h_0 and h_1 are constants and assuming $h_1 \ll h_0$, so that

$$\frac{\partial h}{\partial t} = -i\omega h_1 e^{i(\phi-\omega t)}.$$

Keeping only the leading term of the film thickness $h \sim h_0$, surface velocity can be determined using the Nusselt film approximation as

$$U_\phi = \frac{g\cos\beta}{\nu}h_0^2 e^{i(\phi-\omega t)} + \mathcal{O}(h_1).$$

The depth-averaged velocity, using equation 6.25, is then

$$\bar{u}_\phi = \frac{1}{h}\int_0^h u_\phi dr \approx \frac{g\cos\beta}{\nu} h_0^2 e^{i(\phi-\omega t)}.$$

If $r \sim R$, then

$$\frac{1}{R}\frac{\partial}{\partial\phi}\bar{u}_\phi h = \frac{g\cos\beta}{\nu R} h_0^3 i e^{i(\phi-\omega t)}$$

and equation 6.26 becomes

$$-i\omega h_1 e^{i(\phi-\omega t)} + \frac{g\cos\beta}{\nu R} h_0^3 i e^{i(\phi-\omega t)} = 0.$$

The ratio of thickness variations can be approximated as

$$\left|\frac{h_1}{h_0}\right| \sim \frac{g\cos\beta}{\omega^2 R}\frac{\omega h_0^2}{\nu}.$$

Both elements on the right-hand side are small, with centrifugal force being the larger than the gravitational force $g\sin\beta \ll \omega^2 R$ and with the film thickness being smaller than the boundary layer thickness, $\omega h_0^2 \ll \nu$. Thus

$$\left|\frac{h_1}{h_0}\right| \ll 1.$$

Hence, as assumed, the thickness variations in the ϕ direction are small compared to the mean thickness and can be ignored. In order to treat the spin–up as a two–dimensional problem in the r–z plane we assumed $u_\phi \ll u_z$, thus we proceed to determine u_z in order to validate the approximation.

The pressure gradient in the r direction, caused by the centrifugal force is influenced by viscosity while the gravitational force is ignored ($g\cos\beta \ll \omega^2 r$), as

$$0 = -\frac{\partial P}{\partial r} + \rho\omega^2 r + \mu\nabla^2 u_r.$$

The scalar Laplacian operator, for $h \ll L$, and using the scaling from continuity equations $u_r \sim \frac{h}{L}u_z$, can be expressed as

$$\nabla^2 u_r \sim \frac{1}{r}\frac{\partial}{\partial r}\left(r\frac{\partial u_r}{\partial r}\right) \sim \frac{u_r}{h^2} \sim \frac{u_z}{Lh}.$$

Balancing if the viscous term is much smaller than the centrifugal term, so that

$$u_z \ll \frac{\omega^2 RhL}{\nu},$$

then the viscous term can be considered small. For $h \ll R$ and $h \ll L$, the viscous term can be considered small. Thus P within the film can be determined, from the r momentum equation, using the dynamic boundary condition taking into consideration surface tension at the contact line, as

$$\int_{R-h}^{R}\frac{\partial P}{\partial r}dr = \int_{R-h}^{R}\left(\rho\omega^2 r\right)dr,$$

which gives

$$P = \rho\omega^2[R^2 - (R-h)^2] + \gamma\frac{\partial^2 h}{\partial z^2} - \gamma\frac{1}{R-h}.$$

The pressure at the wall of the tube, where $r = R$, is

$$P_{r=R} = \frac{1}{2}\rho\omega^2(2Rh - h^2) + \gamma\frac{\partial^2 h}{\partial z^2} - \gamma\frac{1}{R-h}. \tag{6.27}$$

The velocity in the main direction of the flow can be obtained by the z momentum equation, with the velocity gradient being small in the z direction, where $u_z \gg u_r$ due to the thin film approximation. Thus, the viscous term is expressed as

$$\nabla^2 u_z \sim \frac{1}{r}\frac{\partial}{\partial r}\left(r\frac{\partial u_z}{\partial r}\right). \tag{6.28}$$

The force balance in the z momentum equation, using equation 6.28 becomes

$$0 = -\frac{\partial P}{\partial z} + \rho g \sin\beta + \mu\left[\frac{1}{r}\frac{\partial}{\partial r}\left(r\frac{\partial u_z}{\partial r}\right)\right]. \tag{6.29}$$

with the pressure gradient, determined by differentiating equation 6.27, as

$$\frac{\partial P}{\partial z} = \rho\omega^2(R-h)\frac{\partial h}{\partial z} + \gamma\frac{\partial^3 h}{\partial z^3} - \frac{\gamma}{(R-h)^2}\frac{\partial h}{\partial z}.$$

Substituting this to equation 6.29 and rearranging gives

$$A = \frac{1}{r}\frac{\partial}{\partial r}\left(r\frac{\partial u_z}{\partial r}\right) = \frac{1}{\mu}\left[\rho\left[\omega^2(R-h)\right]\frac{\partial h}{\partial z} - \frac{\gamma}{(R-h)^2}\frac{\partial h}{\partial z} + \gamma\frac{\partial^3 h}{\partial z^3} - \rho g\sin\beta\right], \tag{6.30}$$

where A is independent of r. We integrate once with respect to r, applying also the kinetic boundary condition at the interface, which ensures that no fluid passes through the liquid-gas interface ($\frac{\partial u_z}{\partial r} = 0$ at $r = R-h$), to obtain

$$\frac{\partial u_z}{\partial r} = A\frac{r}{2} - A\frac{(R-h)^2}{2r}.$$

Integrating again, using the no-slip condition, where $u_z = 0$ at $r = R$, the velocity u_z becomes

$$u_z = \frac{A}{4}\left[(r^2 - R^2) - 2(R-h)^2\ln\frac{r}{R}\right]. \tag{6.31}$$

We introduce the new coordinate $\tilde{r} = R - r$, and using a Taylor series expansion to the leading order in $\tilde{r}$, equation 6.31 becomes

$$u_z = \frac{A}{4}\left[(r^2 - R^2) + 2(R-h)^2\frac{R-r}{R}\right]. \tag{6.32}$$

We return now to our starting assumption that $u_\phi \ll u_z$, and making use of the scaling of $u_\phi \sim \frac{g\cos\beta h^2}{\nu}$ and equation 6.35 we express the condition as

$$\frac{g\cos\beta}{\nu}h^2 \ll \frac{\omega^2 R^2 h^2}{\nu L} \rightarrow C_M\tan\beta \gg \frac{L}{R},$$

where

$$C_M = \frac{\omega^2 R}{g\sin\beta}$$

is the non–dimensional coefficient, retrieved by the film shape model in section 6.3.1 (equation 6.9) and represents the relative magnitude of centrifugal acceleration to gravitational acceleration. This condition is not valid asymptotically for $t \rightarrow \infty$ as L becomes large, except for $\beta \rightarrow 90°$. At late times there will be an oscillatory u_z due to the Coriolis force and the oscillating u_ϕ.

From volume conservation, and with u_r and u_ϕ being much smaller than u_z we get

$$\frac{\partial h}{\partial t} = -\nabla\cdot q = -\cancel{\frac{1}{r}\frac{\partial}{\partial r}(q_r r)} - \cancel{\frac{1}{r}\frac{\partial q_\phi}{\partial\phi}} - \frac{\partial q_z}{\partial z}$$

where

$$q_z = \int_{R-h}^{R} u_z dr = \frac{A}{4} \int_{R-h}^{R} \left[(r^2 - R^2) + 2(R-h)^2 \frac{R-r}{R} \right] dr.$$

Integrating using the no–slip condition, for $h \ll R$ and keeping only the higher order terms we get

$$q_z = \bar{u}_z h = \int_{R-h}^{R} u_z dr = \frac{A}{4} \frac{h^3}{3}. \tag{6.33}$$

Considering equation 6.33, replacing A from equation 6.30 and for $h \ll R$, we get

$$\frac{\partial h}{\partial t} - \frac{\omega^2 R}{48\nu} \frac{\partial}{\partial z} \left(h^3 \frac{\partial h}{\partial z} \right) - \frac{\gamma}{R^2} \frac{\partial}{\partial z} \left(h^3 \frac{\partial h}{\partial z} \right) - \frac{\gamma}{12\mu} \frac{\partial}{\partial z} \left(h^3 \frac{\partial^3 h}{\partial z^3} \right) + \frac{g \sin\beta}{12\nu} \frac{\partial h^3}{\partial z} = 0. \tag{6.34}$$

There are three regimes that can be explored theoretically from equation 6.34. First, the steady state of rotation can be approximated by a balance between the centrifugal and the gravitational term. This approximation leads essentially to the film shape model analysed in section 6.3.1. Secondly at early times the time dependence of the film thickness can be obtained by balancing the first two terms of the equation. If $h \sim t^a$ and $z \sim t^b$, then we would expect that the length of the film increases as $L \sim t^{1/5}$, while the thickness decreases as $h \sim t^{-1/5}$. Thirdly, the thickness evolution can be determined by taking into consideration all the terms including surface tension effects near the contact line. Lastly, a linear stability analysis can be employed to determine whether there are fingering instabilities at the contact line and along the free surface of the film.

Considering the Nusselt approximation, following the approach of section 2.2.2 of the literature review, we assume uniform thickness and equation 6.32 can be scaled as

$$u_z \sim \frac{\omega^2 R^2 h^2}{\nu L}. \tag{6.35}$$

The scaling of equation 6.32 was formed taking into consideration the term containing the centrifugal force only under the conditions

$$\gamma \ll \rho\omega^2 R^3 \text{ and } C_M \gg \frac{L}{h}.$$

The last condition implies that the component of gravity cannot be ignored at late times as L becomes large. Before gravity becomes important and considering volume conservation so that $h \sim \frac{V}{LR}$ and $L = 0$ at $t = 0$, then

$$L \sim \left(\frac{\omega^2 V^2}{\nu} \right)^{\frac{1}{4}} t^{1/4}. \tag{6.36}$$

Hence the evolution of the length of the film has a time dependence $L \sim t^{1/4}$. As the film thickness is considered constant, the time dependence is slightly different than the time dependence determined by the analytical approximation as expressed in equation 6.34.

Although the theoretical approach for an instant spin–up is an interesting problem, it is beyond the spectrum of this thesis. The acceleration of the motor and the imperfections of the tube make this problem relevant but not representative of the spin–up observed in the VFD. It should be noted that the experimental observations analysed in section 6.3.2 show a linear dependence due to the acceleration of the motor. In reality, the film does not evolve with fixed ω but with an increasing ω, dependent on the acceleration of the motor. To our knowledge

there is no publication of a film going uphill on an inclined plane. A similar problem has been solved by Bertozzi & Brenner (1997) for a thin film flowing down an inclined plane and could give useful insights to the appropriate scaling for equation 6.34. Hence future research could investigate the film thickness evolution for instant spin–up.

6.5 Other considerations

Several variations of parameters could be investigated the VFD. In this section the focus is on the film formation using two liquids of different density, the spreading pattern in CF and the fluid mechanics instabilities that could enhance chemical reactivity. Although each variation consists of a separate set of experiments, the observations are mainly qualitative. The sets are described in this section to give a broader idea of the fluid motion but they could definitely consist individual research projects.

6.5.1 Multi-fluid film development

Consider two liquids of different density stationary in the VFD. The liquids form a density interface, across which a reaction occurs because of diffusion. Adding rotation to the tube, the liquids spread along the walls forming a very thin film. The denser liquid is driven towards the wall while the lighter liquid forms a film over the denser liquid, as shown in Figure 6.24. This mechanism of the VFD leads to increased pressure gradients in the r direction, accelerating the separation of the two liquids even when the solution is premixed. The two solutions maximise their shared interface and consequently their reaction zone, by increasing diffusion and advection, as explained in section 6.3.6. This density separation is observed both in CM and in CF.

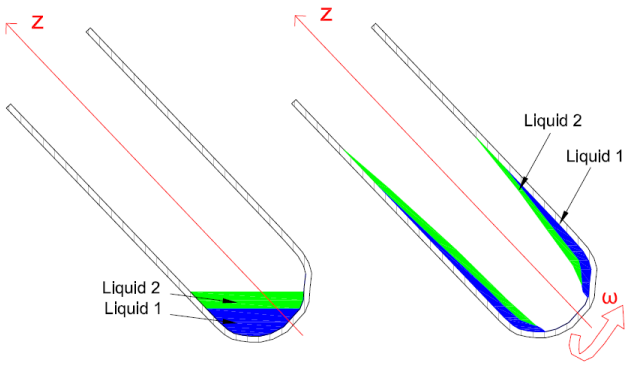

Figure 6.24: Consider liquid 1 being denser than liquid 2. The two liquids are initially at rest. After the spin-up the fluids instantly separate. The denser liquid forms a film attached to the rotating solid substrate. The lighter liquid forms a thin film over the denser liquid.

Miscible fluids tend to react due to diffusion, even immediately after they are placed in a stationary flask. Specifically, considering CM in the VFD, miscible fluids tend to mix while they are placed in the tube. If the fluids mix before the initiation of rotation in the VFD, then the reaction time is not necessarily representative of the performance of the VFD per se. In order to avoid the mixing during the preparation, we focus in experiments with either one liquid or two immiscible fluids. The definition of miscible and immiscible liquids was given in sections 3.2.2.

For immiscible liquids consider 0.3 ml of toluene and 0.7 ml of water placed in the VFD (case CM45GT5000W7T3). Even if the solution is premixed, the two immiscible liquids tend to separate before the initiation of motion. For example, water, which is denser, covers the base of the tube while toluene forms a layer over the water. During the spin-up in CM, the rotating tube brings the fluid into rotation. The fluid in contact with the wall is dragged by the moving substrate, while viscous stresses set more fluid into rotation.

After the spin–up, the two fluids maintain the stratification along the walls, as shown in Figure 6.25a. The part of the toluene that propagates first is not in contact with the water. In the case of chemical reactions, while the fluid is at steady state of rotation, it seems as no reaction will happen for the body of toluene that propagated first towards the upper end of the tube.

When the film is at steady state, patches disrupt the water film. The patches are discontinuities of the denser liquid along the wall of the tube. The patches are observed in different runs, are inconsistent in shape and positioning. There is no consistent pattern between the patches which would justify a fluid mechanics instability mechanism. It seems like some of the toluene reached the side walls or the bottom while the water film was forming. Thus the patches were never covered with water. The patches remain visible and at the same position even 2 minutes after the spin-up, which is the longest obtained recording, as shown in Figure 6.25b.

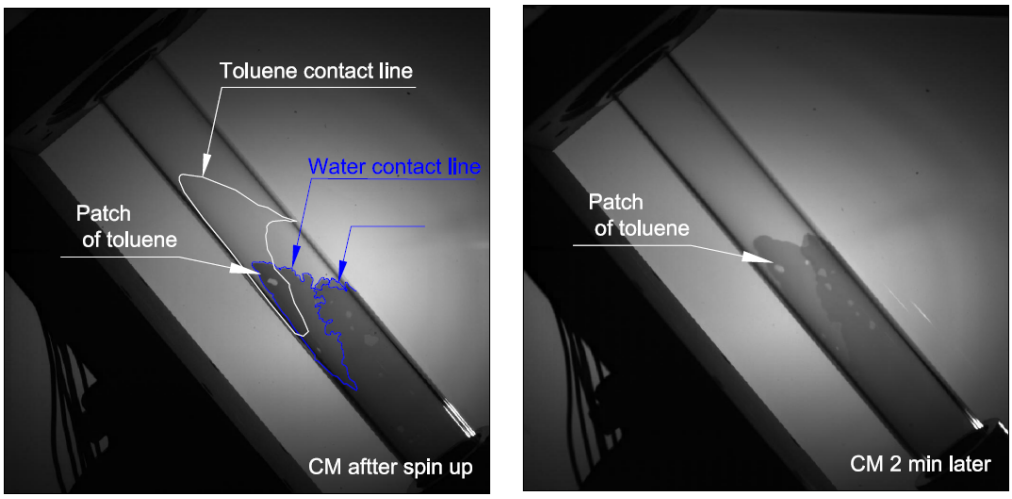

(a) (b)

Figure 6.25: (a) Picture taken immediately after the spin-up of a film of 0.70 ml of water and 0.30 ml of toluene, at steady state, rotating with the tube at 5,000 rpm (case CM45GT5000W7T3). The contact lines of toluene and water are already in phase. (b) Picture taken during the same experiment, 2 min after the spin-up, where the disruptions of the water film in (a) are still present, demonstrating that no significant liquid displacements occurs.

This is a direct demonstration that once the film, reaches its steady state, no significant fluid displacement occurs. Some of the smaller patches might disappear but the larger patches remain almost stationary even minutes later. So there is some motion in the film but not adequate to cause significant displacements. This almost stationary film maintains an increased interface between the two liquids. The wavy structure of the toluene - water contact line is in phase with the air - toluene contact line. The axial position of each contact line and their relative distance is proportional to the volume of each liquid. There are two protrusions that appear at

the same positions, when using the same tube in a sequence of realisations. The repetition of the protrusions' position indicates the ellipticity of the tube, as explained in section 6.2.

6.5.2 Wave instabilities

A wave formation is observed in the VFD under three conditions. The first condition is during the spin-up where a helical wave is observed as shown in Figure 6.26a. The second condition is during the landing of a water droplet, in CF, onto an already developed film of toluene, shown in Figure 6.26b, and analysed in the following section 6.5.2.1. The third condition, of wave formation, is met while the film is at steady state, where there are indications of a persistent free–surface instability, analysed in section 6.5.2.2.

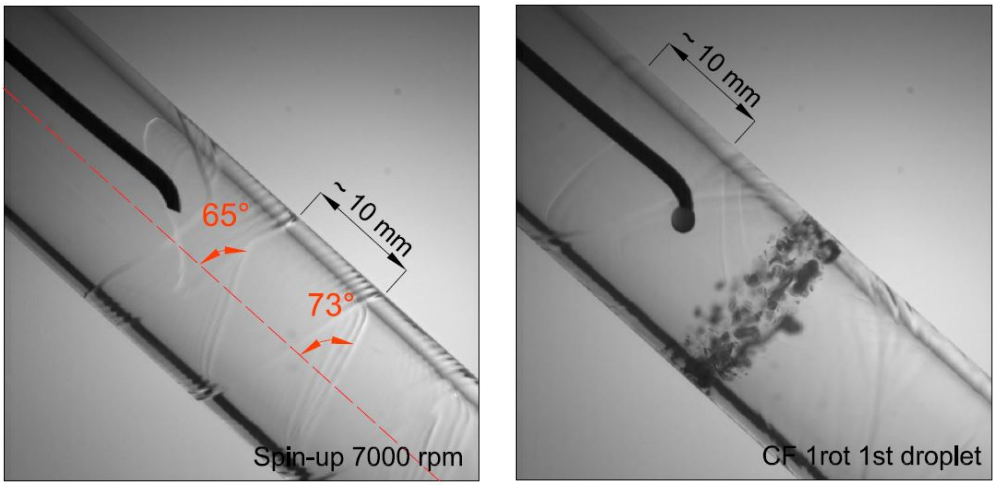

(a) (b)

Figure 6.26: Example of formation of a stretching spiral wave in the VFD (a) during the spin-up in CM (case CM45GT5000T1)and (b) during the landing of the first droplet of water in a film of toluene in CF (case CF7000GT45T2W1).

In the first case where the helix is formed at the base of the tube and as the contact line propagates, the helix stretches, thus the angle of the spiral decreases. When the film is fully developed, i.e. at its maximum extent, the helical wave is no longer visible. The characteristics of the helix, during the spin-up, measured at 4 cm from the base of the tube, are similar for different ω, with the wavelength being approximately 1 cm and the angle with respect to the z axis decreasing as the film propagates along the tube. The similar structure of helix for different ω can be justified when considering that the spin–up is characterised by the motor acceleration. The helix was visible for a range of inclination angles, exhibiting the same evolution characteristics. Thus it seems as gravity has minimal influence to the formation of the spiral.

6.5.2.1 Continuous Flow

The interest in CF is focused on the landing and spreading of droplets in an already rotating tube. In order to visualise the droplet impact, the droplet must land at the walls of the tube, thus the pipette is positioned 4 cm away from the base of the tube. The main body force applied to the falling droplet is gravity. The air, rotating in the tube, could affect the motion of the

droplet. However, we observe experimentally that the droplet motion is characterized by free fall with minimal effects from the recirculating air. This means that while the droplet lands in the tube, there is a downwards motion of the bulk of the droplet, not yet touching the rotating walls. The first droplet lands on a dry surface and moves only downwards due to gravity, forming a helical wet film, as indicated in Figure 6.27a.

When a film of water is already developed in the tube, the droplet of dyed water breaks the film of the uncoloured water and is eventually entrained in the film, causing perturbations, which propagate downwards and upwards from the axis of landing in the form of waves, as shown in Figure 6.27b. The landing droplet spreads in a different pattern than in Figure 6.26b forming an area of intense mixing.

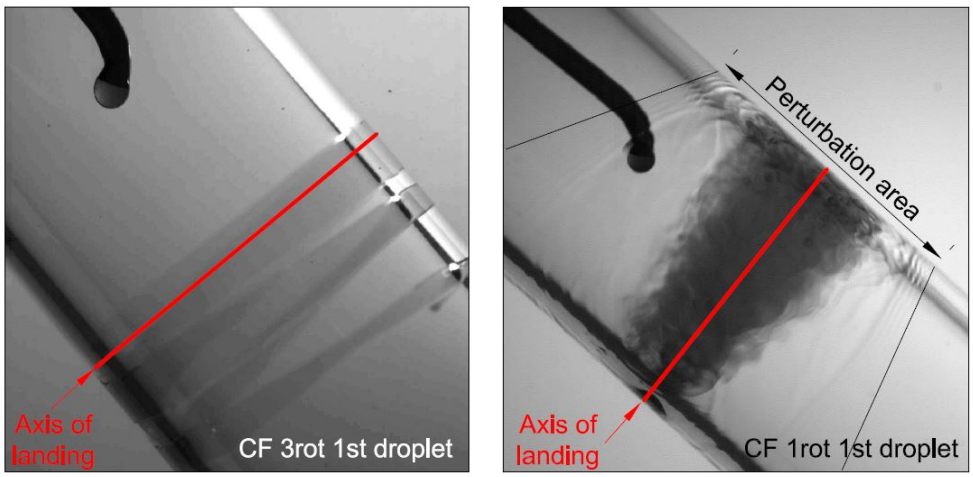

(a) (b)

Figure 6.27: (a) The first droplet, in CF, lands on a dry surface, forming a helical wet area. (b) A droplet, landing in an already developed film of water, causes disruptions in the form of waves (case CF7000GT45W2W1).

The mechanics during the droplet landing and entrainment in the film are better visualised using immiscible liquids. The case CF7000GT45T2W1, shows droplets of dyed water landing onto an already rotating and fully developed film of toluene. The first droplet forms patches of water, along the azimuthal direction, at the height of landing, see Figure 6.28a. Each landing droplet, disrupts the rotating film, causing the formation of waves, which propagate both upwards and downwards, symmetrically from the axis of landing, as shown in Figure 6.28b.

The landing droplet, in the laboratory frame of reference, initially has no rotation. While the droplet lands, it interacts with the film, as a stationary obstacle with the film moving past it. The obstacle breaks the film of toluene that is rotating at steady state, and causes the formation of waves. The obstacle breaks the flow for approximately one rotation period, thus for a distance of $2\pi R$. A finite amplitude disturbance of a length scale that is not very large compared to the film thickness is observed and has a resemblance to Kelvin ship waves. For a mechanism similar to Kelvin ship waves we would require the waves to be dispersive.

However, the film is very thin and capillary effects could be important in the VFD. The capillary length in the VFD is defined as $\left(\frac{\gamma}{\rho\omega^2 R}\right)^{1/2} \sim \mathcal{O}(10^{-4})$ m. If surface tension is dominant, the ship wave pattern, accounting for the surface tension effect, can be totally different from the classical Kelvin ship wave pattern and could be approximated by a Mach-like law with the

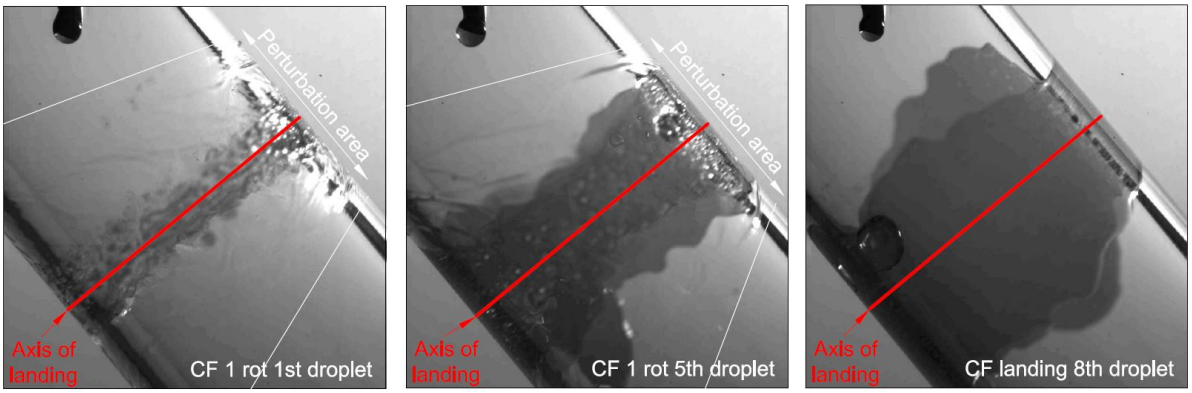

(a) (b) (c)

Figure 6.28: Evolution of film formation, in CF, where droplets of water land in an already developed, rotating at 7,000 rpm and at steady state film of toluene (case CF7000GT45T2W1). (a) The first droplet forms a sequence of patches in the azimuthal direction around the area of landing. (b) Each droplet disrupts the rotating film causing wave formation, with the waves transferring only toluene. The droplet is entrained in the water film rotating with the wall while the film of toluene is restored on top of the water film. (c) The sequence of droplets forms a film of water around the area of landing (set CF-GT45T2W1).

angle of the waves being dependent on the angular velocity of the tube in correlation with the duration of the droplet landing and the width of the droplet (Moisy & Rabaud, 2014). Making use of the scaling and the results of Moisy & Rabaud, in the VFD $Bo \sim 10$ (defined here as the ratio between the diameter of the droplet and the capillary length). The magnitude of Bo is considered very high and so surface tension is not very important.

The wake is a shallow-water wake, of angle governed by the film thickness and differs from the (dispersive) deep-water wakes considered by Moisy & Rabaud. The wake angle is governed by $\sqrt{(g'h)}/u$. where $g' \sim \omega^2 R$ is the rotational acceleration and $u \sim \omega R$ is the velocity of the disturbance. This scaling could be useful in additional experiments where, by measuring the wave angle, the determination of the film thickness near the area of the droplet landing would be possible.

The waves form a helix, which stretches as they propagate along the tube. As the droplet has fluid spun out of it, the disturbance it creates will decrease in amplitude. If the waves are nonlinear, and the wave speed increases with amplitude, then the waves produced later will propagate more slowly, and so give the impression of the spiral being stretched. The extent of the disturbance is approximately the same after every falling droplet, see the area of disturbances in Figure 6.28a, in comparison with the disturbances in Figure 6.28b. The break of the toluene layer might work as a buffer zone between the glass and the water droplet decreasing the kinetic energy acquired by the fall.

After every droplet landing, the waves stretch due to the pressure gradients caused by the increased centrifugal force and due to the volume entrained in the film. It seems as only toluene is transferred with the spiral wave. The repetition of this phenomenon for every falling droplet indicates that the droplet breaks the layer of toluene and then forms a water film under the toluene film. The water film expands along the wall while toluene restores the gap created after every fall. The restoration is a result of the pressure gradient applied on the liquid. The process

of (a) breaking the toluene film, (b) forming the water film and (c) restoring the toluene film causes increased shearing between the two reactants. To confirm the nature of the waves we need to investigate further the rate of change of the angle of the envelope of the waves.

The sequence of droplets forms a film of water developed around the landing point, which remains almost stationary in the rotating frame, as shown in Figure 6.28c. As droplets are added, the length of the water film is increased both upwards and downwards, with the azimuthal distribution following also the expected asymmetries due to the ellipticity of the GT (explained in section 6.2). The liquid extracted from the top of the tube is equal to the volume of water entrained in the film in the form of droplets.

The almost static water film and the restored layer of toluene, due to density differences form essentially two films, maximising their interface, which works as a reaction zone. As the denser liquid forms a film close to the point of landing, the two liquids interact locally and the chemical reaction must be initiated or even completed at the same area. After landing, some discontinuities in the film appear, in the form of gaps or droplets. At 7,000 rpm and after approximately 20 rotations, the discontinuities slowly disappear, suggesting a slow fluid displacement. This displacement seems to be slightly faster than in CM. A possible explanation is the layer of toluene returning above the water film, carrying away toluene trapped in the water film.

Overall, it seems that in CF the liquid-liquid separation happens almost instantly as in CM. However in CF, the break and restoration of the rotating liquid, repeated after every droplet landing, works in favour of fluid shearing. Therefore this mode of processing should present increased performance in comparison to CM. Additionally by moving the pipette during the process or by using multiple pipettes, several reaction zones can form locally in the tube. This characteristic makes the VFD attractive for a sequence of concurrent reactions or for products that require a sequence of reactions within the same processing set-up.

6.5.2.2 Vapour effects

Spiral waves can be observed when the film is in a quasi–steady state, although the mechanism for their formation is slightly different than the spirals during the spin–up or due to the landing droplet. The main difference is that the spiral in the vapour case has constant angle and wavelength along the tube. A helical formation appears in a fully developed film of bromothymol blue while a droplet of acetic acid forms at the edge of the pipette, as shown in Figure 6.29b (set V-QT45B3A40). The experiment uses the same configuration with the reaction experiment, described in section 6.3.6, of a fully developed film of bromothymol blue but replacing the droplet of sulfuric acid with acetic acid (16M), of pH 1.78: $C_2H_4O_2 \xrightarrow{H_2O} C_2H_2O_2{}^{2-}$.

The helix reported here is only observed when acetic acid is used. A comparison of the two experiments, using a droplet of sulfuric or acetic acid respectively, is shown in Figure 6.29. The helix remains visible at the front of the colour change, when acetic acid is used, at all times, as shown in Figures 6.29b and 6.29d, in comparison with no helical formation for sulfuric acid in Figures 6.29a and 6.29c.

The helix is stationary in the rotating frame of reference, but becomes visible as the reaction front propagates, producing the colour change. The wavelength and spiral angle decrease with

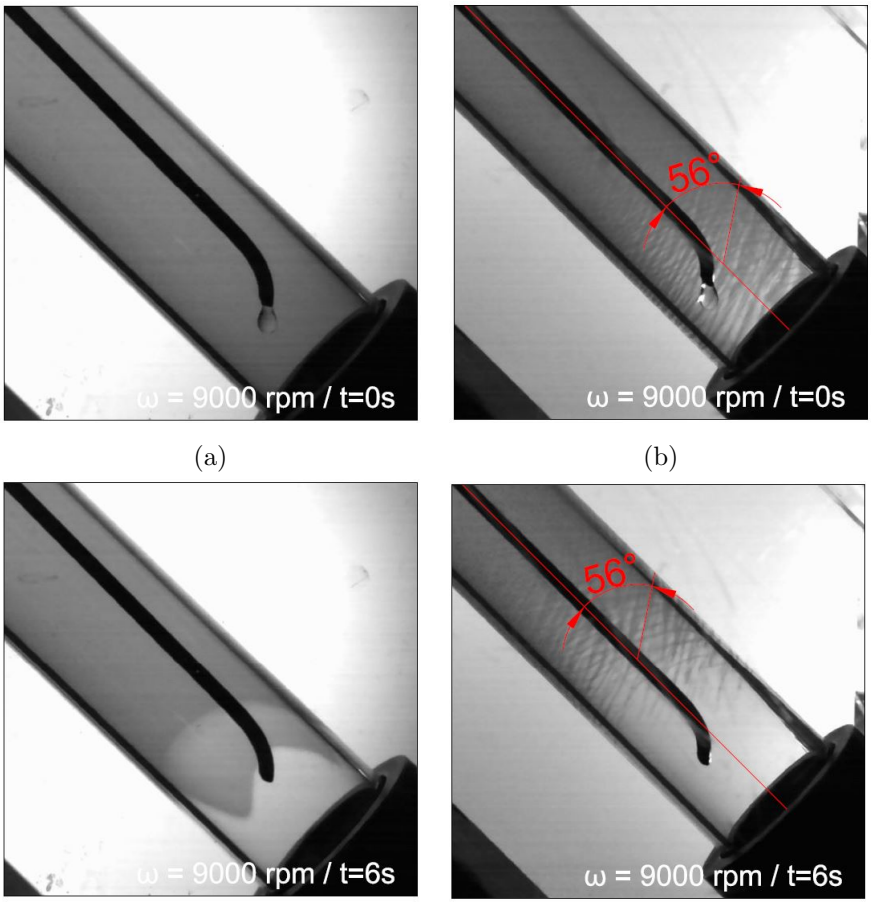

Figure 6.29: Initial stage of droplet formation at the pipette for (a) sulfuric acid (case D9000QT45B3S40) and (b) acetic acid (case V9000QT45B3A40), with the later forming a helix of colour change in the already developed film of bromothymol blue, due to infusion of acid in the air. After the entrainment of the droplet (c) the reaction propagates almost uniformly while (d) the reaction due to acetic acid maintains the helical structure at all times.

increased ω, thus the best visualisation of the spiral occurred at 9,000 rpm, where the wavelength was approximately $\mathcal{O}(1)$ mm and the angle at 56°. For comparison, at 5,000 rpm, the wavelength was measured ~ 1.5 mm and the spiral angle at 70°. The length scale of the wavelength is smaller than R and similar to the characteristic capillary length of $\mathcal{O}(10^{-4})$ m.

The helix becomes visible when using acetic acid, due to vapour acidification of the indicator. The infusion of acid in the air inside the VFD, even before the landing of the droplet, makes the vapour effect visible throughout the reaction progress. The distribution of acid in the air works as an indicator for the visualisation of the helical waves. For comparison, the vapour pressure of acetic acid is 3458 Pa at 20°, while for sulfuric acid is 0.133 Pa at 20°C. The constant angle and wavelength indicate the persistence of the phenomenon, despite the fact that there is no significant fluid displacement.

Knowing that the liquid thickness is decreased going upwards in the tube, we would expect variations in the wavelength of the spiral. However the spiral maintains the same characteristics, thus the focus moves to the air rotating in the tube. The disturbance of the circulating air could trigger the presence of a permanent helical wave at the interface with the air boundary. Factors

that could cause the disruption of the air boundary are the presence of the pipette, the formation and the free fall of the droplet or tube imperfections.

In conclusion, the rate of stretching of the spiral after a landing droplet and the wavelength of the fixed helix of vapour are related to ω. The vapour effect increases dramatically the evolution of the chemical reaction. Within the experiments available, we cannot obtain the appropriate measurements to quantitatively investigate these characteristics further. New experimental set-up is required with more advanced visualisation techniques, especially for the investigation of the air circulation in the VFD.

6.6 Summary

The fluid mechanics in the VFD are explored for the two modes of processing, CM and CF, at steady state and during spin-up. Two tubes are used for the experiments and both are found to have geometrical imperfections. The ellipticity measured in the GT and the eccentricity measured in the QT, cause the formation of protrusions, due to local alterations of the magnitude of centrifugal force. For increased ω, the protrusions prevent azimuthal circulation, guiding the liquid fast towards the exit of the tube. As soon as the protrusions form, the azimuthal motion of the fluid is very restricted within the protrusion. Assuming that the protrusions are a disadvantage for the performance of the VFD, from the perspective of the work at Flinder University, assessing the symmetry of the tubes should be a priority.

During steady state, in CM, the volume capacity experiment shows that most of the fluid forms a thin film at the walls, only when $\omega \geq 4,000$ rpm. Below that limit we observe swirling flow. Beyond that limit, the total volume of liquid develops as a thin film along the walls of the VFD.

The thin film thickness can be close to the boundary layer thickness under laminar flow or can be thicker, exhibiting a not–trivial flow pattern. Thus, film thickness tends to be the most critical parameter for the performance of the device as it defines whether the reaction occurs under turbulent or laminar conditions. Neutron imaging experiments, conducted at ANSTO, gave an insight to the film thickness at steady state in CM. The technique is more appropriate for stationary objects, thus a new methodology is developed in this chapter, based on the projection of the depth of the film over more than 1,000 rotations. The results are in good agreement with the film thickness determined from the film shape model for rotation rates up to 6,000 rpm. At the higher end of rotation rates the protrusion creates a very thin film and the film profile is deviated from the expected parabolic shape. Knowing the film thickness, pressure gradients across the thickness of the film are determined and are found to increase with increased ω. The pressure differences are small compared to the absolute values of pressure $\sim \mathcal{O}(10^8)$ Pa, that would cause increase in D.

Pressure gradients in the r direction might be more important for enhanced chemical reactivity. Increased film length increases the area over which pressure gradients act across the thickness of the film. Density differences separate the reactants which form two layers both in CM and in CF. Especially in CF, the experiments conducted with immiscible liquids show that when a droplet of a denser liquid lands on an already rotating film with reduced density, the denser liquid breaks the film and forms a layer between the lighter liquid and the wall. The

process of the separation forms a front of the denser liquid, entering the area between the wall and the lighter liquid, which would lead to enhanced advection and vorticity at the interface of the two liquids. In support of this argument, the rate of ionic diffusion in the VFD, measured from 5,000 to 9,000 rpm, shows that the reaction rate increases with increased ω, and is well correlated with a relevant mathematical approximation also developed in this chapter.

The spin-up in CM considers the evolution of the film when the tube rotates with constant rotation rate and the fluid is already predominantly rotating and is spreading along the length of the tube towards its equilibrium shape. The problem is approached using the Navier–Stokes equations and a thin film approximation. The main characteristics of the spin–up problem are described, along with the assumption that turn the three–dimensional problem into a two–dimensional problem. The acceleration of the motor and the imperfections of the tube make this problem relevant but not representative of the spin–up observed in the VFD. To our knowledge there is no publication of a film going uphill on an inclined plane. A similarity solution and linear stability analysis could give useful insight into the film development for instant spin–up and the stability of the system.

In CF, we mainly explore the entrainment of droplets in an already rotating film at steady state. Experimental observations show that the droplet breaks the rotating film, lands onto the moving substrate and is eventually entrained in the film. During landing, the droplet works as an obstacle, appearing to excite waves that have a resemblance to Kelvin ship waves. The waves develop from the axis of the landing droplet, forming a helical wave structure. The helix stretches until it becomes invisible. A similar helical structure but with fixed angle is caused by the air rotating in the tube. The length scale of the wavelength $\sim \mathcal{O}(10^{-3})$ m, is smaller than R and similar to the characteristic capillary length. Thus, surface tension may be important and dispersive mechanisms may exist. The main restoring mechanism is the pressure gradient varying due to centrifugal force and the thickness of the fluid. The helical formation could be an important mechanism of shearing and require further investigation.

Overall, this chapter describes the main fluid mechanics characteristics in the device that could enhance reactivity. The thin film in the VFD ensures fluid uniformity and increased reaction zones, while the increased pressure gradients enhance diffusion and advection rates.

Chapter 7

Conclusions

7.1 General remarks

Our collaborators, Prof. Colin Raston (the inventor of the VFD) and his team at Flinders University, Australia, have concluded that the best performance of the VFD, in terms of chemical reactivity for a wide range of reactions, is achieved when the existing VFD apparatus is tilted at 45° and rotating from 7,000 to 8,000 rpm. One of the main goals of this thesis is the description of the fluid mechanics in the VFD, exploring parameters such as the rotation rate, and tilting of the device. Another goal is to understand why the operational configuration of the Raston group is optimal and to provide insight into how the performance can be improved further.

The methodology is designed according to the two modes of operation in the VFD. In confined mode (CM), a fixed volume of liquid is placed at the base of the VFD before rotation is initiated. The development of the thin film is essentially the spin–up problem in the VFD and was investigated by a series of experiments in the device. The spin–up problem in the VFD is different from a spin–up in a vertically positioned tube, as the tube is inclined with $\beta < 90°$. The characteristics of the film at steady state are less strongly affected by the tilt but describe the fluid mechanics environment for most of the processing time. Hence more attention is paid to a film rotating at steady state.

In continuous flow (CF), droplets fall periodically inside a rotating tube, with the tube sustaining a liquid thin film developed along the walls. The dynamics of CF are investigated by conducting experiments of single droplets landing on rotating disks and inside the VFD. Thus, three classes of experiments are formed. In the first class, droplets land on a flat rotating surface. In the second class, droplets land on a hemispherical disk and in the third class, droplets land inside the VFD. All the experiments are conducted at room temperature as one of the aims of green technologies in flow chemistry is the avoidance of elevated temperature.

Experiments on flat and hemispherical disks investigate the dynamics of droplet landing, the film development, the onset of contact line instabilities at r_c, the instabilities at the contact line and along the free surface of the film. Most of the research is focused on the flat disks, as the changing curvature of the hemispherical disk makes experimental measurements challenging. The experiments reveal the presence of a ring growing in volume before r_c and shrinking in volume, i.e. leaving fluid behind beyond r_c. The parameters of variation are the rotation rate, the height of release, the droplet volume, the smoothness of the disk and the inclination of the

device. By increasing ω, fluid is entrained faster in the ring and r_c is decreased. By increasing the height of release, shape oscillations after landing seem to have a long lasting effect, decreasing r_c. By decreasing the droplet volume, the value of r_c is almost constant and consistently larger than for increased liquid volume. By using a smoother disk, r_c is increased. Assuming a thin film, the lubrication approximation is used for the formulation of equations, taking into account simplifications, aiming mainly to neglect azimuthal motion and turn the spreading from a three–dimensional to a two–dimensional problem.

On the flat disks after the contact line becomes unstable at r_c, two instabilities are observed, a fingering instability and spiral waves at the free surface of the film. Although we clearly observe fingering instabilities on the flat and the hemispherical disks, the VFD does not develop similar instabilities, thus these phenomena are not analysed further. Prograde spirals at the free surface of the film suggest a shear–induced instability. The initial observation of the spirals was accidental and achieved only when the optical axis of one of the halogen lamps was placed immediately above the disk surface. The spirals are formed after the front reaches r_c, while the ring volume is shrinking, and the direction of the spirals suggests an instability which could be correlated to the film rotating almost at steady state and to the ring leaving fluid behind.

As there is minimal literature on the fluid mechanics for the film development in the VFD, mathematical approximations are determined to describe the experimental results. One mathematical model is formed to describe the shape of the thin film at a steady state of rotation, taking into account ω, tube inclination β and fluid volume V. The shape model is in good agreement with the film thickness experiments at rotation rates up to 6,000 rpm. Beyond that limit the protrusion forms a very thin film and the profile is deviated from the expected parabolic shape. The film thickness experiments are conducted using neutron imaging while the present author was visiting ANSTO, Sydney, Australia. The shape model is also developed in parallel with the Raston group, as the two laboratories are in collaboration and we were unaware of the time the publication of Solheim et al. (2019) would be publicly available.

The neutron imaging experiments in the VFD are the first attempt at ANSTO to use the technique in rotating objects and certainly the first for the VFD. Hence, a mathematical approach is suggested in this thesis, based on the attenuation of neutrons passing through the rotating tube. During the experiment, the camera exposure time requires the capture of the film thickness to be averaged over more than a 1,000 rotations. Thus, the tube imperfections and the asymmetry of the film are not captured in detail and are only approximated by the method. The resolution of the images allows measurements for a film thickness $h > 10^{-5}$ m. Consequently, the shape of the contact line and the film with thickness lower than that limit are not accessible from the experimental results. However, the developed mathematical method, explaining the neutron imaging results, gives an insight to the film shape and thickness at steady state.

From the neutron imaging experiment we obtain the film thickness from 1,000 to 9,000 rpm. At 7,000 rpm, the film thickness is of $\mathcal{O}(10^{-4} - 10^{-5})$ m, close to the Stokes layer thickness of $\mathcal{O}(10^{-5})$ m, assuming that the boundary layer at the side walls scales as a Stokes layer, $\delta \sim \left(\frac{\nu}{\omega}\right)^{1/2}$. From the spin–up experiment, recorded with the high–speed camera, we see that the film at steady state is almost static to the walls, thus there is small azimuthal motion.

Based on the experimental observations, there are no specific fluid mechanics conditions that are met only at approximately 7,000 to 8,000 rpm. In contrast, as the rotation rate increases the

film becomes thinner and more uniform, while pressure gradients increase. Assuming that the increased pressure gradients enhance diffusion and advection, from a fluid mechanics perspective, one could argue that reactivity could be even more enhanced with increased ω as long as the appropriate residence time is secured.

The inclination of the tube also enhances film uniformity. However, for a given flow rate, increased ω and decreased inclination come with the expense of reduced residence time in CF. The residence time is also related to the formation of film protrusions due to tube imperfections. The protrusions limit the processing time as they guide the liquid faster towards the exit, limiting azimuthal displacements. The residence time varies for different chemical reactions, thus for reliable measurements of the performance of the VFD, experiments should be conducted with the same tube. The inclination of the VFD can also achieve better control over the chemistry by controlling the residence time.

The experimental observations show significant increase in the reaction rate with increased rotation rates. A new mechanism, that may help explain enhanced chemical reactivity in the VFD, is proposed in this thesis. The chemical processing in the VFD is typically conducted by the use of two liquid reactants, which are usually of different densities. Due to density differences and the centrifugal force, the denser liquid forms a front between the wall and the lighter liquid, attempting to achieve layering between the two liquids. During this process, (a) shearing is present at the interface of the two liquids, (b) the increased interface enhances diffusion and (c) the density differences initiate vorticity. Thus, both diffusion and advection are present at the interface. The theoretical approximation of the above hypothesis determines an enhanced reaction coefficient D_m, which is in good agreement with the experimental results measuring reaction rates. Thus, we can come to the conclusion that this is the main mechanism explaining why the VFD outperforms other processing devices.

Another mechanism that could enhance reactivity is the process of a droplet landing in an already rotating film. The break of the film causes the formation of waves which propagate away from the axis of landing. The film is restored along the landing axis, reaching a new equilibrium. The process of (a) breaking the film, (b) having waves propagating along the film and (c) the restoration of the film reaching a new equilibrium, is another mechanism, repeated with every falling droplet, that could be beneficial for chemical reactions.

In conclusion, it appears that the Raston group has found a golden rule of ω and β, that secures increased pressure gradients for enhances reactivity and enough residence time for the completion of the reaction. Chemical reactivity depends on diffusion and advection. The fluid mechanics in the VFD, mainly due to the increased centrifugal force, can increase the reaction rate. Increased rotation rates and an inclination angle of 45° lead to increased interface between the reactants along which diffusion and advection occur due to pressure and density differences.

7.2 Connections with the literature

This section connects the literature review with the findings of the thesis. The main mechanisms of enhanced reactivity identified in this thesis are also mentioned in an attempt to explain the optimum performance of the VFD at 7,000 to 8,000 rpm.

Regarding droplet spreading in spinning disks, the process of spreading is divided in three stages. The first stage is the transient stage, which starts at the first contact of the droplet with the disk and ends when the droplet reaches the quasi–steady radius at early times after the fall and before centrifugal force becomes the main driving force of motion. In order to form a scaling argument for the transient radius, the theory of droplets landing in stationary surfaces is explored (Pasandideh-Fard et al., 1996). The scaling is formed in the rotating frame of reference, using an energy balance between the release time, the contact time and the transient time. The scaling uses a viscous dissipation term proportional to the maximum radial velocity during the transient stage and the vertical velocity at the contact time $\frac{u_r^2}{u_{z(t=0)}}$, assuming that $u_r \sim u_{z(t=0)}$. This approximation is not found in the literature. Although further analysis could be employed for the viscous dissipation term, the scaling is in good agreement with the experimental results. Thus we conclude that viscous dissipation can be approximated with this scaling.

At the next stage we explore the time dependence of a droplet spreading beyond the transient stage and before the contact line becomes unstable at r_c. There is extensive literature on the spreading rate and the fingering instability of single droplets spreading on spinning disks at rotation rates lower than 3,000 rpm ($Bo < 100$) (Bhatelia et al., 2009). This thesis takes into consideration existing literature on spinning disks and tests the relevant methodologies and approximations on rotation rates greater than 3,000 rpm ($Bo \geq 100$). Similarly to other publications on spinning disks, the spreading is divided in two areas, the film and the ring (Emslie et al., 1958). Typically, under constant flux for $Bo < 100$, the spreading is scaled with the Nusselt approximation ($r_r \sim t^{1/4}$), assuming a uniform film (Burns et al, 2003). However, simple flow visualisation experiments, using a high–speed camera, show that the radial evolution of the droplet front scales as $r_r \sim (C_0 - C_\omega t)^{-3}$. We attribute the deviation from the Nusselt film to the behaviour of the ring. The PIV experiments shows that the film and the ring move with different velocities, with the film moving faster than the ring, for $r_r < r_c$. The different velocities indicate that the film guides fluid to the ring, with the latter growing in volume. The ring is modelled as a growing semi–toroid and the model is in good agreement with the experimental results for variations in the rotation rate, height of release, droplet volume and disk smoothness.

The contact line becomes unstable at the critical radius r_c, defined when the spreading pattern is deviated more than 10% from a perfect circle. For a droplet volume of $80\mu l$, at r_c the thickness of the film ($\sim 10^{-5}$ m) is 10 times smaller than the thickness of the ring ($\sim 10^{-4}$ m). The ring thickness is slightly larger than the boundary layer thickness, assuming that the boundary layer in the rotating disk scales as a von Kármán layer layer, $\delta \sim \left(\frac{\nu}{\omega}\right)^{1/2}$.

When the thickness of the film is greater than the boundary layer thickness, the Coriolis force becomes important (Momoniat & Mason, 1998). According to Cho et al. (2005), the wet area is increased due to the deflection of the fingers. In a similar way, we suspect that the Coriolis force is responsible for the redistribution of liquid in the azimuthal direction inside the ring. This effect of Coriolis force could delay the onset of contact line instabilities by suppressing the magnitude of capillary pressure gradients, hence we suggest that the Coriolis force works as a stabilising factor for axisymmetric spreading.

Based mostly on the results from droplet volume variations, and although there is no solid evidence, we suggest that contact line instabilities occur only when the film stops feeding fluid to the ring. By using a droplet of 40 μl, the value of r_c and t_c are increased compared to

experiments of a droplet of 80 μl, at all rotation rates. The spreading time for a droplet of 40 μl is slightly increased, compared to the spreading time for a droplet of 80 μl. Thus, the contact–line instability is delayed until the feeding of the ring is stopped. This observation can be related to the work of Wang et al. (2014), showing that the effect of the discharge rate on r_c and t_c is almost negligible as long as the whole volume of liquid has been discharged before the onset of fingering instability. This observation suggests that as long as the area near the contact line is fed by liquid, r_c and t_c are increased. Similarly in our case we can argue that once the ring stops being fed by liquid becomes unstable.

We were able to find only one publication that mentions some first observations of a similar ring behaviour. Fraysse & Homsy 1994 identified the deviation from the Nusselt spreading and used a coefficient as an error correction ($\sim 10\%$ of the radius of the wet area) to account for the thickness variation between the film and the ring. However, that publication only explored the fingering instability of spreading droplets up to 600 rpm, for droplets initially stationary on the rotating surface. They observed a ring slightly increased in volume which was then leading to a fingering instability. Thus within the range of their experiments it is unlikely that they could see the third stage of a shrinking ring.

The film thickness experiments shows that beyond r_c the ring decreases in volume, leaving fluid behind. To our knowledge there is no other publication describing that initially growing and the later shrinking in volume ring. The radial evolution $r_r \sim (C_0 - C_\omega t)^{-3}$, although determined only for the ring growing stage, is in good agreement with the experimental results even during the shrinking stage. Regarding the ring growing stage, there are some visual similarities with a hydraulic jump. However, a hydraulic jump is predominantly an inertial phenomenon, while in the thin film inertia is negligible. The interesting new work by Bhagat et al. (2018) of a jet impinging normally to a plate, raises questions about the role of surface tension in hydraulic jumps. Bhagat et al. showed experimentally that for a given jet diameter and flow rate, the radius of the hydraulic jump is the same, irrespective of the orientation of the surface. Bhagat et al. concluded that gravity plays no role in the formation of the jump and suggested that a thin film hydraulic jump results from energy loss due to surface tension and viscous forces alone. In our case centrifugal force is important. Thus when investigating the possibility of a hydraulic jump, we would have to identify the dynamics between centrifugal force, viscosity and surface tension. As the main aim is the understanding of the VFD, this thesis describes experimentally the ring behaviour and further analysis should follow, exploring the possibility of a hydraulic jump.

The third stage describes the droplet spreading beyond r_c, where the ring decreases in volume. Two main instabilities are observed. At the contact line, fingers form due to capillary pressure gradients, as first described for single droplets by Melo et al., (1989). The fingering instability at the contact line is a well documented fluid mechanics problem (Holloway et al., 2007). Although we clearly observed fingering instabilities on the flat and the hemispherical disks, the VFD does not develop similar instabilities, thus these phenomena were not investigated further.

The second instability is the formation of spirals that starts at r_c, at the intersection between the film and the ring. The spiral formation has been described in experiments of constant flux by Woods (1995). Woods described three flow regimes: a laminar regime towards the centre of

the disk, spiral waves stationary in the rotating frame beyond the laminar regime and finally irregular waves towards the edge of the disk. In our experiments, although we investigate the spreading of single droplets, we identify the laminar area up to r_c and the spiral area.

A correlation between the wave formation and the von Kármán boundary layer instabilities was reviewed by Lingwood & Alfredsson (2015). It is a boundary layer that exhibits a cross–flow instability, giving rise to cross–flow vortices that are stationary, with respect to the rotating surface. The growth of stationary vortices saturates at $Re \sim 550$. The cross-flow instability is essentially a transition of a laminar boundary layer to turbulence. In this project, the spirals are dissipated in the film and there is no indication of an irregular regime beyond the area of the spirals. Taking into consideration the magnitude of Re at r_c, we are unable to find a correlation with the Lingwood & Alfredsson limit.

The spiral orientation indicates whether the spirals are caused by a boundary layer or a shear flow instability. Moisy et al. (2003) made the distinction of retrograde spirals for boundary layer instabilities and prograde spirals for shear flow instabilities. The spirals observed in this thesis are prograde spirals, suggesting a shear–induced instability. Our experimental observations suggest that the spirals are formed due to the shrinking stage of the ring volume, observed beyond r_c. The spirals observed in this thesis exhibit a radial and an azimuthal motion in the rotating frame of reference. We attempt to relate the spirals to roll waves. Roll waves on an inclined plane travel at a speed proportional to the velocity of the gravity current (Aghebatie & Hosseini, 2016). Similarly to roll waves, we found that the radial velocity of the spirals is proportional to ωr. Measurements in the azimuthal direction were inadequate to give reliable results.

After exploring the spreading pattern on a flat disk we move to experiments on the hemispherical disk. In the hemispherical disk, the component of the centrifugal force normal to the disk surface suppresses the formation of the ring and the tangential component of gravity works against the film flow. The observations focus on the arc length evolution, varying the rotation rate and the height of release. The arc length evolution is described similarly to the flat disk and is in good agreement with the experimental results. The term accounting for the gravitational force that resists the flow is ignored. The good agreement of the scaling with the experimental results indicates that gravity had little effect on the time dependence of spreading. However, the tangential component of gravity resists the film flow and we believe that the force works against the accumulation of liquid in the ring. The ring appears to behave in a similar way as in the flat disk, first increasing in volume up to L_c and then decreasing in volume. Spiral waves also appear beyond L_c. Detailed measurements of the growing ring and the spirals proved challenging, due to the constantly changing curvature of the disk. Hence most of our measurable results focus on the flat disk while the spreading pattern on the hemispherical disk is described mostly qualitatively.

After completing the experiments on rotating disks the focus moves to the VFD. As the VFD is a novel device, many of the observations are not related to existing literature. The Raston group refers to the fluid mechanics of the VFD and hypothesises that the performance of the device is due to enhanced shearing and the presence of Faraday waves (Britton et al., 2016, Britton et al., 2015). A main hypothesis is formed at the beginning of this thesis, based on the idea that the fluid mechanics in the VFD can enhance chemical reactivity. Chemical

reactivity depends on diffusion and advection. According to the literature review, enhanced diffusion can be achieved proportional to pressure gradients (Gibbs, 1873). Reactivity can also be enhanced, due to advection, according to the advection–diffusion equation proportional to velocity gradients in the main direction of the flow (Katayama & Terauti, 1996).

One of the crucial components for our approach is the determination of the film thickness. The film thickness is compared to the boundary layer thickness and is useful for the determination of the pressure gradients in the r and the z direction, across the thickness of the film and along the film respectively. The film thickness is determined using neutron imaging experiments and by developing a new methodological approach for the processing of the experiments.

A very recent publication described the film shape of the film and presented a first round of neutron imaging experiments at ANSTO (Solheim et al., 2019). This work is a collaboration between the Raston group, DAMTP and ANSTO. The images obtained from the first round of experiments were processed manually, with the user obtaining measurements of pixel intensity at two specific cross–sections along the tube. A second round of more detailed experiments was conducted while the present author was visiting ANSTO. Comparing the two rounds of experiments, most of the measurements of the second round are within the relatively large error limit of the first round of experiments. A comparison of the experimental details is presented in Table 8.1.

Table 8.1: Neutron imaging experimental details

	First round	Second round
Liquid	water	toluene
Liquid volume	1 ml	1 ml
Rpm range	2,000 - 5,000	1,000 - 9,000
Ratio of collimator–detector length to inlet collimator diameter	500	1,000
Pixel size (μm)	67	13
Error (pixels)	10	4
Exposure time (s)	1	90
Neutron per pixel (for maximum flux 4.75×10^8 neutrons/s)	80	7,200
Thickness measurements (mm)	at 7,8 and 18.7 from the base of the tube	along the total length of the tube

For the second round of experiments, a new methodology is developed for the determination of the film thickness. We are able to determine the free surface of the film but the determination of the wall of the tube is challenging, due to the tube eccentricity. Taking two measurements, one at wall of the tube and one along the axis of rotation, we determine the film thickness up to 9,000 rpm. Knowing the film thickness, we conclude that for $\omega \geq 7,000$ rpm, the film moves for most of its length within the boundary layer. The maximum pressure differences is of $\mathcal{O}(2000)$ Pa and can be found at the area between the lower O rings, where the film thickness is maximised. As mentioned in the literature review, the maximum diffusion in water can be achieved at approximately 10^8 Pa (Walker et al., 2016). The magnitude of pressure differences determined by the neutron imaging experiment is much lower than the pressure for maximum

diffusivity, hence the focus moves to pressure gradients in the r direction and the conditions of advection in the film.

Experimental observations on reaction rates show that increased reactivity can be achieved with increased ω and that the length of the reaction propagates upwards in the tube with a time dependence of $(D_m t)^{1/2}$, with $D_m > D$. A mathematical approximation is suggested, attributing enhanced reactivity to a combination of diffusion and advection. The scaling is based on the advection–diffusion equation, assuming that density differences between the two liquids form an interface between the two reactants, where diffusion and vorticity are present. The approximation determined a D_m which is in good agreement with the experimental results. We believe that this mechanism is present both in CM and in CF and can explain to some extent the enhanced reactivity in the VFD.

Regarding Faraday waves, we are unable to identify a mechanism that could be relevant and we believe that the wavelength of the disturbance would be small and impossible to be captured by the high speed camera. However, two additional disturbances are observed that can be related to enhanced shearing. In CF, a droplet is detaches from the pipette falls under the force of gravity and lands in a film that is already rotating at steady state. The droplet behaves as an obstacle, forming waves for approximately one revolution. The waves propagate upwards and downwards from the axis of landing as a stretching spiral, which eventually dissipates in the film. The break of the film, the presence of the waves and the restoration of the film are repeated with every droplet landing, thus constitute of a constant mechanism of shearing in CF.

In CM, we observe the presence of a spiral formation of waves with fixed wavelength and spiral angle along the free surface of the film when using acetic acid. As the film thickness is reduced, towards the higher end of the tube, we expect that a wave mechanism related to the liquid film would be affected by the film thickness reduction. The fixed characteristics of the spiral indicate an instability mechanism due to the air circulation in the tube. Assuming that the air could ideally rotate symmetrically in the tube, then any deviation from that symmetric configuration could cause disturbances in the air layer that interacts with the free surface of the film. In reality, due to tube imperfections, axisymmetry is not possible. Other examples that could cause disturbances are the asymmetric shape and possible movements of the pipette, the formation and the free fall of the droplet.

7.3 New developments on the VFD

A recent visit of Prof. Raston in DAMTP gave an insight to new research outcomes on the VFD. The Raston group tested the performance of the VFD using modulations in the rotation rate during the processing time. The results did not indicated enhanced reactivity, hence we speculate that it is the processing within the very thin film and the advection–diffusion mechanism that work in favour of chemical reactivity. A new VFD has also been designed with extended tube length at 40 cm. Although the experiments are still in progress, we expect, assuming a perfectly shaped tube, that a longer tube would lead to a longer film with extended pressure gradients along the r direction over a greater length. Assuming that for a longer tube the liquid volume would be increased, then the film would be thicker at the base and might require increased ω to achieve a film thickness similar to the smaller tube. The Raston group recently identified

that, at approximately 4,500 rpm, there is also a peak in the product yield slightly smaller in magnitude than the peak at 7,500 rpm. Although they are currently beginning to explore the performance of the VFD at 4,500 rpm, they believe that at approximately 4,500 and 7,500 rpm both in CF and in CM, the product yield is increased, thus reactivity is enhanced.

Going back to our hypothesis that the film thickness is an important component for the fluid mechanics condition, under CF the tube must operate in its full volume capacity. From the volume capacity experiment we establish that liquid volume takes the form of a thin film for rotation rates greater than 4,000 rpm. Below that limit, we observe swirling flow and beyond the limit, the film decreases in thickness. Thus we believe that it is the thin film formation that exposed the liquid to increased pressure gradients in the r direction that affect chemical reactivity. Therefore, a larger tube diameter would increase the pressure gradients and enhance chemical reactivity further.

The Raston group has formed a number of hypotheses regarding why the VFD outperforms other devices. Some of the hypotheses related to fluid mechanics and investigated in this thesis are collisions due to shear, fluctuating pressure, pressure gradients, enhanced diffusion and thin film formation with increased interface area. The results of this thesis consist of the first macro-scale approach in the VFD. The micro-scale approach in the VFD, dealing with the nano–metre level, is an unexplored area which could give useful information in terms of molecular interactions and the presence of Faraday waves.

7.4 Steps forward

This section is compiled with thoughts and ideas for future research on spinning devices, based on the main findings of this thesis. The section is divided in three sub–sections: the rotating disks, the VFD and the connection of the findings in all devices. Especially for the rotating disks, the focus is on the flat disks, as the shape of the disk and the light attenuation allowed the completion of more experiments, in comparison to the hemispherical disk.

The ideas for future work are based on observations that could not be investigated further in this thesis. The thesis covers a broad range of phenomena that could be studied quantitatively and are more important at this stage of the VFD development. The main characteristics that are investigated are the spreading rate and the thickness of the film. However, due to the complexity of the VFD fluid mechanics, many phenomena are described only qualitatively. Most of the mechanisms described could form individual research projects. The reasons for not moving forward with these ideas are technological challenges in the measurements and limited time.

7.4.1 Spinning disks

The spreading pattern is investigated on spinning disks, for different disk materials (painted brass and glass) and curvature (flat and hemispherical) for a range of heights of release, rotation rates, and droplet volumes.

The height of the pipette above the rotating disk can affect the volume of the droplet. As shown in section 5.1.1, using the same pipette, a height of release at 5 mm leads to more frequent discharges and to a droplet volume of ~ 67 μl, while for a height or release at 10 mm and at

15 mm the volume is $\sim$ 80 μl. The frequency of droplet release, for $H \leq 5$ mm, depends on the volume flux feeding the pipette, the surface tension of the liquid, the drag from the disk and the air boundary spiralling out within the boundary layer, at a mean rotation rate lagging behind the disk's. Experiments exploring the frequency of detachment, varying the flux of the syringe pump, the rotation rate, the height and the position of the droplet release, could give an insight to the fluid characteristics of the droplet and the air rotating with the disk, during droplet formation, detachment and landing.

At low rotation rates (up to 3,000 rpm) and for axial landing, a single rivulet carries away most of the liquid. Experiments defining the rivulet formation and the droplet being carried away, for a range of heights of release and rotation rates, could give an insight to the fluid mechanics inside the rivulet for potential applications in chemical reactions. Additional experiments should be conducted to determine the limits below which the droplet maintains its sessile shape on the rotating disk, resulting in plots of sessile radius with ω, V, γ and H, respectively.

A mathematical model is developed in section 4.2.2, describing the droplet spreading and taking into consideration the conditions of landing by incorporating the initial radius and thickness after landing. Although the model is in good agreement with the experimental results, we also observe, in section 4.4, that a scaling incorporating the critical radius r_c, is also a good fit. Therefore, further developments in the mathematics of spreading, both for the film and the ring, could be useful.

The volume distribution in the ring, presented in section 4.3, is one of the observations first described in this thesis. Before the front reaches r_c, the fluid moves faster in the film, thus fluid is entrained in the ring, which is growing in volume. Beyond r_c, the film reaches almost a steady state of rotation and the fluid is left back from the ring coating the disk, with the ring volume shrinking. The fluid mechanics environment during the volume growth and the shrinkage of the ring should be investigated further with respect to shearing, mixing and chemical reactivity.

Varying the droplet volume, in section 4.5.2, we find that r_c increases, with minor variations over a range of rotation rates, when the droplet volume is reduced to approximately 40μl. The combination of increased r_c and t_c are indications that r_c increases while the ring grows. The mechanism of ring growth and a scaling for the time that the feeding of liquid stops require further investigation with a broader variation in droplet volumes.

The unstable contact line leads to the formation of fingers. At the higher end of rotation rates under investigation, the fingers are caught back up by the main flow and consequently it is decided not to investigate further their dynamics. The size of the disk in use restricts the observations of the finger development to a radius of 25 mm from the axis of rotation. A wider disk could give more insight to the entrainment of the fingers back to the ring or the formation of new fingers as the contact line moves further away.

Advancing and receding contact angles are not investigated in this thesis. Research on the contact angles varying fluids properties, surface materials and surface finishes would be valuable on both sides of the ring, at the ring front and at the intersection with the film. Initial experiments on the painted brass disk show that both contact angles are approximately 90° at r_c. The sharp contact angle at the intersection with the film, to our knowledge is not investigated in literature. Attempting to explain the angle at the intersection between the film and the ring, further experiments would be useful with respect to parameters such as V, γ, ν and ω. Especially

the shrinkage of the ring could also provide information for the mechanism of the formation of the prograde spirals.

A comparison with the spreading pattern on the hemispherical disk would be also important for the understanding of the ring behaviour. The arc length of the film follows a scaling similar to the flat disk, indicating that the role of gravity to the spreading rate, before the onset of the instabilities is insignificant. However, the component of gravity normal to the wall and the tangential component of gravity suppress the formation of the ring and could be related to the onset of contact–line instabilities. Experiments comparing the evolution of the thickness of the ring on a flat and a hemispherical disk could be indicative of the role of the disk geometry to the ring dynamics. The visualisation of the ring thickness on the hemispherical disk is challenging, as the constantly changing curvature in combination with the stationary light sources restrict the light attenuation captured by the camera. A new methodology is required, which was not feasible within this thesis.

The prograde spirals, analysed in section 4.6, could be an important factor for the chemical reactions in spinning disks. They seem to have a retrograde phase velocity, a feature which should be investigated further. The form and the velocity of the spirals should be investigated for a range of heights of release, rotation rates, droplet volumes and under continuous flux. A PIV experiment would give an insight to the phase velocities and focusing on the motion of particles as they enter or exit a spiral wave, could indicate the level of interaction between particles along that region. Given the time scale of the spreading, a PIV experiment is challenging. A horizontal laser light sheet coincident immediately above the surface of the disk, could be useful for the visualisation of the particles. For this PIV experiment, further planning is required to obtain reliable results.

Regarding the landing of droplets away from the axis of rotation, in section 4.7.2 we show that the fluid carried away by the disk is related to the height of release and the rotation rate. The rate of drainage is related to the level of shearing within the film. In order to be more conclusive on the benefits of the off–axis landing, both the rate of discharge from the pipette and drainage of droplets from the disk, for different distances from the axis of rotation, heights of release and rotation rates, could give feedback about the role of the air boundary layer rotating with the disk.

A wet disk, explored in section 4.7.1, shows a different pattern of instabilities with capillary waves visible at the free surface throughout the spreading and with additional local fingering instabilities along the spirals. Experiments with droplets landing on wet disks, coated with liquids of different viscosity and surface tension could indicate a correlation between the free surface capillary waves and the local fingers to surface tension.

Several flow chemistry devices have been found to enhance chemical reactivity, with increasing research focused on the fluid mechanics environment, imposed by each device. Although spinning disks have been used previously in flow chemistry and have been investigated in many different flow regimes, one of the challenges with spinning disks is the decreased residence time at high rotation rates. The dimensionless collision rate Z is introduced to connect the fluid mechanics on the spinning disks with advection and chemical reactivity. The approach is based on the idea that the reaction rate is proportional to shearing and shearing is proportional to the velocity gradient $\frac{\partial u_r}{\partial z}$. However, this approach is based on the Nusselt film approximation

under laminar flow and assumes a uniform film. The pressure gradients that exist within the ring could trigger molecular displacements. Thus, Z should be determined incorporating the waves and the growing and shrinking ring. Further experiments should be correlated with the scaling of Z, and test whether the Nusselt film approximation and the ring dynamics have an impact on chemical reactivity.

Combining our experimental observations, we can conclude that there are several fluid mechanics processes that could enhance chemical reactivity, with a special focus on the ring evolution, that could reduce the required residence time. Further analysis at high rotation rates and a new disk design, such as a hemispherical disk, achieving increased residence time, could attract interest from many industries.

7.4.2 VFD

The VFD works in CM with a fixed volume of liquid and in CF with constant flux, fed in the tube in the form of a train of droplets. The rotation rate, the orientation of the tube and the liquid properties set the fluid mechanic conditions under which chemical reactions take place.

The results of the Raston laboratory have shown that reaction rate increases with ω. However, there is a maximum limit of ω beyond which reactivity is significantly reduced. Each tube has unique imperfections which lead to the formation of different film shapes as explained in section 6.2. The ellipticity or eccentricity of the tubes could be important for the fluid motion in the tube and the total processing time. The imperfect tubes form protrusions, which guide the liquid towards the exit of the tube, limiting azimuthal displacements. On the other hand, the protrusions might lead to longer films at steady state and could work in favour of enhanced reactivity. Thus, the tube imperfections should be measured and correlated with results on chemical performance. If the performance of the device is related to the shape of the film, then from the perspective of the work at Flinders University, assessing the symmetry of the tubes should be a priority.

By increasing ω, for a given flow rate, we obtain longer films, as shown in section 6.3.2. Longer films might increase reaction rates, but the volume contained within the tube is decreased. This leads to a reduction of the total residence time in the VFD. An optimisation parameter that requires further investigation is the residence time in the VFD compared to the required time for the completion of the reaction. The inclination of the tube, as shown in section 6.3.3, is another parameter that affects both the film thickness and the residence time. A more vertically positioned tube leads to increased film thickness and residence time. Experiments for the same reaction, using the same tube, for a range of ω and β could give an experimental correlation between residence and reaction times.

Additional film thickness experiments using neutron imaging as in section 6.3.5, and reactivity experiments, as in section 6.3.6, should be conducted for a range of ω and β, determining a correlation with the reaction rates. The repetition of experiments for a range of reactions could form a database of VFD performance interconnected with reactions that require either free movement or specific orientation of molecules, assuming that thinner films impose specific molecular orientation, while thicker films allow more degrees of freedom in molecular movement. This database could offer a guide for future applications useful for household use.

The mathematical framework developed in this thesis for the processing of neutron imaging results on rotating objects worked well on the VFD. However, each tube is characterised by a unique eccentric or elliptic shape. Further analysis including scenarios of imperfect rotating tubes in combination with more experiments on a range of eccentric objects could improve the processing in the future.

The technique of neutron imaging allowed us to determine the film thickness at steady state. Neutron imaging is only available in nuclear reactor facilities and the experiments require substantial amount of time ($\sim$ 60 min for each test) compared to the experiments with a high–speed camera ($\sim$ 1 min for each test). Flow visualisation techniques using dye attenuation could determine the film thickness. Some first experiments were attempted towards the end of this thesis. The water was dyed with blue food dye and we used a LED background of red light. Although the results were not adequate to be presented in this thesis, the method could potentially give reliable results and requires more testing with respect to dye concentration and background lights. However, optical techniques are affected by the refractive index (unlike neutron imaging) and so they cannot give reliable results, except near the contact line. If the high–speed camera can capture the film thickness near the contact line at steady state via light attenuation then there is also potential for capturing experimentally the film thickness evolution during the spin–up.

The shape model, developed in section 6.3.1, is compared to the neutron imaging results, and is found to be in good agreement with the film thickness of liquids with surface tension similar to toluene and water. Similarly, the model should be compared with the film thickness of liquids with increased surface tension. Initial experiments conducted at ANSTO, using 1 ml of glycerol, show increasing deviations from the predictions of the model, with increased ω. Hence, a more detailed model incorporating surface energy would be beneficial.

In addition, another model is developed, in section 6.4, describing the advancement of the film along the tube during the spin-up. The model is based on the lubrication approximation, where centrifugal and gravitational forces are balanced by viscosity. Coriolis force is ignored and surface tension is important only at the contact line. A similarity solution could be developed for the simulation of the film development, followed by linear stability analysis exploring the stability of the system.

Pressure differences within the film could enhance reactivity, as shown in section 6.3.6. Detailed analysis on the theoretical level, using collision theory could investigate further the effect of pressure gradients in the VFD and could potentially constitute of a new project. Collision theory can be combined with collision probability and random walks of molecules due to Brownian motion only, or in combination with shearing. Molecular dynamics simulations under very large pressure gradients could give insight to the influence of pressure in molecules' displacement and orientation.

Waste streams are also an important factor in the performance of the VFD. The separation of the two phase mixtures in CM, in section 6.5.1, indicates that part of the volume of the lighter liquid is never in contact with the denser liquid during the processing. Furthermore, the denser liquid in CF, even if it lands on an already rotating film of the less dense fluid, breaks the film, lands onto the solid surface and forms another film between the less dense film and the solid substrate. Thus, for two fluids of different density, the processing time might vary and density

differences should be taken into consideration while placing the liquids or during the feeding of the reactants in CF.

Considering CF in the VFD, as shown in section 6.5.2.1, the fluid moves along the tube during the processing. There might be a specific height where the reaction is complete and assuming that the reaction happens close to the point of landing, there is no benefit of further processing or making the product climb up the tube. Assuming that the reaction is complete approximately at the landing area, the product of the reaction travels a significant distance towards the exit of the tube, where conditions such as heat could have unexpected consequences, such as the presence of by-products. By adding obstacles and multiple pipettes feeding reactants at different heights, we could succeed in multiple reactions. The addition of obstacles can also alter the film development and control the formation of protrusions. Additional processing of the tubes, such as coating with wax could also control the formation of protrusions. Initial experiments conducted by coating the tube with wax of a spiral shape, while visiting Flinders University, showed that the wax coating enforced a spiral film formation.

It has been hypothesised that vibrations within the fluid could enhance chemical processing. Vibrations could increase the internal energy of the molecules, leading to more frequent molecular displacements. Enhanced reactions in the VFD have already been attributed by the Raston group, to Faraday waves imposed on the fluid via uncontrolled vibrations. Uncontrolled vibrations from mechanical responses of different parts of the VFD could be related to increased product yields. An initial experiment was conducted by placing 4 three–axis accelerometers in different areas of the device. The most interesting part of the device in terms of vibrations is the tube but due to the rotation, the placement of accelerometers at the walls of the tube was impossible. All the accelerometers give a frequency peak at harmonics of the rotation rate. Whether these peaks are related to enhanced reactivity is unknown, but we are unable to visualise the effect. However, additional experiments using acetic acid and imposing vibrations could give an insight to whether this could be an enhancing mechanism in the VFD.

Controlled vibrations could act as smooth steering, forming helical structures, similar to the waves observed in the ionic infusion experiment in section 6.5.2. The observations of vapour acidification of bromothymol blue are achieved by using acetic acid. A similar experiment but using absorbent cotton at the lower end of the pipette would prevent the droplet falling and could give interesting insights to the air dynamics by tracking the gas–vapour vortex along the tube. In addition, even small displacements of the pipette could cause disturbances in the air layer rotating in the tube. The unstable air could enhance infusion or create an unstable interface with the film, enhancing the reaction.

Regarding the VFD performance, neutron scattering experiments (as opposed to neutron imaging experiments reported in this thesis), in CM and CF for a range of rotation rates, could give an insight to the effect of fluid mechanics on the product yield. Neutron scattering shows the polydispersity that characterises the structure of the product and the number of structures produced in the VFD. Neutron scattering experiments should be conducted with the same tube to achieve the same film shape, using two different reactions, one requiring increased degrees of freedom and the other requiring specific molecule orientation.

Some reactions are more successful when the movement of molecules has increased degrees of freedom, while others depend on the enforced orientation of the molecules. The shape and

the thickness of the film along with shearing, could affect the movement, the bending and the orientation of molecules. Free movement of molecules can be achieved at low rotation rates, where swirling flow is observed and the reaction might happen in a turbulent environment. The pressure gradients in the film in combination with turbulence could enhance the molecules' movement. The conditions of swirling flow in the VFD have not been explored in this thesis due to the observations of chemists in the Raston laboratory, that the VFD works best at rotations rates from 7,000 to 8,000 rpm. Increased centrifugal force, at rotation rates beyond 4,000 rpm, creates a very thin film, that reaches a steady state of rotation, under laminar flow, and possibly enforcing molecules' orientation.

Hydrophobic coating would also be an interesting application in the VFD. We expect a decreased film length, compared to a hydrophilic tube. The most appropriate hydrophobic coating is under consideration by the Raston group. After determining the most appropriate hydrophobic coating, spin–up experiments could give an insight to the spreading pattern over hydrophobic surfaces.

7.4.3 Connecting the devices

The axisymmetric spreading of droplets on the flat and the hemispherical disks is related with axisymmetric spreading in the VFD, which can be achieved only when the device is vertically positioned. The current design of the VFD confines the tube in inclination angles between 0° and 85°. A new design, allowing the vertical placement of the tube, could be beneficial for performance of the device. For a vertically positioned tube and axial landing of droplets, the fluid spreading is expected to be axisymmetric, experiencing enhanced shearing as on the flat disk.

The off–axis landing of droplets on spinning disks is related to the landing of the first droplet in CF at the walls in the VFD. Although the landing creates the highest shear rate, it is only a very small fraction of the processing, as most of the droplets in the VFD land into an already rotating film. A more representative experiment would be designed by using a confined rotating disk, i.e. with walls maintaining a film rotating with the disk and droplets landing off–axis in the film. By adding vertical walls at the rim of the disk under specific rotation rates, a uniform thin film could be created. Another option could be a disk with paraboloidal surface with a film rotating at a steady state. The hemispherical disk could be also used for this experiment. Having droplets landing either on the axis or off axis, could give an insight to the mechanics of the entrainment of reactants in an already rotating film. However, if the disk is not confined by vertical walls, the range of rotation rates should be reduced compared to the range of rotation rates used in the VFD.

The radius of the disks (25 mm) is much larger than the internal radius of the current VFD tube (10 mm). Thus the spreading pattern and the instabilities observed during the spreading on the disks are not directly related to the film development in the current generation of the VFD. However, the scaling up of the VFD is in progress and the experimental results and future work on spinning disks could be useful for future developments of the device.

Future work on the collision rate Z could be mainly focused on CF in the VFD, where advection is important. The definition of Z on the flat disk can be used at the base of the

VFD for the early times of spreading while further scaling of Z should be developed for the liquid climbing the walls of the VFD. All scalings of Z can only be validated when correlated to experiments exploring the performance of chemical reactivity over a range of rotation and flow rates. For the limiting case of a vertically positioned tube, and considering the scaling developed in this thesis, it seems as the most significant area of shearing is during the spin–up in CM and after the droplet landing in CF. Increased shearing would be mostly met at the base of tube, where a von Kármán layer is formed. Therefore, a new design of the VFD allowing a vertically positioned tube should be explored.

7.5 Final remarks

Overall, this thesis is the first attempt to understand the fluid mechanics of the VFD. The main hypothesis is that the performance of the device is related to enhanced diffusion and shearing. The VFD is investigated according to the modes of processing. The followed approach addresses the hypothesis for a range of parameters, i.e. $\omega, V, Q, \gamma, \nu, \beta$.

In CM we explore the film development and the film at a steady state of rotation. Most of the research focuses on the film at a steady state of rotation as the film development is a very small part of the processing. We anticipate from the beginning that a critical component for the determination of the fluid mechanics conditions is the thickness of the thin film. The film shape is parabolic with the area of increased thickness at the lower part of the tube (between the two O rings). We find that the film thickness, even in the vicinity of the O rings, is very close to the boundary layer thickness $\sim \mathcal{O}(10^{-5})$ mm at rotation rates greater than 7,000 rpm. The thickness is reduced as we go higher in the tube, thus the film moves within the boundary layer. The exact point of transition to a film thickness approximately equal to the boundary layer thickness cannot be determined as it is within the error of the neutron imaging measurements and estimated beyond the base of the protrusion in the tube. We believe that a film thickness close to the boundary layer thickness is the main characteristic that makes the performance of the VFD optimum from 7,000 to 8,000 rpm.

In CF we focus mostly on the fluid mechanics during droplet landing and entrainment in an already rotating film at steady state. We believe that the breaking and restoration of the film after every droplet landing, creates disturbances that enhance shearing. To understand the droplet landing and spreading in rotating surfaces, experiments are conducted on spinning disks. Through this experimental processing a new unexpected spreading pattern is observed in droplets spreading on flat disks.

Both in CM and in CF, density differences and pressure gradients in the radial direction create the conditions of shearing and advection, enhancing chemical reactivity. We suggest a mechanism combining advection and diffusion and a mathematical approximation which is found to be in good agreement with experimental results on reaction rates.

Combining our experimental observations, we can conclude and propose a combination of CM and CF as another method of processing. The VFD might work better if the denser liquid is already rotating at steady state in the tube. The denser liquid will stay attached to the walls, while the less dense liquid will form a layer on top of the denser liquid and close to the area of landing. Every time a droplet is released, the less dense layer will propagate towards the exit,

increasing shearing between the reactants. The pipette feeds liquid in the form of droplets and after every landing droplet, a stretching helix can increase mass transfer and shearing. The two liquids form an interface at the area of landing, thus reaction must occur locally in the tube. By relocating the pipette, we might be able to create multiple zones of reactions and consequently minimise waste streams. Depending on the required reaction time, the pipette can feed a specific amount of liquid starting from the upper end or the lower end.

Several flow chemistry devices enhance chemical reactivity, with increasing research focused on the fluid mechanics environment imposed by each device. The VFD offers a range of fluid mechanics conditions. At lower ω, the film thickness at the lower parts of the tube could be greater than the boundary layer thickness, forming a turbulent environment with increased degrees of freedom for molecular displacement. It can also achieve at high ω, a thinner film and a laminar environment, with high pressure gradients and possibly specific molecular orientation. The two processing environments, in combination with the control of processing time and the flexibility of pipette displacements, make the VFD attractive to many applications of chemical processing.

In conclusion this thesis addresses the main hypothesis and makes several observations regarding the spreading pattern of droplets on spinning disks and the processing in the VFD. Apart from the mathematical approximations and the experimental results, there are a number of observations that require further investigation. Hence, this thesis is a fundamental step for further developments and further research on the fluid mechanics and the chemical performance of the VFD.

Bibliography

Aghebatie, B. & Hosseini, K. (2016), 'Investigation on the formation of roll waves in chutes', *Water and Environment Journal* **30**(1-2), 113–118.

Ahmed, M. & Youssef, M. S. (2012), 'Characteristics of Mean Droplet Size Produced by Spinning Disk Atomizers', *Journal of Fluids Engineering* **134**(7), 071103.

Ashmore, J., Hosoi, A. E. & Stone, H. A. (2003), 'The effect of surface tension on rimming flows in a partially filled rotating cylinder', *Journal of Fluid Mechanics* **479**, 65–98.

Baldyga J. & Pohorecki R. (1995), 'Turbulent micromixing in chemical reactors - a review', *Chemical Engineering Journal* **58**(2), 183–195.

Benilov, E. S. & Billingham, J. (2011), 'Drops climbing uphill on an oscillating substrate', *Journal of Fluid Mechanics* **674**, 93–119.

Bertozzi, A. L. & Brenner, M. P. (1997), 'Linear stability and transient growth in driven contact lines', *Physics of Fluids* **9**(3), 530–539.

Bhagat, R. K., Jha, N. K., Linden, P. F. & Wilson, D. I. (2018), 'On the origin of the circular hydraulic jump in a thin liquid film', *Journal of Fluid Mechanics* **851**, 1–11.

Bhatelia, T. J., Utikar, R. P., Pareek, V. K. & Tade, M. O. (2009), 'Characterizing Liquid Film Thickness in Spinning Disc Reactors', *Proceedings of the Seventh International Conference on CFD in the Minerals and Process Industries* pp. 1–6.

Bhattacharjee, A. K., Balakrishnan, K., Garcia, A. L., Bell, J. B. & Donev, A. (2015), 'Fluctuating hydrodynamics of multi-species reactive mixtures', *Journal of Chemical Physics* **142**(22), 1–53.

Boettcher, K. E. & Ehrhard, P. (2014), 'Contact-line instability of liquids spreading on top of rotating substrates', *European Journal of Mechanics - B/Fluids* **43**, 33–44.

Boiarkina, I., Pedron, S. & Patterson, D. A. (2011), 'An experimental and modelling investigation of the effect of the flow regime on the photocatalytic degradation of methylene blue on a thin film coated ultraviolet irradiated spinning disc reactor', *Applied Catalysis B: Environmental* **110**, 14–24.

Bonn, D., Eggers, J., Indekeu, J., Meunier, J. & Rolley, E. (2009), 'Wetting and spreading', *Reviews of Modern Physics* **81**(2), 739–805.

Boodhoo, K. V. K. & Al-Hengari, S. R. (2012), 'Micromixing Characteristics in a Small-Scale Spinning Disk Reactor', *Chemical Engineering and Technology* **35**(7), 1229–1237.

Britton, J., Dalziel, S. B. & Raston, C. L. (2015), 'Continuous flow Fischer esterifications harnessing vibrational-coupled thin film fluidics', *RSC Advances* **5**(3), 1655–1660.

Britton, J., Dalziel, S. B. & Raston, C. L. (2016), 'The synthesis of di-carboxylate esters using continuous flow vortex fluidics', *Green Chemistry* **18**(7), 2193–2200.

Brunet, P., Eggers, J. & Deegan, R. D. (2007), 'Vibration-induced climbing of drops', *Physical Review Letters* **99**(14), 3–6.

Burns, J. R., Ramshaw, C. & Jachuck, R. J. (2003), 'Measurement of liquid film thickness and the determination of spin-up radius on a rotating disc using an electrical resistance technique', *Chemical Engineering Science* **58**(11), 2245–2253.

Cafiero, L. M., Baffi, G., Chianese, A. & Jachuck, R. J. (2002), 'Process intensification: Precipitation of barium sulfate using a spinning disk reactor', *Industrial and Engineering Chemistry Research* **41**(21), 5240–5246.

Chandler, D. (1974), 'Equilibrium structure and molecular motion in liquids', *Accounts of Chemical Research* **7**(8), 246–251.

Chandra, S. & Avedisian, C. T. (1991), 'On the Collision of a Droplet with a Solid Surface', *Proceedings of the Royal Society A: Mathematical, Physical and Engineering Sciences* **432**(1884), 13–41.

Charwat, A. F., Kelly, R. E. & Gazley, C. (1972), 'The flow and stability of thin liquid films on a rotating disk', *Journal of Fluid Mechanics* **53**(2), 227.

Chen, X., Dobson, J. F. & Raston, C. L. (2012), 'Vortex fluidic exfoliation of graphite and boron nitride.', *Chemical communications (Cambridge, England)* **48**(31), 3703.

Cho, H.-C., Chou, F.-C., Wang, M.-W. & Tsai, C.-S. (2005), 'Effect of Coriolis Force on Fingering Instability and Liquid Usage Reduction', *Japanese Journal of Applied Physics* **44**(No. 19), L606–L609.

Cloutman, L. D. (2001), A Note on Differencing the Viscous Dissipation Terms for a Newtonian Fluid, Technical report, Lawrence Livermore National Laboratory.

Craster, R. & Matar, O. (2009), 'Dynamics and stability of thin liquid films', *Reviews of Modern Physics* **81**(3), 1131–1198.

D'Alonzo, N. J., Eggers, P. K. & Raston, C. L. (2017), 'Vortex fluidics synthesis of polymer coated superparamagnetic magnetite nanoparticles', *New Journal of Chemistry* **41**(2), 552–558.

Edward, J. T. (1970), 'Molecular volumes and the Stokes-Einstein equation', *Journal of Chemical Education* **47**(4), 261.

Emslie, A. G., Bonner, F. T. & Peck, L. G. (1958), 'Flow of a Viscous Liquid on a Rotating Disk', *Journal of Applied Physics* **29**(5), 858.

Eroglu, E., D'Alonzo, N. J., Smith, S. M. & Raston, C. L. (2013), 'Vortex fluidic entrapment of functional microalgal cells in a magnetic polymer matrix.', *Nanoscale* **5**(7), 2627.

Esmail, M. N., Hummel, R. L. & Smith, J. W. (1975), 'Instability of two-phase flow in vertical cylinders', *Physics of Fluids* **18**(5), 508–516.

Espig, H. & Hoyle, R. (1965), 'Waves in a thin liquid layer on a rotating disk', *Journal of Fluid Mechanics* **22**(4), 671–677.

Fraysse, N. & Homsy, G. M. (1994), 'An experimental study of rivulet instabilities in centrifugal spin coating of viscous Newtonian and non-Newtonian fluids', *Physics of Fluids* **6**(4), 1491.

Froehlich M. (2009), 'Two Coating Problems : Thin Film Rupture and Spin Coating', *Duke University* .

Garbe, U., Randall, T., Hughes, C., Davidson, G., Pangelis, S. & Kennedy, S. J. (2015), 'A New Neutron Radiography / Tomography / Imaging Station DINGO at OPAL', *Physics Procedia* **69**(2014), 27–32.

Ghai, I., Samuel, J., DeVor, R. E. & Kapoor, S. G. (2013), 'Analysis of Droplet Spreading on a Rotating Surface and the Prediction of Cooling and Lubrication Performance of an Atomization-Based Cutting Fluid System', *Journal of Manufacturing Science and Engineering* **135**(3), 031003.

Ghiasy, D., Tham, M. T. & Boodhoo, K. V. (2013), 'Control of a spinning disc reactor: An experimental study', *Industrial and Engineering Chemistry Research* **52**(47), 16832–16841.

Gibbs, J. W. (1873), 'A method of geometrical representation of the thermodynamic properties of substances by means of surfaces', *Transactions of the Connecticut Academy of Arts and Sciences II* pp. 382–404.

Goh, Y. A., Chen, X., Yasin, F. M., Eggers, P. K., Boulos, R. A., Wang, X., Chua, H. T. & Raston, C. L. (2013), 'Shear flow assisted decoration of carbon nano-onions with platinum nanoparticles.', *Chemical communications* **49**(45), 5171.

Goodwin, R. & Homsy, G. M. (1991), 'Viscous flow down a slope in the vicinity of a contact line', *Physics of Fluids A: Fluid Dynamics* **3**(4), 515–528.

Haseidl, F., Pottbäcker, J. & Hinrichsen, O. (2016), 'Gas-Liquid mass transfer in a rotor-stator spinning disc reactor: Experimental study and correlation', *Chemical Engineering and Processing: Process Intensification* **104**, 181–189.

Holloway, K. E., Tabuteau, H. & de Bruyn, J. R. (2009), 'Spreading and fingering in a yield-stress fluid during spin coating', *Rheologica Acta* **49**(3), 245–254.

Holloway, K., Habdas, P., Semsarillar, N., Burfitt, K. & de Bruyn, J. (2007), 'Spreading and fingering in spin coating', *Physical Review E* **75**(4), 046308.

Huppert, H. E. (1982), 'Flow and instability of a viscous current down a slope', *Nature* **300**(5891), 427–429.

Iwashita, T. & Yamamoto, R. (2009), 'Short-time motion of Brownian particles in a shear flow', *Physical Review E - Statistical, Nonlinear, and Soft Matter Physics* **79**(3), 1–5.

Julien, P. Y. & Hartley, D. M. (1986), 'Formation of roll waves in laminar sheet flow', *Journal of Hydraulic Research* **24**(1), 5–17.

Kashid, M. N., Renken, A. & Kiwi-Minsker, L. (2011), 'Gas-liquid and liquid-liquid mass transfer in microstructured reactors', *Chemical Engineering Science* **66**(17), 3876–3897.

Katayama, Y. & Terauti, R. (1996), 'Brownian motion of a single particle under shear flow', *European Journal of Physics* **17**(3), 136–140.

Konermann, L. (1999), 'Monitoring reaction kinetics in solution by continuous-flow methods: The effects of convection and molecular diffusion under laminar flow conditions', *Journal of Physical Chemistry A* **103**(36), 7210–7216.

Lai, C.-C. & Chou, F.-C. (2008), 'Effect of Relaxation Time on Spin Coating Instability', *Japanese Journal of Applied Physics* **47**(8), 6569–6573.

Landel, J., Thomas, A., McEvoy, H., & Dalziel, S. B. (2015), 'Cleaning of Viscous Droplets on an Inclined Planar Surface Using Film Flows', *Proceedings of the Nineteenth Australasian Fluid Mechanics Conference* **93**, 210–217.

Lee, J. B., Derome, D., Dolatabadi, A. & Carmeliet, J. (2016), 'Energy budget of liquid drop impact at maximum spreading: numerical simulations and experiments', *Langmuir* **32**(5), 1279–1288.

Lee, J. S., Weon, B. M., Je, J. H. & Fezzaa, K. (2012), 'How does an air film evolve into a bubble during drop impact?', *Physical Review Letters* **109**(20), 1–5.

Leneweit, G., Roesner, K. G. & Koehler, R. (1999), 'Surface instabilities of thin liquid film flow on a rotating disk', *Experiments in Fluids* **26**(1-2), 75–85.

Lin, T. S. & Kondic, L. (2010), 'Thin films flowing down inverted substrates: Two dimensional flow', *Physics of Fluids* **22**(5), 1–10.

Lingwood, R. J. & Henrik Alfredsson, P. (2015), 'Instabilities of the von Kármán Boundary Layer', *Applied Mechanics Reviews* **67**(3), 1–13.

Matar, O. K., Sisoev, G. M. & Lawrence, C. J. (2004), 'Evolution scales for wave regimes in liquid film flow over a spinning disk', *Physics of Fluids* **16**(5), 1532–1545.

Matar, O. K., Sisoev, G. M., Lawrence, C. J., Energiteknikk, I., Box, P. O. & Kjeller, N. (2006), 'The flow of thin liquid films over spinning discs', *Canadian Journal of Chemical Engineering* **84**(6), 625–642.

Matar, O., Sisoev, G. & Lawrence, C. (2008), 'Thin film flow over spinning discs: The effect of surface topography and flow rate modulation', *Chemical Engineering Science* **63**(8), 2225–2232.

Matsumoto, Y., Ohara, T., Teruya, I. & Ohashi, H. (1989), 'Liquid film formation on a rotating disk (numerical analysis at the initial stage)', *JSME international journal* **32**(1), 52–56.

Mavromoustaki, A., Matar, O. K. & Craster, R. V. (2012), 'Dynamics of a climbing surfactant-laden film–I: base-state flow.', *Journal of colloid and interface science* **371**(1), 107–20.

Mehdi-Nejad, V., Mostaghimi, J. & Chandra, S. (2003), 'Air bubble entrapment under an impacting droplet', *Physics of Fluids* **15**(1), 173–183.

Melo, F., Joanny, J. & Fauve, S. (1989), 'Fingering instability of spinning drops', *Physical Review Letters* **63**(18), 1958–1961.

Moisy, F., Doaré, O., Pasutto, T., Daube, O. & Rabaud, M. (2004), 'Experimental and numerical study of the shear layer instability between two counter-rotating disks', *Journal of Fluid Mechanics* **507**, 175–202.

Moisy, F., Pasutto, T. & Gauthier, G. (2003), 'Spiral patterns in swirling flows', *Europhysics News* **39**(1), 22–24.

Moisy, F. & Rabaud, M. (2014), 'Mach-like capillary-gravity wakes', *Physical Review E - Statistical, Nonlinear, and Soft Matter Physics* **90**(2), 023009.

Momoniat, E. & Mason, D. (1998), 'Investigation of the effect of the Coriolis force on a thin fluid film on a rotating disk', *International Journal of Non-Linear Mechanics* **33**(6), 1069–1088.

Moore, S. R. (1986), Mass transfer of thin liquid films on rotating surfaces, with and without chemical reaction, PhD thesis, University of Newcastle.

Moran, K., Inumaru, J. & Kawaji, M. (2002), 'Instantaneous hydrodynamics of a laminar wavy liquid film', *International Journal of Multiphase Flow* **28**(5), 731–755.

Moulin, F. Y. & Flór, J.-B. (2004), 'On the spin-up by a rotating disk in a rotating stratified fluid', *Journal of Fluid Mechanics* **516**, 155–180.

Mundo, C., Sommerfeld, M. & Tropea, C. (1995), 'Droplet-wall collisions: Experimental studies of the deformation and breakup process', *International Journal of Multiphase Flow* **21**(2), 151–173.

Myers, T. G. & Charpin, J. P. F. (2001), 'The effect of the Coriolis force on axisymmetric rotating thin film flows', **36**, 629–635.

Nernst, W. & von Lerch, F. (1904), 'Über die Verwendung des elektrolytischen Detektors in der Brückenkombination', *Annalen der Physik* **320**(14), 836–841.

Orihara, H. & Takikawa, Y. (2011), 'Brownian motion in shear flow: Direct observation of anomalous diffusion', *Physical Review E* **84**(6), 1–5.

Pasandideh-Fard, M., Qiao, Y. M., Chandra, S. & Mostaghimi, J. (1996), 'Capillary effects during droplet impact on a solid surface', *Physics of Fluids* **8**(3), 650.

Pask, S. D., Nuyken, O. & Cai, Z. (2012), 'The spinning disk reactor: An example of a process intensification technology for polymers and particles', *Polymer Chemistry* **3**(10), 2698–2707.

Pereira, A., Trevelyan, P. M. J., Thiele, U. & Kalliadasis, S. (2007), 'Interfacial hydrodynamic waves driven by chemical reactions', *Journal of Engineering Mathematics* **59**(2), 207–220.

PhysiologyWeb (2016), 'Diffusion Time Calculator'.
URL: *http://www.physiologyweb.com/calculators/diffusion_time_calculator.html*

Povarov, O. A., Nazarov, O. I., Ignat'evskaya, L. A. & Nikol'skii, A. I. (1976), 'Interaction of drops with boundary layer on rotating surface', *Journal of Engineering Physics* **31**(6), 1453–1456.

Sarma, G. S., Lu, P. C. & Ostrach, S. (1971), 'Film stability in a vertical rotating tube with a core-gas flow', *Physics of Fluids* **14**(11), 2265–2277.

Schwartz, L. W. (1989), 'Viscous flows down an inclined plane: Instability and finger formation', *Physics of Fluids A: Fluid Dynamics* **1**(3), 443.

Serdyuk, I. N., Zaccai, N. R., Zaccai, J., Zaccal, N. & Zaccal, P. (2007), *Methods in Molecular Biophysics*, Cambridge University Press.

Silvi, N. & Dussan V, E. B. (1985), 'The rewetting of an inclined solid surface by a liquid', *Physics of Fluids* **28**(1), 5–7.

Sisoev, G. M., Matar, O. K. & Lawrence, C. J. (2003), 'Axisymmetric wave regimes in viscous liquid film flow over a spinning disk', *Journal of Fluid Mechanics* **495**, 385–411.

Sisoev, G. M., Matar, O. K. & Lawrence, C. J. (2005), 'Gas absorption into a wavy film flowing over a spinning disc', *Chemical Engineering Science* **60**(7), 2051–2060.

Solheim, T. E., Salvemini, F., Dalziel, S. & Raston, C. L. (2019), 'Neutron imaging and modelling inclined vortex driven thin films', *Scientific reports* **9**(1), 2817.

Spaid, M. A. & Homsy, G. M. (1996), 'Stability of Newtonian and viscoelastic dynamic contact lines', *Physics of Fluids* **8**(2), 460.

Sveen, J. K. & Dalziel, S. B. (2005), 'A dynamic masking technique for combined measurements of PIV and synthetic schlieren applied to internal gravity waves', *Measurement Science and Technology* **16**(10), 1954–1960.

Takagi, D. & Huppert, H. E. (2010), 'Flow and instability of thin films on a cylinder and sphere', *Journal of Fluid Mechanics* **647**, 221.

Thoroddsen, S. T. & Van Atta, C. W. (1996), 'Baroclinic generation of vorticity by an axisymmetric vortex in a linearly stratified fluid; in the passive limit', *Physics of Fluids* **8**(10), 2774–2776.

Tong, C., Boulos, R., Yu, C., Iyer, K. & Raston, C. (2013), 'Continuous flow tuning of ordered mesoporous silica under ambient conditions', *RSC Advances* **3**(41), 18767–18770.

Troian, S. & Herbolzheimer, E. (1989), 'Fingering instabilities of driven spreading films', *Europhysics Letters* **10**(1), 25–30.

Van de Vooren, A. I. (1992), 'The Stewartson layer of a rotating disk of finite radius', *Journal of Engineering Mathematics* **26**(1), 131–152.

Vimalanathan, K., Gascooke, J. R., Suarez-martinez, I., Marks, N., Kumari, H., Garvey, C. J., Atwood, J. L., Lawrance, W. D. & Raston, C. L. (2016), 'Fluid dynamic lateral slicing of high tensile strength carbon nanotubes', *Scientific Reports* **6**(1), 4–10.

Wahid, M. H., Eroglu, E., Chen, X., Smith, S. M. & Raston, C. L. (2013*a*), 'Entrapment of Chlorella vulgaris cells within graphene oxide layers', *RSC Advances* **3**(22), 8180.

Wahid, M. H., Eroglu, E., Chen, X., Smith, S. M. & Raston, C. L. (2013*b*), 'Functional multi-layer graphene–algae hybrid material formed using vortex fluidics', *Green Chemistry* **15**(3), 650.

Walker, J. A., Mezyk, S. P., Roduner, E. & Bartels, D. M. (2016), 'Isotope Dependence and Quantum Effects on Atomic Hydrogen Diffusion in Liquid Water', *Journal of Physical Chemistry B* **120**(8), 1771–1779.

Wang, M.-W. & Chou, F.-C. (2001), 'Fingering Instability and Maximum Radius at High Rotational Bond Number', *Journal of The Electrochemical Society* **148**(5), G283.

Wang, M.-W., Ma, J.-L. & Hourng, L.-W. (2014), 'Effects of dispensing flow rate on fingering instability during spin coating', *Japanese Journal of Applied Physics* **53**(3), 036501.

Whitman, W. (1923), 'The Two-Film Theory of Gas Absorption', *Chemical and Metallurgical Engineering* **29**(4), 146–148.

Wilkes, J. O. & Bike, S. G. (1999), *Fluid mechanics for chemical engineers*, Prentice Hall.

Wilson, S. K., Hunt, R. & Duffy, B. R. (2000), 'The rate of spreading in spin coating', *Journal of Fluid Mechanics* **413**, 65–88.

Woods, W. (1995), The hydrodynamics of thin liquid films flowing over a rotating disk, PhD thesis, University of Newcastle.

Yasin, F. M., Boulos, R. A., Hong, B. Y., Cornejo, A., Iyer, K. S., Gao, L., Chua, H. T. & Raston, C. L. (2012), 'Microfluidic size selective growth of palladium nano-particles on carbon nano-onions.', *Chemical communications* **48**(81), 10102.

Appendices

Appendix A

Flat disk

A.1 Set FB-H5V80

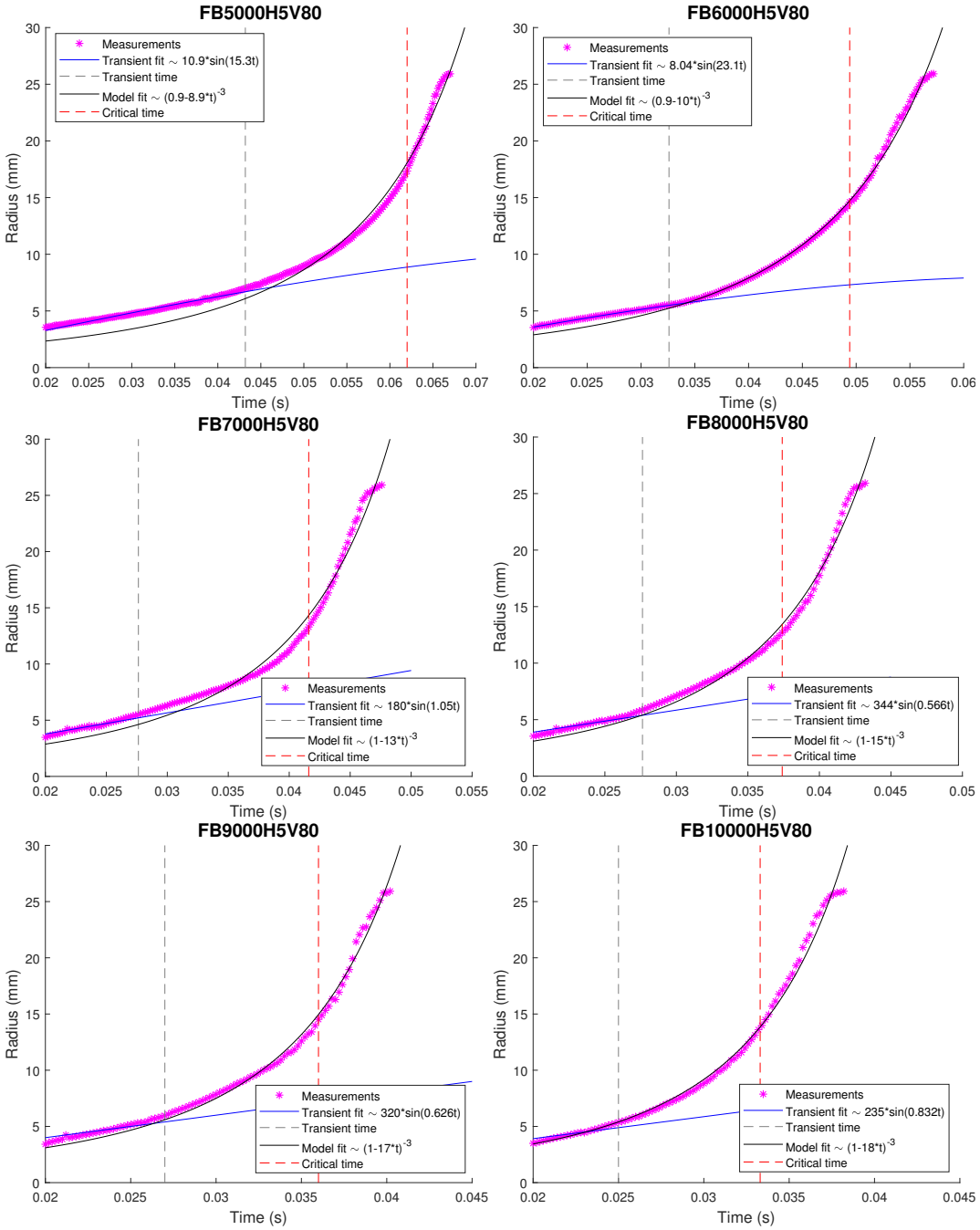

Figure A.1: Radius evolution for the set FB-H05V80.

A.2 Set FB-H10V80

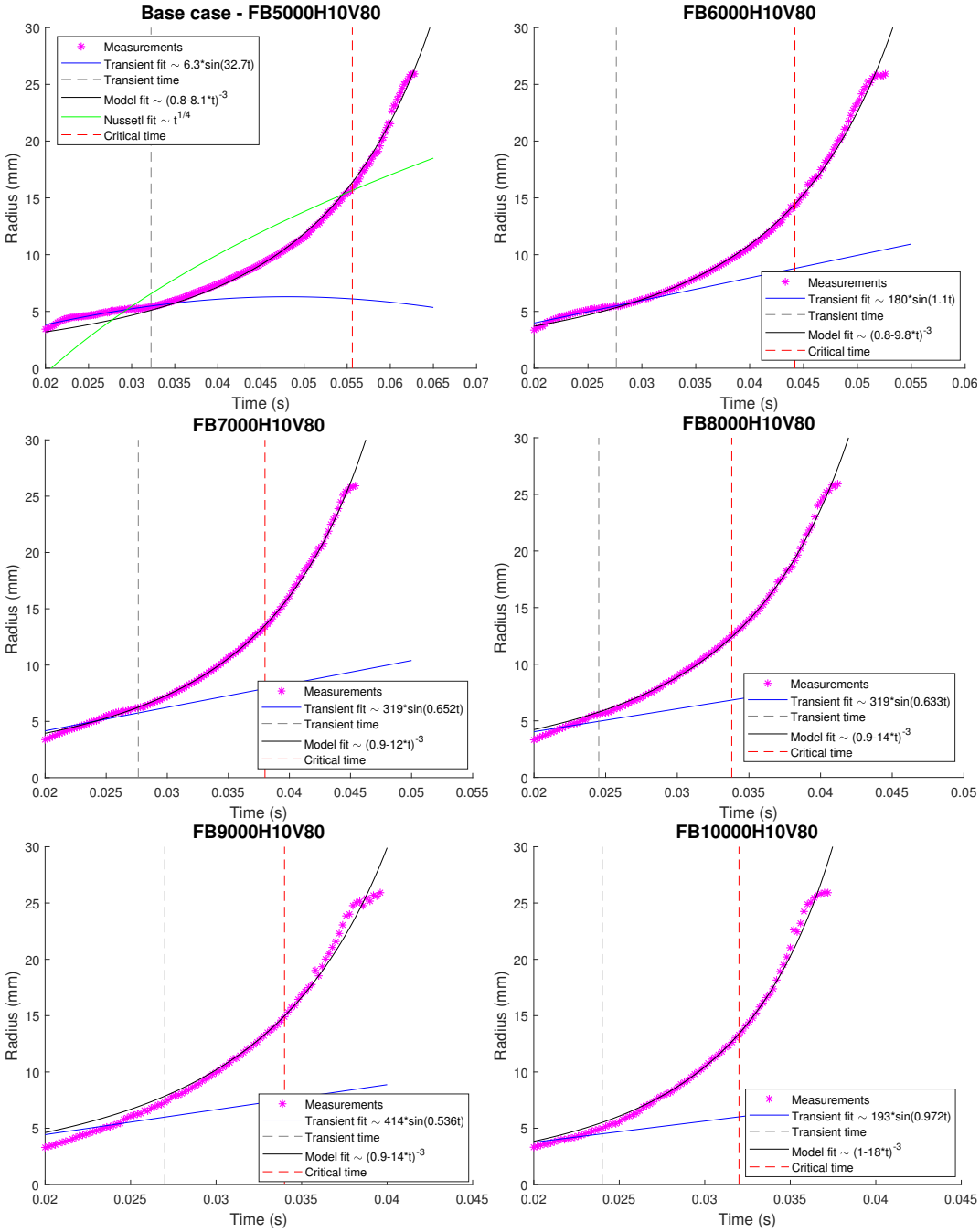

Figure A.2: Radius evolution for the set FB-H10V80.

A.3 Set FB-H15V80

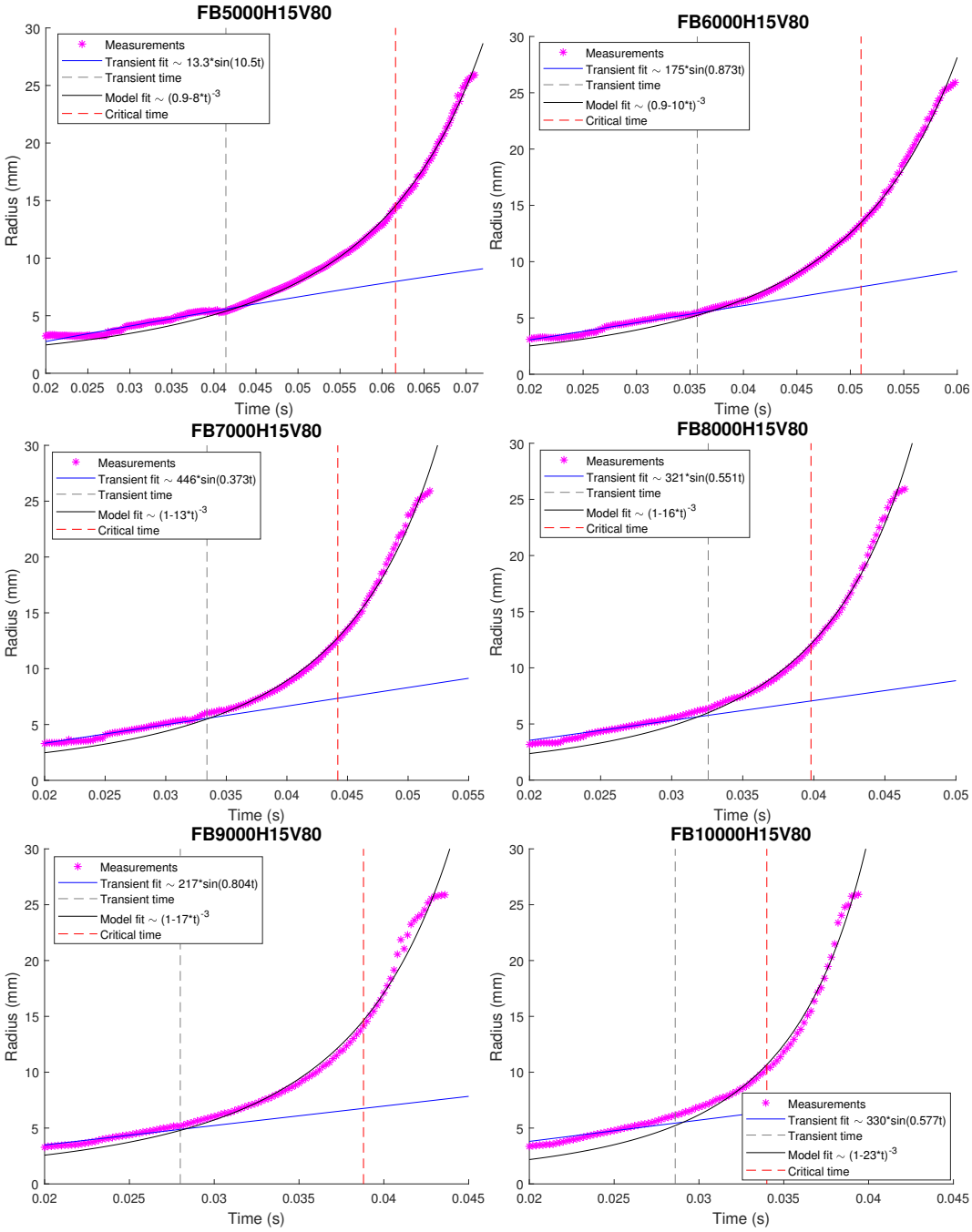

Figure A.3: Radius evolution for the set FB-H15V80.

A.4 Set FB-H10V40

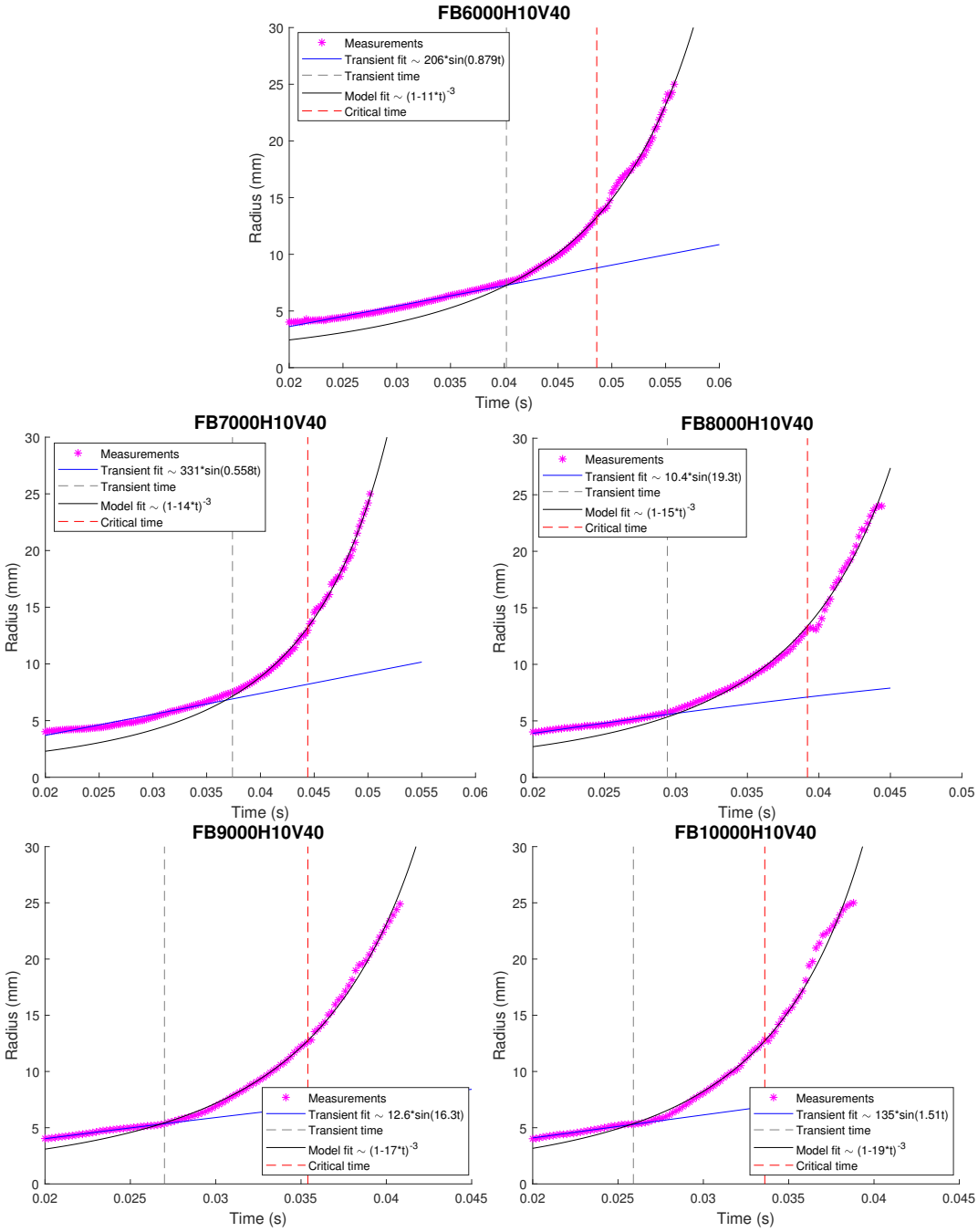

Figure A.4: Radius evolution for the set FB-H10V40.

A.5 Set FG-H10V80

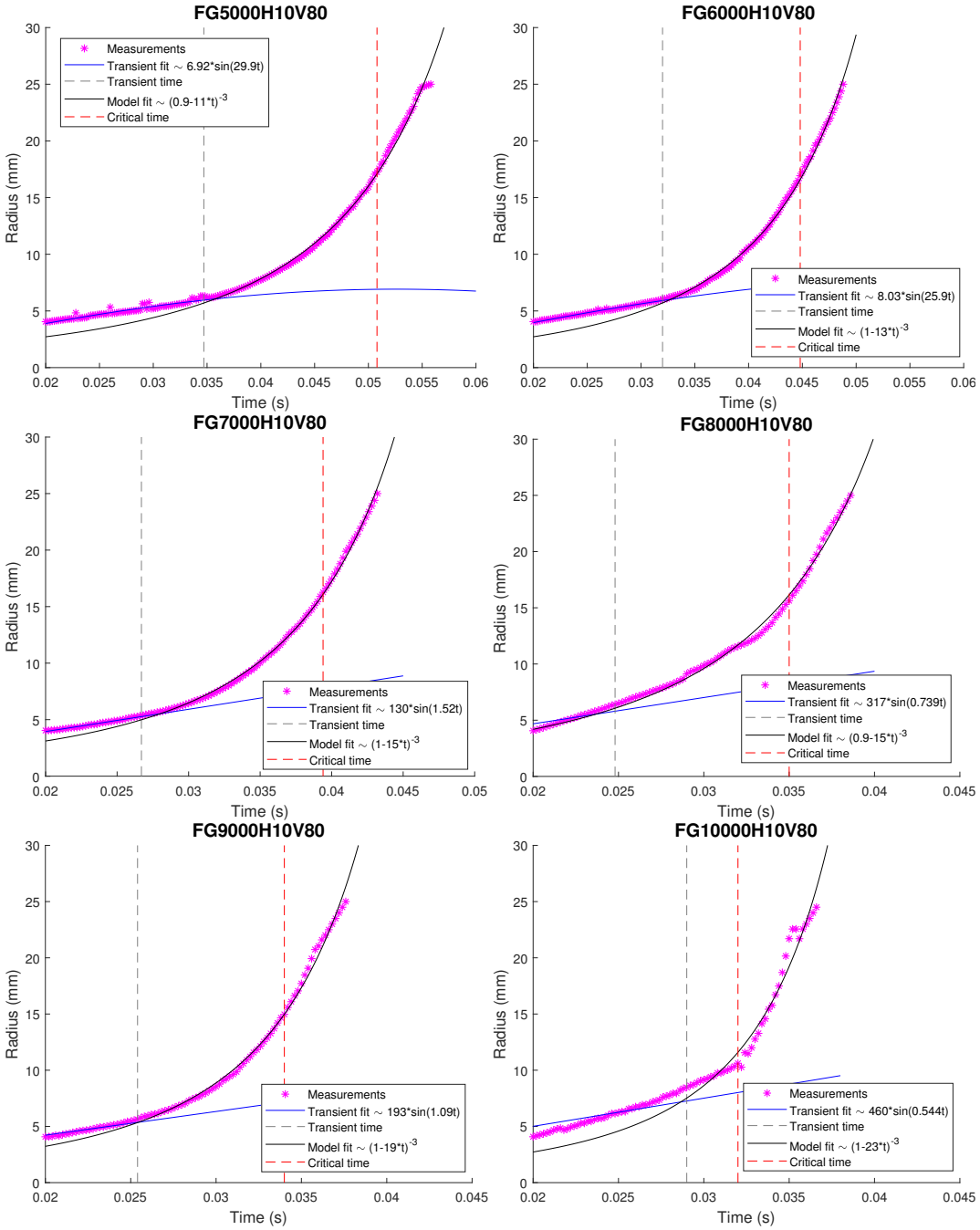

Figure A.5: Radius evolution for the set FB-H10V80.

A.6 Set FB-H10V80 (spiral waves)

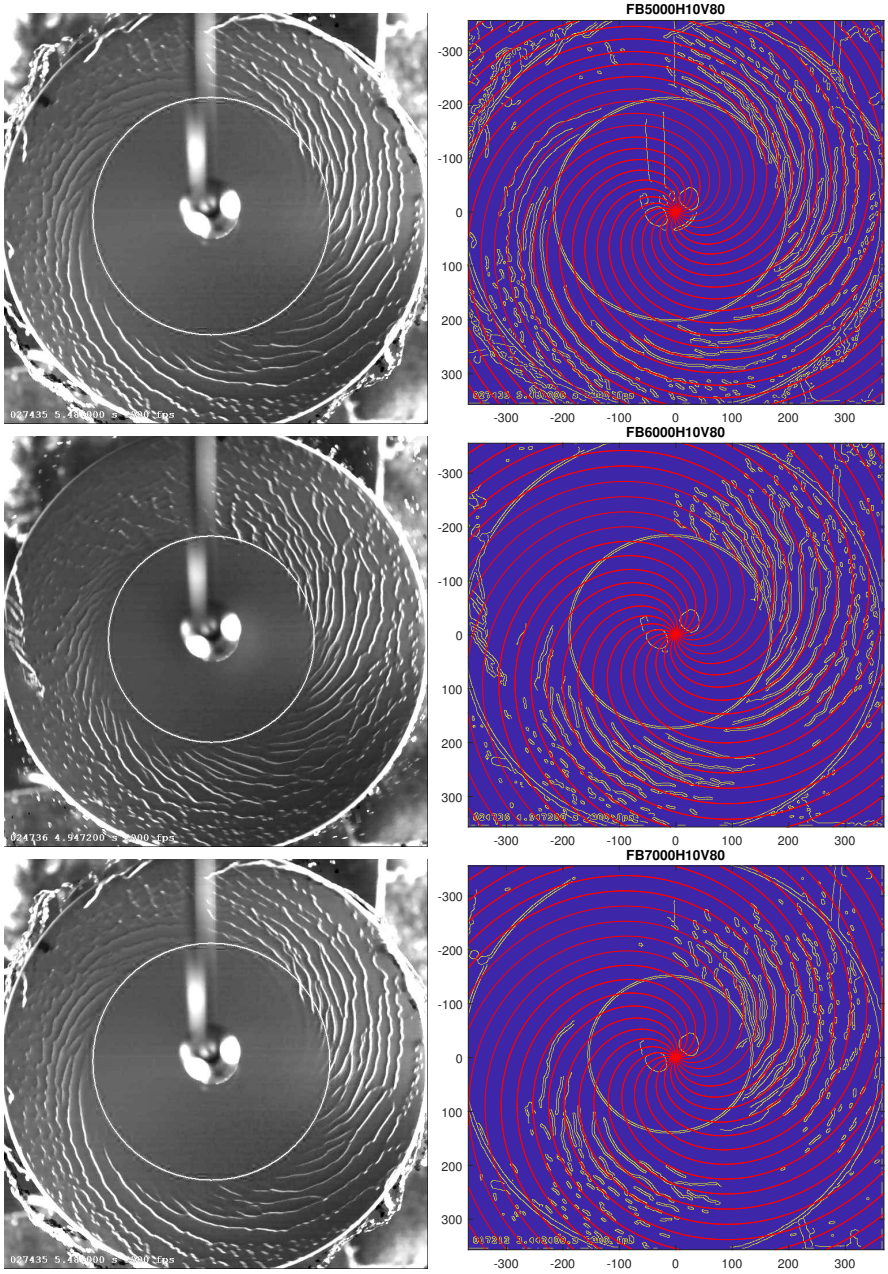

Figure A.6: Spiral waves for the set FB-H10V80.

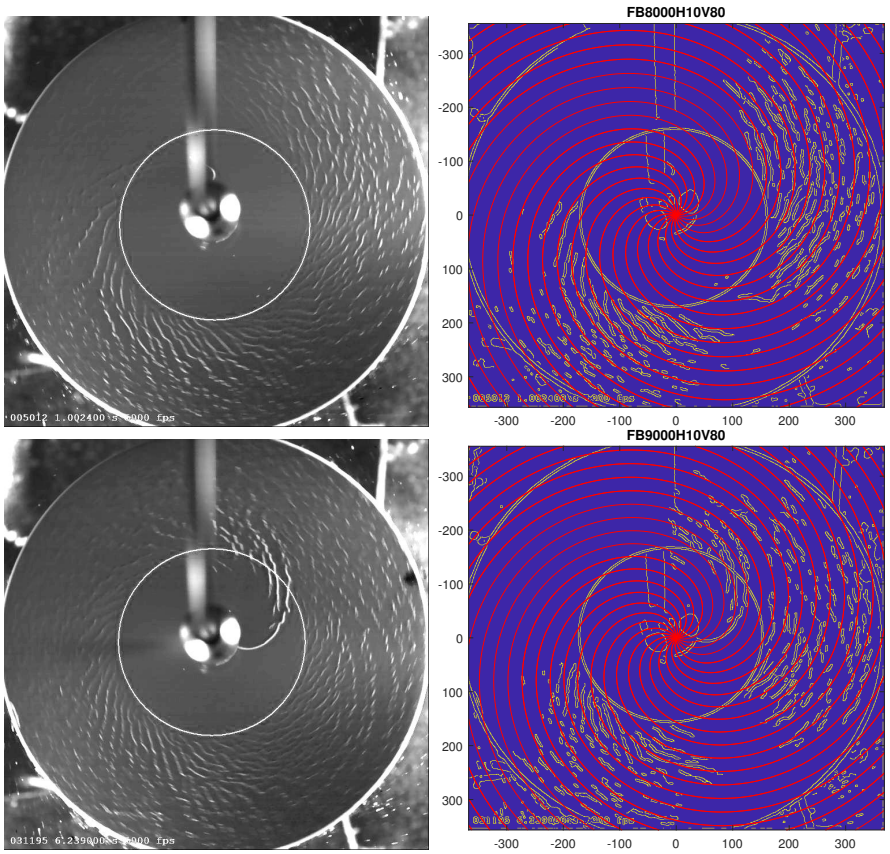

Figure A.7: Spiral waves for the set FB-H10V80.

Appendix B

Hemispherical disk

B.1 Set HB-H5V80

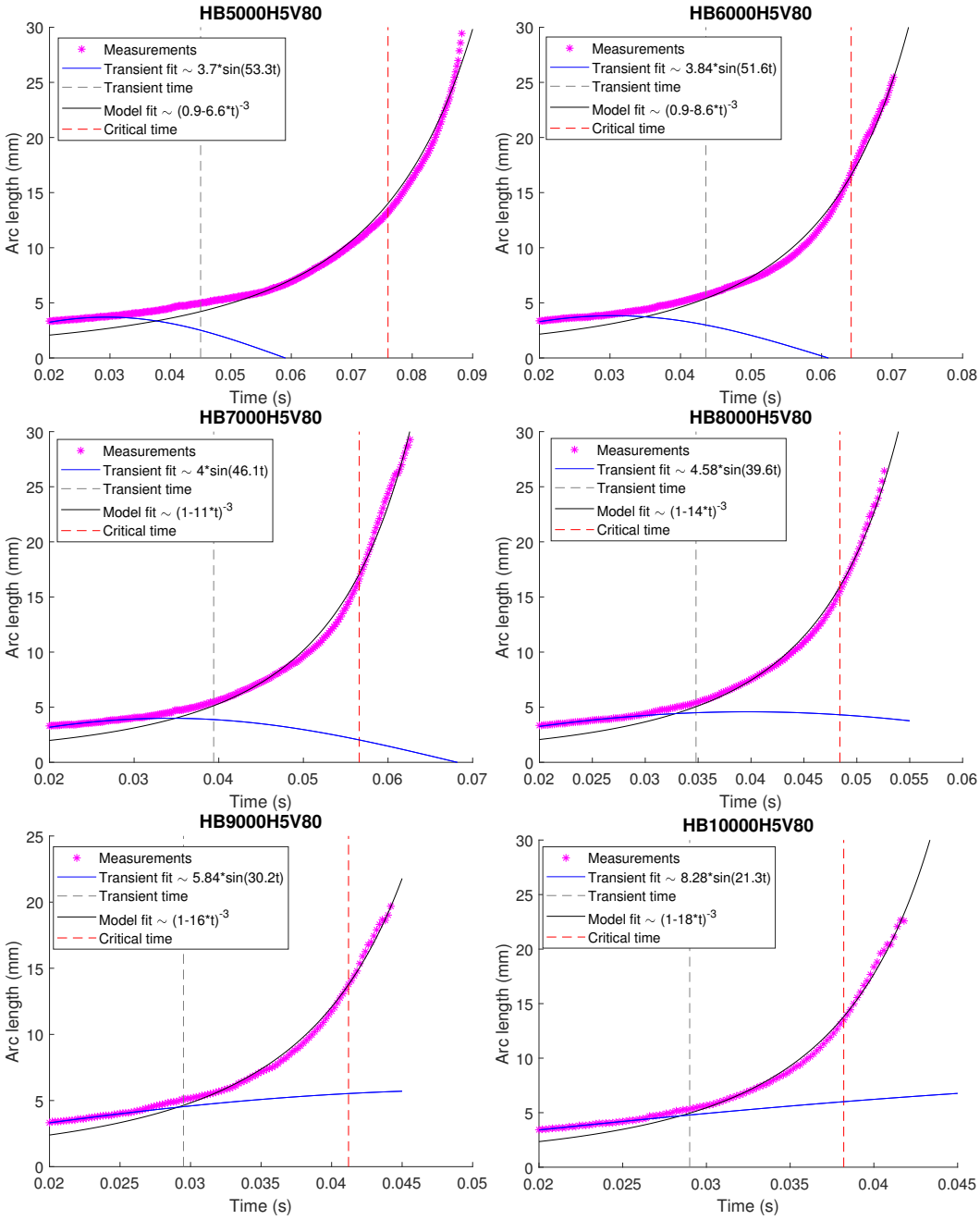

Figure B.1: Radius evolution for the set HB-H5V80.

B.2 Set HB-H10V80

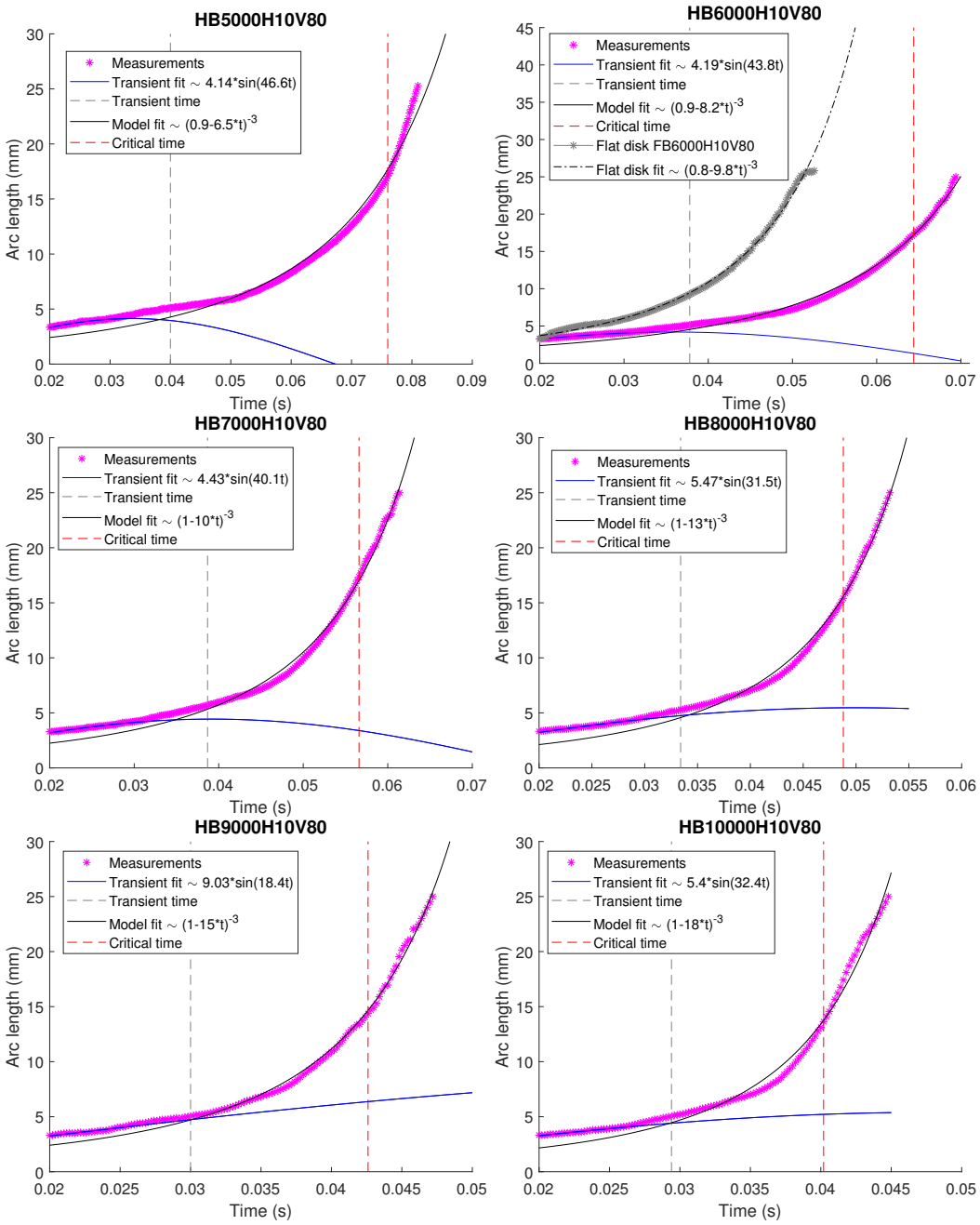

Figure B.2: Radius evolution for the set HB-H10V80.

B.3 Set HB-H15V80

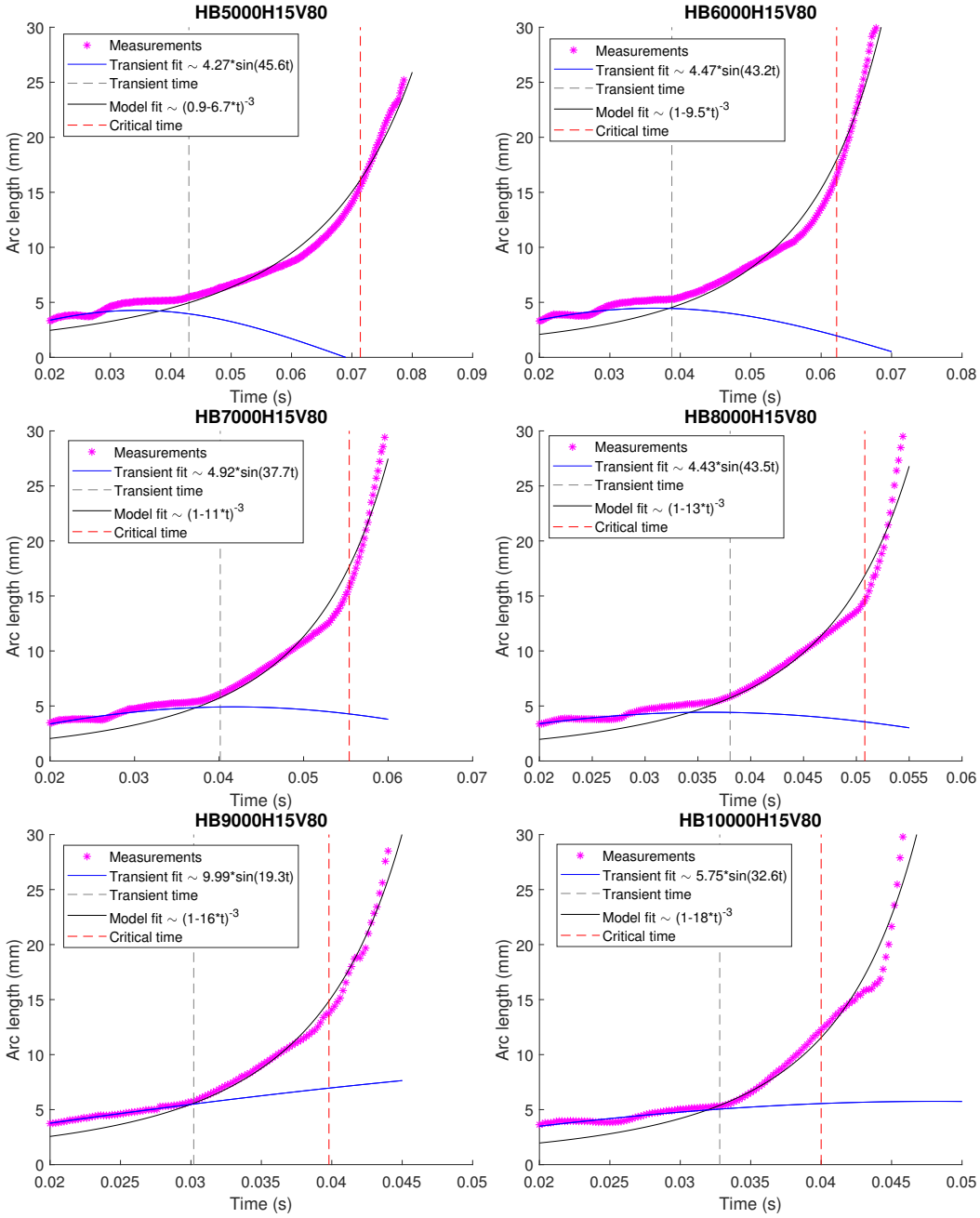

Figure B.3: Radius evolution for the set HB-H15V80.

Appendix C

VFD

C.1 CM45GT-W1

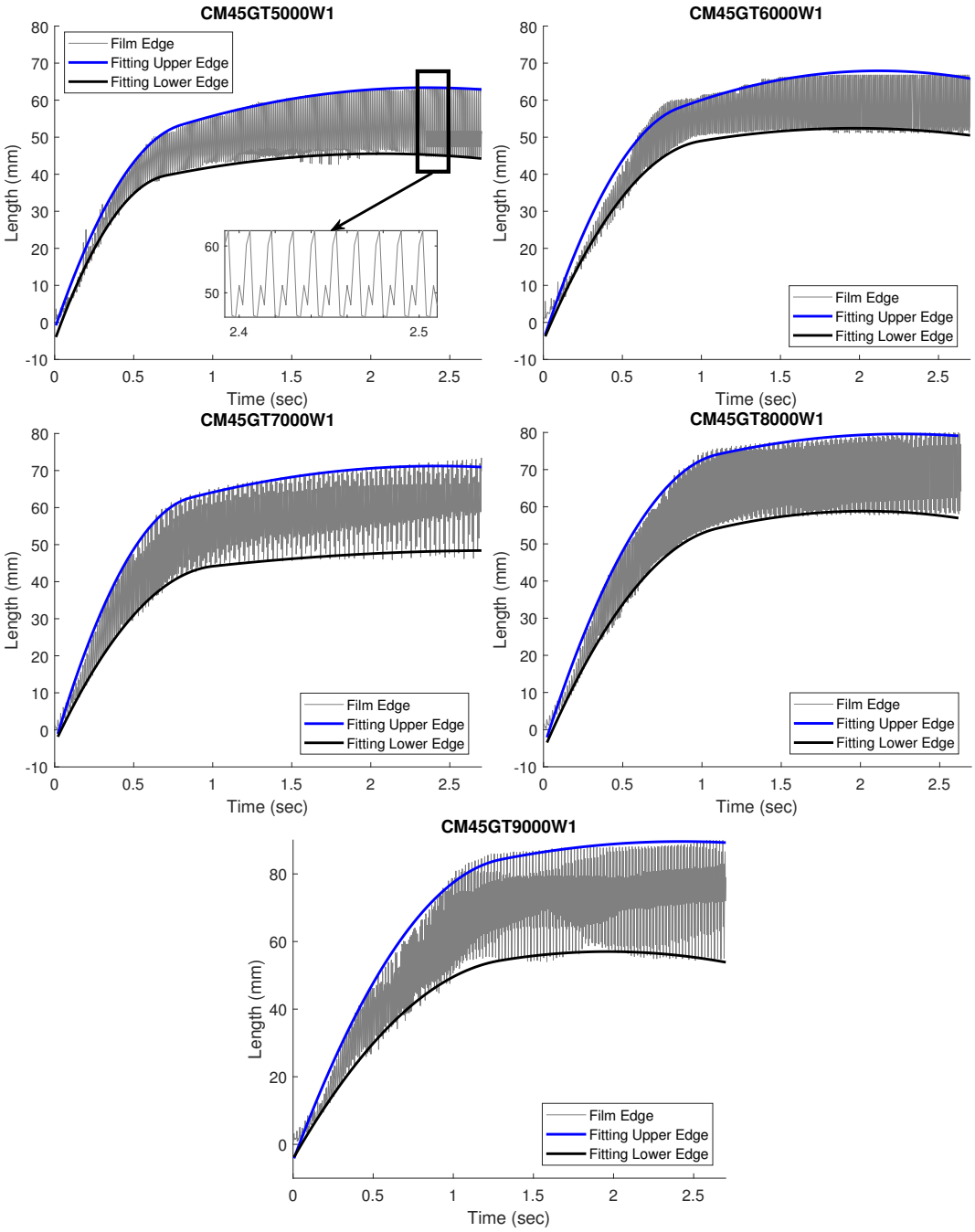

Figure C.1: Film evolution for the set CM45GT-W1.

C.2 CM85GT-W1

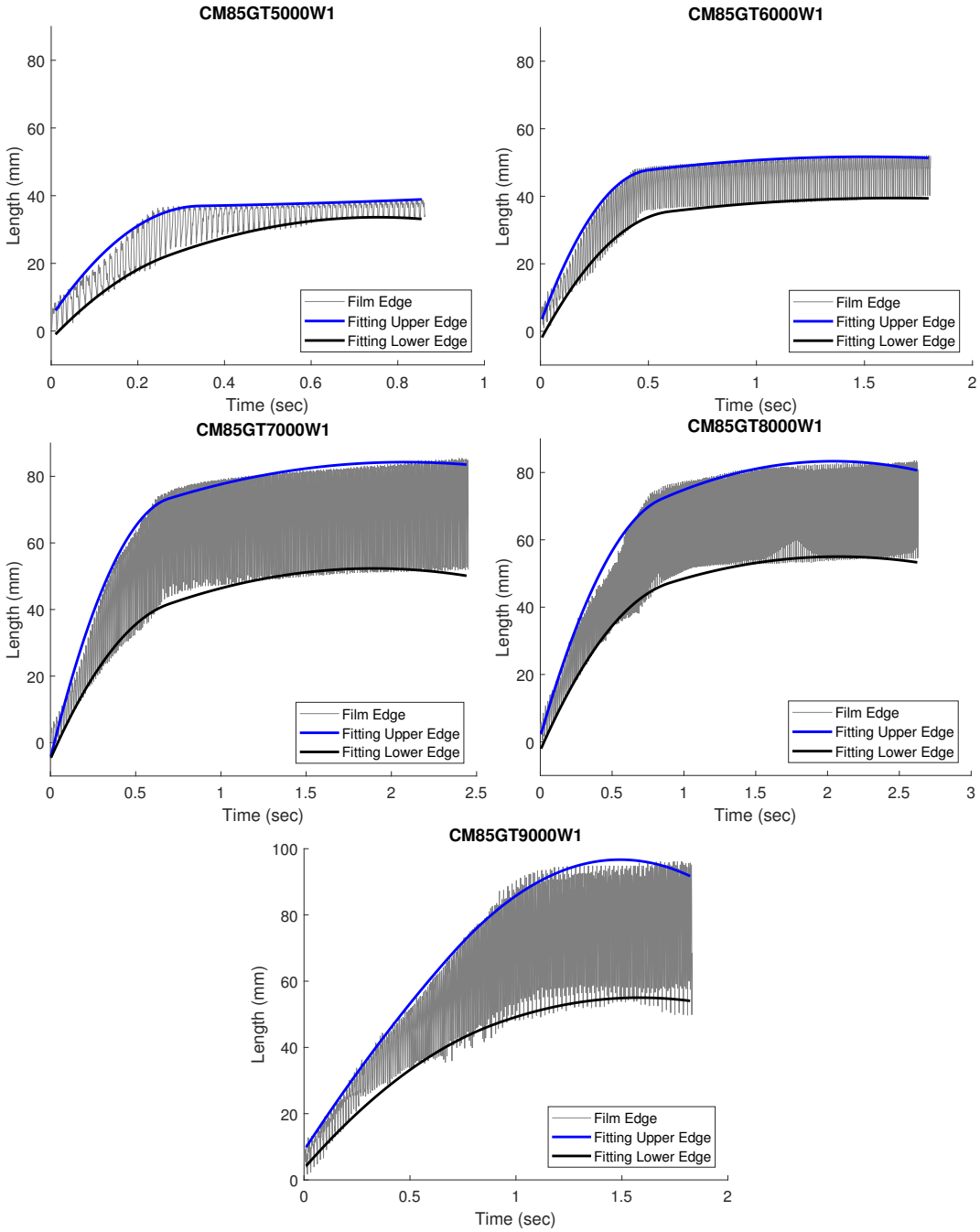

Figure C.2: Film evolution for the set CM85GT-W1.

C.3 CM45QT-W1

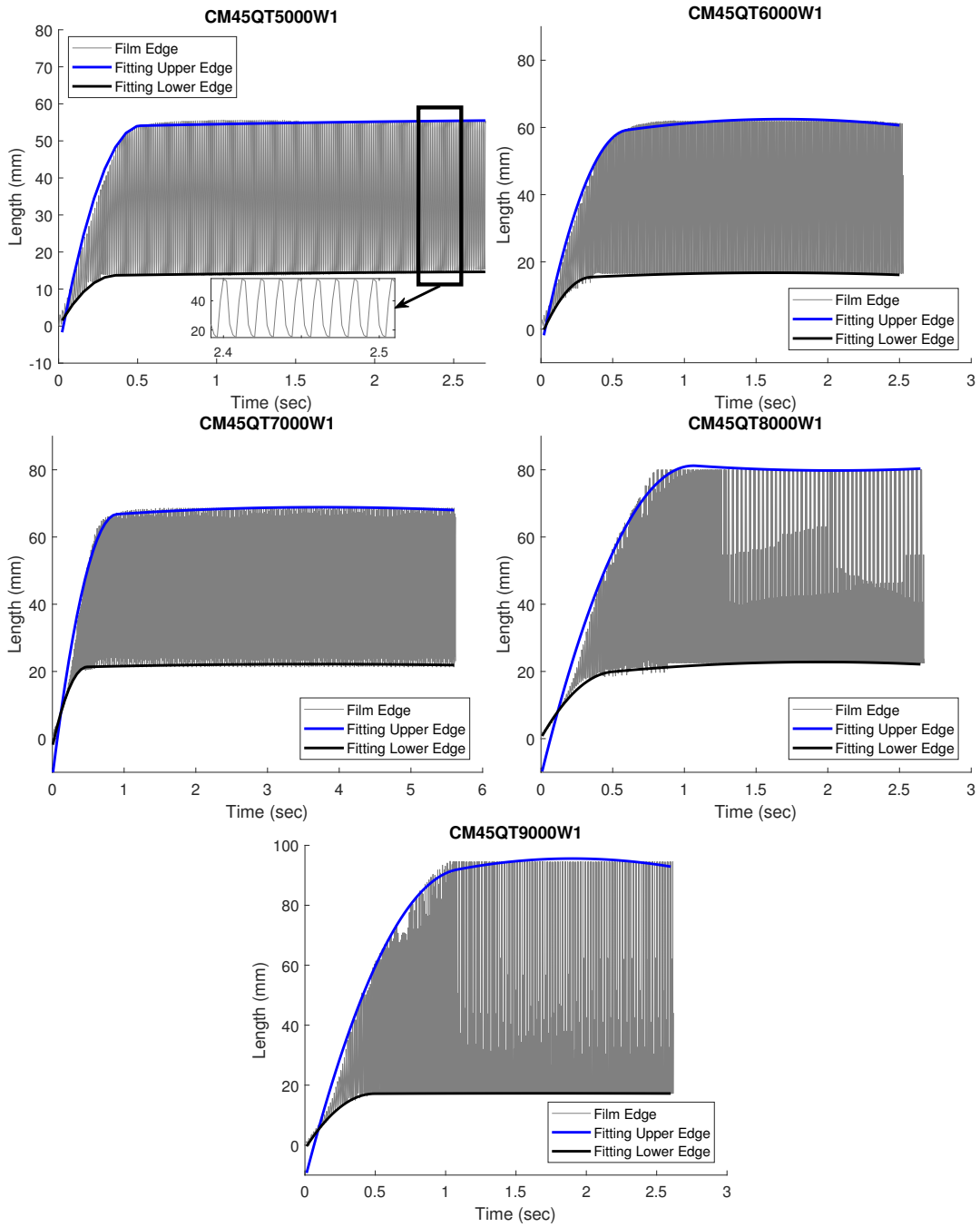

Figure C.3: Film evolution for the set CM45QT-W1.

C.4 CM45QT-T1

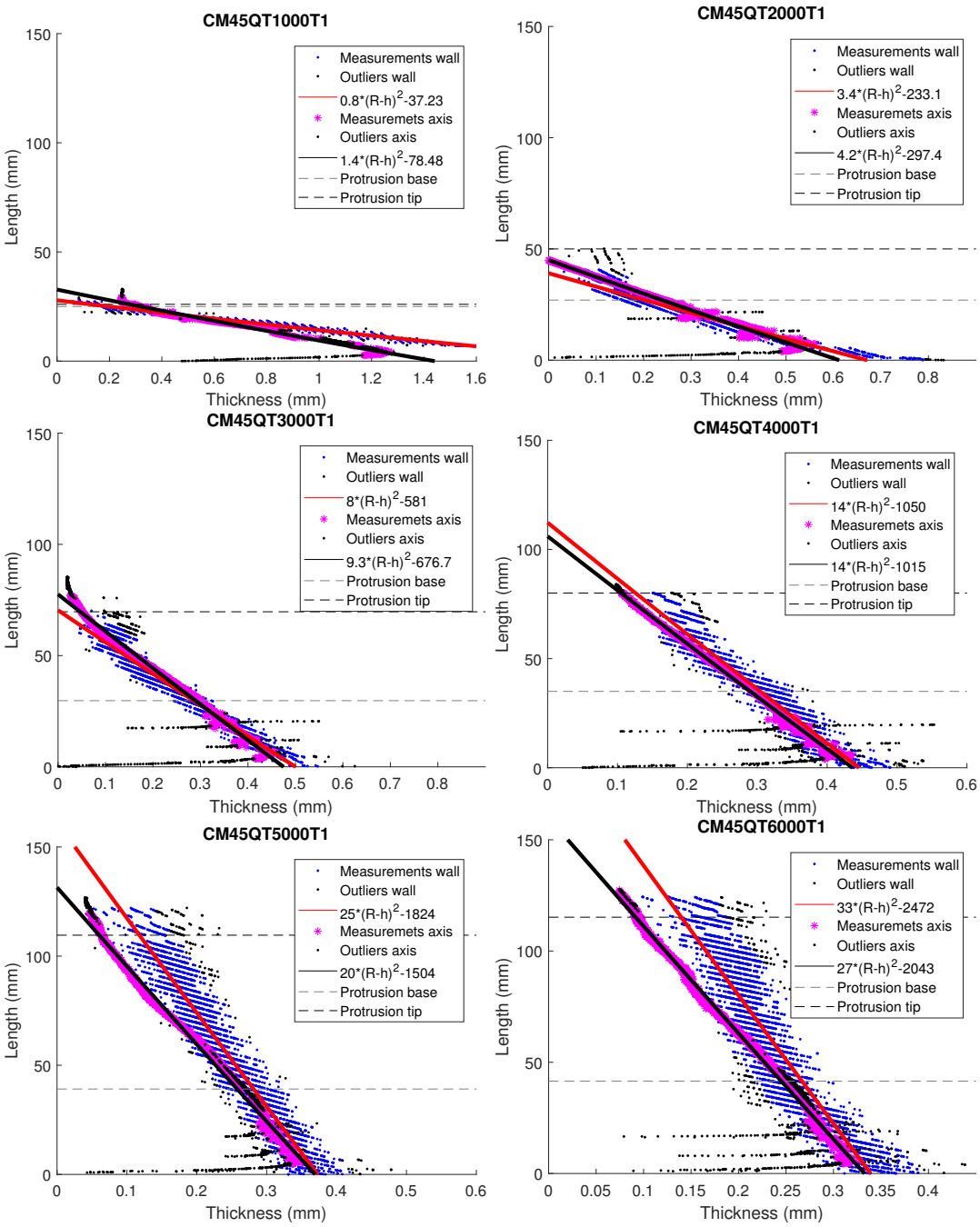

Figure C.4: Film thickness for the set CM45QT-T1.

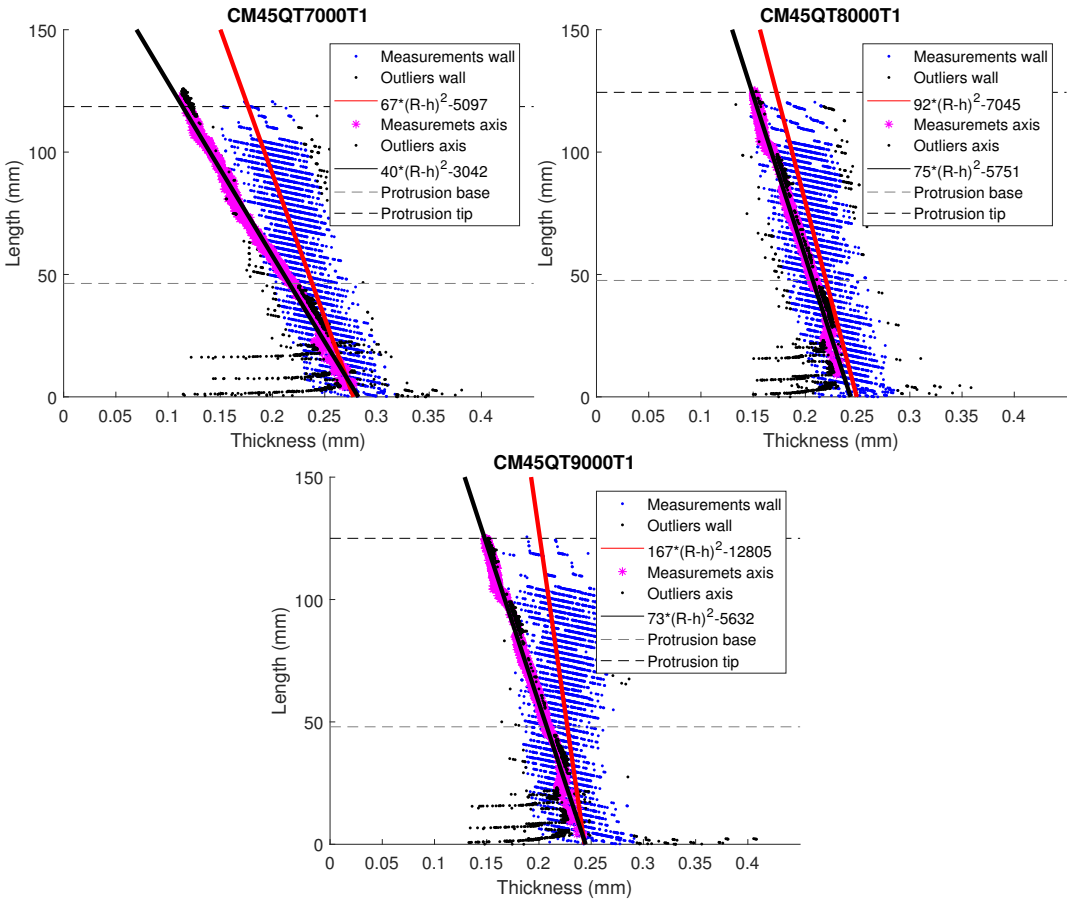

Figure C.5: Film thickness for the set CM45QT-T1.

C.5 D-QT45B3S40

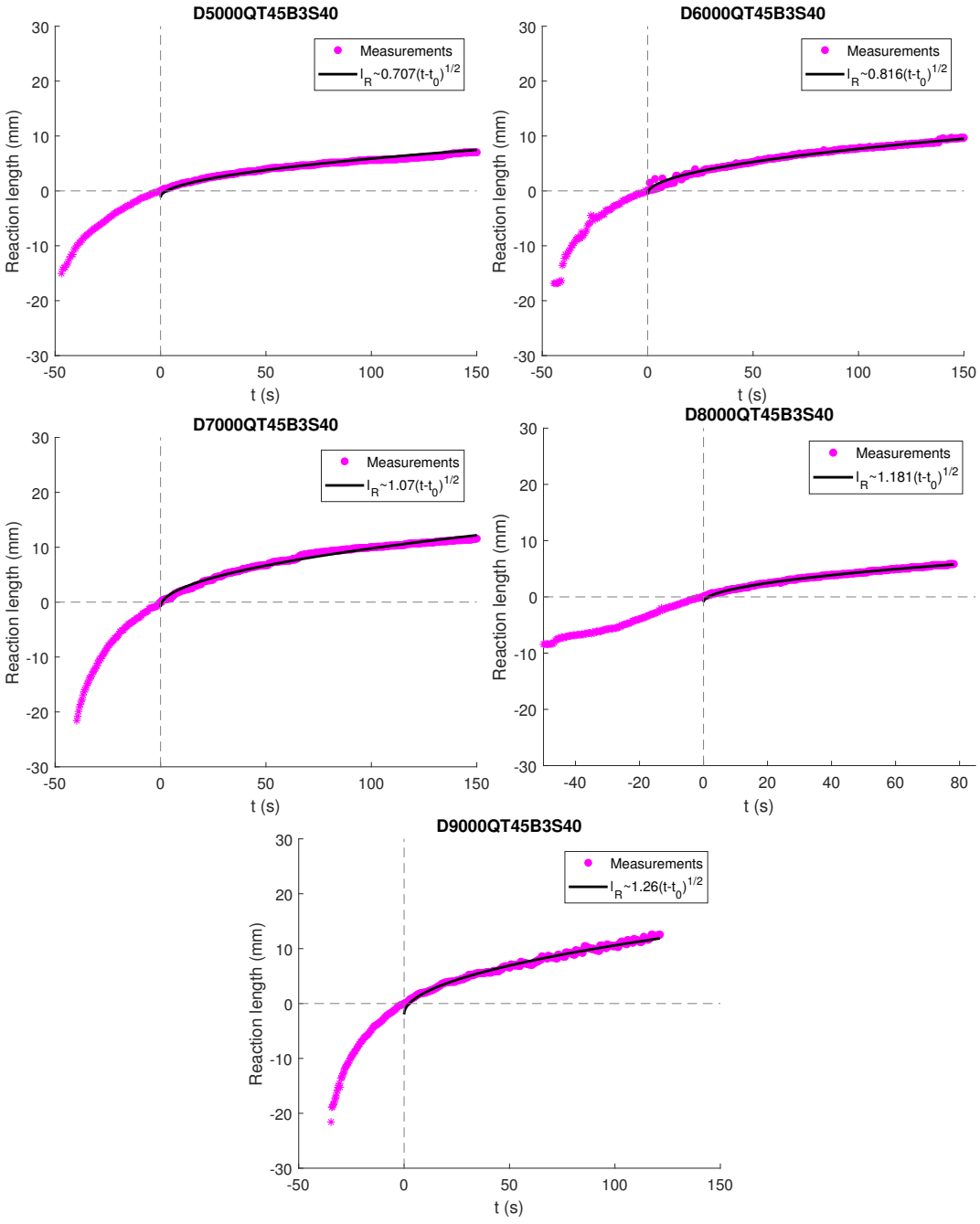

Figure C.6: Reaction evolution for the set D-QT45B3S40.